AD NUMBER

ADB023441

NEW LIMITATION CHANGE

TO

Approved for public release, distribution unlimited

FROM

Distribution authorized to U.S. Gov't. agencies only; Test and evaluation; 28 Jul 1977. Other requests shall be referred to AF Flight Dynamamics [FBE], Wright-Patterson AFB, OH, 45433.

AUTHORITY

AFWAL ltr, 16 Sep 1982

AD B023441

AUTHORITY: AF WAL
7TH 16 Sep 82

AFFDL-TR-77-59
Volume I

ADB023441

PREDICTION OF PRESSURE FLUCTUATIONS ASSOCIATED WITH MANEUVERING RE-ENTRY WEAPONS

GENERAL ELECTRIC COMPANY
RE-ENTRY AND ENVIRONMENTAL SYSTEMS DIVISION
PHILADELPHIA, PENNSYLVANIA 19101

JULY 1977

FINAL REPORT AFFDL-TR-77-59

AIR FORCE FLIGHT DYNAMICS LABORATORY
AIR FORCE WRIGHT AERONAUTICAL LABORATORIES
AIR FORCE SYSTEMS COMMAND
WRIGHT-PATTERSON AIR FORCE BASE, OHIO 45433

DDC

DEC 6 1977

B

NOTICE

When Government drawings, specifications, or other data are used for any purpose other than in connection with a definitely related Government procurement operation, the United States Government thereby incurs no responsibility nor any obligation whatsoever; and the fact that the Government may have formulated, furnished, or in any way supplied the said drawings, specifications, or other data is not to be regarded by implication or otherwise as in any manner licensing the holder or any other person or corporation, or conveying any rights or permission to manufacture, use, or sell any patented invention that may in any way be related thereto.

This technical report has been reviewed and is approved for publi- cation.

LEONARD L. SHAW
Project Engineer

ROBERT M. BADER, Chief
Structural Integrity Branch
Structural Mechanics Division

FOR THE COMMANDER

HOWARD L. FARMER, Colonel USAF
Chief, Structural Mechanics Division

REPORT DOCUMENTATION PAGE	READ INSTRUCTIONS BEFORE COMPLETING FORM	
1. REPORT NUMBER AFFDL-TR-77-59 — Vol-1	2 GOVT ACCESSION NO	3 RECIPIENT'S CATALOG NUMBER
4. TITLE (and Subtitle) Prediction of Pressure Fluctuations Associated with Maneuvering Re-entry Weapons. Volume I.		5. TYPE OF REPORT & PERIOD COVERED Final Report April 1975 — July 1977
		6. PERFORMING ORG. REPORT NUMBER AFFDL-TR-77-59
7. AUTHOR(s) Anthony L. Laganelli John R. Howe		8. CONTRACT OR GRANT NUMBER(s) F33615-75-C-3065
9. PERFORMING ORGANIZATION NAME AND ADDRESS General Electric Company Re-entry and Environmental Systems Division Philadelphia, Pennsylvania 19101		10. PROGRAM ELEMENT, PROJECT, TASK AREA & WORK UNIT NUMBERS 1367-04-05
11. CONTROLLING OFFICE NAME AND ADDRESS Air Force Flight Dynamics Laboratory (AFFDL/FBE) Air Force Systems Command Wright-Patterson AFB, Ohio 45433		12. REPORT DATE July 1977
		13. NUMBER OF PAGES 224
14. MONITORING AGENCY NAME & ADDRESS(If different from Controlling Office) 245p.		15. SECURITY CLASS. (of this report) Unclassified
		15a. DECLASSIFICATION/DOWNGRADING SCHEDULE

16. DISTRIBUTION STATEMENT (of this Report)

Distribution limited to U.S. Government agencies only; test and evaluation; statement applied 28 July 1977. Other requests for this document must be referred to AF Flight Dynamics Laboratory, (FBE), Wright-Patterson AFB, Ohio 45433

17. DISTRIBUTION STATEMENT (of the abstract entered in Block 20, If different from Report)

18. SUPPLEMENTARY NOTES

19. KEY WORDS (Continue on reverse side if necessary and identify by block number)

Aeroacoustic loads, rms fluctuating pressure, power spectral density, cross-power spectral density, cross-correlation functions, ballistic re-entry vehicles, maneuvering re-entry vehicles, attached turbulent boundary layers, transitional boundary layers

20. ABSTRACT (Continue on reverse side if necessary and identify by block number)

An experimental program was conducted at the AEDC von Karman facility, Tunnels A and B, in which acoustic pressure fluctuation data were acquired on a 7° half-cone-angle model featuring a control surface. The objective was to define the aeroacoustic environment applicable to re-entry vibration response analysis for both ballistic and maneuvering vehicles. Wind tunnel measurements were obtained at Mach 4 and 8 for several values of freestream Reynolds number and model angle of attack. Stationary zones of laminar, transitional, and turbulent flow over the model were achieved. Acoustic

404 884

data were reduced to rms fluctuating pressure, and power and cross-power spectral densities. Results were normalized using local boundary layer parameters for comparison with previous high speed measurements.

The present study re-examined the aeroacoustic environment prediction capability relative to compressible flow conditions. Moreover, boundary layer characteristic lengths and velocities were reviewed in order to develop normalization procedures required for development of appropriate aeroacoustic scaling laws. It was determined that fluctuating pressure characteristics described by incompressible theory as well as empirical correlations could be modified to a compressible state through a transformation function. In this manner, compressible data were transformed to the incompressible plane where direct use of more tractable prediction techniques are available for engineering design analyses.

Efforts performed in this investigation are discussed in two volumes. Volume I contains the analysis and representative data from the wind tunnel test program. This volume emphasizes development of appropriate aeroacoustic environment prediction techniques for re-entry vehicle vibration response analyses. Volume II, which is classified, contains detailed description of the wind tunnel model and test program, and presents the raw data from several select test conditions analyzed in this investigation. This second volume also describes the vibration analysis program and subsequent application of upgraded aeroacoustic load prediction techniques to ballistic and maneuvering type re-entry vehicles.

FOREWORD

TABLE OF CONTENTS

LIST OF TABLES

LIST OF ILLUSTRATIONS .

LIST OF SYMBOLS

A	Parameter, $1.7 < A < 3$, incompressible flow
C_f	Skin-friction coefficient
$C(\xi, \eta, f)$	Co cross-power spectral density (ϕ_R)
f	Frequency
h	Enthalpy
k_ξ, k_η	Longitudinal wave length, lateral wave length
l	Characteristic length
l_m	Mixing length
L	Model axial length
m	Viscous power law exponent
M	Mach number
MF	Mangler factor
n	Velocity power law exponent
p_{rms}	Measured root-mean-square (rms) acoustic pressure
$\bar{p}$	Measured rms pressure in current program (20 Hz – 20 kHz)
p_e	Local boundary layer static pressure
q	Dynamic pressure
$Q(\xi, \eta, f)$	Quad cross-power spectral density (ϕ_i)
r	Recovery factor (0.896 for turbulent flow)
r_e	Recovery type factor defined by Houbolt
Re	Reynolds number
R_N, R_B	Nose radius, base radius
$R(\xi, \eta, t)$	Broad-band space-time correlation

s	Wetted length of surface or generalized separation distance between two points (ξ or η)
SPL	Sound pressure level
St	Stanton number (heat transfer coefficient)
T	Temperature
t	Time
u, v (U,V)	Velocity in stream directions, normal direction
u_c, u_{c_b}	Convection velocity, broad-band value
u_τ	Shear velocity
V	Characteristic velocity
x, y	Coordinate distance in stream and normal direction, respectively

GREEK SYMBOLS

α	Angle of attack
γ	Ratio of specific heats (1.4 for air)
δ	Boundary layer thickness
δ^*	Boundary layer displacement thickness
δ_F	Flap deflection angle
ϵ_T	Compressibility factor
ϵ_m, ϵ_o	Turbulent eddy viscosity, molecular (inner) and turbulent (outer), respectively
η	Lateral separation distance (normal to flow)
θ	Boundary layer momentum thickness
θ_c	Cone half angle
λ_∞	Dimensionless blowing rate, $(\rho v)_w / (\rho u)_\infty$
$\lambda_\xi, \lambda_\eta$	Wave length in stream and normal direction, respectively

μ	Dynamic viscosity
υ	Kinematic viscosity
ξ	Longitudinal separation distance (stream direction)
ρ	Density of fluid
σ	Theoretical value of rms fluctuating pressure $(0 - \infty$ Hz)
τ	Shear stress
φ	Power spectral density
Φ	Cross-power spectral density
ω	Frequency - radians per second

SUBSCRIPTS

aw	Adiabatic wall
b	Broad-band
c	Compressible conditions
cw	Cold wall
e	Evaluated at edge of boundary layer
i	Incompressible conditions
s, x	Based on wetted length, axial length
w	Wall
1	Location in boundary layer near the wall, site of most intense eddy formation
∞	Freestream conditions
ξ, η	Based on stream and lateral directions, respectively
θ, δ, δ^*	Based on boundary layer momentum, velocity and displacement thickness, respectively
τ	Based on shear stress conditions

SUPERSCRIPTS

*   Based on reference temperature conditions

ABBREVIATIONS

S.C.   Sharp cone

F.P.   Flat plate

O.C.   Ogive cylinder

W.T.W.   Wind tunnel wall

TBL   Turbulent boundary layer

LBL   Laminar boundary layer

Tr BL   Transitional boundary layer

SECTION I

INTRODUCTION

1.0 PROBLEM DEFINITION

High performance ballistic vehicles are subject, during re-entry, to an intense fluctuating pressure field which can affect the integrity of the vehicle structure and impose adverse vibration levels on internal components. It has been observed that maneuvering re-entry vehicles possessing the added complication of a control device (such as a flap) experience vibration responses which exceed levels measured for ballistic vehicles. The pressure fluctuations arise from instability and unsteady motions of fluid flow within the transitional/turbulent boundary layer. Several hypotheses have been proposed to describe the random motion of the momentum-deficient fluid which focus on intermittent eruptions of the viscous sublayer. Research in this field has been conducted both theoretically and experimentally with emphasis on incompressible flow. Pressure fluctuations classically have been examined by relating the phenomenon to velocity fluctuations through Poisson's equation. Moreover, further simplification has been invoked by considering only an interaction of the turbulent structure and mean shear stresses. In this manner, mean square pressure fluctuations for attached flows have been predicted. However, the phenomenon is still understood only vaguely, and design criteria have been developed primarily on the basis of experimental data.

The design resolution to this problem can be divided into two parts: first, providing a definition of the fluctuating pressure environment, and second, predicting the vehicle structure and internal component response. The present investigation will focus initially on the first part. Empirical correlations developed then will be applied to the second part, in particular, to a ballistic and a maneuvering re-entry vehicle. Empirical modeling of aeroacoustic loads for axisymmetric or two dimensional bodies currently exists; however, adjustments are required to obtain agreement with experimental data. These data were acquired from wind tunnel tests, aircraft flight tests, rocket and missile flight measurements as well as limited re-entry vehicle flight measurements. One should keep in mind that the aeroacoustic environmental empirical models are subject to the following constraints; namely: (1) they have been developed

primarily from data on non-ablating two dimensional shapes, (2) the models do not consider flow over control surfaces, and (3) they require further modifications to achieve agreement with existing experimental data.

2.0 OBJECTIVE

The objective of the present investigation is to formulate methods for predicting the fluctuating pressures associated with maneuvering type vehicles. An assessment has been made concerning applicability of both existing data and present analytical capability to fluctuating pressure characteristics associated with vehicle control surface regions. The current program includes a review of scaling laws utilizing normalization of aeroacoustic parameters, definition and implementation of a wind tunnel test program to acquire data that will verify or redefine existing prediction schemes, and application of upgraded aeroacoustic load prediction methods to a ballistic and a maneuvering re-entry vehicle.

SECTION II

CONCLUSIONS AND RECOMMENDATIONS

In general, the maneuvering re-entry vehicle model that was studied in this investigation displayed characteristics that were approximately the same as a ballistic type re-entry vehicle except for conditions local to the control surface region. The following algorithms are recommended to describe the aeroacoustic environment relative to rms pressure, power spectral density and cross-spectral coefficients for various flow and model geometric conditions.

1.0 ATTACHED TURBULENT BOUNDARY LAYER FLOW

1.1 Cone/Slice Region ($\alpha = 0°$)

Root-Mean-Square Pressure

$$(\sigma/q_e)_o = (\sigma/q_e)_i \, \varepsilon_T \tag{90}$$

where

$$(\sigma/q_e)_i = 0.006; \text{ incompressible value} \tag{69}$$

$$\varepsilon_T = (T^*/T_e)^{[2m-(1+n)]/(3+n)}$$

$$T^*/T_e = [1/2 \, (1 + T_w/T_e) + .22r \, \frac{\gamma - 1}{2} \, M_e^2 \,] \tag{56}$$

for

$$m = 3/2 + \frac{\ln \, [(T_e + 198.6)/(T_w + 198.6)]}{\ln \, (T_w/T_e)} \tag{68}$$

r = turbulent recovery factor = .896

n = velocity power law exponent = 7 for fully developed turbulent flow

n = 9 for most wind tunnel data and values of TBL just after transition

Power Spectral Density

$$\frac{\varphi(\omega)u_e}{q_e^2 \, \delta^*}\Big)_c = \frac{(2/\pi)(\sigma/q_e)_i^2 \, \varepsilon_T^2}{1 + (1/\varepsilon_T^4)(\omega \, \delta^*/u_e)_c^2} \tag{94}$$

Cross-Spectra Coefficients

Cone

$$A_\xi(\xi,\omega) = e^{-.1\omega \xi/u_c(\omega)}[.58 + .42 \, e^{-.0486\,\xi/\delta^*}]$$

$$A_\eta(\eta,\omega) = e^{-1.4\omega\eta/u_c(\omega)}[e^{-0.0195\,\eta/\delta^*}] ; \; \alpha \le .7\,\theta_c$$

Section V

2.3.1

Slice

$$A_\xi(\xi,\omega) = e^{-.2\omega\xi/u_c(\omega)}[.35 + .65 \, e^{-.073\xi/\delta^*}] \tag{98}$$

$$A_\eta(\eta,\omega) = e^{-1.4\omega\eta/u_c(\omega)}[.3 + .7 \, e^{-.055\,\eta/\delta^*}] \tag{99}$$

1.2 Flap Region ($0 \le -\delta_F \le 20$)

Root-Mean-Square Pressure

$$(\sigma/q_e)_c = (1 + |\delta_F|/\theta_o)_i^{1/2} (\sigma/q_e)_i \, \varepsilon_T \tag{91}$$

Power Spectral Density

$$\frac{\varphi(\omega)u_e}{q_e^2 \, \delta^*}\Big)_c = \frac{(2/\pi)(\sigma/q_e)_i^2 \, \varepsilon_T^2 (1 + |\delta_F|/\theta_o)^2}{1 + (1/\varepsilon_T^4)(\omega \, \delta^*/u_e)_c^2} \tag{95}$$

4.

In the above, it is noted that functional variation for extended flap angles is not consistent from rms pressure measurements to those for power spectral density i.e., the exponent for PSD values was anticipated to be unity (square of the rms pressure value). However, the above is recommended on the basis of limited data analyzed in these experiments.

Cross-Spectral Coefficients

$$A_\xi (\xi, \omega) = \text{Equation (98)}$$

$$A_\eta (\eta, \omega) = \text{Equation (99)}$$

2.0 TRANSITIONAL BOUNDARY LAYER FLOW

As a consequence of the voluminous potential of acoustic data that could be generated from the wind tunnel test program, a data sub-set was selected for analysis. The data sub-set was established on the basis of angle of attack and flap deflection combinations that are compatible with re-entry vehicle applications. As a result, the data sub-set did not provide sufficient transition information that could be used to interpret control surface characteristics. Accordingly, only conical frustum transition measurements will be presented in this section.

2.1 Conical Frustum

Root-Mean-Square Pressure

$$(\sigma/q_e)_c = (\sigma/q_e)_i / [(1/2)(1 + T_w/T_e) + .11\, r\, (\gamma-1)M_e^2\,]^{\frac{1.6-(1+n)}{(3+n)}} \qquad (92), (93)$$

$$n = 6 \text{ peak transition values}$$

$$n = 4 \text{ for start to middle of transition zone}$$

Power Spectral Density

An attempt was made to incorporate the compressibility factor (ϵ_T) into the power spectral density algorithm for transitional flow as developed for rms pressure with the appropriate value of n. However, no direct fluid dynamic logic appeared feasible. On the other hand, the zero intercept values of PSD appeared to be predictable using

the inverse of the compressibility factor, i.e.,

$$\frac{\varphi(o)u_e}{q_e^2 \, \delta^*})_c \approx (2/\pi)(\sigma/q_e)_i^2 \, / \epsilon_T^2 \tag{97}$$

and should be used accordingly with $n = 4$.

Cross-Spectral Coefficients

$$A_\xi(\xi,\omega) = e^{-0.06\omega\xi/u_c(\omega)}[.6 + .4 \, e^{-.024\xi/\delta^*}], \text{ all values of } \alpha \tag{100}$$

$$A_\eta(\eta,\omega) = e^{-.68\omega\eta/u_c(\omega)}[.6 + .4 \, e^{-.024\eta/\delta^*}], \; \alpha \le 0.7 \, \theta_c \tag{101}$$

$$A_\eta(\eta,\omega) = e^{-.446\omega\eta/u_c(\omega)}[.6 + .4 \, e^{-.024\eta/\delta^*}], \quad \begin{array}{l} \text{windward} \\ \alpha > 0.7 \, \theta_c \end{array} \tag{102}$$

3.0 ANGLE OF ATTACK EFFECTS

Although limited angle of attack data were analyzed in this program, it was deter-
mined that angle of attack effects did exist in the measured data. In particular,
normalized acoustic in the cone and flap regions exhibited significant α variations
compared to the slice region in which angle of attack effects appeared to be compen-
sated for by changes in the compressibility parameter. Consequently, it is recommended
that cone and flap rms pressure equations for windward ray environments be divided
by the function $(1 + \alpha/\theta_c)$ i.e.

Cone

$$(\sigma/q_e)_c = \frac{\text{Equation (90)}}{(1 + \alpha/\theta_c)}$$

Flap

$$(\sigma/q_e)_c = \frac{\text{Equation (91)}}{(1 + \alpha/\theta_c)}$$

6.

4.0 GENERAL COMMENTS

An examination of the fluctuating pressure data indicated that overall sound pressure levels (OASPL) measured on the slice were less than those obtained over the conical frustum. This is believed to be a result of the expansion wave at the cone/slice intersection. The condition was consistent for all acoustic functions. In turbulent flow, the OASPL for the cone was approximately 5 to 10 dB higher than slice values. With respect to the control surface region characteristics, there did not appear to be any upstream effects on the slice or the cone resulting from flap deflections. For deflections up to 20°, all flap characteristics were local except in the case of zero deflection for which measured acoustic functions were virtually the same as slice values. At Mach 4 with 20° flap angle, the OASPL experienced by the flap was approximately 20 dB greater than the slice and 15 to 20 dB greater than conical frustum values. On the other hand, at Mach 8 conditions, the 20° flap angle showed OASPL levels of 20 to 25 dB greater than slice values and 15 to 20 dB greater than cone levels. When transitional flow was experienced along the control surface region, for Mach 4 tests, the 20° flap deflection exhibited levels 30 to 35 dB higher than turbulent levels.

When root-mean-square fluctuating pressure and power spectral density are non-dimensionalized using the edge dynamic pressure (i.e., $\bar{p}/q_e$ & $\varphi(f)u_e/q_e^2 \delta^*$), measurements from the current program exhibit a significant Mach number effect which is consistent with previous wind tunnel data. It is evident that values of rms pressure and PSD so-normalized generally decrease with increasing edge Mach number. Lower values of these functions are noted both for the higher Mach number measurements of Tunnel B, and for the slice data which exhibit effects of increased velocity associated with the flow expansion. Mach number effects are explicitly introduced into the prediction formulae for rms pressure and PSD through the compressibility factor ϵ_T, whose dependence on M_e is described in Equations (69) and (56).

5.0 RE-ENTRY RANDOM VIBRATION-BALLISTIC AND MANEUVERING RE-ENTRY VEHICLES

Prediction of vibration response characteristics for a ballistic re-entry vehicle at component mounting locations (under a specific aeroacoustic environment) demonstrates overall validity of the present analytical technique by exhibiting good correlation with maximum response levels (.022 g^2/Hz) derived from applicable flight data in fully turbulent boundary layer flow.

Two sets of maneuvering vehicle response predictions were made in order to demonstrate how much effect the fluctuating pressure environment associated with a deployed control surface has on structural response for a specific maneuvering configuration. When a hypothetical, symmetric acoustic excitation is applied, maximum internal levels of .044 g^2/Hz at 2013 Hz and .028 g^2/Hz at 1657 Hz result. When the environmental description is modified in the control surface region to account for deployed flap acoustic characteristics, a significant shift in contributing modes occurs. Maximum response levels are now directly associated with those modes in which there is coupling between the flap and other vehicle structure. Maximum internal (component) levels under the appropriate maneuvering R/V loading are now increased to .066 g^2/Hz at 154 Hz and .063 g^2/Hz at 454 Hz, with significant motion evident at flap, R/V nose, and shell locations. Maximum responses therefore increased only by a factor of approximately 2.4 when modes above 2000 Hz are not included. However, at frequencies for which there is significant flap-vehicle coupling R/V internal accelerations went up by an order of magnitude or more. It is to be emphasized therefore that detailed characteristics of vehicle dynamic response (i.e., explicit coupling behavior) must be known before specific conclusions can be reached regarding the influence of control surface excitations on a maneuvering R/V.

Shell acceleration levels (accounting for 0th and 1st harmonics) under the cone/ slice/deployed flap environment reached maximum levels of .1 g^2/Hz. If effects of harmonics higher than the 1st had been included, maneuvering shell response would have been significantly higher, resulting in levels comparable to actual flight data (.8 g^2/Hz maximum). However, inclusion of higher harmonics would not appreciably alter predicted internal levels, since component packages are generally mounted on support structures such that their primary behavior is simple beam-column motion. The support structure does not transmit vibration levels associated with high harmonic

8.

shell response. It is therefore to be concluded that measured shell accelerations on the order of .5 to 1.0 g^2/Hz are not inconsistent with internal levels (for components on shelves or bulkheads) of less than .1 g^2/Hz, as computed for the specific maneuvering configuration.

On the basis of flight data as well as vibration levels predicted herein, it is possible to specify general environmental levels for ballistic and maneuvering R/V components. The levels discussed below are strictly applicable only to the ballistic and maneuvering R/V configurations considered in this report; other vehicles should be similarly evaluated before applying recommended environments to additional R/V programs. For components in the ballistic re-entry vehicle, a maximum level of .05 g^2/Hz would effectively envelope both measured and computed internal responses. Re-entry vehicle shell levels of .036 g^2/Hz were computed in the present analysis; however, higher harmonics are not accounted for, and shell responses are consequently underpredicted. Flight data indicate that 0.1 g^2/Hz is an appropriate upper bound for axial and radial shell responses applicable to the ballistic vehicle.

For maneuvering vehicle components mounted on internal structures, the present analysis and data included in Volume II indicate that .1 g^2/Hz represents a reasonable upper bound on re-entry vibration level. On the other hand, actual flight response measurements on maneuvering vehicle shell structure reveal that a range of approximately 0.2 - 1.0 g^2/Hz would envelope anticipated vibration environments for shell-mounted items in maneuvering configurations.

SECTION III

EVALUATION OF EXISTING DATA AND PREDICTION METHODS

1.0 PREVIOUS WORK

An inspection of the literature has revealed that considerable work has been devoted to incompressible flow fields and more recently to compressible flow in the supersonic range (M < 5). With the exception of the limited work by Heller et al[10,11,12,13] very sparse information was developed relative to aeroacoustics in hypersonic flow prior to the AFFDL sponsored detailed work by Chaump et al[1] in 1972. The investigation of Reference 1 is considered a comprehensive review of surface pressure fluctuation characteristics of ground and flight test data relative to overall magnitude, spectra, cross-correlation functions and convection velocity. The data were categorized into various boundary layer type flow conditions including attached turbulent, attached transitional, separated turbulent and base flow. In addition to this review of ground and flight data, Reference 1 also reports on a wind tunnel program in which pressure fluctuations were measured on a 7.2 degree half angle cone. The test program considered transitional, turbulent, separated (induced by crossflow on a cone), and base flow conditions at various angles of attack, Mach number and nose radii. Measurements were correlated with data obtained from the literature to develop improved prediction methods. Consequently, with the exception of attached or separated flow conditions over a control surface (such as a flap), Reference 1 is an ideal starting point for reviewing existing data.

A list of references that are directly or indirectly related to the present study has been compiled. While the list emphasizes work completed in the present decade, many well known documents, both experimental and analytical, have not been included inasmuch as accessibility and general contents are noted in the papers presented in the Reference section. The reference list can be sub-divided into several categories which include the following:

1) General Electric/AFFDL sharp cone pressure fluctuation data (References 1 through 8). It should be noted that Reference 7 re-examined the spatial and temporal properties of the data of Reference 1 while Reference 8 was a direct result of the literature review of the present study.

2) NASA Ames flat plate work of Raman (Reference 9).

3) Bolt, Beranek and Newman work by Heller et al on a sharp cone and straightwing orbiter configuration (References 10 through 13).

4) The NASA Ames work of Coe, Chyu, Hanly, and Dods on an ogive-cylinder and wind tunnel walls (References 14 through 20).

5) Flight data from several sources (References 21 through 26).

6) Several auxiliary studies relating to specific aeroacoustic data (References 27 through 35).

7) Flow separation and pressure gradient effects on pressure fluctuations (References 36-39, also References 14-19 and 28-29).

8) Boundary layer survey (hot wire probes) work for validation of aeroacoustic phenomena (References 40-45) and freestream noise effects (References 32-34 and 95).

9) Analytical, semi-analytical, empirical correlation work describing aeroacoustic characteristics (References 46 through 80).

The present investigation will be primarily concerned with supersonic/hypersonic flow conditions and, as such, will not be concerned with a detailed literature review of subsonic flow. Concerning the latter, interested readers are referred to the excellent survey paper by Willmarth[46] as well as Reference 9.

1.1 Evaluation of Existing Data

When assessing data reported in the majority of references cited above, it was difficult to extract raw data from the graphical representations. This was generally due to the lack of available aerodynamic parameters that were used in the references for normalization. Moreover, model size, geometric construction and model mounting techniques rendered very questionable data results. For example, data employing freestream instead of local boundary layer conditions with the state of the boundary layer being transitional at best, must be carefully weighed before being used in fully developed, hypersonic turbulent boundary layer predictions. As a result, the present study has concentrated on attached flow conditions where emphasis has been placed on the work associated with References 1, 9, and 18. Finally, it should be noted that the prediction methods developed to date have been founded on turbulent attached flow criteria where modifications have been made to consider transitional and separated flow effects. Also, the data sub-set analyzed from the experimental task of this study

considered attached flow behavior only. This was a consequence of using realistic design criteria (i.e., flap angle versus angle of attack variations) for maneuvering reentry systems.

1.1.1 Power Magnitude

The overall magnitude of pressure fluctuations in attached turbulent flow from a number of experiments is shown in Figure 1. Here the root-mean-square (rms) pressure normalized by the local dynamic pressure is shown as a function of local Mach number. A significant variation in the data is noted when plotted in these coordinates. It is interesting to note an increase in normalized rms pressure with Mach number ($M > 5$) for various experiments except for the data point represented by Reference 11. Moreover, data were obtained on several geometric configurations including flat plates, sharp and blunt cones, wind tunnel walls and an ogive cylinder. The use of local boundary layer conditions is considered more reasonable for extension to flight application than freestream values. In experiments involving wind tunnel walls and flat plates, local and freestream conditions are identical. However, for those data points reflecting geometries other than the above, no attempt was made in the current study to determine the local boundary layer properties, and reported values corresponding to freestream conditions were used accordingly.

1.1.2 Power Spectral Density

Figures 2 through 4 display various normalized spectra formats for wind tunnel data for subsonic and hypersonic conditions. These data show the normalized power spectral density as a function of Strouhal number for attached turbulent boundary layer flow conditions. Several authors have noted that the spectra can be graphically displayed as a function of frequency in terms of the Strouhal number, fl/v, utilizing characteristic length and velocity parameters. However, choice of the proper typical length and velocity has been a topic of discussion. In general, the freestream or local boundary layer edge velocity has been chosen as the characteristic velocity parameter, while the boundary layer thickness or displacement thickness are commonly used characteristic length parameters.

Figure 2 shows the dimensionless form of power spectral density (PSD) where the boundary layer edge velocity and displacement thickness parameters have been

chosen for normalization. While a general collapse of the data is evident, no discernable Reynolds number or Mach number effects are apparent. Figure 3 shows the PSD as a function of Strouhal number where freestream velocity and boundary layer thickness are used for normalization parameters. Data in Figure 3A represent the PSD on wind tunnel walls while Figure 3B compares tunnel wall data with those obtained on an ogive-cylinder at supersonic conditions. It should be noted that the tunnel wall measurements agree with the model data using freestream parameters. This is a consequence of the flow expansion along the ogive section where the local boundary layer edge values approach freestream values as one approaches the cylindrical section (the recording station $X/D = 2.9$ is approximately at the intersection of the ogive and cylinder). One should also note the dramatic increase in the normalized PSD in the low frequency range ($f \delta/u_\infty < 10^{-2}$). For data that have been reported in the literature, a significant variation exists in this range. Data have also been reported that tend to decrease at Strouhal number $< 10^{-1}$. As a result of the disparities in this region, many experimentalists have not reported low frequency data.

Figure 4 shows a plot of the PSD distribution with Strouhal number. Here, the dimensionless spectra are normalized by the ratio of the square of rms pressure and dynamic pressure. The authors of Reference 1 chose this format because of the apparent coalescence of the data. However, when data of recent experiments are added, a significant variation is observed. Assessing the spectral measurements as a function of Strouhal number, it is apparent that the dimensionless form of PSD decreases with Strouhal number, in particular for values of the Strouhal number greater than 10^{-1} when represented in the coordinates of Figures 2 through 4. It will be shown, in effect, that normalizing one dimensionless quantity with another is actually an attempt to transform compressible data into an incompressible plane.

Data describing spectral distribution of flight measurements are very limited. Inasmuch as ground test data have been primarily used to develop prediction capability, the flight test data will be used only when deemed appropriate. Consequently, these limited data will be discussed when prediction techniques are applied to re-entry vehicles (Vol. II).

1.1.3 Cross Correlation Functions

References describing broad- and narrow-band cross correlation function measurements for attached turbulent boundary layer flow conditions have been compiled by Howe[7] and Chaump et al.[1] Measurements in the supersonic/hypersonic range are very limited. It should be noted that data from the experiments of Heller and Holmes[10] and Raman[9] were not included in the investigation of Reference 7. This was a consequence of the graphical format which required assumptions for explicit use (Reference 10). On the other hand, Reference 9 displayed only one trace (for a given Mach number condition) of a common space-time and auto-correlation function. This investigation will not repeat any data that has been compiled in References 1 and 7 except for comparison purposes in the data evaluation section. However, considerable attention will be given to the data interpretation, in particular to the effects of fluid flow compressibility which must explicitly be accounted for at hypersonic conditions.

1.1.4 Convection Velocity

Figure 5 shows broad-band and narrow-band convection velocities for both incompressible and compressible flow data obtained from a variety of geometries. It is quite interesting to note that the broad-band values appear to coalesce for both the incompressible and compressible states. Moreover, the incompressible prediction technique of Lowson,[55] when modified to include displacement thickness, adequately describes the variation of the broad-band behavior with separation distance. On the other hand, the narrow-band characteristics reflect a variation between incompressible and compressible data when expressed as a function of frequency. It should be observed, however, that the incompressible data indicate a specific trend of attenuation in the normalized convection velocity with decreasing separation length.

The characteristic distance for spatial normalization has been chosen as the boundary layer displacement thickness. Keeping in mind that incompressible flow allows for the interchangeability of δ and δ^* (i.e., $\delta = 8\delta^*$), one would expect the same results if δ were used. Some further comments concerning characteristic lengths will be given in the following sections. Finally, it is interesting to note that Reference 7 presents compressible data for angle of attack conditions (using local parameters for normalization) which are consistent with results achieved under symmetric flow conditions

(i.e., $\alpha = 0$). This phenomenon appears to be valid for angles of attack less than or equal to approximately 70% of the cone half angle. This result demonstrates the importance of using local boundary layer properties for normalization as opposed to freestream values.

1.2 Evaluation of Prediction Methods

It was previously noted that prediction techniques for describing aeroacoustic loads have been developed from sound theoretical principles appropriate for attached turbulent boundary layer flow behavior. Modifications were made to the attached flow methods to account for flow separation, transition and base flow effects primarily on the basis of experimental data. Such an approach was adopted in Reference 1, which considered a sphere-cone type configuration (ballistic R/V). Consequently, these results will form the reference point for the maneuvering type configuration of this study. This section will discuss briefly existing prediction techniques for describing aeroacoustic environments subject to attached flow conditions for ballistic type R/V's. While it is not the intent to develop a historical review of the pressure fluctuations in turbulent flow relative to prediction capability, an examination of current techniques will be made regarding the fluid dynamic phenomenology and subsequent assumptions invoked in developing the prediction methods.

1.2.1 Power Magnitude

Reference 1 outlines the correlation for predicting the magnitude of pressure fluctuations as developed by Houbolt[56] that was modified further to include wall temperature effects in unpublished work. A careful examination of the work of Lowson[55] indicated an approach similar to that of the unpublished Houbolt concept. Inasmuch as the Lowson result is available, details concerning its development will not be given. It should be noted that a synopsis of the Lowson work was given by Laganelli et al.[8] Houbolt considered a fluid where the eddy velocities were proportional to the freestream velocities, and assumed the local density (region of maximum noise potential) as the significant variable governing noise production. The region of maximum noise production is that which corresponds to maximum shear flow or, by Reynolds analogy, where maximum temperature occurs. If one considers the momentum deficit of the fluid, this phenomena occurs within the classic law of the wall region.

15.

Houbolt considered the divergence of Euler's equation, where the properties consist of a sum of the mean and fluctuating components, such that

$$\nabla^2 p = - \nabla \cdot \rho \ \frac{D\vec{u}}{Dt} \tag{1}$$

where D/Dt is the substantial derivative. The above expression is recognized as a Poisson type equation with the right hand side representing a source or sink, but with steady pressure. Equation (1) has the solution

$$p = \frac{1}{4\pi} \int_V \frac{\nabla \cdot \rho \frac{D\vec{u}}{Dt}}{r_o} \ dV \tag{2}$$

where r_o is a distance to a general field point. The above is recast into dimensionless form by introducing the boundary layer thickness, and a local mean density (ρ_1) at a position in the boundary layer where the maximum noise production occurs (δ_1). Equation (2) is then written

$$p = \rho_1 \frac{\delta}{\delta_1} \ u_e^2 \ [\frac{1}{4\pi} \int_V \ \frac{-\delta \nabla \cdot \frac{\rho}{\rho_1} \frac{\delta}{u_e} \frac{D(\vec{u}/u_e)}{Dt}}{r_o/\delta_1} \ d(\frac{V}{\delta^3})] \tag{3}$$

where δ, δ_1 and u_e are scalar quantities.

The mean and fluctuating velocities were considered to be proportional to the free-stream velocities such that the density profile remains fixed; hence, the terms in the bracket remain invariant to the flow velocity. The pressure field can then be described as

$$p = \rho_1 u_e^2 \ \frac{\delta}{\delta_1} \ f(t) \tag{4}$$

which incorporates the far field velocity (u_e) as well as the governing density (ρ_1) and location (δ_1) at the site of intense eddy formation. While Houbolt recognized that δ/δ_1 can be expressed as a function of Mach number, its dependence is weak. Consequently, consideration was given only to the influence of ρ_1. The rms value of pressure can then be expressed as

$$p_{rms} = c \rho_1 u^2_e = c_1 q_e \rho_1/\rho_e \tag{5}$$

where q_e is the dynamic pressure and c_1 a constant. Equation (5) is the starting point of the analysis given by Lowson.[55]

For an adiabatic flow, one can define the recovery temperature as

$$T_{aw}/T_e = 1 + r \left(\frac{\gamma-1}{2}\right) M^2_e \tag{6}$$

and, in an analogous fashion, it is assumed that the temperature at the site of maximum noise generation can be defined by a recovery type factor

$$T_1/T_e = a_1 \left(1 + \frac{a_2}{a_1} \frac{\gamma-1}{2} M^2_e\right) \tag{7}$$

where the coefficient a_2/a_1 is analogous to the recovery factor, r, of Equation (6). If we consider the equation of state together with the boundary layer assumption $\partial P/\partial y = 0$, Equation (7) becomes

$$\rho_1/\rho_e = T_e/T_1 = \frac{1/a_1}{1 + \frac{a_2}{a_1}\left(\frac{\gamma-1}{2}\right) M^2_e} \tag{8}$$

and the rms pressure is expressed as

$$p_{rms} = \frac{(c_1/a_1) q_e}{1 + \frac{a_2}{a_1}\left(\frac{\gamma-1}{2}\right) M_e} \tag{9}$$

In order to evaluate the new recovery type factor, a_2/a_1, the Crocco linear temperature-velocity relationship is used; namely,

$$T/T_e = T_w/T_e + (1-T_w/T_e)u/u_e + \left(\frac{\gamma-1}{2}\right)M^2_e (1-u/u_e)u/u_e \tag{10}$$

17.

For adiabatic wall conditions ($T_w = T_{aw}$) about the position δ_1, the above becomes

$$T_1/T_e = 1 + (\tfrac{\gamma-1}{2})M_e^2 (1-u_1/u_e)(r+u_1/u_e) \tag{11}$$

A comparison of Equations (7) and (11) allows for

$$a_1 = \text{unity}$$

$$a_2/a_1 = (1 - u_1/u_e)(r + u_1/u_e) \tag{12a}$$

For a non-adiabatic condition, the above becomes

$$a_2/a_1 = (1 - u/u_e)(r + u/u_e) \tag{12b}$$

Lowson considered the velocity ratio u_1/u_e to be 1/2 and the constant c_1 to be 0.006 which was experimentally determined from subsonic flow data. The resulting rms pressure was then expressed, using Equations (5) and (11), as follows:

$$(p_{rms}/q)_{comp} \approx 0.006/(1 + 0.14\, M_e^2) \tag{13}$$

On the other hand, Houbolt considered the constant c_1 to be 0.007 and found the new recovery type factor (a_2/a_1) to be 0.06 as a conservative choice when considering the general Crocco equation over a range of wall temperature ratio T_w/T_e (4 to 7) and velocity ratio u/u_e (0.4 to 0.7). The rms pressure was then expressed as

$$p_{rms}/q_e \approx 0.007/(1 + 0.12\, M_e^2) \tag{14}$$

which when generalized to include wall temperature effects, gas density, and composition becomes

$$p_{rms}/q_e \approx 0.007/[\,1 + r_e (\tfrac{\gamma-1}{2})M_e^2\,] \tag{15}$$

where $r_e = a_2/a_1$ and is given by Equation (12b).

If one considers the definition of the dynamic pressure ($q_e = \gamma/2\, p_e M_e^2$) the rms pressure, when normalized by the static value for the Lowson and Houbolt results, becomes respectively:

$$p_{rms}/p_e \big)_L \approx 0.0042\, M_e^2/(1 + 0.14\, M_e^2) \qquad (16)$$

and

$$p_{rms}/p_e \big)_H \approx 0.0049\, M_e^2/(1 + 0.012\, M_e^2) \qquad (17)$$

At this point, several factors concerning the above formulations should be noted. These are: (1) the constant c_1 (.006 or .007) was obtained at through experimental observations of subsonic flow conditions, (2) the compressible state had been developed by use of a density formulation only, (3) the use of the Crocco linear temperature-velocity relationship is questionable in turbulent flow (for example, data have indicated a quadratic relationship exists); (4) the velocity ratio (u_1/u_e) of 1/2, while considered as a representative average of, say, the viscous sublayer velocity to freestream value, can vary in the law of the wall region where turbulent intensity prevails; and (5) use of adiabatic wall (hot wall) conditions is not justified for all cases, in that many flights/experiments were conducted under cold wall conditions.

While Lowson considered compressibility through a density change, he also examined the works of Bies[63] for predicting τ_w through heating near the wall whose key effect results from viscosity rather than density. Good agreement was noted between the two methods; however, one must keep in mind that data are limited to the low supersonic range where the comparisons were made. Moreover, Lowson noted that T_w/T_{aw} would probably not be less than 0.8 in practice; hence, T_w effects would be insignificant for his adiabatic wall prediction. However, it should be noted that the condition $T_w/T_{aw} < 0.8$ can exist on re-entry vehicles and, for that matter, in wind tunnel tests where T_w/T_{aw} can be less than 0.5 especially at hypersonic conditions.

Figure 1 shows the prediction methods of Lowson and Houbolt compared to data. It is noted that the adiabatic wall results of both authors appear to give the best agreement to the measured experimental data.

Raman[9] considered several correlations of the rms pressure using the dynamic pressure, wall shear stress and static pressure as normalization parameters. Polynomial or exponential type fits to his data indicated that

$$p_{rms} = f_1 (q_\infty, M_\infty); f_2 (M_\infty, Re_{\delta*}); f_3 (Re_\theta)$$

Inasmuch as these correlations were not developed on the basis of fluid dynamic principles and no comparisons to other data were made, the functional representations of Raman will be used when deemed applicable to the present study. It should be noted however, that the functional form representing p_{rms}/q_∞ can be derived through fluid dynamic principles.

If one considers the concept subsequently developed in Section 3.0, Equation (59), it is easily shown that

$$p_{rms}/q_e = \frac{0.03A}{Re_x^{1/5}[\frac{1}{2}(1 + T_w/T_e) + 0.04 M_e^2]^{.64}} \tag{18}$$

From boundary layer theory for a flat plate[83]

$$Re_x^{1/5} = 2.275 \, \epsilon_T^{-1/4} \, Re_\theta^{1/4} \tag{19}$$

where ϵ_T is defined by Equation (57). The ratio of displacement thickness to momentum thickness is given as[83]

$$\delta*/\theta = -1 + [(\frac{n+2}{n}) T_w/T_{aw} + 1][1 + 0.208 M_e^2] \tag{20}$$

If one considers A to be equal to 2, an average of the range predicted by Lilley,[70] together with a 1/7 velocity power law (i.e., n = 7), Equation (18) subject to Equations (19) and (20) will have two ranges. These are the cold wall case $(T_w << T_{aw})$ and the adiabatic wall case $(T_w = T_{aw})$. Hence, Equation (18) becomes

$$p_{rms}/q_e)_{aw} \approx 0.061 \, Re_{\delta*}^{-1/4}/[\frac{1 + .08 M_e^2}{M_e^{5/8}}]^{4/5} \tag{21}$$

and

$$P_{rms}/q_e)_{aw} \approx 0.052 \, Re_{\delta*}^{-1/4} / [9/7 + .48 \, M_e^2]^{-1/4} [1 + .13 \, M_e^2]^{4/5} \quad (22)$$

In Equations (21) and (22), the exponent of the displacement thickness Reynolds number (-1/4) is a consequence of a 1/7 fully developed turbulent velocity profile power law. A comparison to the data of Reference 9 indicates that the data are over-predicted for $M_\infty = 5.2$ and 7.4 and underpredicted for the $M_\infty = 10.4$ case. It should be noted that the cold wall prediction was used inasmuch as the adiabatic case was significantly underpredicted. The slope of the Raman data indicated a 1/5 distribution which is synonomous with a 1/9 velocity profile, a condition indicating a non-fully developed turbulent boundary layer.

1.2.2 Power Spectral Density

The mean square fluctuating pressure in terms of the power spectral density function is defined as[72]

$$\sigma^2 = \int_0^\infty \varphi(f)df = \int_0^\infty \varphi(\omega)d\omega \quad (23)$$

where the mean square value is equal to the total area under a power spectrum corresponding to a sample time history record. For attached turbulent boundary layer flows, power spectra have been found to scale with Strouhal number. The Strouhal number represents a normalized frequency using characteristic length and velocity of the flow field. The choice of the characteristic length and velocity parameters has been a subject of considerable debate; in particular, for high speed applications. This topic will be further considered in a following section.

Lowson[55] and Houbolt[56, 57] developed empirical representations of the power spectrum on the basis of subsonic and available supersonic flow data. Houbolt, applying engineering logic, considered a system of rolling eddies to characterize the convective velocity which are located a distance above the wall at a site of intense noise distribution to formulate the Strouhal number. It was determined that spectra appeared to scale in terms of rms pressure as

$$\varphi(\omega) = \frac{2}{\pi} \frac{\delta^*}{u_c} p_{rms}^2 / [1 + (\frac{\omega \delta^*}{u_c})^2] \tag{24}$$

Houbolt[56] further noted from the definition of the rms pressure and PSD the following relationship

$$\sigma^2 = p_{rms}^2 = \int_0^\infty \varphi(\omega) d\omega = \int_0^\infty \omega \varphi(\omega) dZ \tag{25}$$

where $dZ = d\omega/\omega$. Hence, a plot of the density distribution of the power magnitude together with the product $\omega \varphi(\omega)$, namely

$$\frac{\pi}{2} \frac{u_c}{\delta^*} \frac{\omega \varphi(\omega)}{p_{rms}^2} = f(\frac{\omega \delta^*}{u_c}) \tag{26}$$

would maximize the power magnitude when the Strouhal number was unity. It should be noted that the above concept is quite similar to the first moment of the power magnitude when employing the definition of the latter; i.e.,

$$p_{rms}^2)_{f.m.} = \int_0^f f\varphi(f) df \tag{27}$$

This approach, which is similar to that of Black,[59] is essentially a weighted residual technique and will be further discussed in the following section.

Lowson[55] developed an expression similar to Equation (24) that considered subsonic data and the supersonic data of Reference 37. It was determined that the data appeared to coalesce when the Strouhal number was based on boundary layer thickness rather than displacement thickness. The expression developed by Lowson is given by

$$\varphi(\omega) = p_{rms}^2 / \omega_o [1 + (\omega/\omega_o)^2]^{3/2} \tag{28}$$

where $\omega_o = 8u_e/\delta$. Robertson[28] re-examined the correlation developed by Lowson when comparing the above formulation to supersonic data obtained in References 18 and 19. It was found that the Lowson prediction underestimated spectral levels at low Strouhal numbers. As a consequence, Robertson modified the Lowson result to include

boundary layer displacement thickness and freestream velocity and also changed the exponents. Robertson's result is given as

$$\frac{\varphi(\omega)u_\infty}{q_\infty \, \delta^*} = \frac{p_{rms}^2/q_\infty^2}{\frac{\omega_0 \, \delta^*}{u_\infty} \cdot [1 + (\omega/\omega_0)^{.9}]^2} \tag{29}$$

where $\omega_0 = 1/2 \, u_\infty/\delta^*$.

Figures 2 and 6 show spectral data of several experimenters compared to prediction methods of Houbolt and Lowson, respectively. There does not appear to be any advantage in using either concept (i.e., displacement thickness or boundary layer thickness). It should be noted that the convection velocity in Equation (24) was replaced by the local boundary layer edge value. Moreover, the Mach number effect represented in these figures was a result of the use of Equation (13) for both methods. It is also noted that neither method agrees well with the data over the spectrum range. One feature of the data variation is the apparent Reynolds number effect.

Raman[9] found that the PSD distribution for the Mach numbers of his experiment followed the expression

$$\frac{\varphi(f)u_\infty}{q_\infty^2 \, \delta^*} = A_1^2/[1 + (f\delta^*/u_\infty)^2]^{3/2} \tag{30}$$

where A_1 is a constant. The above expression is recognized as the formulation by Lowson[55] with slight modification. Raman integrated the above and noted that the left hand side contained the definition of the rms pressure, such that over the limits of integration the following results:

$$p_{rms}/q_\infty = \sqrt{p_{rms}^2/q_\infty^2} = [\frac{A_1^2 \, f\delta^*/u_\infty}{\sqrt{1 + (f\delta^*/u_\infty)^2}} \Big|_0^\infty]^{1/2} \to A_1 \tag{31}$$

Equation (30) is then written as

$$\frac{\varphi(f)u_\infty/q_\infty^2 \, \delta^*}{(p_{rms}/q_\infty)^2} = 1/[1 + (f\delta^*/u_\infty)^2]^{3/2} \tag{32}$$

As previously indicated, the advantage to using the above format for displaying PSD distribution is to incorporate compressibility effects with an incompressible algorithm. Moreover, Equation (30) pre-supposes a solution of the PSD as a function of Strouhal number with the arbitrary constant A_1, a methodology suggested by Houbolt. It should be noted that the left hand side of Equation (30) considers the dynamic pressure as opposed to the rms pressure for normalization. Manipulation of the constant A_1 together with the definition of the rms pressure yielded the result obtained by Lowson and Houbolt.

1.2.3 Cross-Correlation Functions

Because of the importance of the narrow-band spatial correlation function to describe the impinging effect of a fluctuating pressure field on a structure and its response, a detailed examination of the field must be made at many points. Moreover, the complexities of describing cross-correlation and cross-spectrum functions for an aeroacoustic environment (equivalent representations related through their Fourier transforms), has required a semi-empirical approach coupled with physical reasoning. One such method was developed by Lowson[55] and later modified by Robertson[28,29] and Chaump et al.[1] The analytical development of Lowson was primarily based on the incompressible experiments of Bull.[80] Coe et al[14] considered a different approach whereby an attenuation coefficient function was introduced that considered a decaying exponential of the moduli of the cross-spectra. A complete discussion concerning the analytical development and subsequent modifications of the cross spectra coefficients is given by Howe.[7] The following is concerned with the application of analytical techniques developed from incompressible flow behavior to compressible flow situations. Consequently, some repetition of the work from Reference 7 will be required for continuity.

Inasmuch as the criteria developed by Lowson was based on sound mathematical and physical principles, its foundation together with the data of Bull will be emphasized here. Lowson found it mathematically convenient to assume a product solution of the correlation coefficients where the spatial dependence was separated. In this manner, the real contribution of the complex cross-power spectral density function (ϕ_R) relating points 1 and 2 assumed the form

$$\Phi_R(\xi,o,\omega) = A_\xi(\xi,\omega)\cos\frac{\omega\xi}{u_c}\left[\varphi(\xi)_1(\omega)\varphi(\xi)_2(\omega)\right]^{1/2}$$

and

$$\Phi_R(c,\eta,\omega) = A_\eta(\eta,\omega)\left[\varphi(\eta)_1(\omega)\varphi(\eta)_2(\omega)\right]^{1/2}$$

where φ_1 and φ_2 are the power spectral densities at locations 1 and 2, respectively. Lowson allowed for a correction to the separable solution by a factor of $\pi/2$ to compensate for possible underestimation of the correlation area. This was a consequence of more probable elliptical contours of the data about the origin as opposed to the diamond patterns suggested by a separable form of the equations. The separable cross-spectral density factors A_ξ and A_η (i.e., correlation coefficients) were further separated into exponentials of spatial and mixed spatial/frequency terms; namely

$$A_s(s,\omega) = e^{-c_1|s|/\delta^*}e^{-c_2|s|\omega/u_c} \tag{33}$$

where s is a generalized separation distance (η or ξ) and c_1 and c_2 are empirical constants.

(a) <u>Longitudinal Correlation</u> (Incompressible)

Lowson considered the work of Bull to obtain the spatial/frequency asymptotic high frequency exponential function of Equation (33), shown in Figure 7. Moreover, one notes a divergence in the narrow-band correlation function at the low frequency end of the spectrum. To account for this divergence, the data were extrapolated to the ordinate ($\omega \to 0$) to obtain the asymptotic values of the coefficients at constant ξ. These asymptotic values are shown as a function of ξ/δ^* in Figure 8. Also shown is a curve fit to the data. The empirical formula representing the incompressible data of Bull was expressed by Lowson as

$$|A_\xi| = \exp\left[-\left\{(0.1\omega\xi/u_o)^2 + (0.27\xi/\delta)^2\right\}^{1/2}\right] \tag{34}$$

It should be noted that Lowson considered the boundary layer thickness rather than displacement thickness for normalization. For a fully developed turbulent, adiabatic

flow with a 1/7 velocity power law, the ratio of boundary layer and displacement thickness δ/δ^* is 8, hence the change in constants shown in Figure 8 (i.e., 0.034 ξ/δ^* = 0.27 ξ/δ).

Robertson[28] considered a modified version of Equation (34) in the form

$$A_\xi (\xi, \omega) = e^{-0.1 \omega \xi/u_c} e^{-0.27 \xi/\delta} \tag{35}$$

which was also adopted by Chaump et al.[1] If one were to plot both Equations (34) and (35), a negligible difference results, Equation (35) is considered a more readily usable formulation.

Before proceeding, some further discussion concerning the Bull data is in order. Relative to the longitudinal correlation function, Bull notes that the data of Figure 7 exhibit a coalescence of all values of ξ/δ^* at high frequency which suggests identifying frequencies with convected wave-numbers according to the relation $\omega = k_\xi u_c(\omega)$. Hence, the longitudinal high wave-number components will lose coherence in times which are proportional to the times required for them to be convected distances equal to their wavelengths. On the other hand, the amplitude of the correlation coefficients tends to be independent of frequency for low values of Strouhal number at a given ξ/δ^*. Accordingly, Bull hypothesizes a rapid loss of coherence in a period of the development for the initial wave-number component where similarity of $\omega\xi/u_c$ is required. Once these high wave-number components have lost coherence, the remaining large scale, low wave-number components of the field are still correlated until complete development of the field entails their gradual loss of coherence. Here, the general shape of the spectrum-producing components remain fairly constant in the process. Moreover, this narrow-band asymptotic trend was found to be consistent with broad-band cross-correlation results.

In order to justify the above-postulated asymptotic state, Bull noted the low frequency divergence occurs at higher values of $\omega\xi/u_c$ for corresponding higher values of ξ/δ^*. This implies that the divergence occurs at approximately the same dimensionless frequency $\omega\delta^*/u_c$ for all values of ξ/δ^*, thereby yielding a characteristic Strouhal number and scale consistent with the final phase of evolution of components in the pressure field. To find this scale in the pressure field, associated with low frequency

turbulence, one considers values of $\omega\xi/u_c$ at which the asymptotic high frequency curve $(e^{-.1\omega\xi/u_c})$ has a value equal to $R_{pp}(\xi, 0, 0)$ for a given value of ξ/δ^* to obtain the corresponding value of $\omega\delta^*/u_c$. This Strouhal number based on δ^* is considered a measure of the largest value associated with the large-scale pressure eddies. With reference to Figure 7, for the case in which $M_\infty = 0.5$ and $\xi/\delta^* = 19.75$, the high frequency component of the low frequency asymptotic value of $R_{pp} \approx 0.5$ is $\omega\xi/u_c \approx 7.2$. The corresponding Strouhal number, based on δ^* becomes

$$\omega\delta^*/u_c(\omega) \approx 0.36$$

It was found that the Strouhal numbers for the range of displacement thickness of Bull's investigation were nearly constant with an average value of approximately 0.36. Hence, the large scale pressure eddies, with wavelength λ_ξ in the stream direction, are those greater than $\lambda_\xi/\delta^* = 2\pi/0.36 = 17.4$. If we again consider the incompressible ratio $\delta^*/\delta = 1/8$, the wavelengths would be greater than about twice the boundary layer thickness. On the other hand, the amplitude of the high frequency response appears to reach a value of 0.05 when $\omega\xi/u_c$ is 24.5. Here, the component has been convected a distance $\xi/\lambda_\xi = 24.5/2\pi \approx 4$. Consequently, high frequency components in incompressible flow appear to lose their identity when convected a distance approximately 4 times their wavelength.

(b) Lateral Correlations (Incompressible)

The lateral cross-correlation coefficients were found to have a more simple decay characteristic. Figure 7 shows the asymptotic high frequency envelope which can be expressed by the curve $e^{-.72\omega\eta/u_c}$. As in the longitudinal case, the data reflect a divergence at the low frequency end of the spectrum. Lowson considered the extrapolated amplitudes, shown plotted on Figure 8 from Bull results, and suggested a curve fit to the data in the form $e^{-2\eta/\delta}$. Again, using the incompressible relationship δ^*/δ equal to 1/8 (such that $e^{-2\eta/\delta} = e^{-.25\eta/\delta^*}$), this exponential form of Lowson is shown compared to the Bull data. It is quite apparent that the asymptotic form of the data for $\omega \to 0$ does not decay as suggested by the data fit of Lowson. It should be noted that Robertson considered the same form as Lowson, which was believed to be valid for both subsonic and supersonic speeds. However, this condition will be shown to be invalid for compressible data. Also shown in Figure 8 for the lateral narrow-

band coefficient is the expression proposed in Reference 1 which provides a much better fit to the data. Accordingly, the expression representing the lateral cross-spectrum coefficient for incompressible flow becomes

$$A_\eta(\eta, \omega) = e^{-0.72\,\eta\omega/u_c}[0.3 + 0.7\,e^{-0.5\,\eta/\delta^*}] \tag{36}$$

As in the longitudinal case, the scaling for the high and low frequency contributions to the correlation coefficients are desired. The amplitude for the lateral correlation coefficient at a value of 0.05 is $\omega\eta/u_c = 4.7$ which indicates a convected distance $\eta/\lambda_\eta \approx 0.75$. Hence, a high frequency component with a given longitudinal wavelength is laterally coherent over a distance of approximately 1 1/2 times its wavelength. In Figure 8, one notes that the asymptotic values of the lateral cross-correlation function (as $\omega \to 0$) did not decay in a pure exponential characteristic as might be expected. By considering the low frequency correlation amplitudes, one can find the corresponding points on the high frequency curve ($e^{-.72\omega\eta/u_c}$) where values equal to $R_{pp}(0, \eta, 0)$ represent the smallest of the low frequency pressure eddies in which the correlation amplitude is independent of frequency (see dotted line, for example, in Figure 7). The average value of the Strouhal number was determined to be 0.36 as in the longitudinal case. Here, it is important to note that the low frequency longitudinal and lateral correlation amplitude characteristics are due to the same source of eddies within the pressure field, i.e., the pressure source with longitudinal wavelengths greater than twice the boundary layer thickness.

The above methodology can be extended to surfaces that are not flat, in particular to structures that are axisymmetric or feature irregularities such as control surfaces. However, additional complexities must be accounted for, such as those effects arising from a non-symmetric transition front as developed on an R/V at angle of attack. In general, any surface obstruction, mode of ablation or angle of attack situation that will produce a non-uniform flow pattern over a surface should reflect different characteristics in the low frequency range.

(c) Compressible Effects (Longitudinal Correlation)

As previously indicated, Howe[7] re-examined the spatial and temporal properties of fluctuating pressure data obtained in Reference 1. Figures 9 and 11 show the normalized longitudinal Co and Quad functions of the cross spectral data of Reference 7. The data are compared to the exponential high frequency asymptotic envelope $e^{-0.1(2\pi)f\xi/u_c}$ which characterized the incompressible data of Bull.[80] Howe noted that at finite values of ξ the asymptotic amplitude for $f\xi/u_c \rightarrow 0$ should be < 1. Consequently, measured cross-PSD's should be compared to an exponential envelope which has a factor to account for spatial attenuation. Accordingly, a factor of 0.8 or 0.9 was incorporated in the figures to account for measured attenuation corresponding to $\xi = 0.5$ inches. He attributed the apparent increasing correlation for $\xi f/u_c > 1.5$ to possible tunnel tare noise, as seen in Figure 9. Moreover, at the higher Mach number conditions, the cross-spectral properties appear to exhibit a greater attenuation compared to the incompressible asymptotic high frequency response.

Figure 12 shows the normalized Co asymptotic values $[\phi_R(\xi, 0, f\rightarrow 0)]$ as a function of ξ/δ^* at Mach 4 and 8. As in the case of Lowson,[55] these values were obtained by extrapolating the amplitudes to $\xi f/u_c = 0$. The data are shown compared to the asymptotic, incompressible equation developed by Lowson. It is quite apparent that the data do not exhibit a pure exponential trend as in the incompressible case. Howe postulated, with reservation, that the high frequency components could be characterized by the incompressible exponential envelope but modified the asymptotic low frequency contributions (as shown in Figure 12). When combining frequency and spatial effects, he proposed that the longitudinal cross-spectral coefficient in fully turbulent flow takes the form

$$A_\xi(\xi, f) = e^{-0.1\omega\xi/u_C(\omega)}[0.5 + 0.5\,e^{-0.07\,\xi/\delta^*}]. \tag{37}$$

The fact that the compressible data show a different characteristic is not at all surprising. The effects of compressibility on the fluctuating pressure field should increase the wavelength and change the corresponding small and high scale coherence characteristics.

As an indication of this phenomena, consider the methodology employed by Bull where a characteristic non-dimensional frequency and scale can be obtained. Here, we consider the pressure field associated with the low frequency asymptotic state for which a Strouhal number, $\omega\xi/u_c$, has a value at which the high frequency asymptotic curve is equal to $\Phi(\xi, 0, f \rightarrow 0)$ for given values of ξ/δ^*. The corresponding wavelength can then be obtained. From Figure 9, consider the data point with spatial distance $\xi = 1.1$ inches. The high frequency contribution gives $\xi f/u_c \approx 0.4$ about $\Phi(\xi, 0, f, 0) \approx 0.7$. The Strouhal number associated with the large scale eddies becomes $\omega\delta^*/u_c = 0.25$ which is less than the incompressible value obtained by Bull. The large scale pressure eddies having wavelength λ_ξ will be greater than $\lambda_\xi/\delta^* = 2\pi/.25 \approx 25$. For the Mach 4 condition, the ratio of boundary layer thickness to displacement thickness is $\delta/\delta^* \approx 2$; hence the wavelengths would be greater than approximately 13δ, a significant departure from the incompressible case.

If we consider the asymptotic high frequency amplitude for the compressible state, it appears to be characterized as in the incompressible case. From Figure 9, $\Phi(\xi, 0, f) \rightarrow 0.05$ for $\xi f/u_c \rightarrow 4$ which corresponds to a value of $\xi\omega/u_c \approx 25$, implying that the pressure component has convected a distance $\xi/\lambda_\xi = 25/2\pi \approx 4$. Again, the high frequency component appears to lose identity when convected a distance approximately 4 times its wavelength; the same condition experienced in the incompressible case.

From the above it appears that the effects of compressibility tend to decrease the wave-number whereby the low frequency (large scale) components convect more rapidly in the stream direction than the corresponding incompressible result, such that they lose their identity even more slowly. On the other hand, the high frequency (low scale) components are characterized by large wave-numbers, travel slowly in the stream direction, and subsequently lose their identity rapidly. These findings are consistent with the hypothesis of Bull[80] and the compressible experiments of Raman.[9] The effect of compressibility is quite apparent when considering the high frequency decay envelopes of Figures 10 and 11. A postulated envelope has been constructed to fit the data at Mach numbers 8 and 10. It is clear that when a characteristic Strouhal number $\omega\delta^*/u_c$ is obtained corresponding to points where the high frequency asymptotic curve has values of $\Phi(\xi, 0, f \rightarrow 0)$, (which represents the smallest of the low frequency pressure eddies

for that portion of the field where the correlation amplitude is independent of frequency) smaller values of $\omega\delta^*/u_c$ or $k_\xi \delta^*$ (wave-number) will be obtained. This in turn will yield high values of wavelength. It is interesting to note that such a postulated envelope yields values of the characteristic Strouhal number (associated with the large scale pressure eddies) that are consistently less than the incompressible values, and subsequently yield wavelengths an order of magnitude greater than δ for the compressible flow case compared to the incompressible flow values.

(d) Compressible Effects (Lateral Correlation)

Figure 13 shows a comparison of typical circumferential Co cross-power spectral density for incompressible data to the compressible data of Reference 1 which were re-examined by Howe.[7] It is noted that the incompressible data acquired at a given frequency for various separation distances were implicitly attenuated as a result of the pure spatial dependence suggested by Equation (36). Hence, comparing these data to a function of mixed dependence such as $e^{-.72\eta\omega/u_c}$ can be misleading. Accordingly, Howe compiled the Mach 4 and 8 data of Reference 1 at several frequencies for fixed separation distances. These data are shown in Figure 14 where one notes that the decay function is not asymptotic to unity. A comparison to Figure 13 indicates that neither exponential form shown fits the compressible data of Howe. Consequently, in Reference 7 a curve fit was applied to the compressible data and is shown in Figure 14.

As in the longitudinal case, variation of circumferential cross-power spectral data can be determined by plotting asymptotic values ($f \rightarrow 0$) as a function of separation distance η/δ^*. Figure 15 shows the results for Mach 4 and 8 conditions from Reference 7. Also shown is the low frequency, asymptotic, incompressible equation suggested in Reference 1. It is apparent that the compressible data exhibit a higher correlation than that implied by the incompressible data fit expression. A curve fit to the compressible data, developed by Howe, is also shown. Consequently, if one considers the high frequency asymptotic amplitudes, the recommended equation for circumferential cross-power spectral density for a fully developed turbulent boundary layer is[7]

$$A_\eta (\eta, f) = e^{-1.4\,\omega\eta/u_c(\omega)} [0.3 + 0.7\,e^{-0.055\eta/\delta^*}], \ \alpha \leq 0.7\,\theta_c \qquad (38)$$

31.

The lack of attenuation in the circumferential direction of the cross-power spectral density indicates the strong effect of compressibility. As previously noted, the low frequency longitudinal and lateral (here, circumferential) correlation amplitude characteristics are a result of the same source of eddies within the pressure field. Inasmuch as the low frequency longitudinal components (large scale) lose their identity slowly, the same phenomena can be expected in the lateral direction for compressible flow.

1.2.4 Convection Velocity

It has been determined that the convection velocity is a function of frequency and spatial separation. The variation with frequency is a consequence of momentum (different size eddies) variation of the pressure field in the boundary layer. Lowson[55] noted that the variation with spatial separation could be a result of accelerated eddy trajectories within the boundary layer as well as varying coherence lengths. This is consistent with turbulent boundary layer phenomenology whereby transition and turbulence are a result of bursting of fluid particles from the viscous sublayer with subsequent exchange of momentum with the surrounding fluid. Lowson, recognizing the difficulty of defining convection velocity, accordingly accepted the definition of Bull.[80] Moreover, the incompressible data of Bull were used to develop an empirical curve for the narrow-band and broad-band convection velocities.

Bull expressed the convection velocity as a function of Strouhal number based on displacement thickness $\omega\delta^*/u_\infty$. Lowson obtained the broad-band values by extrapolating broad-band results to their asymptotic values and plotting results in terms of the spatial coordinate ξ/δ. A cross-plot of the Bull data at a given value of $\omega\delta^*/u_\infty$ along lines of constant ξ/δ^* provided the convection velocity as a function of ξ/δ^*. Empirical curves through the data yielded the following results

$$u_c(\omega)/u_\infty = 0.675 + 0.3\, e^{-0.11\omega\delta/u_\infty} - 0.25\, e^{-1.2\xi/\delta} \tag{39}$$

where the broad-band convection velocity curves correspond to $\omega\delta/u_\infty = 8$, such that

$$u_{c_b}/u_\infty = 0.8 - 0.25\, e^{-1.2\xi/\delta} \tag{40}$$

32.

If we consider an adiabatic, incompressible, 1/7 velocity power law flow, $\delta/\delta^* = 8$ and Equations (39) and (40) become

$$u_c(\omega)/u_\infty = 0.675 + 0.3\, e^{-0.88\,\omega\delta^*/u_\infty} - 0.25\, e^{-0.15\,\xi/\delta^*} \qquad (41)$$

$$u_{cb}/u_\infty = 0.8 - 0.25\, e^{-0.15\,\xi/\delta^*} \qquad (42)$$

Equation (42) is shown to adequately describe the data shown in Figure 5 for both the incompressible and compressible flow states.

When the incompressible formulation of Lowson, based on δ, was compared to the compressible data of Howe[7] a departure was observed that was not reflected when δ^* was used. Figure 16 shows the normalized broad-band convection velocity as a function of spatial distance ξ/δ. As a consequence of this disparity, Howe suggests a modified version of the Lowson result to account for the apparent compressible effects. However, we must keep in mind the usage of boundary layer characteristic lengths. In Figure 16, δ was used for normalization whereas Figure 5 employed δ^*. Again if we consider the incompressible relation between δ and δ^*, the value of ξ/δ where the incompressible and compressible curves join in Figure 16 is about 8. This value corresponds to ξ/δ^* equal to unity in Figure 5, a region where the data show a slight deviation. In effect, Figure 16 has enlarged the scale by the ratio of the boundary layer thicknesses (i.e., by a factor of 8) for the region $\xi/\delta^* \leq 1$ of Figure 5. Further discussions concerning choices of normalization length and velocity parameters will be given in the next section. It will be shown why δ^*, when used as in Equations (41) and (42), is a more effective parameter than δ when considering compressible flow effects.

Bull noted that it was possible to assign a unique value of $u_c = u_c(u_\infty)$ for a given value of the Strouhal number $\omega\delta^*/u_\infty$, which we previously indicated had near constant values. This implies that the fluctuating pressure components have characteristic velocities at some distance from the wall with a mean velocity of $u_c(\omega)$. An estimate of the mean velocity was taken to be about $0.6\, u_\infty$ at a position from the wall of approxi-

mately 2% of the boundary layer thickness. This corresponds to law of the wall coordinates $y^+ = yu_\tau / v_w \approx 100$ (see sketch in Section 2.0). Inasmuch as $u_c(\omega)$ does not appear to exceed $0.9\, u_\infty$, it was postulated that the eddy system whose location from the wall exceeded $1/2\, \delta$ would make no significant contribution to the wall pressure fluctuations.

Consequences of the above observation are two-fold. First, it establishes a relative position in the boundary layer where phenomenological laws can be used to develop prediction methods that characterize the fluctuating pressure field, as for example, in References 8, 55, 56, 63, and 67. Second, the law of the wall coordinates are applicable to both incompressible and compressible flow conditions. This characteristic of boundary layer behavior could be used to interpret the coalescence of incompressible and compressible broad-band velocity distribution with spatial distance as shown in Figure 5.

2.0 EVALUATION OF AERODYNAMIC NORMALIZATION PARAMETERS

The empirical basis of the theory of turbulent boundary layers has hampered development of turbulent aeroacoustic technology because the independent variables controlling production of turbulent noise cannot be derived on a strictly theoretical basis, but must be inferred from data correlations or from a phenomenological view-point. A number of empirically developed prediction techniques have been proposed for the calculation of turbulent boundary layer induced acoustic levels and spectra. As previously noted, the choice of characteristic length and velocity associated with the boundary layer is not a standard selection process. This problem is further compounded for supersonic flow conditions where the typical characteristic lengths vary significantly with Mach number and wall temperature ratio.

Early investigators considered the boundary layer thickness (δ) and displacement thickness (δ^*) as obvious choices of the characteristic lengths. In particular, the choice of the latter together with the boundary layer edge velocity appeared to scale the power spectra. The use of δ^* appears to be satisfactory for both subsonic and supersonic flow conditions as determined from wind tunnel experiments over the last decade. However, its use in hypersonic flow conditions (for flight applications) must be done with caution. This is a consequence of the sensitivity of δ^* for highly cooled wall and pressure gradient regions such as the nosetip where the displacement thickness can become negative.

34.

In an early paper, Willmarth[81] recognized that the power spectral density $\varphi(\omega)$ could be expressed in non-dimensional form as

$$\frac{\varphi(\omega) u_\infty}{q_\infty^2 \, \delta^*} = F\left(\frac{\omega \, \delta^*}{u_\infty}, \, M_\infty, \, Re\right)$$

Several investigators have used the rms pressure p_{rms}, or wall shear stress τ_w, rather than the dynamic pressure q_∞, and δ or θ (momentum thickness) rather than δ^*. The above can be re-written as

$$\frac{\varphi(\omega) u_\infty}{q_\infty^2 \, \delta^*} = (p_{rms}/q_\infty)^2 \, F\left(\frac{\omega \, \delta^*}{u_\infty}\right)$$

where $p_{rms}/q_\infty = f(M, Re, T_w/T_{aw}, \gamma)$ and is consistent with the findings of Willmarth. One notes that the functional form of p_{rms}/q_∞, which will be developed in Section 3.0, depends on the wall temperature ratio as well as properties of the flow environment. Moreover the above representation, as previously mentioned, allows for a comparison of compressible data with incompressible algorithms.

Other normalizing characteristic velocities of the boundary layer consist of the shear velocity $u_\tau (= \sqrt{\tau_w/\rho})$ or convection velocity u_c rather than u_∞. In a recent paper, Willmarth[46] noted that low frequency (large scale) wall pressure fluctuations scale with u_∞ and δ^* while high frequency (low scale) fluctuations scale with the wall parameters u_τ and ν_w (kinematic viscosity). This concept, originally proposed by Corcos[82] and later advanced by Black,[59] has as its basis the fact that the turbulent boundary layer is not a self-similar flow, in the sense that average quantities are not functions of a single non-dimensional length or a single non-dimensional velocity.

The outer part of the flow has a characteristic velocity V_∞ (or u_e for flight application/non-flat plate wind tunnel models). The characteristic length in the outer wake region is the boundary layer thickness. Since incompressible flow was being considered, δ^* was essentially interchangeable with δ. In the law of the wall region (that region associated with the site of intense eddy formation) the characteristic length suggested by Corcos is ν_w/u_τ. Corcos noted that in the law of the wall region, some of the length scales of the eddies are impressed upon it from the outer region. On the other hand, Black showed that using the length scales of the outer flow correlates the low frequency

power spectra while failing to do so in the high frequency range. The opposite was shown to be true in the use of the inner region scales.

To further support the concept of two distinct regions characterizing low and high frequency scaling, classic boundary layer phenomenology will be used to indicate choice of length and velocity parameters. If one considers the momentum boundary layer equation for a turbulent flow, there results

$$\rho u \frac{\partial u}{\partial x} + \rho v \frac{\partial u}{\partial y} = -\frac{\partial p}{\partial x} + \frac{\partial}{\partial y} (\tau_t)$$

where τ_t is the combined molecular (laminar) and turbulent shear stress. If one introduces the Prandtl mixing length concept, the shear stress can be expressed as

$$\tau_t = \mu \frac{\partial u}{\partial y} - \rho \overline{u'v'} = \mu \frac{\partial u}{\partial y} + \rho l_m^2 \left(\frac{\partial u}{\partial y}\right)^2$$

where the unprimed terms represent the mean motion (viscous stress) and the prime terms the turbulent fluctuations (Reynolds stress terms). The term l_m is the classical mixing length.

Prandtl considered the mixing length to be proportional to the coordinate from the wall, such that $l_m = ky$ for k equal to 0.41, a universal constant. VanDriest[73] argued that the Reynolds stress is of considerably greater magnitude away from the wall than the viscous stress, such that, as the wall is approached the effect of the viscous stress should start to become more significant until, at the wall, viscosity dominates. Consequently, a damping function was suggested that modified the mixing length to give $l_m = ky (1-e^{-y/D})$. The term D represents the properties of the fluid and the frequency of oscillation of its movement.

If one introduces the following dimensionless groups

$$u^+ = u/u_\tau$$

$$y^+ = \rho u_\tau / \mu$$

then the mixing length becomes

$$l_m^+ = ky^+ (1 - e^{-y^+/D^+})$$

where $l_m^+ = \rho u_\tau l_m / \mu$ and $D^+ = \rho u_\tau D/\mu$. For an incompressible flow, the constant D^+ has been determined empirically to be approximately 26. For compressible flow,

Cebeci[74] has modified the above formulation to give

$$l_m^+ = k \, y_w^+ \, (1 - e^{-y_w^+/D^+})$$

where

$$y_w^+ = y \, u_{\tau_w}/\upsilon_w \text{ and } D^+ = 26 \, (\rho_w/\bar{\rho})^{1/2} \, (\bar{\mu}/\mu_w)$$

The universal law of the wall plot is schematically shown below together with a typical turbulent velocity profile.
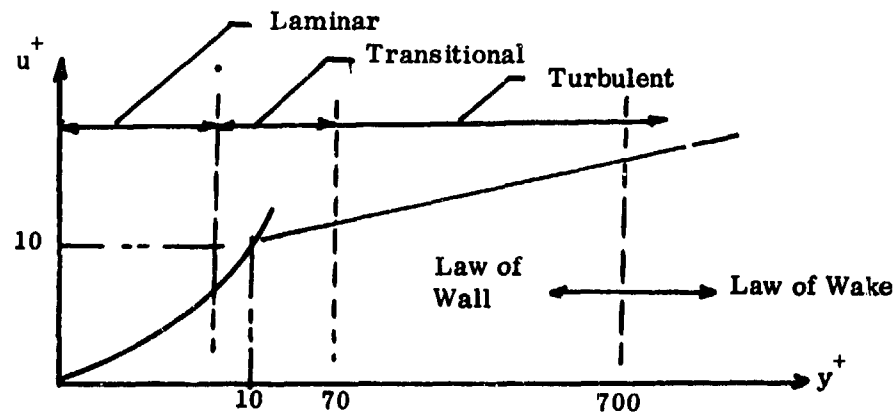
Universal Velocity Profile
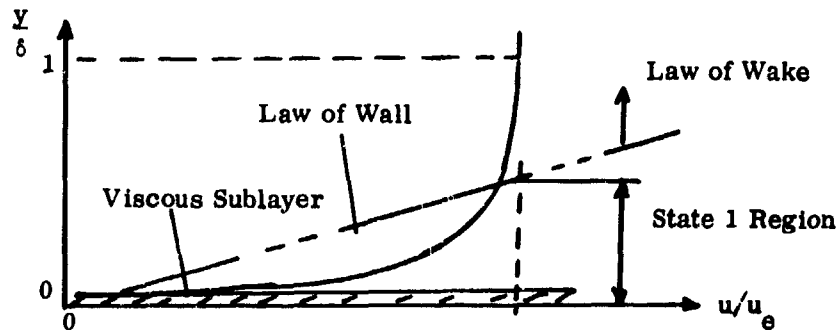
Typical Turbulent Velocity Profile

Cebeci considered two regions where scales of the eddy terms have different characteristics. The two-layer closure model has been compared to a number of experimental data indicating feasibility of the concept for predicting turbulent flow characteristics. The inner region is characterized by an eddy viscosity model based on Prandtl mixing length, namely

$$- \rho \overline{u' v'} = \rho l^2_m \, (\partial u / \partial y)^2 = \rho \, \epsilon_{m_i} \, \partial u / \partial y$$

$$\text{for } \epsilon_{m_i} = l^2_m \, | \partial u / \partial y |$$

and represents the region $0 \le y^+ \le 700$ on the above sketch. In the outer region, represented by $y^+ > 700$, a constant eddy viscosity is used that considers the Klebanoff intermittency factor (γ_K). The eddy viscosity for this region given by

$$\epsilon_{m_o} = 0.0168 \, \gamma_K \, \delta^* u_e$$

where

$$\gamma_K = [1 + 5.5 \, (y/\delta)^6]^{-1}$$

Since the two-layer closure model of Cebeci is synonomous with the high and low frequency regions observed from acoustic data, an analogy between the turbulent closure model and the spectrum of the fluctuating pressure field can be made. The mixing length will be the characteristic length of the high frequency (low scale) region represented by the law of the wall, including the viscous sub-layer. On the other hand, δ^* represents the characteristic length in the low frequency (high scale) region of the law of the wake. Moreover, characteristic velocities are the shear velocity (u_τ) for the wall region while boundary layer edge velocity appears reasonable for the wake region.

The characteristic Strouhal numbers are accordingly

$$\omega \, l / u_\tau = \omega \, \nu_w / u^2_{\tau_w} \qquad \qquad \text{low scale}$$

and

$$\omega \, \delta^* / u_e \qquad \qquad \text{high scale}$$

This result is consistent with those reported previously with the exception of Black[59] who considered u_τ and δ as representative velocity and length for the low scale region.

Non-dimensionalizing the pressure fluctuations at the wall has been accomplished throughout the literature by using local dynamic pressure, local static pressure and

wall shear stress. Corcos[82] and Laufer[58] note that normalizing with τ_w minimizes variation of the results with Reynolds number. Moreover, Laufer reported that the radiated energy spectrum contains considerably less high wave-number components than the pressure spectrum measured at the wall. Bull[61] proposed the same phenomenological reasoning which was implicitly supported by Corcos' and Black's viewpoint and more recently by Willmarth.[46] The use of τ_w as a normalizing parameter for the fluctuating pressure has theoretical basis as proposed by the early works of Lilley.[70] This approach will be used in the current investigation to be presented in the following section. Inasmuch as the shear stress is a difficult parameter to determine, a method has been prescribed that converts the shear stress into local boundary layer parameters. In the development, it was found that Reynolds number was a weak function compared to Mach number for the fluctuating pressure field. Moreover, viscous effects are included in the analysis together with compressible effects, whereas heretofore investigators considered only the latter.

When assessing various fluid parameters used for non-dimensionalizing acoustic parameters in attached boundary layer flows, it has been found that: (1) the boundary layer thickness and displacement thickness have been the primary characteristic lengths, (2) local boundary layer edge velocity or a convection velocity based on some fraction of the edge value are characteristic velocities used almost exclusively, and (3) the dynamic pressure has been primarily used for normalizing fluctuating pressure, with shear stress and local static pressure seldom employed. Until recently, the wall shear stress, the friction velocity, and the inner layer thickness v_w/u_τ have been neglected parameters. However, inasmuch as the low frequency energy is the dynamic driving function in most aerostructural applications, and the source of the low frequency energy is from the outer portion of the boundary layers, those parameters associated with this region appear to be preferable for design considerations.

2.1 Further Comments Concerning δ^* and δ

It has been previously indicated that for incompressible flow conditions, characteristic boundary layer thicknesses δ and δ^* can be readily interchanged. However, for supersonic flow conditions the effects of compressibility do not allow for such an interchange process; hence interpretation of prediction methods based on incompressible flow behavior must be carefully weighed. Because of the effect of compressibility, a

39.

position on a body where the incompressible boundary layer thickness, δ_i, would equal that for a compressible flow case, δ_c would necessarily be a different position. This is shown in the following sketch.

$$x_c > x_i \text{ for } \delta_c = \delta_i$$
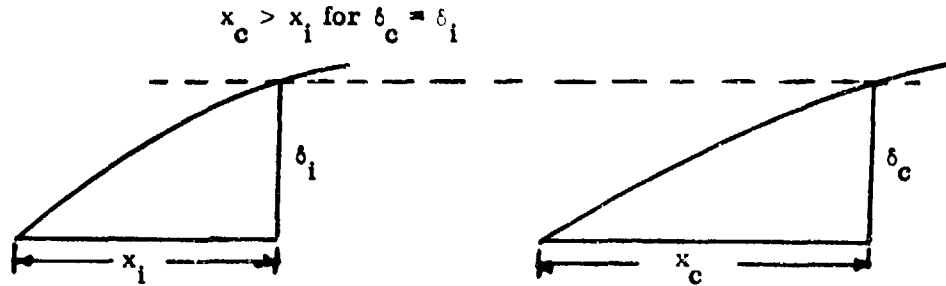
For an adiabatic, incompressible, 1/7 velocity power law turbulent flow, the ratio δ^*/δ is 1/8. On the other hand, for a compressible, adiabatic, 1/7 velocity power law flow, the ratio $\delta^*/\delta > 1/8$. According, the ratios of δ_i^*/δ_c^* and δ_i/δ_c should afford some insight as to the proper choice of length when considering compressible effects. Consider then the boundary layer thickness developed for an arbitrary velocity power law by Laganelli et al[83]

$$\frac{\delta}{\theta} = (n+1) + [\ (\frac{n+2}{n})\ \frac{h_w}{h_{aw}}\ + 1][1 + 0.303\ M_e^2\ ] \tag{43}$$

together with Equation (20) for the boundary layer displacement thickness.

For an adiabatic wall and 1/7 power law (n = 7), Equations (20) and (43) become

$$\delta/\theta = 10.286 + 0.693\ M_e^2 \tag{44}$$

$$\delta^*/\theta = 1.286 + 0.475\ M_e^2 \tag{45}$$

From boundary layer theory,[88] the boundary layer thickness can be expressed as

$$\delta_i = 0.371\ x\ Re_x^{-1/5} \tag{46}$$

and the compressible momentum thickness as[83]

$$\theta = 0.0371 \, x \, \epsilon_T \, Re_x^{-1/5} \qquad (47)$$

where ϵ_T, the compressibility parameter defined by Equation (57), is unity for incompressible flow conditions. Substitution of Equation (47) into Equation (45) for an incompressible flow, gives

$$\delta_i^* = (9/7)(.0371) \, x \, Re_x^{-1/5} \qquad (48)$$

On the other hand, substitution of Equations (47) and (58) into Equation (45) gives

$$\delta_c^* = [9/7 + .0475 \, M_e^2] \, [.0371 \, x \, (1 + .13 \, M_e^2)^{.64} Re_x^{-1/5}] \qquad (49)$$

The ratio of the above two expressions yields

$$\delta_i^*/\delta_c^* \approx \frac{(9/7)(1 + .13 \, M_e^2)^{.64}}{9/7 + .475 \, M_e^2} \qquad (50)$$

One notes that for $M_e \to 0$, the ratio $\delta_i^*/\delta_c^* \to$ unity. However, the ratio decreases rapidly with increasing values of M_e. It was assumed in the development of Equation (50) that the value $x/Re_x^{1/5}$ is invariant between the incompressible and compressible state, i.e., a fixed position on a model subject to the two different flow conditions.

In a similar manner, the ratio of boundary layer thickness becomes

$$\delta_i/\delta_c \approx \frac{10 \, (1 + .13 \, M_e^2)^{.64}}{10.286 + .693 \, M_e^2} \qquad (51)$$

Equations (50) and (51) are plotted below to illustrate the functions' behavior in compressible flow.

41.
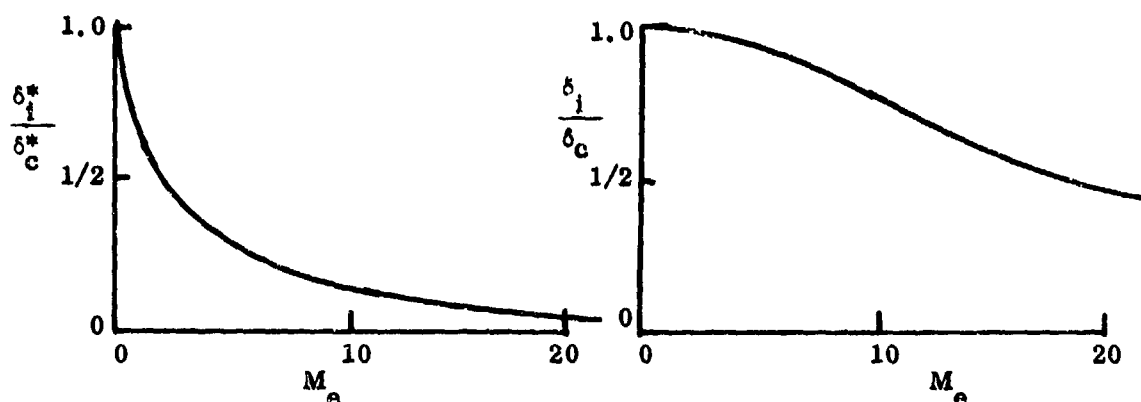
Here, one clearly sees the effect of compressibility on displacement thickness compared to boundary layer thickness. The boundary layer thickness does not change significantly until hypersonic conditions are approached (i.e., $M_e > 5$). Consequently the use of δ in prediction schemes founded on incompressible flow principles does not appear to be a valid parameter as compressible conditions occur over a surface. On the other hand, the displacement thickness reflects a significant change with compressible effects and should be used accordingly.

Based on the preceeding developments, the characteristic lengths and velocities that are recommended for compressible flow are the same as those used for incompressible flow. These consist of:

low scale (high frequency)

ν_w/u_τ length

u_τ velocity

high scale (low frequency)

δ^* length

u_e velocity

3.0 MODIFICATION OF PREDICTION METHODS

This section is concerned with development or modification of prediction techniques that express the power magnitude, power spectral density and cross-spectral coefficients as functions of local boundary layer characteristics. The objective here is to develop methods that are logically constructed from fluid dynamic and acoustic principles while

maintaining an easy to use format for use in design analyses. The rationale is primarily based on concepts and data existing prior to the experiments of this investigation. This is a consequence of the requirement to establish a baseline case of attached turbulent boundary layer flow behavior.

3.1 Power Magnitude

The following methodology will consider the power magnitude for an attached turbulent boundary layer flow using the theoretically based concept of Lilley that p_{rms}/τ_w is bounded from subsonic to supersonic flow conditions.[70] Inasmuch as the shear stress is not a readily derivable term for engineering type predictions, other normalization terms will be used as suggested by experimental data trends and the phenomenological laws of boundary layer flow. The procedure will be generalized for an arbitrary power law turbulent boundary layer and takes into account wall temperature and viscous effects. The results will be compared to the works of Houbolt[56] and Lowson,[55] who considered density variations only, and will demonstrate how to obtain the constants which were previously derived only from experimental data. It should be noted that a similar approach was developed in Reference 67.

Lilley[70] found that the normalized power magnitude for subsonic conditions was bounded in the range

$$1.7 < p_{rms}/\tau_w < 3 \qquad @ \; M_\infty < 1$$

whereas, for a compressible flow, the ratio p_{rms}/τ_w ranged from 2.2 at zero frustum Mach number to 5.6 at a Mach number of 10. The above limits were experimentally observed by Kistler and Chen,[68] Raman[9] and Martellucci et al.[2] These investigators noted that the ratio appeared to be a weak function of the Reynolds number and Mach number. Based upon the above premise, the ratio can be expressed as

$$p_{rms}/\tau_w = A, \quad \text{where A is a parameter.} \tag{52}$$

Using the definition of skin friction coefficient together with dynamic pressure, the wall shear stress can be expressed as

$$\tau_w = (C_f/2)(\rho u^2)_e = 2 q_e (C_f/2) \tag{53}$$

Considering the Blasius form of skin friction generalizing to include a variable power law (see Reference 83), there results

$$C_f/2 = MF \ K(n) \ \varepsilon_T \ (Re_s)^{-2/(3+n)}$$ (54)

where MF is the Mangler factor (unity for flat plates), K(n) is a parameter (.0296 for a 1/7 power law), and the compressibility factor is defined as

$$\varepsilon_T = (\rho*/\rho_e)^{(1+n)/(3+n)}(\mu*/\mu_e)^{2/(3+n)}$$ (55)

In the above, starred properties are based on the classic Eckert Reference Temperature method, namely

$$T*/T_e = 1/2 \ (1 + T_w/T_e) + 0.22 \ r \ (\frac{\gamma-1}{2}) \ M_e^2$$ (56)

which, in effect, represents an average through the boundary layer. However, it is important to note that the compressibility parameter includes both density and viscosity. If one considers a constant mean pressure boundary layer ($\partial p/\partial y = 0$) together with the equation of state and the Sutherland power viscosity law ($\mu \approx T^{4/5}$), Equation (55) becomes

$$\varepsilon_T = (T*/T_e)^{-16/25} = [1/2 \ (1 + T_w/T_e) + .22 \ r \ \frac{\gamma-1}{2} \ M_e^2 \ ]^{-.64}$$ (57)

where a 1/7 (n = 7) velocity power law was assumed. Figure 17 shows the compressibility factor as a function of Mach number with wall temperature ratio as a parameter. It is quite interesting to note that incompressible data (M < 1) could reflect wall temperature effects for $T_w/T_{aw} < 1.0$.

For an adiabatic flow ($T_w = T_{aw}$), Equation (57) becomes

$$\varepsilon_{T_{aw}} = (1 + 0.13 \ M_e^2)^{-.64}$$ (58)

Considering a flat plate geometry (MF = unity) and a 1/7 power law, Equation (52) can then be expressed as

$$p_{rms}/q_e = 2A\, C_f/2 = \frac{2A\, (.0296)}{Re_s^{1/5}[1/2\, (1 + T_w/T_e) + .22\, r\, \frac{\gamma-1}{2}\, M_e^2\,]^{-.64}} \qquad (59)$$

and for adiabatic flow

$$p_{rms}/q_e \Big|_{aw} = \frac{2A\, (.0296)}{Re_s^{1/5}\, [1 + .13\, M_e^2\,]^{.64}} \qquad (60)$$

Keeping in mind that the objective here is to lend some rationale to constants obtained from experimental data, we will allow for the following values: A = 2 which represents an average of the incompressible results and $10^6 < Re_s < 10^7$. Specifically for an average Reynolds number condition, i.e., $Re_s \approx 3.2 \times 10^6$, $Re_s^{1/5} \approx 20$. Hence, Equation (60) becomes

$$p_{rms}/q_e \Big)_{aw} = 0.006/(1 + .13\, M_e^2)^{.64} \qquad (61)$$

A comparison of the above to the Lowson result (Equation (13)) indicates that the coefficient 0.006 is a reasonable choice. Moreover, the essential difference in the two techniques appears in the exponent of the denominator. Here, the true effect of viscosity is noted inasmuch as the viscous effect tends to lower the value of the exponent from the Lowson result. The value chosen for the parameter A and Reynolds number (realistic for turbulent flow requirements), although selected to acquire the value of 0.006, is considered valid for comparative purposes. This is a consequence of several combinations of the two parameters which remain in the observed limits of p_{rms}/τ_w with corresponding wind tunnel local Reynolds number values.

Figure 18 shows Equation (61) compared to predictions of Lowson (adiabatic) and Houbolt (cold wall). It should be noted that Houbolt has modified his cold wall prediction

45.

to an adiabatic result, which is essentially the same as Lowson. Also shown
are data from several experimental studies for both incompressible and compressible
flows. While a large scatter is evident in the experimental data, quite clearly the
effects of viscosity and wall temperature appear to be significant with increasing Mach
number, a result that is not surprising. This is believed to be a consequence of the
increase in p_{rms} resulting from the viscous layer adjacent to the wall.

As an indication of the importance of wall conditions Equation (59) is rewritten
as

$$p_{rms}/q_e = 0.006/[1/2(T_w/T_{aw} \cdot T_w/T_e + 1) + .22 r \frac{\gamma-1}{2} M_e^2]^{.64} \qquad (62)$$

where for recovery factor $r = 0.9$ and $\gamma = 1.4$ together with the definition of the re-
covery temperature (Equation (6)), Equation (62) becomes

$$p_{rms}/q_e = 0.006/[1/2 + (T_w/T_{aw})(1/2 + .09 M_e^2) + .04 M_e^2]^{.64} \qquad (63)$$

Several values of T_w/T_{aw} were chosen and the results are plotted in Figure 19. A
comparison to the Lowson result indicates the importance of viscosity particularly
for the region $M_e > 1$.

3.1.1 Normalizing with Static Pressure

The previous arguments, together with experimental verification, have shown that
root-mean-square pressure fluctuation when normalized by dynamic pressure tends
to be a function of Mach number and wall temperature under the influence of viscosity.
In order to determine the magnitude of p_{rms} relative to the local static pressure for re-
entry conditions, Equation (63) was cast into a different format using the definition of
dynamic pressure, i.e., $q_e = \gamma/2 P_e M_e^2$, such that

$$p_{rms}/P_e = \frac{(\gamma/2)(.006)}{[1/2 M_e^{-3.125}(1 + T_w/T_{aw}) + M_e^{-1.125}(.04 + .09 T_w/T_{aw})]^{.64}} \qquad (64)$$

46.

The two limits that can be developed from the above equation are as follows:

Cold Wall $(T_w/T_{aw} << 1)$

$$p_{rms}/p_e)_{cw} = 0.0042 \left[1/2 \, M_e^{-3.125} + 0.04 \, M_e^{-1.125} \right]^{-0.64} \tag{65a}$$

for $M_e >> 1$

$$p_{rms}/p_c)_{cw} \rightarrow 0.033 \, M_e^{18/25} \tag{65b}$$
$$M_e >> 1$$

Hot Wall $(T_w = T_{aw})$ - Adiabatic

$$p_{rms}/p_e)_{aw} \approx 0.0042 \left[M_e^{-3.125} + 0.13 \, M_e^{-1.125} \right]^{-0.64} \tag{66a}$$

for $M_e >> 1$

$$p_{rms}/p_e)_{aw} \rightarrow 0.0155 \, M_e^{18/25} \tag{66b}$$
$$M_e >> 1$$

Here one sees that the power magnitude will increase with increasing Mach number, which now includes viscous effects through the exponent. Figure 20 shows rms pressure normalized by static pressure as a function of Mach number. Data from several experiments are shown compared to Equations (65a) and (66a). Again, one must keep in mind that no attempt was made to fine-tune the analysis relative to a generalized velocity profile, i.e., fully developed attached turbulent flow was assumed. Good agreement is noted, and most importantly, the theory predicts the correct trend. Finally, one notes that the present concept shows an order of magnitude difference from that predicted by Lowson for $M >> 1$.

Also shown in Figure 20 are data of freestream noise measurements as well as data obtained on the surface of a cone in laminar boundary layer. It is quite interesting to note the difference in level of the rms pressure between the freestream and cone

47.

surface in the works of Stainback et al.[33] The authors noted that at low shock strengths, the model shock had little effect on the ratio of rms sound pressure and local pressure and that the disturbances behind the shock are still predominantly sound. Also, fluctuating pressure levels measured underneath the laminar portion of the boundary layer differed significantly for the various facilities where data were obtained. An examination of the unpublished measurements of Donaldson[87] as well as Laderman[95] indicates a high level of tunnel noise when compared to the cone data of Reference 1 ($M_e = 6.7$) which were obtained in the same facility.

As noted previously, use of the Crocco linear temperature-velocity relationship may be questionable in turbulent boundary layer type flows (Reference 83). If the Crocco relation is modified to a quadratic distribution, as suggested by turbulent profile data, the corresponding temperature distribution at the site of most intensive eddy formation can be expressed as

$$(T_1^\circ - T_w)/(T_e^\circ - T_w) = (u_1/u_e)^2$$

For adiabatic wall conditions, the static temperature distribution becomes

$$T_1/T_e)_{aw} = 1 + r \frac{\gamma-1}{2} M_e^2 [1 - (u/u_e)^2]$$

and for $u_1/u_e = 1/2$, the quadratic relation gives

$$T_1/T_e)_{aw} = 1 + .135 M_e^2$$

which is essentially the same as the linear result.

In order to assess the difference between the Lowson result (density change) and the present method (which combines both density and viscous changes), the GE Equilibrium Non-Similar Boundary Layer Program (ENSBL)[84] was used. This program provides detailed boundary layer profile characteristics using a finite-difference solution of the boundary layer equations and an eddy viscosity model for closure in turbulent flows. An examination of profiles subjected to wind tunnel conditions of Reference 1 indicate that the choice of v_1/u_e is reasonable for the site of eddy intensity; however, the temperature distribution as provided by Lowson at this site appears to be adequate for the low supersonic range only (i.e., $M_e < 4$). On the other hand, while

48.

under-predicting the ENSBL result, the present method gave reasonable temperature predictions throughout the supersonic and hypersonic range.

3.1.2 Generalization to Arbitrary Velocity Power Law

A generalization of the present prediction technique to include both an arbitrary velocity power law exponent and a viscosity power law exponent will be made in this section. Equation (54) will retain its form subject to Equations (55) and (56). Moreover, assumption of a constant pressure boundary layer and use of the equation of state, $\rho^*/\rho_e = (T_e/T^*)$ is also maintained. The Sutherland viscosity law is now generalized to give[35]

$$\mu^*/\mu_e = (T^*/T_e)^m \tag{67}$$

where

$$m = 3/2 + \frac{\ln\left[\dfrac{T_e + 198.6}{T_w + 198.6}\right]}{\ln(T_w/T_e)} \tag{68}$$

The compressibility factor expressed by Equation (55) for an arbitrary velocity power law exponent when transformed into the Eckert reference temperature to include the variable viscosity exponent, becomes

$$\epsilon_T = (T^*/T_e)^{[2m - (1+n)]/(3+n)} \tag{69}$$

where T^*/T_e is given by Equation (56). The Mangler factor, subject to the arbitrary velocity exponent, becomes[83]

$$MF = [2(2+n)/(1+n)]^{2/(3+n)} \tag{70}$$

and Equation (59) is generalized to read

$$P_{rms}/q_e = \frac{2A\,K(n)\,MF(n)}{Re_s^{2/(3+n)}\,[1/2\,(1 + T_w/T_e) + .22\,r\,\dfrac{\gamma-1}{2}\,M_e^2\,]^{\frac{2m-(1+n)}{(3+n)}}} \tag{71}$$

49.

The following table gives values of K(n) and MF (n) as functions of n.

VELOCITY POWER LAW PARAMETERS

n	7	8	9	10
K(n)	.0297	.02276	.01852	.0153
MF (n)	1.176	1.156	1.1404	1.1275
K(n) MF (n)	.0332	.0263	.0211	.0173

It should be noted that MF is applicable to axisymmetric shapes and has the value of unity for flat plates and wedges.

3.1.3 Sensitivity Considerations Concerning Velocity Power Law Exponent -n

As previously noted, the power law velocity exponent has a value of 7 for a fully developed turbulent boundary layer flow. It has been demonstrated[83,86] that this value can be as high as 16 for flows corresponding to the end of transition as defined by surface heat transfer. An examination of Equation (71) indicates that the state of the flow development will not change the rms pressure inasmuch as the ratio

$$\frac{K(n) \, MF \, (n)}{Re_s^{2/(3+n)}} \rightarrow \text{invariant for all values of } n.$$

Hence, variations in rms pressure will be a consequence of changes in the parameter A, Mach number, or wall temperature ratio.

In the previous development, it was demonstrated that inclusion of viscous effects is the primary variation from the work of References 55 and 56. In particular, the exponent on the compressibility factor of 0.64, due to the viscosity contribution, differed from the value of unity when considering density changes only. The value of m was taken to be 0.8 for the method presented within. An examination of flight data[85] has indicated that m has an average value of approximately 0.64 while wind tunnel data from References 1 and 8, as well as from the present experiments, has indicated that the average value of m is 0.90. If one considers a fixed value of n for the compres- sibility parameters as well as the range of wall temperature and Mach number reported in References 1 and 9, the parameter m was allowed to vary between 0.6 and 1.0. It

was found that the low Mach number cases showed a small variation in the compressibility factor (approximately 10%) due to changes of m, a result that had been noted by other analysts.[55, 56, 67, 85] However, for hypersonic conditions, variations in the exponent m resulted in significant changes in the compressibility factor (as high as 50%).

If on the other hand, one fixes the value of m and Mach number (for an adiabatic wall situation), a variation in the velocity power law exponent indicated only a 6% change from $M_\infty = 4$ to 10. Consequently, with the exception of the choice of the parameter A, the most significant effect in use of the compressibility parameter appears to be in the coupling of density and viscosity as opposed to density changes only (i.e., exponent 0.64 instead of unity). This result appears to be amplified for high Mach number values.

The premise of the method presented within is based on the work of Lilley[70] that p_{rms}/τ_w is bounded over a small range from subsonic to supersonic conditions. Others have noted that the parameter A, of Equation (52), was probably a weak function of Reynolds number but should be a function of Mach number. No one has reported the potential wall temperature ratio effect on A. Raman[9] correlated the p_{rms}/τ_w data as a function of momentum thickness Reynolds number and noted that

$$p_{rms}/\tau_w = a \, Re_\theta^b = A \tag{72}$$

for a and b constants. It is easily demonstrated[88] from boundary layer theory that $Re_\theta = Re_\theta(Re_s)$, such that

$$Re_\theta = \text{constant } MF \, \epsilon_T \, Re_s^{4/5} \tag{73}$$

where one notes the compressibility factor, ϵ_T, is a function of T_w/T_{aw} and M_e.

When data from Reference 1 were plotted according to the above formulation, a significant variation in slope was noted (the constant b in Raman's result). Moreover, the dimensionless ratio p_{rms}/τ_w was plotted as a function of Mach number in Reference 9 and showed a decrease with increasing Mach number, a trend that was opposite to the theory of Lilley[70] as well as the tunnel wall data of Kistler and Chen.[68] However,

data of Chyu and Hanly[18] (ogive cylinder), Speaker and Ailman[37] (wind tunnel wall), Willmarth[81] (tunnel wall), and Chaump et al[1] (sharp cone), also indicated a downward trend with increasing Mach number. Evaluation of the parameter A will require more details of thermodynamic and aerodynamic characteristics from reported experiments before attempting to assess a definition for more exacting prediction capability.

When assessing the sensitivity of the velocity power law exponent (n) and the viscous power law exponent (m), it was found that the state of development of the turbulent boundary layer had no effect on terms that constitute the empirical constant 0.006. The most dramatic effect of the power law exponents was found to be on the compressibility parameter; in particular for hypersonic flow conditions. The main contribution was due to viscous changes at these higher speeds. It is apparent that wall temperature effects and subsequent viscous changes in the wall region of the boundary layer must be considered in prediction techniques for hypersonic flow conditions.

It is recommended that Equation (63), which was subsequently generalized for arbitrary velocity and viscosity power laws in Equation (71), be used to predict the rms fluctuating pressure. The normalizing parameter considered for the prediction technique consists of the local dynamic pressure. In order to determine the relative magnitude of the pressure fluctuating field compared to the mean static value, Equation (64) can be used.

3.2 Power Spectral Density

This section discusses the concepts of Black[59] and Houbolt[56] who considered a first moment type representation of the power spectral density (PSD). Black had noted that the strength of a pressure signature beneath a vortex system will generally be determined by local wall shear stress, τ_w. Moreover, for a particular class of vortex systems of mean spacing l_x, and wave velocity u_i, the mean frequency of passage for this system over the wall will be u_i/l_x. As a result, the contribution of the vortex system to the fluctuating wall spectrum should scale with τ_w and u_i/l_x, such that

$$\frac{d\, p_{rms}^2 / \tau_w}{d\left(\frac{\omega l_x}{u_i}\right)} = f\left(\frac{\omega l_x}{u_i}\right) \tag{74}$$

For small vortex systems, where heights are of the order of the viscous sub-layer thickness, length and velocity scales are governed by near wall conditions and Equation (74) is represented as

$$\frac{d\,p^2_{rms}/\tau^2_w}{d\left(\frac{\omega\,\nu_w}{u^2_{\tau_w}}\right)} = F_1\left(\frac{\omega\,\nu_w}{u^2_{\tau_w}}\right) \tag{75}$$

On the other hand, large vortex systems will scale to boundary layer edge values and Equation (74) can be written as

$$\frac{d\,p^2_{rms}/\tau^2_w}{d\left(\frac{\omega\,\delta}{u_{\tau_w}}\right)} = F_2\left(\frac{\omega\,\delta}{u_{\tau_w}}\right) \tag{76}$$

It should be noted that most investigators have chosen δ^* and u_e as the representative scaling parameters for the region associated with Equation (76).

Black found it more convenient to examine the first moment of the PSD rather than the power spectrum per se. In terms of first moment representation, the functional forms of Equations (75) and (76) become

$$\frac{\omega}{\tau^2_w}\,\frac{d\,p^2_{rms}}{d\omega} = F_3\left(\frac{\omega\,\nu_w}{u^2_{\tau_w}}\right) \tag{77}$$

and

$$\frac{\omega}{\tau^2_w}\,\frac{d\,p^2_{rms}}{d\omega} = F_4\left(\frac{\omega\,\delta}{u_{\tau_w}}\right) \tag{78}$$

Black further noted that dimensionless frequencies represented above are related by the parameter $\delta u_{\tau_w}/\nu_w$, such that the overall rms value of the pressure field should have the functional form

$$\frac{(p^2_{rms})^{1/2}}{\tau_w} = F_5\left(\frac{u_{\tau_w}\delta}{\nu_w}\right) \tag{79}$$

Equation (79) again suggests a possible means of evaluating the parameter A as determined by Equation (52). However, if the boundary scaling parameters δ^* and u_e are used for the far field region $(y > \delta_1)$, the right hand side of Equation (79) becomes $\delta^* u_{\tau_w}^2 / v_w u_e$.

Houbolt[56] considered the empirical representation of the PSD as a function of Strouhal number, Equation (24), such that the density distribution of a plot of p_{rms}^2 as given by $\omega \varphi (\omega)$ would maximize when the Strouhal number is unity. This was accomplished by a change in variable, Equation (25), to the definition of the rms pressure. The rationale used by Houbolt is as follows. Suppose one considers Equation (24)

$$\varphi (\omega)/p_{rms}^2 \; (\pi/2) \; u_c(\omega)/\delta^* = 1/[1 + (\omega \delta^*/u_c)^2]$$

One can take any function, say F, of an arbitrary variable x to give

$$F = 1/(1 + x^2)$$

analogous to the above empirical formulation of the PSD. If one plots the function F versus x on a linear scale, the ordinate has a value of unity $(x = 0)$ and becomes asymptotic to the abscissa. If one multiplies both sides of the equation by x and plots xF versus x on a linear scale, the ordinate has a maximum value of 1/2 about $x = $ unity and becomes slowly asymptotic to the abscissa once again. Houbolt then noted that if the product xF (linear scale) were plotted as a function of the ln x (log scale), that the xF product would maximize at 1/2 when $x = $ unity, and rapidly decay to asymptotic values of the abscissa for ln x < 1 and ln x > 1. This is shown below schematically
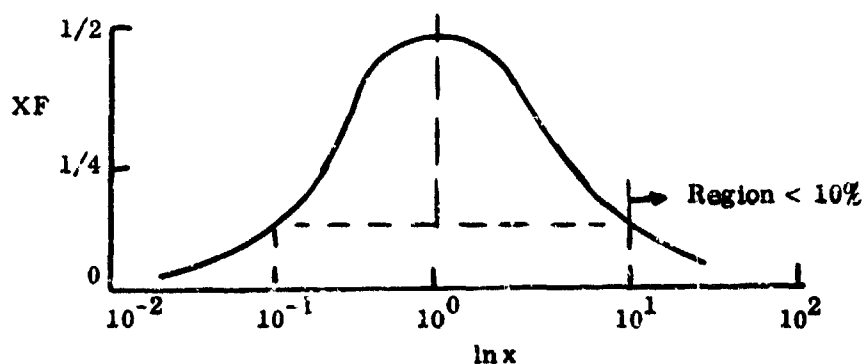
Houbolt considered the change of variable represented by Equation (25) together with the form of the PSD correlation, Equation (24) and suggested the functional relationship represented by Equation (26) with the moment product $\omega \varphi(\omega)$. Although Houbolt did not compare any measurements with the above format, Black compared his method to data of several experiments, both subsonic and supersonic. Inspection indicated that the first moment type representation of data and Black's method display the characteristics suggested by Houbolt and by the sketch provided above.

The following is the analogy adapted in the present investigation regarding first moment type representation of the PSD. Consider a typical plot of the PSD spectrum, shown below schematically
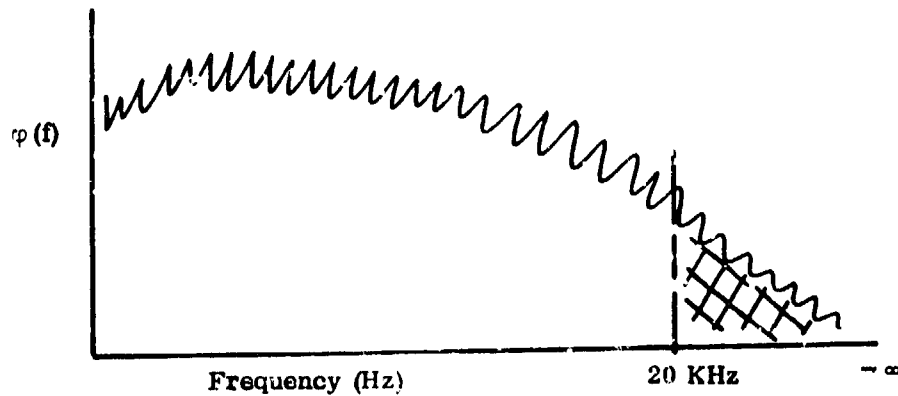
By definition, the rms pressure (0th moment) is expressed as

$$p_{rms}^2 = \int_0^\infty \varphi(\omega)d\omega = \int_0^\omega \varphi(\omega)d\omega + \int_\omega^\infty \varphi(\omega)d\omega \qquad (80)$$

Much of the data considered throughout the literature is analyzed out to approximately 20 KHz. Hence, if one considers the second integral on the right hand side above negligible, the first moment can be approximated

$$p_{rms}^2 \bigg|_{f.m.} \approx \int_0^\omega \omega \varphi(\omega)d\omega \qquad (81)$$

and differentiation gives

$$dp_{rms}^2/d\omega = \omega \varphi \omega \qquad (82)$$

One immediately recognizes the similarity of the above to both Black's and Houbolt's interpretation. From Equation (82), the functional form

$$\omega \varphi (\omega)/p^2_{rms} = \text{function} \left(\frac{\omega l}{v}\right) \tag{83}$$

should be representative of the PSD distribution. Here the characteristic length l, and velocity v take the required near field (wall) values v_w and u_{τ_w} and far field $(y > \delta_1)$ parameters δ^* and u_e, respectively. Moreover, p^2_{rms} is the rms value obtained to the frequency cut-off point. One notes that the above is actually a weighted residual type fit to data where the spectrum is weighted in the frequency range where data were obtained.

As an indication of the first moment type representation for displaying data, Figures 21 and 22 were prepared. Data were taken from References 1, 9, 14, and 18 for attached flow conditions. Moreover, the data represent fluctuating pressure environments over cones, plates, ogive-cylinders and wind tunnel walls. Figure 2 shows the PSD as a function of Strouhal number for high scale coordinates. Spectra have been normalized using conventional techniques in the literature. It is quite apparent that there is a significant scatter in data displayed in this fashion; in particular the ogive-cylinder in the low frequency portion and the $M_\infty = 4$ sharp cone measurements mid-range portion of the spectrum. The latter is believed to be a consequence of transitional flow behavior.

The same data were replotted in first moment type format in Figures 21 and 22 for the far field and near field (wall) forms of the Strouhal number, respectively. In Figure 21 one notes that the spectra tend to coalesce rather significantly within each data group. On an overall basis, the data appear to be more uniformly represented in the coordinates shown. From these representations, no discernable Mach number or Reynolds number trend is noted.

Figure 22 shows the first moment type representation with the high frequency scaling of the Strouhal number. Again, a coalescense of data is noted as well as a definite pattern. Here, a Mach number effect is apparent for the data group represented by Reference 1. These data were taken because of the difficulty in obtaining the wall conditions, v_w and u_{τ_w}, for the experiments of References 9, 14, and 18.

It is also quite interesting to note that data appearing in first moment type format displayed the characteristics suggested by Houbolt; for both the near and far field Strouhal numbers. For example the ordinate appears to peak at approximately one-half for a Strouhal number approaching unity. It is noted that if the circular frequency were used, the abscissa would shift the data to the right by a factor of 2π.

3.2.1 Further Comments on Power Spectral Density

Houbolt[57] examined the data of several experiments[58,68,78] and noted that the spectra could be represented by the empirical formula

$$\frac{\varphi(\omega)u_e}{q_e^2\,\delta^*} = \frac{2 \times 10^{-5}}{1 + (\frac{\omega\,\delta^*}{u_e})^2} \tag{84}$$

in the range of $0.2 < \omega\,\delta^*/u_e < 20$ which is schematically represented below
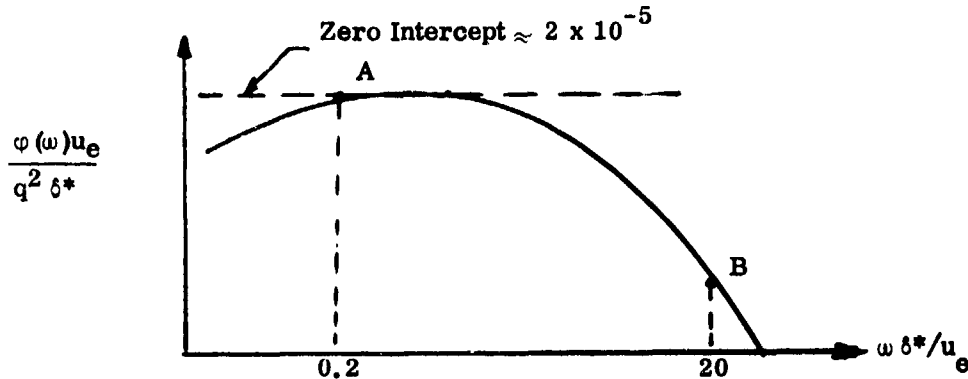
Inasmuch as the data indicate a peak in the low frequency range (point A), the empirical representation was considered to be flat in this range. This situation is considered a conservative approach in structural applications where low frequency responses (f < 1000 Hz) tend to predominate. From the definition of the mean square pressure and utilizing Equation (84), there results

$$\sigma^2 = p_{rms}^2 = \int_0^\infty \varphi(\omega)d\omega = 2 \times 10^{-5}\,\frac{\pi}{2}\,q_e^2$$

Here, we note that the constant $\pi/2$ is a consequence of the functional form of the empirical formula representing the spectrum. Normalized rms pressure is determined to be $\sigma/q_e = 0.0056$ which is approximately the value of measured incompressible flow data.

On the basis of the above development, it appears that a reasonable approach to evaluate empirical formulae for power spectral density, i.e., Equations (24), (28), and (29), is to assess the zero frequency intercept value and the normalized rms pressure values resulting from integration of the various equations. Moreover, the incompressible data of Bull[61] and Blake[64] will be used as a baseline for testing the techniques. It should be noted that these data have been well documented and reviewed in the scientific community. Moreover, the recent assessment of these data by Willmarth[46] and counterargued by Bull and Thomas[62] indicate the credibility of the Bull[61] data for a baseline case.

To integrate the various empirical power spectral density equations, consider the following definite integral

$$\int_0^\infty \frac{x^{r-1}}{(p+q\,x^s)^{n+1}} dx = \frac{1}{s\,p^{n+1}} \left(\frac{p}{q}\right)^{r/s} \frac{\Gamma\left(\frac{r}{s}\right) \Gamma\left(1+n-\frac{r}{s}\right)}{r\,(1+n)} \tag{85}$$

for the condition $0 < r/s < n+1$. In the above $\Gamma(z)$ is the gamma function $= \int_0^\infty e^{-t}t^{z-1}dt$. The three equations to be evaluated are Houbolt, Equation (24), Lowson, Equation (28), and Robertson, Equation (29) and will be designated as H, L and R, respectively. Considering incompressible flow and the format of Equation (84), the three equations become

$$\left.\frac{\varphi(\omega)\,u_\infty}{q_\infty^2\,\delta^*}\right|_H = \frac{\bar{\varphi}(o)}{1 + (\omega\delta^*/u_\infty)^2}$$

$$\left.\frac{\varphi(\omega)\,u_\infty}{q_\infty^2\,\delta^*}\right|_L = \frac{\bar{\varphi}(o)}{[1 + (\omega\delta^*/u_\infty)^2]^{3/2}}$$

$$\left.\frac{\varphi(\omega)\,u_\infty}{q_\infty^2\,\delta^*}\right|_R = \frac{2\,\bar{\varphi}(o)}{[1 + (2\omega\delta^*/u_\infty)^{.9}]^2}$$

58.

where $\bar{\varphi}(0)$ is the normalized zero intercept (low frequency) value of the power spectra. Figure 23 shows the data of Bull,[61] Blake[64] and Schloemer.[89] It appears that the intercept value of the Bull data is approximately 2.2×10^{-5} while that of Blake approximately 1.3×10^{-5}

If we consider the definition of the rms pressure and integrate each of the above expressions, there results

$$\left(\sigma/q_\infty\right)^2_H = \frac{\pi}{2}\,\bar{\varphi}(0); \quad \left(\sigma/q_\infty\right)^2_L = \bar{\varphi}(0); \quad \left(\sigma/q_\infty\right)^2_R = \frac{10}{9}\,\bar{\varphi}(0)$$

which respectively yields

$$\sigma/q_\infty\big)_H = .0056; \quad \sigma/q_\infty\big)_L = .00447; \quad \sigma/q_\infty\big)_R = .00471$$

Hence, it appears that the Houbolt functional form best represents the measured incompressible normalized rms pressure data. Relative to the zero intercept value, if we allow σ/q_∞ to take on the value 0.006 and consider the following

$$\frac{\varphi(\omega \to o)\,u}{q^2\,\delta^*} = \frac{\varphi(\omega \to o)\,u}{\sigma^2\,\delta^*}\,(\sigma/q)^2$$

then

$$\frac{\varphi(o)\,u}{q^2\,\delta^*}\bigg|_H = \frac{2}{\pi}\,(3.6 \times 10^{-5}) = 2.29 \times 10^{-5} \sim \text{Bull's data}$$

$$\frac{\varphi(o)\,u}{q^2\,\delta^*}\bigg|_L = 3.6 \times 10^{-5} > \text{Bull's data}$$

$$\frac{\varphi(o)\,u}{q^2\,\delta^*}\bigg|_R = \sqrt{\pi}\,(3.6 \times 10^{-5}) = 6.48 \times 10^{-5} \gg \text{Bull's data}$$

Thus, considering a limiting representation $(M \to 0)$ of each empirical format, it appears again that the Houbolt concept best represents the data of Bull. One should note that $\sigma/q = f\,[M, Re, T_w]$ and approaches a value of approximately 0.006 for incompressible flow conditions.

If the Houbolt algorithm is reconsidered over the entire spectrum

$$\varphi(\omega) = \frac{\varphi(o)}{1 + K^2 \omega^2} \qquad (86)$$

where $K = k \, l/V$, for l and V some arbitrary length and velocity and k a parameter. Again using the definition of the power magnitude and Equation (86) there results

$$\sigma^2 = \int_0^\infty \varphi(\omega) d\omega = \frac{\varphi(o)}{K} \frac{\pi}{2}$$

and Equation (86) becomes

$$\frac{\varphi(\omega) v}{q^2 l} = \frac{(\sigma/q)^2 \frac{2}{\pi} \bar{k}}{1 + (\bar{k})^2 (\frac{\omega l}{v})^2} \qquad (87)$$

where $\bar{k} = k/2\pi$. For zero intercept values, the above is written as

$$\frac{\varphi(o) v}{q^2 l} = (\sigma/q)^2 \frac{2}{\pi} \bar{k} \qquad (88)$$

Now Bull reported values of $\sigma/q_\infty = 0.005$ while Blake reported values of $\sigma/q_\infty = 0.00876$; the latter result is considered quite high. If we allow for $\bar{k}$ = unity, the normalized zero intercept values of PSD become 1.59×10^{-5} for Bull and 4.89×10^{-5} for Blake. One sees from Figure 23 that these values are not in concert with the data.

In order to match the data as $\omega \to 0$, $\bar{k}$ would have values of 1.3825 and 0.266 for Bull and Blake, respectively. If these values were used in Equation (87) with the measured values of σ/q_∞, the equation would underpredict the Bull data while significantly overpredicting the Blake data. If we allowed $\sigma/q_\infty = 0.006$ and $\bar{k}$ = unity (Houbolt result), the zero intercept value by Equation (88), would be 2.29×10^{-5} a result that matches the Bull data quite nicely. Consequently, Equation (87) with $\bar{k}$ = unity is considered the most appropriate algorithm for predicting incompressible power spectral density.

Keeping in mind that Houbolt's functional form does not preclude compressible conditions, the following is offered as an appropriate generalization. Using Bull's data

as a baseline as well as the Houbolt functional form, Equation (87) can be written as

$$\frac{\varphi(\omega)u_e}{q_e^2 \, \delta^*})_i = \frac{(\sigma/q_e)_i^2 \, \frac{2}{\pi} \bar{k}}{1+(\bar{k})^2(\omega\delta^*/u_e)^2} \quad , \quad \bar{k} \not< \text{unity}$$

Raman[9] determined a similar expression for compressible flow that considered the functional form of Lowson, namely Equation (32). It was previously stated that the incorporation of the $(\sigma/q_e)^2$ in the above acts like a transformation function for compressible effects as given by Equation (53). Thus for $\omega \to 0$, we can write

$$\frac{[\varphi(o)u_e/q_e^2 \, \delta^*]_c}{(\sigma/q_e)_i^2 \, \epsilon_T^2} = \frac{2}{\pi} (\bar{k}) \tag{89}$$

We recognize that the right hand side of the above is constant, as well as $(\sigma/q_e)_i$ which has a value of 0.006. Inasmuch as the compressibility factor, ϵ_T, is an inverse function of Mach number (Figure 17), then the zero intercept value for compressible flow should decrease with increasing M_e. Moreover, use of the incompressible formulation for PSD via the Houbolt format that considers q_e^2 instead of σ^2 for normalization should allow for compressible data to be transformed into the incompressible plane using the compressibility factor. Figure 24 shows the results from several compressible experiments as well as the incompressible data of Bull and Blake. The compressible data indicate that the zero intercept values are indeed less than the incompressible value (2.29×10^{-5}). Hence, Equation (89) will serve as the basis for which compressible data will be evaluated in the current investigation.

Some comments are in order relative to gage size and measuring errors in the high frequency range. Willmarth[46] noted that earlier investigations (prior to Blake) used large transducers that could not resolve small scale fluctuations even when using gage size corrections. Figure 23 shows such a disparity between the data of Bull and Blake for Strouhal numbers > 1. Bull and Thomas[62] performed an experiment to determine the difference between pinhole microphone measurements (such as Blake) and piezoelectric transducers as used previously. It was found that the pinhole caused spurious contributions to $\varphi(\omega)$, up to factors of 4. Consequently, assuming some error

in the Bull data such that the integrated area of the spectra would yield slightly higher values of σ/q than the measured values (.005). we will assume that the normalized power magnitude has a value of 0.006 for incompressible flow. This appears to be a reasonable choice due to the possible high frequency errors from both experiments. Hence, use of the above value for σ/q_∞ and $\bar{k}$ = unity yields the desired result for the zero intercept value. When these values are used in Equation (87), the Houbolt format fits the Bull data over his predicted range $0.2 < \omega\delta^*/u_e < 20$.

It is observed that a significant dispersion of the data occurs for Strouhal numbers $< 5 \times 10^{-2}$. Due to the high velocities attained at hypersonic conditions the compressible Strouhal number can be less than the incompressible values by over an order of magnitude. This is reflected in the compressible data. Moreover, Dods and Hanly[15] noted that at low frequencies spurious contributions are accorded to the pressure fluctuating field from tunnel noise. We have already noted, Figure 20, that the AEDC von Karman A and B Facilities are considered high noise level tunnels. Also Coe et al[14] recognized that statistical accuracy is reduced in the low frequency range. Willmarth[46] in his review commented that many experimenters terminate the spectra for $\omega\delta^*/u_\infty < 10^{-1}$ because measurements are obscured due to tunnel noise. Other factors leading to spurious results are attributed to exact definitions of the transition zones, vibration modes, surface/gage roughness, pressure gradient, gage size (high frequency range) and the interaction of turbulence with turbulence.

SECTION IV

EXPERIMENTAL PROGRAM

1.0 INTRODUCTION

This section presents a brief review of the ground test program, described in detail in Volume II. Wind tunnel experiments were conducted at Arnold Engineering Development Center (AEDC) in the von Karman Gas Dynamics Facilities Tunnels A and B at Mach numbers 4 and 8, respectively. The objective of the test program was to obtain acoustic data for the purpose of verifying or redefining aeroacoustic prediction techniques currently used in the aerospace community. In particular, tests were made on a maneuvering configuration that featured a control surface. Tunnel operating conditions and acoustic sensor (Gulton and Kulite gages) locations were chosen such that measurements were made in regions of laminar, transitional and turbulent boundary layer flow. Variations resulting from the effects of Mach number, Reynolds number, angle of attack, yaw, nose bluntness and control surface flap angles were examined. Several acoustic gages were located in regions where laminar boundary layer conditions prevailed for the purpose of measuring tunnel tare noise levels.

Figure 25 shows a schematic of the model with surface sensor locations. Stations 3.6 and 8.35 represent the flap and slice regions, respectively. Further details concerning the instrumentation are given in Volume II. Table I shows a test summary of tunnel conditions, model attitude and model geometric variations for which data were obtained. Because of the potential volume of data that could be generated from all the tests run, a data sub-set was established for analysis in this investigation. Table II shows the conditions for this sub-set. Also included in this table are the transition zones (onset and end) as determined from heat transfer data. Tables III and IV present nominal local flow properties generated from the GE-RESD 3DFF[93] and 3DV[94] programs for the data sub-set tunnel and model geometric conditions. It is noted that properties shown are those identified as important normalization parameters for aeroacoustic phenomenology. Tables V and VI present the calculated displacement thickness values of the data sub-set for main ray sensor locations. It should be noted that Tables III and IV consider nominal values of the properties along the important sections of the model (i.e., conical, slice and flap regions) where acoustic sensor arrays exist. While it is recognized that some variation does exist, reported values can be used for quantitative results.

2.0 SUMMARY OF TEST DATA

2.1 Thermal and Acoustic Distributions - Mach 4

Figure 26 shows a typical result where the extent of transition is determined from a plot of the Stanton number as a function of axial distance. Transition onset is defined as the point where the local heat transfer is a minimum and the end of transition is defined as the point where the local heat transfer is a maximum. Also noted in this figure is the decrease in heat flux over the slice areas which results from flow expansion from the conical to the flat (parallel to freestream) surface.

Figures 27 through 32 summarize the overall measured sound pressure level (dB, 20 Hz - 20 KHz) as well as the corresponding heat transfer distribution along the model surface for several of the Mach 4 test conditions. Values of overall sound pressure level (OASPL) shown therein have been adjusted from raw sound pressure level data to account for obviously spurious contributions to the total acoustic signal resulting from vibration-induced sensor output at low frequency (i.e., < 1000 Hz). This procedure reduced scatter in most data, but high frequency contributions, which appeared to affect sensor A-9 (also A-3 in Run 10), were not explicitly eliminated in Figures 27 to 32. The transition zones shown in these figures were inferred from experimental data as well as analysis. This was required to insure that measured heat flux levels were consistent with the assumed state of the boundary layer flow. In particular, the complexity of flow over the control surface region yielded heat flux levels that were difficult to interpret relative to transition effects. For all test conditions examined, the flap region experienced turbulent flow behavior. Finally, it should be noted that when values of acoustic data from run to run at identical angle of attack were within experimental scatter (i.e., approximately ± 1 dB), average values of OASPL are shown, in order to simplify graphical representation.

Data in Figures 27 through 29 illustrate the effect of increased flap deflection. While both the acoustic and thermal levels over the flap increased with flap deflection, there does not appear to be any upstream effects along the cone and slice regions. This condition prevailed at both 0° and 7° angles of attack (at $Re_\infty/ft. = 3.6 \times 10^6$) for flap angles ranging from 0° to 20° in spite of increases in flap acoustic levels of up to 17 dB

for the higher flap angles. At $Re_\infty/ft. = 2.5 \times 10^6$, data along the conical portion of the model exhibited similar behavior; however, for the lower Reynolds number a variation in acoustic and heat transfer level over the slice is noted with increasing flap angle (Figure 29). It should be noted that this region is in a transitional flow state such that increased flap deflections could accentuate the flow instability in the area of the joint between the slice and flap.

Figures 27 and 28 exhibit a coincidence of peak acoustic level with transition zone along the conical portion of the model. This maximum level occurs near the end of transition where the heat transfer is also maximum. A clear indication of flow expansion from the conical part of the model to the slice is noted in lower levels of both acoustic and thermal data. This is a consequence of the pressure drop as the flow turns through the expansion wave at the intersection of the cone-slice region. Moreover, non-center line acoustic gages (located on the cone) show a higher level due to the local pressure of the conical region. As might be expected, increased levels in the acoustic and thermal data with increasing flap deflections are a consequence of the higher local pressure associated with these deflections. The same characteristic can be noted on the conical portion of the model when comparing the 0° and 7° angle of attack data.

Figure 30 illustrates the Reynolds number effect for identical model conditions ($\alpha = R_N/R_B = \lambda_\infty = 0$ for $\delta_F = -15°$). It is evident that the transition zone over the cone moves forward for increasing values of Re_∞. As an example, acoustic sensor A-19 is measuring levels near the end of transition for Run 69, while the peak value has moved forward to approximately the location of A-10 in Run 27. On the slice, although there is no clear trend in acoustic data, thermal measurements indicate that heat transfer levels associated with turbulent flow in Run 27 are higher than levels of early transition exhibited by Run 69. On the flap, this relationship is reversed. Inasmuch as the heat transfer coefficient is proportional to $Re_x^{-1/2}$, the lower Reynolds number case will yield higher Stanton numbers along the conical portion of the model. On the other hand, lower values of Reynolds number delay transition; hence, the reason for lower heat flux values along the slice (Figure 29 shows the slice in a transitional mode). Since the flap region is in a turbulent flow, the lower Reynolds number case again yields higher Stanton numbers (here, the heat transfer coefficient is proportional to $Re_x^{-1/5}$).

As indicated by the acoustic and thermal data of Figure 31, the effect of increased angle of attack $(R_N/R_B = \lambda_\alpha = \delta_F = 0$ for $Re_\infty/ft. = 3.6 \times 10^6)$ is to drive maximum transitional levels forward on the cone. Increasing peak values of OASPL as angle of attack increases (i.e., A-10/9/3 for Runs 6,9,10, respectively) primarily result from high frequency contributions to the sound pressure level. Turbulent levels of fluctuating pressure and heat transfer on the slice and on the flap also increase with increasing angle of attack.

Figure 32 demonstrates the effect of nose bluntness including mass transfer at Mach 4 (i.e., injection of mass into the boundary layer at the nosetip). Shown for comparison is a fairing of the sharp nose data of Run 42. The reason for injecting mass at the nosetip is twofold. First it destabilizes the boundary layer thereby rendering an effective boundary layer control mechanism. Second, it simulates an actual ablation process experienced on a re-entry vehicle. In Run 102, it is evident that the relatively constant levels on the cone ($\approx$ 124 dB) are indicative of laminar flow (tunnel nois^\, while sensors A-19, 20 and ?1 are monitoring hig_u levels near the end of transition. The slice is in transitional flow, a fact borne out by the monotonically increasing acoustic levels from sensors A-13, 14, 15 and 17 as well as from theoretical predictions of the heat transfer distributions (when compared to measured data).

The laminar sharp cone heat transfer data fairing (of Run 42) agrees very well with th_it of the blunt nose data indicating that the entropy layer has recovered to the sharp co^ ^ case prior to the first recording heat flux sensor. Moreover, the blowing case exhibits heat flux levels identical with the sharp cone values at the end of transition (conical) as well as along the slice and flap. The acoustic data present a different picture. Sharp cone values show a significantly higher dB level than the blunt cases along the mid-cone region, which is a consequence of transition. The slice characteristics are similar while the sharp cone values appear much lower along the flap than the blunt values. Of particular interest along the slice is the apparent lower acoustic levels than tunnel noise values (as measured on the conical frustum). It is believed that this phenomenon is a result of deflecting the noise pressure waves from the tunnel wall as they pass through the bow shock and expansion wave (at the intersection of cone-slice).

The latter causes the pressure waves to accelerate toward the freestream direction as a consequence of increasing velocity gradient through the expansion wave.

2.2 Thermal and Acoustic Distributions - Mach 8

Figure 33 presents data corresponding to the basic zero angle of attack, sharp cone configuration for values of flap deflection between 0° and -20° at $Re_\infty = 3.7$ x 10^6/ft. It is evident from a comparison with Figure 27 that the transition zone has moved forward on the model for the higher Mach number condition. Also, laminar acoustic levels (A-2 in Figure 33) are higher in Tunnel B than those monitored in Tunnel A. Both these trends were noted in the 1972 experiments conducted at AEDC discussed in Reference 1.

Fluctuating pressure levels measured in turbulent flow on the slice and presented in Figure 33 are approximately 5 dB lower at Mach 8 than corresponding OASPL data at Mach 4. This relationship in the acoustic data is consistent with slice values of heat flux, respectively shown for Mach 4 and Mach 8 in Figures 27 and 33. Flap deflection has virtually no effect on slice acoustic and thermal environments for turbulent flow conditions, a situation also noted in the Mach 4 data of Figures 27 and 28. However, fluctuating pressure loading on the flap itself at Mach 8 is more affected by flap deflection than is loading at Mach 4. This is apparent in Figures 27 and 33, where flap OASPL values at Mach 4 and 8 are seen to increase by less than 20 dB, and by more than 25 dB, respectively, for δ_F between 0° and -20°.

Acoustic and thermal measurements at $Re_\infty = 2.5$ x 10^6/ft., shown in Figure 34, indicate that the transition zone has moved aft on the cone from its location at the higher Reynolds number condition. The same trend was noted in Mach 4 data of Figure 30. Peak acoustic levels in transition apparently were not measured in these runs, with the end of transition occurring between frustum sensors A-10 and A-19 through A-22. Examination of heat transfer data in this region suggests that acoustic gages A-9 and A-10 are registering respectively too high and too low. Increasing the flap deflection from -15° to -20° has no significant effect on conical frustum or slice acoustic/thermal measurements, for example at $\delta_F = 0°$, heat transfer levels are virtually coincident with other data ($\delta_F \neq 0°$) everywhere except on the flap itself. At the lower Reynolds number (2.5 x 10^6/ft.), values of flap OASPL at $\delta_F = -20°$ are slightly below those measured at $Re_\infty = 3.7$ x 10^6/ft., however, noting the flap data of Figure 29 it is evident

that the Mach 8 levels are significantly less than Mach 4 acoustic data at $Re_\infty = 2.5 \times 10^6/ft$.

Effects of model angle of attack at Mach 8 and $\delta_F = 0°$ are indicated in Figure 35. For conical frustum measurements in Tunnel A (i.e., Figure 31), the end of transition apparently moves forward with increasing angle of attack. However, a less clear trend is exhibited by the Mach 8 data of Figure 35. The beginning of transition remains approximately constant while the end moves aft on the model at $\alpha = 14°$. Contributing to the uncertain situation are the anomalous outputs of sensors A-9 (too high) and A-10 (too low). It is evident, however, that peak levels are 5-10 dB higher for the $\alpha = 7°$ and 14° cases than for the $\alpha = 0°$ case. Heat transfer data on the cone similarly exhibit an upward trend with increasing angle of attack at Mach 8. This presents a different picture from the corresponding Mach 4 runs (Figure 31), where levels of both peak acoustic and heat transfer data show less dependence on model angle of attack. Slice and flap measurements at Mach 8 are also more sensitive to α changes than are those at Mach 4 (as a comparison between Figures 35 and 31 will reveal).

Data measured utilizing the blunt nosetip ($R_N/R_B = 0.1$) are shown in Figure 36, which presents OASPL distributions for both a blowing and a non-blowing case. At Mach 8 ($\lambda_\infty = .018$), mass transfer trips the boundary layer resulting in a transition zone on the conical frustum that extends approximately from $X/L = .2$ to $.7$. In addition, acoustic levels in turbulent flow (sensors A-19 through A-22) are only slightly greater than the laminar levels indicated by Run 87. However, at Mach 4 ($\lambda_\infty = .021$) virtually the entire model is emersed in turbulent flow, acoustic levels of which are approximately 5 dB greater than laminar measurements of Run 102 in Tunnel A.

On the slice at Mach 8, turbulent fluctuating pressure levels for the blunt cone are almost identical to the sharp cone acoustic environment, indicated by data in Figures 36 and 33. As on the cone, these levels are only slightly higher than the laminar environment of Run 87, although thermal data do indicate increased levels of heat transfer. High flap levels in Run 100, approximately the same as those associated with the sharp model (Run 58), evidently arise from the -20° flap deflection. Similarity of characteristics between the blowing case and the sharp cone case at Mach 8 is evident in the heat transfer data as well, wherein levels aft of the transition zone and on the slice and flap are almost identical for Runs 100 and 58.

Figure 37 shows the results of a combination of geometric effects. For the blunt case, Run 90 exhibited the same characteristics as Run 100 along the conical and slice regions. Inasmuch as the flap was on the zero angle position, both the heat flux and OASPL there indicated levels consistent with the slice values. In the same manner, Run 99 showed conditions quite similar to Run 87 along the conical and slice regions. It is interesting to note the change in heat transfer and acoustic characteristics along the flap region. Here the 20° flap angle for the non-blowing nosetip (Run 99) shows levels for both heat and OASPL that are less than those of the blowing case (Runs 100 and 102). This phenomenon is somewhat surprising since the injectant gas at the nose-tip should have negligible effect (compared to that entrained from the freestream) at a downstream position of $x >> R_N$. Finally, Run 50 ($\alpha = 7°$) again reflects variations in the transition zone when compared to the comparable case at Mach 4 (Figure 28), relative to heat flux and OASPL.

(a) 2.3 Sound Pressure Level Data - Mach 4

Conical Frustum Measurements

Figures 38 through 40 present fluctuating pressure data corresponding to fully turbulent and transitional flow at zero and 7° angle of attack, as well as transitional/ turbulent flow at 14° angle of attack. Figure 38 demonstrates the essentially similar spectral content of the fluctuating pressures in turbulent flow over a relatively large distance (X/L = .5 to .86). In Figure 39, progression of transitional flow through onset, peak and decay into turbulent flow is presented in terms of sound pressure level (SPL) curves from the mid-cone acoustic sensor array. It appears that the maximum influence of transition occurs in the high frequency portion of the fluctuating pressure spectrum. At the point of peak transition, levels across the complete spectrum (20 Hz-20 KHz) are increased 4-15 dB when compared to Tunnel A tare noise and 3-10 dB when compared to turbulent flow. Figure 40 illustrates the decay of transitional flow spectra at 14° angle of attack. In this case, there appears to be much more high frequency scatter in the SPL data for sensors A-3, 8, and 9. Levels below 8 KHz, however, are approximately coincident for these three sensors, and drop off several dB to the values indicated by A-10 and A-19.

Effects of Reynolds number and model angle of attack variation on acoustic levels forward of transition (indicative of tunnel tare) are illustrated in Figure 41. These SPL data reveal that measured levels increase with both Re_∞ and α.

(b) Slice Measurements

Figures 42 through 44 present acoustic data for sensors A-13, 14, and 15 in the slice longitudinal array and for A-17 in the lateral array (A-16 and A-18 provided erroneous data in Tunnel A). Sound pressure level curves in Figure 42 for A-17 (Runs 6, 23, 27, and 42) demonstrate that in fully turbulent flow, slice acoustic levels are essentially independent of flap deflection, for $0 \le |\delta_F| \le 20°$. In these zero angle of attack cases, differences evident in the A-17 spectra (for frequencies < 5 KHz, there is agreement to within $\pm$ .5 dB) are a consequence of experimental data scatter, since no definitive trends with flap deflection are exhibited.

Figure 43 illustrates the spatial distribution of Mach 4 turbulent spectra along the slice at a flap deflection of -20° for the sharp nosetip. Generally decreasing levels are evident from slice forward to slice aft locations. A similar trend for turbulent flow was noted in the slice spectra for the blunt nosetip configuration (with blowing). This situation is reversed, however, for slice transitional cases. The wide variation among slice SPL data indicated by Figure 44 is typical of all spectra measured in transitional flow over the slice (Runs 69, 84, 89 and 102 - Mach 4).

(c) Flap Measurements

The flap was exposed to turbulent flow conditions for all Mach 4 cases in the data sub-set (Table II); given detailed examination the following trends were noted in flap SPL data:

1.) At a given station (e.g., sensor A-27) and for identical model and freestream conditions, spectral levels increase with increasing flap deflection.

2.) In a given run, acoustic levels as measured by A-26, 27, and 28 were monotonically decreasing across the flap.

These two trends are illustrated respectively by Figures 44 and 45.

2.4 Sound Pressure Level Data - Mach 8

2.4.1 Comparison of Laminar and Turbulent/Transitional Measurements

Figure 47 presents conical frustum data in laminar flow for various conditions of freestream Reynolds number and model angle of attack. These measurements reveal the same trends as analogous Mach 4 data (Figure 41), i.e., sound pressure levels increase with larger values of Re_∞ and α. Mach 8 laminar data also suggest that a higher level of freestream noise exists in Tunnel B than in Tunnel A.

A comparison of laminar and turbulent fluctuating pressure data along the model surface at zero angle of attack is shown in Figures 48-50. The first of these figures presents Mach 8 sound pressure levels measured over the blunt configuration without mass injection. Two characteristics are evident in these laminar data. There is essentially similar spectral content for conical frustum measurements (A-6 and A-19). An analogous situation exists for the control region which presents an effective continuous flat surface from station 24.25 aft due to the zero flap angle for Run 87. A general collapse of these latter data (for A-13, 16, 26, 27) is evident between frequencies of 250 Hz and 12500 Hz at a level approximately 5-10 dB lower than the conical frustum laminar sound pressure levels. This situation suggests that the expansion wave which exists at the cone-slice interface may be responsible for attenuation of tunnel freestream noise impinging on the model. This drop in level occurs both longitudinally (compare A-6 and A-13) as well as circumferentially (compare A-19 and A-16).

Figures 49 and 50 (Runs 90, 44, respectively) present measurements corresponding to primarily turbulent flow over both the conical frustum and the slice/flap region. (In both plots sensor A-6 is registering in different regimes of the transition zone). Comparing data for the two blunt configurations (with and without mass injection), it is apparent that conical frustum levels are from 0-2 dB greater than corresponding laminar data of Figure 48. Turbulent levels on the flap ($\delta_F = 0$) indicate a 0-1 dB increase over laminar spectra. These relationships hold except at the high frequencies where turbulent data generally exhibit an upswing. Analogous turbulent measurements over the sharp cone model shown in Figure 50 (Run 44) are quite similar to those of Run 90.

Figures 51 and 52 respectively, present longitudinal and circumferential variation of sound pressure level on the sharp cone model at 7° angle of attack. The data of

Figure 51 indicate that the maximum influence of transition occurs in the high frequency portion of the spectrum, an effect also noted in the Mach 4 sound pressure level data. Measurements from A-19 in this figure show both the effect of lower levels in the turbulent boundary layer region and the effect of the sensor being off the windward meridian. Figure 52 indicates the variation of sound pressure level in the circumferential direction at $\alpha = 7°$. The applicable sensors (i.e., 19, 22, 21) are located at angles 328°, 90°, 180°, respectively, and register OASPL values of 130.2, 126.6 and 120.5 dB. These data indicate that a minimum of 10 dB variation can exist between windward and leeward fluctuating pressure levels at model angles equal to or greater than 7°.

(a) Slice Measurements

Figure 53 presents slice longitudinal array data for the sharp cone at a flap deflection of -20°. (Sensors A-17 and A-18 in the lateral array provided erratic data in Tunnel B.) These measurements reveal that a general reduction in level is exhibited across the slice going aft. However, A-15 indicates a much greater reduction and appears to be inconsistent with the rest of the data. This same trend occurs in Figure 54 which compares sound pressure levels from A-15 and A-16 for various values of δ_F. Hence explicit levels associated with sensor A-15 should be treated with caution, recognizing that the measurements are perhaps 5-10 dB low at Mach 8. The slice data are generally insensitive to flap deflection, a fact that was similarly noted in the Mach 4 data.

(b) Flap Measurements

The data trend with flap deflection apparent in flap acoustic measurements at Mach 4 was also exhibited by sound pressure level data at Mach 8. Figure 55 reveals that flap acoustic levels increased by approximately 25 dB throughout the frequency range when δ_F was increased from 0 to -20°. At Mach 8, the general trend in spectrum level with flap location was to increase across the flap going aft. However, OASPL values do not necessarily follow this trend due to the difference in high frequency data for sensors A-27 and A-28. This effect is indicated by the data of Figure 56.

2.5 Root-Mean-Square Pressure

Figure 57 illustrates rms fluctuating pressure data along the conical portion of the model for both test Mach numbers. The attached turbulent boundary layer predictions of Lowson and the present method (Equation (61)) are shown for comparison as well as the transitional boundary layer prediction of Reference 1. With exception of the mass injection cases, the conical region acoustic gages were experiencing transitional flow characteristics, thereby limiting data from fully developed turbulent flow conditions. Also shown in the figure are typical normalized rms pressure levels in laminar flow (indicative of tunnel noise). Higher values of rms pressure are noted for the blunt configuration, a consequence of the lower edge dynamic pressure (entropy effect). The data are generally in good agreement with other reported results for zero angle of attack conditions; in particular, the data of Reference 1 which was acquired in the same facility. Increasing angle of attack tends to introduce significant data scatter, particularly for transitional flow. The data appear to indicate decreasing values of normalized rms pressure with increasing α. It is difficult to discern Reynolds number effect with the small data sample available. The blunt nose data represent conditions where mass injection was introduced at the nosetip for the purpose of inducing turbulent flow characteristics. Here, both transitional and turbulent data appear to be consistent with sharp measurements acquired through natural transition.

Normalized rms pressures for the slice region are shown as a function of local Mach number in Figure 58. The data for both test Mach number conditions appear to be in general agreement with other reported results (Figure 1) and show a continued decrease in p_{rms}/q_e for values of $M_e > 6$. Also shown in this figure are the flap sensors A-26 and A-27 for zero flap deflection (continuation of the slice). There appears to be a decrease in rms pressure with increasing angle of attack as experienced on the conical region. However, the data (at least for $M_\infty = 8$) appear to be consistent with prediction for this condition. Slice measurements appear to reflect a Reynolds number effect, such that higher levels of normalized rms pressure occur with decreasing freestream unit Reynolds number. Donaldson[87] has noted higher freestream noise content at this unit Reynolds number condition than for the other reported value $Re_\infty/ft. = 3.6 \times 10^{-6}$).

It is evident that measured laminar boundary layer levels on the slice (Run 87, $M_\infty = 8$) are lower than the conical values, a fact similarly noted in the discussion of SPL in Section 2.4 above. This would indicate that the tunnel radiated noise is attenuated as a result of the expansion wave from the geometry change of the cone to the slice.

Normalized rms pressure fluctuations for the flap environment are shown in Figure 59. Increasing the flap deflection increases the rms pressure for both zero and non-zero angle of attack conditions. It is quite interesting to note, however, that for zero angle of attack and $0 \leq -\delta_F \leq 15°$ data tend to follow the pattern experienced on the cone and slice. The most significant depature appears to be for flap deflections $>-15°$, lower freestream unit Reynolds number (i.e., $2.5 \times 10^{+6}$), and blunt body tests. Concerning the bluntness effect, the non-injectant data tend to yield higher values of rms pressure than the injectant cases. The former might be experiencing transitional effects in the flap region. It is also interesting to note that the entropy layer significantly reduces the local pressure field for the Mach 8 condition ($-\delta_F > 10°$) compared to a negligible effect at the Mach 4 condition. This effect appears evident in the data, such that the rms pressure at Mach 8 tend to be lower than those measured at Mach 4. One must also keep in mind that the shock emanating from the hinge joint together with the expansion wave from the conical/slice intersection can interact, causing high rms pressure levels at the extended flap positions. Although not an obvious trend, increasing model angle of attack tends to decrease the rms pressure level. However, as in the slice case, flap data tend to follow the Mach number dependent predictions indicated in Figure 59.

2.6 Power Spectral Density - Mach 4

(a) Conical Frustum Measurements

Figure 60 presents normalized power spectral density as a function of Strouhal number for the Mach 4 test conditions. Normalizing parameters can be obtained from Tables III and V or from third octave PSD plots of actual data presented in Volume II. The data are generally separated into two categories consisting of transitional and turbulent flow. For transitional flow, the data reveal an angle of attack effect, i.e., a decrease in normalized PSD with increasing α. The same trend is exhibited for the turbulent flow behavior, in particular for $f\delta^*/u_e > 10^{-3}$. This latter observation should be considered with caution inasmuch as the reporting sensor (A-19) is not in line with the windward meridian for which local flow properties at angle of attack were evaluated. The turbulent boundary layer data also indicate a possible bluntness effect which is believed to be a consequence of the entropy layer yielding lower values of dynamic pressure. Insufficient data do not allow for speculation of Reynolds number effects. In general, these normalized spectral measurements agree with data obtained in a previous study[1] in the same facility.

(b) Slice Measurements

Normalized power spectral density data for the slice portion of the model are shown in Figure 61. These measurements reflect turbulent boundary layer conditions for the high unit free Reynolds number cases. Expressed in this format, the data do not appear to indicate any specific trends with angle of attack. However, bluntness effects are reflected by the higher levels in PSD. In general, the magnitude of normalized PSD along the slice tends to be less than values measured on the conical frustum. As a consequence of flow expansion resulting from the conical to slice geometry change, the local pressure decreases and subsequently could attenuate the fluctuating pressure field. One should also keep in mind that the expansion wave has the effect of also attenuating the tunnel radiated noise thereby rendering less contaminated noise levels on the slice region.

(c) Flap Measurements

Figures 62 and 63 display the normalized power spectra for the flap region of the model. In Figure 62, a significant Reynolds number effect is exhibited. Two

phenomena relative to this condition should be noted. First, for Re_∞/ft. $+ 2.5 \times 10^6$, possible shock interaction between the weak expansion wave (cone/slice intersection) and strong hinge shock may be contributing to measured values. Second, the lower freestream Reynolds number runs exhibited transition zones over the control surface region. Figure 29 shows the OASPL for this Reynolds number condition to be greater than other reported measurements when the slice was experiencing turbulent flow characteristics.

An examination of the zero flap deflection condition indicates no discernable angle of attack effects. However, with increasing flap angles, a slight effect of α is noted, such that, within a given flap angle data set ($\delta_F = 0$), an increase in angle of attack tends to decrease the normalized power spectral density. A significant increase in normalized PSD, however, is experienced with increasing flap angle. This condition can be expected as a consequence of higher local pressure and subsequently increased rms fluctuating pressure levels. It should be noted that the zero flap angle condition (which is a continuation of the slice) yields levels that are consistent with those obtained on the conical frustum as well as the slice. However, the higher flap angle conditions yield levels of normalized PSD up to an order of magnitude higher. This situation mandates a modification to the prediction algorithms developed in the literature for more conventional geometric configurations.

Figure 63 shows the normalized PSD distribution along the flap surface for a $\delta_F = -20°$ condition at the higher unit freestream Reynolds number condition (3.6 x 10^6). Data from both sharp and blunt nosetip configurations are represented. The latter features conditions with and without mass injection at the nosetip. While the data reflect a significantly higher level than that experienced on the cone or slice region, a still further departure is exhibited for the non-blowing blunt case (Run 102). Here, the normalized PSD level appears to be in the range of data reported for lower freestream unit Reynolds number of Figure 62 which featured transitional flow along the slice. An examination of Figure 32 indicates that the non-blowing blunt run is also experiencing transitional flow along the slice and has OASPL's exceeding values where turbulent flow prevailed on the slice. The condition when the slice experiences turbulent boundary layer flow, as in Runs 42 (sharp) and 103 (blunt with mass injection),

normalized flap measurements fall generally into the same range (Figure 63). In order to ensure that the effect being observed is a consequence of transitional flow along the slice, an examination was made relative to the shock angle interaction. The bow shock angle ($\approx 15.7°$) did not intersect with either the expansion wave (conical/slice) or flap shock for the sub-set conditions analyzed in this study (Table II). Hence, the high levels of normalized PSD's shown in Figures 62 and 63 appear to be a consequence of transition occurring on the slice foward of the flap.

2.7 Power Spectral Density - Mach 8

(a) Conical Frustum Measurements

Figure 64 presents normalized power spectral density as a function of Strouhal number. As in the Mach 4 tests, data generally separate into two categories corresponding to transitional and turbulent boundary layer flow conditions. Moreover, the blunt nose run (100) features higher levels of nor nalized PSD for turbulent flow, a condition that also existed at Mach 4 (see Figure 60). However, it should be noted that the transitional data reflect an angle of attack trend that is opposite to that exhibited at Mach 4; i.e., an increase in level with increasing α. For turbulent flow conditions, no discernable trend in normalized PSD with angle of attack is evident. The data are in general agreement with results of the Mach 4 tests as well as data with other transitional and turbulent reported in the literature.[1,9,14]

(b) Slice Measurements

Normalized power spectra for the slice sector of the model are shown in Figures 65 and 66. Unlike the Mach 4 data, a more significant variation in the zero intercept values (flat portion of spectra) is evident. The level of sensor A-15 appeared to be much lower than measurements for comparable gages along the slice (see 2.3 above). Although a careful examination of the raw data was made, which did not include any malfunction, the absolute data for this sensor are considered of dubious validity. However, the general trend of the measurements relative to bluntness, angle of attack, and Reynolds number can be used to determine fluid dynamic effects. The blunt nose-tip runs again reflect the significant effects of transition. Run 102 represents a controlled test that featured a transition zone over the conical frustum of the model.

Figure 36 show. the transition zones for both Runs 100 and 102 based on thermal measurements. Here a longer transition zone yielded higher values of OASPL and ultimately affected flap readings as well. It should be noted that the predicted end of transition for both runs was approximately the same (x ≈ 23 inches); however, the heat transfer data of Run 102 were much more difficult to assess. The sharp cone values of normalized PSD over the slice (Run 58) indicate levels that are lower than the Mach 4 results.

Figure 66 displays normalized power spectral density at several conditions for sensor A-15 (sharp cone model). The most significant effect exhibited by these slice data appears to be the angle of attack variation for the zero intercept value. Moreover, a comparison of the $\alpha = 0^\circ$ data indicate higher levels of normalized PSD for the lower freestream unit Reynolds number, a result that is consistent with the Mach 4 data. However no disparity in angle of attack was observed at the Mach 4 condition as noted at Mach 8.

(c) Flap Measurements

Figures 67 and 68 present normalized PSD's for the flap region of the model. As for the Mach 4 runs, a significant effect of Reynolds number is noted (i.e., Run 77 at $Re_\infty/ft. = 2.5 \times 10^6$). However, unlike the Mach 4 tests, the slice at Mach 8 was not exposed to transitional flow characteristics. Moreover, the zero intercept value appears to be lower than the comparable Mach 4 case (Run 84). It is interesting to note the disparity of angle of attack effects for zero flap deflection. There is a marked increase in normalized spectral levels with increasing α which did not occur at Mach 4. Data for $\alpha = 0^\circ$ reveal zero intercept values that are an order of magnitude less than the Mach 4 test (Run 6). The data also show the same trend as Mach 4 measurements with increasing flap deflection. For the 20° flap deflection, normalized PSD levels are generally of the same magnitude. Finally, it should be noted that normalized levels on the flap at zero deflection (continuation of the slice) indicate higher values than the slice (Figure 66). It is speculated that the field joint (flap hinge) might act as a roughness mechanism which in turn enhances the fluctuating pressure field. However, this situation appeared to occur only for the Mach 8 tests.

Figure 68 displays normalized power spectral density along the flap surface for the higher unit freestream Reynolds number and for 20° flap angle. Levels of normalized

PSD are generally the same as those experienced at Mach 4 (Figure 63). One will recall that Run 102 (Mach 4) exhibited high values of PSD as a consequence of transitional flow characteristics along the slice, thereby, enhancing the flap values. As previously indicated Run 102 (Mach 8) exhibited a transition zone over the conical frustum and subsequently influenced the slice and flap region OASPL's (see Figure 36).

2.8 Broad-Band Cross-Correlation Functions

(a) Conical Frustum Measurements

Figures 69 and 70 present longitudinal broad-band correlation functions for laminar transitional and turbulent flow. The laminar data at Mach 4 and 8 provide an indication of the correlation characteristics of the tare acoustic environment present in Tunnels A and B respectively. For Mach 4 and Mach 8 transitional data over the conical frustum levels of correlation are generally compatible with results presented in Reference 1, even to the extent that Mach 8 levels are higher than those of Mach 4. Current data, however, exhibit a much more marked decrease with increasing model angle of attack. This may be due to shifting of the transition zone relative to the conical sensor array with changes in model orientation. Longitudinal correlation data corresponding to turbulent flow on the cone (Runs 103 and 10 – Tunnel A) are shown in Figure 69, and results demonstrate quite good agreement with turbulent data of Reference 1. Reduced levels of correlation present in Run 10 are evidently related to the fact that the acoustic environment is in an intermediate state between transitional and fully turbulent flow (see Figure 28). In the data of Run 103, turbulence was induced through tripping the boundary layer utilizing mass injection over the nosetip, whereas transition occurred naturally in the 1972 program[1] and turbulent measurements were taken at model locations aft of the transition zone.

Figure 71 presents circumferential cross-correlation functions relating sensors A-5 and A-6 only, due to the fact that A-7 did not provide valid data. As in the case of longitudinal functions, transitional data exhibit slightly higher correlation than turbulent, and Mach 8 transitional data are higher than analogous Mach 4 circumferential functions. At Mach 8, there was little difference between circumferential correlation

values obtained over the blunt cone with mass injection, hence only examples of this former are shown in Figure 71.

(b) Slice Measurements

Figure 72 presents Mach 4 longitudinal correlation functions applicable to transitional and turbulent flow on the slice. For the latter data at zero angle of attack, there is only slight variation in the slice cross-correlation characteristics between $\delta_F = 0°$ and $\delta_F = -20°$. It is apparent that increasing the model angle of attack tends to increase both the rate of decay with separation distance and the time of maximum correlation. These effects were also noted in measurements over the conical frustum (Figure 69).

Longitudinal cross-correlation functions measured at Mach 8 are shown in Figure 73. Laminar flow occurs over the slice for the blunt nosetip configuration without mass injection at the nosetip. A typical set of broad-band functions corresponding to laminar flow is presented and values of correlation are seen to be generally higher than turbulent levels. This phenomenon was also evident in the conical frustum data of Mach 4. For the Mach 8 condition, it is apparent that for Run 100 (where turbulent flow is induced by mass injection) the rate of cross-correlation decay is greater than for those cases wherein natural transition occurs forward of the slice at zero angle of attack (e.g., Run 58). As is the case of Mach 4 turbulent data, the rate of correlation decay with separation distance increases for $\alpha = 7°$ and $14°$.

(c) Flap Measurements

Longitudinal cross-correlation functions measured on the flap are presented in Figures 74 and 75 for Mach 4 and Mach 8, respectively. The initial set of functions in Figure 74 corresponds to those Tunnel A cases wherein the slice environment was designated as transitional (Runs 69, 84, and 102). Flap overall sound pressure level for these cases (Figures 26 and 29) are the highest of all acoustic measurements in either Tunnel A or B, ($\delta_F \leq 20°$) and the environments are further characterized by relatively large differences in level among sensors A-26, -27, and - 28 ($\Delta dB \approx 12$ between A-26 and A-28). Corresponding cross-correlation functions shown in Figure 74 depict a rapid decay in correlation over the flap. These phenomena suggest a type of incipient transitional/turbulent flow may be impinging on the flap for these cases,

80.

analogous to the "overshoot" effect on acoustic level exhibited by transitional flow on a cone.

Also shown in Figure 74 are data indicating the effect of flap deflection on longitudinal correlation functions. It is evident that the rate of decay with separation distance increases for increasing flap angle. The final data of Figure 74 consist of turbulent cross-correlations which show that the respective effects of high model angle of attack and mass injection induced turbulence are apparently to increase the rate of correlation decay with separation distance.

Cross-correlation data for the flap in Run 87 (Mach 8 - $R_N/R_B = 0.1$) are presented in Figure 75. Heat transfer data as shown in Figure 36 suggest that with no mass injection over the nosetip, the boundary layer over the flap is laminar or perhaps in an early transitional state. As in previous conical frustum and slice data corresponding to laminar or transitional boundary layer flow, relatively high values of correlation are indicated. For the sharp cone at Mach 8, generally lower values of correlation over the flap occurred at the higher flap deflection angles, following the trend for Mach 4 data. The final data of Figure 75 consist of Mach 8 flap cross-correlations corresponding to the sharp cone model at 14° angle of attack and to the blunt cone model mass injection induced turbulence.

2.9 Broad-Band Convection Velocity

Values of broad-band convection velocity were computed for array sensors in the conical, slice, and flap regions of the model following procedures outlined in Section V. Based on conical frustum results obtained in the 1972 wind tunnel program at AEDC,[1] it was anticipated that transitional convection velocities expressed as $u_{c_{BB}}/u_\infty$ would be generally less than those measured in turbulent flow, for all portions of the model. However, data obtained in the current program do not follow that relationship, and actually exhibit a wide degree of scatter. Indeed, there appear to be no definitive trends with model geometry or with boundary layer flow characteristic and normalized convection velocities vary between .5 and 1.0.

SECTION V

DATA PROCESSING AND ANALYSIS

1.0 DATA RECORDING AND PROCESSING

A brief description of the recording procedures utilized in this test program is included here. For additional details the reader is referred to Volume II (Classified). The transducer channel recording network is shown in Figure 76. Signals from the thirty-three accustic sensors were routed through multi-conductor twisted pair cables from the model to a junction box outside the wind tunnel where they interfaced with line drivers provided by the Air Force Flight Dynamics Laboratory (AFFDL) mobile data van. The microphone acoustic signals were further amplified within the van and recorded using three rack-mounted, fourteen track (IRIG-format), FM Record/Reproduce Magnetic Tape Recorders. The data were recorded at a tape speed of 60 inches per second using Medium Band FM recording to achieve frequency response from 20 Hz to 20 kHz (limited at the low end by the amplifiers on-board the model). Magnetic tape format was set up to assure that all data from a given microphone array were recorded on tracks common to a particular recording head stack so that subsequent cross-correlation could be done with as little attendant phase variation as possible.

When the wind tunnel model in the derived geometric configuration had been inserted into the flow to achieve a specified environment, and steady state aerodynamic conditions were established, a sample of the output from each acoustic sensor was recorded for a minimum of 5 seconds. These samples of fluctuating pressure versus time for the data subset of Table II were then subjected to the spectral and correlation analyses shown in Table VII and Figure 77, using the digital processing system at AFFDL. Both sound pressure level and power spectral density were obtained for each desired sensor output using a one third octave band analysis. High frequency correlations ($\geq$ 5kHz) to these data were included on the basis of the Corcos sensor size criterian.[82] The maximum correction so applied was 3 dB at 20 kHz for Tunnel A data. Cross-spectral properties (e.g., normalized co- and quad-spectrum, phase angle, narrow-band convection velocity, and coherence) were also processed as functions of third-octave center frequency for selected cone, slice and flap sensor arrays. Broad-band cross-correlation functions were computed by performing the inverse Fourier transform of

the cross-power spectral density. Values of broad-band convection velocity were calculated both through the appropriate relationship expressed in Table VII, and by dividing the sensor separation distance by the time delay corresponding to the cross-correlation maximum value. Generally close agreement between the two methods was achieved.

2.0 DATA ANALYSIS

The objective of this investigation is to develop aeroacoustic load predictions associated with maneuvering type vehicles; in particular along control surface regions. An experimental and subsequent analytical study was conducted for this purpose. The approach adopted considered a careful assessment of existing prediction capability relative to attached turbulent boundary layer flow characteristics. Moreover, the use of incompressible flow data, which has been well documented and examined in the scientific community, was used as a baseline to test the various prediction schemes. Having established the validity of the prediction technique relative to incompressible, attached turbulent flow behavior, the techniques were assessed relative to compressible flow conditions. Inasmuch as the techniques appear valid for various flow (incompressible/compressible) and geometric conditions (flat plates, cones, wind tunnel walls, ogive cylinder, wings, etc.), it appears reasonable to expect their extension to complex flow regions featuring control surfaces. One must keep in mind that attached turbulent boundary flow is the primary consideration.

Section III of this report presents the methodology adopted to predict environmental aeroacoustic loads. The present section will consider these techniques together with data presented in Section IV as the basis for modification of present capability as well as extension to the control surface area. One must keep in mind that a priori selection of the data sub-set (Table II) was influenced by realistic angle of attack-flap angle conditions. Consequently, limitations in data restrict interpretation of fluid dynamic $(\alpha, \text{Re}, M, T_w/T_{aw})$ and geometric conditions (R_N, δ_F). This section will also consider use of normalizing parameters other than those presented in Section IV. The various boundary layer parameters that have been considered in the literature were discussed in Section III. For this purpose, several select tests will be used where the fully developed turbulent boundary layer flow prevailed along the model at zero angle of attack conditions.

2.1 Root-Mean-Square Pressure

Figures 57 through 59 present the rms fluctuation pressure, normalized with dynamic pressure, as a function of Mach number. Inasmuch as the dynamic pressure $(q_e = \gamma/2 \, P_e M_e^2)$ contains the Mach number, its use as a normalizing parameter (when plotting as a function of Mach number), although apparently valid, is questionable. When the local static pressure was used, Equation (64), shown in Figure 20, it also appeared valid relative to the data required prior to this study. Inasmuch as the prediction technique for the rms pressure was developed on the premise that the ratio ranged from $1.7 < p_{rms}/\tau_w < 3$ for incompressible flow to $1.2 < p_{rms}/\tau_w < 5.6$ for compressible flow,[2,9,68] the current data were plotted using wall shear stress and are shown in Figure 78 as a function of Mach number. The data show a range of the ratio $0.5 < \bar{p}/\tau_w < 4$ which includes turbulent and transitional flow behavior for both the conical frustum and control surface region. Also shown is the freestream noise level measured by Laderman[95] in the AEDC Tunnel B facility.

Some interesting results are observed for the data presentation of Figure 78. It is noted that the conical frustum data indicate normalized rms pressure levels less than unity. The same phenomenon is also experienced on the slice and flap regions. These measured values on the model surface are less than the freestream noise content measured by Laderman. Considering the works of Stainback et al[33] as well as Beckwith,[98] who compared hot wire fluctuating pressure measurements to surface sensor values in laminar boundary layers, there does not appear to be a significant attenuation effect of freestream noise through the shock layer. The current data do not exhibit this behavior; in particular, data representing zero angle of attack, flap deflections $< 7°$ and sharp cone configurations. For $\bar{p}/\tau_w > 1$, these values signify high flap deflections $> 7°$, bluntness, and the lower freestream unit Reynolds number tests (i.e., 2.5×10^6). Inasmuch as the wall shear values are consistent with values obtained in previous studies[1,86] at AEDC, and considering the fact that measured levels of normalized rms pressure in laminar flow are higher than turbulent/transitional levels, one must speculate on possible shock attenuation effects. The laminar flow data (indicative of freestream noise) shown in Figure 78 are twice as high as

reported by Laderman (Tunnel B). Further assessment of freestream noise influence on reported data will be made later in this section.

Figures 79 through 81 display the rms fluctuating pressure normalized with the static value as a function of local Mach number. Figure 79 shows the data on the conical frustum for both Tunnel A and Tunnel B test conditions. The prediction schemes of the present study as well as that of Lowson[55] are also shown for comparison. Although the Lowson concept tends to fit the data for attached turbulent flow along the conical frustum, its validity is deemed inadequate when comparing to other data in the literature (Figure 20).

When the data are presented in the coordinates of Figure 79, both angle of attack and Reynolds number effects appear distinquishable. The same effect was noted when using the dynamic pressure for normalizing the rms fluctuating pressure. Keeping in mind that the data are limited and allowing for speculative license, one might account for the angle of attack effect through division by a parameter such as (1 + α/θ_c), i.e., in Equations (59) or (64). Figure 79 shows this result for the two angle of attack conditions. In each case, the data are overpredicted; however, noting the low values of normalized rms pressure indicates the possibility of the approach.

Figure 80 shows normalized rms pressure data for the slice region of the model. The high Mach number data appear to be consistent with prediction. Although angle of attack effects are noted (in particular, for the Mach 4 data), the data tend to follow prediction in a more orderly fashion than those measured on the conical frustum. One must keep in mind again, that the slice measurements indicated lower levels of rms pressure for laminar boundary layer conditions than on the conical frustum. Moreover, the larger boundary layer thicknesses experienced on the slice would tend to yield smaller errors due to sensor size phenomena. These data together with the data of Figure 20 lend definite support to the present prediction method (Equations (59) or (64)).

Figure 81 presents the normalized rms fluctuating pressure for the flap region. As might be expected, the data exhibit the same variation when normalizing with dynamic pressure (Figure 59). For zero angle of attack and flap deflections in the range $0 < \delta_F < -15°$, the data generally exhibit the same trend as slice data. If we again allow for possible speculation, the higher flap deflections might be accounted by

multiplying Equations (59) and (64) by a function such as $(1 + \delta_F/\theta_c)^{1/2}$. Utilizing such an approach, results are shown in Figure 81 for three flap angles. The 20° flap deflection happens to be coincident with the $T_w \ll T_{aw}$ curve. As previously noted, the highest reported rms pressure values occurred when the slice experienced transition flow or in the test where transition was developed over the entire conical frustum.

When assessing the prediction techniques for rms fluctuating pressure, Equation (71) is recommended; namely

$$p_{rms}/q_e = \frac{2A \; K(n) \; MF(n)}{Re_s^{2/(3+n)}} \; \varepsilon_T \qquad (71)$$

where

$$\varepsilon_T = (T^*/T_e)^{\frac{2m - (1+n)}{3+n}}$$

In Section III, we have noted that the velocity power law exponent (n) does not influence the ratio $K(n) \; MF(n)/Re_s^{2/(3+n)}$. Moreover, attempting to define the value of A $(1.7 < p_{rms}/\tau_w = A < 3.2)$ from incompressible flow was not possible. Also, it was determined that the incompressible value of the normalized rms pressure $p_{rms}/q_e = 0.006$ adequately represented the data and supported the various prediction schemes for power magnitude and power spectral density. Consequently, one can eliminate the need for selecting the parameter A and Equation (71) is written as

$$p_{rms}/q_e = (p_{rms}/q_e)_i \; \varepsilon_T \qquad (90)$$

where $(p_{rms}/q_e)_i = 0.006$.

Prediction techniques of the present study have considered the viscous power law exponent (m) to be 0.8 and the velocity power law exponent (n) to be 7. The latter value assumes fully developed turbulent boundary layer flow. However, Laganelli et al[83] have shown that fully developed turbulent conditions (n = 7) could not be attained even on models five feet long. More realistically, the value of n, as determined from profile measurements, was approximately 9 and this parameter reached values as high as

16 just after transitiun. If a value of n = 9 and m = 0.8 were used, the ratio p_{rms}/q_e would reduce by approximately 15%. If higher values of n were chosen, in particular for the conical frustum region where gages A-19/22/21/22 were located just after transition, the ratio p_{rms}/q_e could reduce by almost 25% and approach the Lowson prediction.

To include both angle of attack and flap deflection effects on the basis of limited data acquired in the present program, Equation (90) might be expressed

$$p_{rms}/q_e = \frac{(1 + \delta_F/\theta_c)^{1/2}}{(1 + \alpha/\theta_c)} \ (p_{rms}/q_e)_i \ \epsilon_T \ ; \ \begin{array}{l} \text{Flap} \\ \text{Region} \end{array} \tag{91}$$

Further acquisition and evaluation of appropriate data are required to confirm the suggested functional form of the first term on the right hand side of Equation (91).

With the exception of data reported in Reference 1 there is no detailed information available for developing rms pressure characteristics in transitional flow regions. In the present tests, transitional data obtained along the conical frustum are shown in Figures 57 and 79. In Figure 57, the measurements of Reference 1 are shown together with a recommended data fit. The algorithm developed empirically from the previous study is expressed as

$$p_{rms}/q_e = .0041/[1 + .013 \ M_e^2] \ ; \ 3.7 \leq M_e \leq 8.1$$

As previously indicated, Laganelli et al[83] examined the effects of the power law velocity exponent (n) in regions of laminar, transitional and turbulent flow. It was determined that the power law exponent was in the range $2 < n < 6$ during transition flow. These results, which were obtained in the AEDC Tunnel B facility, are consistent with the works of other investigators.[83] Considering an average value of $n = 4$, together with the viscosity exponent m = 0.8, Equation (90) can be written as

$$p_{rms}/q_e)_{TR \cdot BL} \approx p_{rms}/q_e)_i /[1/2 \ (1 + T_w/T_e) + .22 \ r \ \frac{\gamma-1}{2} \ M_e^2 \ ]^{.486} \tag{92}$$

Inasmuch as rms pressure levels are not available for incompressible transitional flow, the turbulent value will be used. Equation (92) is shown in Figure 57 with $(p_{rms}/q_e)_i \approx 0.006$.

The present prediction method is seen to be in agreement with the data correlation developed in Reference 1. Moreover, the measurements of Reference 1 together with current test results appear to be adequately represented by the present technique. It should be noted that the transitional data shown in Figure 57 are considered peak or near peak transition levels. Consequently the velocity power law exponent may be closer to 6 than the average value of 4 selected. In this situation, the predicted normalized rms pressure would be reduced by 20% and show excellent agreement with the present data as well as with measurements of Reference 1, in particular for $\alpha = 0°$ conditions. For this condition (n = 6), Equation (90) becomes

$$p_{rms}/q_e)_{TR \cdot BL} \approx p_{rms}/q_e)_i / [1/2 \, (1 + T_w/T_e) + .22 \, r \, \frac{\gamma-1}{2} \, M_e^2 \,]^{.6} \qquad (93)$$

2.2 Power Spectral Density

Figures 60 through 68 present non-dimensional power spectral density measured on the cone as a function of the far field Strouhal number $(y > \delta_1)$ using edge dynamic pressure as a normalizing parameter. In order to examine other means of non-dimensionalizing the PSD, Figures 82 through 84 were constructed. Figure 82 is a replot of Figure 60, at Mach 4, where edge dynamic pressure has been replaced by the local static value. There is no particular improvement in format, and the data do not separate into two general classes of transition and turbulent conditions as was noted with Figure 60. The most significant departure is observed for the blunt transition data whose levels were decreased to values less than turbulent boundary layer values. The data of Figure 82 tend to have the same angle of attack characteristics as displayed in Figure 60.

Figure 83 shows the PSD normalized using rms pressure as a function of far field Strouhal number. The data shown are a replot of Figures 60 and 64 for zero angle of attack conditions at $Re_\infty/ft. = 3.6 \times 10^6$. As in the previous case, the data do not generally separate into turbulent/transitional characteristics. However, a coalescence

of the measurements is observed compared to the cases when dynamic and static pressure were used. A Mach number effect is also apparent for the zero intercept value in that Mach 4 levels are generally higher than those for Mach 8. Although not shown, the data spread (one decade) also includes the angle of attack measurements of Figures 60 and 64.

Figure 84 displays the zero angle of attack conical frustum data from the preceding figure replotted as a function of the near field $(y < \delta_1)$ Strouhal number. The abscissa represents the high frequency (low scale) contribution of the fluctuating pressure field. Inasmuch as the ordinate (normalized PSD) remains invariant, a change in scale along the abscissa is the only notable difference to Figure 83. There is no improvement in collapse of the data. Moreover, it is difficult to interpret any consequences of the high frequency contributions in these measurements.

The coordinates shown in Figure 83 represent the normalized functional forms suggested for power spectral density by several authors.[9,28,55,56] Where measurements are plotted in this fashion, normalizing with rms pressure tends to collapse the data more uniformly than when dynamic pressure is used. Moreover, an examination of measurements of Reference 1 indicated the same effect. Consequently, data from several experiments, compressible and incompressible, were plotted using the parameters of Figure 83 and are shown in Figure 85. It should be noted that the circular frequency (ω) was used in the data display.

In Figure 85, it is apparent that measurements for any one tunnel experiment tended to coalesce the data using the rms pressure. However, with the exception of the high frequency range $(\omega \delta^*/u_e > 0.5)$, when many data sources are considered, a significant scatter exist in the low frequency range yielding zero intercept values with no Mach number consistency. Except for measurements of Raman,[9] the zero intercept values reflect the range of rms pressure ratio p_{rms}/τ_w, i.e., higher zero intercept values are consistent with the lower values of p_{rms}/τ_w.

Considering Equation (89) together with Equation (90), there results

$$\frac{\omega(\omega \to o)\, u_e}{\sigma^2\, \delta^*} = \frac{2}{\pi}\, \bar{k} = 0.6336, \text{ for } \bar{k} = \text{unity}$$

An inspection of Figure 85 indicates significant departures from the above value for the zero intercept levels. Again, one recognizes the use of the incompressible format for representing the spectrum which can be used in a compressible state with a transformation function. The compressibility parameter, ϵ_T, was found to be the transformation function required for rms pressure. On the basis of the above observation, (i.e., wide scatter in PSD normalized by rms pressure) together with the arguments presented in Section III, it appears evident that the most appropriate way to represent non-dimensionalized power spectral density is to use the dynamic pressure as a normalizing parameter.

When rms pressure is plotted as a function of Mach number both the ordinate (p_{rms}/q_e) and the abscissa (M_e) represent dimensionless groups that can be used either for incompressible or compressible conditions. However, no such provision is available when displaying PSD as a function of Strouhal number. Here, the independent variable (Strouhal number) can differ by over an order of magnitude from compressible to incompressible conditions. This is primarily a consequence of the characteristic velocity and is reflected in the data when comparing incompressible and compressible measurements, i.e., $\omega \delta^*/u_e)_c < < \omega \delta^*/u_e)_i$. It would be desirable to extend the logic employed in the development of rms pressure with the compressibility factor to power spectral density.

Consider again Equations (89) and (90), such that

$$\frac{\varphi(o)\, u_e}{q_e^2 \, \delta^*}) = (\sigma/q_e)_c^2 \, \frac{2}{\pi}$$

It has been observed that with increasing Mach number, the zero intercept PSD decreases (Figure 24 and Figures 60-68). Consequently, the right hand side must also decrease with increasing Mach number. Inasmuch as the term $(\sigma/q_e)_c$ behaves in this fashion (Figures 1, 18, 57-59), continuity of the above expression is maintained. The compressible state can be transformed into the incompressible plane through a transformation function, a practice commonly employed in boundary layer theory. For example, the skin friction coefficient can be expressed as

$$C_{f_i} = C_{f_c} \, F_c$$

where F_C is the transformation function. The rms pressure has been transformed by such a process and is represented by Equation (90) i.e., $(p_{rms}/q_e)_i = (p_{rms}/q_e)_c/\epsilon_T$ where $F_C = 1/\epsilon_T$. The above zero intercept level can then be written as

$$\frac{\varphi(o) u_e}{q_e^2 \delta^*} = \frac{2}{\pi} \frac{(\sigma/q_e)_i^2}{F_C^2} = \frac{2}{\pi} (\sigma/q_e)^2 \epsilon_T^2$$

For incompressible flow, one has

$$\frac{\varphi(o) u_e}{q_e^2 \delta^*})_i = \frac{2}{\pi} (\sigma/q_e)_i^2 \bar{k}$$

Hence, comparing the above expressions allows for the arbitrary parameter $\bar{k}$ to be equal to the compressibility parameter ϵ_T^2. The Strouhal number can also be transformed to

$$(\frac{\omega l}{v})_i = F_C (\frac{\omega l}{v})_c$$

where $F_C = 1/\epsilon_T = 1/(\bar{k})^{1/2}$. Equation (87) becomes

$$\frac{\varphi(\omega) u_e}{q_e^2 \delta^*})_c = \frac{(\sigma/q_e)_i^2 \epsilon_T^2}{1 + (1/\epsilon_T^4) (\frac{\omega \delta^*}{u_e})_c^2} \tag{94}$$

where it is noted that the Strouhal number maintains compressible values. The above formulation represents the power spectral density, in which the Houbolt functional relation has been generalized for application to attached compressible turbulent boundary layer flow. Here, one notes that both the dependent variable (PSD) and independent variable (Strouhal number) have the required transformation functions. Equation (94) is shown in Figure 86 for several values of ϵ_T as well as measured data on the conical frustum and slice for the two Mach number conditions of the present experiment. The data are shown with projected levels of the zero intercept value. When compared to the present theory, the data do not precisely match the zero intercept values; however, the general agreement is considered quite good recognizing the existence of experimental errors. It is quite interesting to note that the decrease of normalized PSD with Strouhal number is predicted very well.

Figure 87 shows the present prediction scheme compared to the data of several experiments (see Figure 24) including conical measurements of Figure 86 and an excellent match to data is observed. As previously indicated, the zero intercept value of measured normalized PSD decreases with increasing Mach number and the theory is shown to be in agreement with this trend. However, the decrease of the spectrum with increasing Strouhal number displays different characteristics among the various investigators.

For predicting levels of power spectral density, normalization by edge dynamic pressure and the Houbolt functional form are recommended. The prediction method is shown as Equation (94) where the compressibility parameter has been employed to transform the incompressible theory into a compressible plane. Of particular importance is the transformation on the independent variable (Strouhal number). Concerning angle of attack effects, the disparity in normalized PSD measurements and trends which are opposite from one Mach number condition to another (Figures 60 through 68), it is recommended that Equation (94) be used directly. When angle of attack data for either the cone or slice are represented in the coordinates of Figures 86 and 87, both the zero intercept levels and frequency dependence appear to be predicted within the scatter of the zero angle of attack data. If one compares the slice normalized PSD values of Figures 61 and 62, it is observed that angle of attack effects appear more sensitive for the Mach 8 tunnel test. However, the compressibility parameter accounts for the variation in angle of attack; in particular for the higher Mach number tests.

For the flap region, it is recommended that Equation (94) be used with modification to account for flap deflections. Good agreement between data and theory are accorded, at zero angle of attack and zero flap angle, for both the zero intercept value and spectrum variation with frequency. Again, variation of measurements with angle of attack is accounted for through changes in the compressibility parameter. Examination of Figures 62 and 67 indicate a significant departure of angle of attack effects from Mach 4 to Mach 8 test conditions. In Tunnel B the higher local Mach number (at $\delta_F = 0°$) yields lower levels of the zero intercept value which subsequently increase with increasing angle of attack. However, for the Mach 4 test conditions at zero flap angle, the variation in local Mach number with α was not sufficient to cause significant level changes in the zero intercept value.

When considering flap deflections, it is estimated that the same type of function can be used as that employed for rms pressure; namely, $f(1 + \delta_F/\theta_c)$. In particular, the normalized power spectral density for the flap region can be approximated by modifying Equation (94) to be

$$\frac{\varphi(\omega)u_e}{q_e^2 \, \delta^*}\Bigg)_c = \frac{\frac{2}{\pi}(\sigma/q_e)_i^2 \, \epsilon_T^2}{1 + 1/\epsilon_T^4 \, (\frac{\omega \delta^*}{u_e})^2} \cdot (1 + \frac{|\delta_F|}{\theta_c})^2 \; ; \text{Flap Region} \tag{95}$$

Equation (95) predicts the normalized PSD for the flap region over the range of measured flap deflections $(0 \le -\delta_F \le 20°)$, including angle of attack effects, to within the same degree of accuracy as determined on the conical frustum and slice regions.

Concerning transition prediction capability for power spectral density, direct use of fluid dynamic principles was not possible as was the case for rms pressure. An inspection of the conical frustum transition data of Figures 60 and 64 show that transition measurements yield higher zero intercept values than experienced for turbulent flow. It appeared that direct substitution of either Equation (92) or (93) into Equation (94) would give the desired result. However, use of these equations considered the incompressible zero intercept value as the maximum level (this was done for lack of incompressible transition information). Consequently, increasing compressible effects tended to decrease the normalized PSD zero intercept value regardless of choice of velocity power law exponent.

An examination of transition data of Reference 1 together with the present test results indicated that the zero intercept level tends to increase with increasing Mach number which includes angle of attack effects. Hence, to accommodate an increase in normalized PSD with compressibility, Equation (88) will be modified. For this situation, $\bar{k}$ is assumed to be the inverse of the compressibility function such that

$$\frac{\varphi(o)\,u_e}{q_e^2 \, \delta^*}\Bigg)_{TR \cdot BL} = \frac{2}{\pi} \, (\sigma/q_e)_i^2 \, \frac{1}{\epsilon_T^2} \; ; \text{TR} \cdot \text{BL Zero Intercept} \tag{96}$$

which represents the normalized power spectral density transitional flow zero intercept level. The choice of the above transformation has no direct fluid dynamic foundation as previously employed for rms pressure. Moreover, the spectral dependence with

frequency is difficult to assess. Inasmuch as the data of Reference 1 as well as the current measurements tend to have steep rates of decrease for Strouhal number $f\delta^*/u_e > 10^{-2}$, it is suggested that the spectral distribution with frequency remain unchanged in Equation (94), thus giving

$$\frac{\varphi(\omega)u_e}{q_e^2 \, \delta^*} = \frac{\frac{2}{\pi} \, (\sigma/q_e)_i^2 \, 1/\epsilon_T^2}{1 + 1/\epsilon_T^4 \, (\frac{\omega \delta^*}{u_e})^2} \quad ; \text{TR} \cdot \text{BL} \tag{97}$$

Equation (97) is shown plotted in Figures 60 and 64 over the low frequency range only. Also represented is the range of the compressibility parameter for the current test conditions. It is noted that the velocity power law exponent of $n = 4$ was assumed. The data are in good agreement with theory (Equation (97)) and more importantly are correctly predicted relative to compressible effects.

2.3 Cross-Power Spectral Density

Detailed analysis was performed for those data considered most applicable to the flight application situation to be discussed in Section II of Volume II. It was desired to have as much of the model as possible emersed in fully turbulent flow (at $\alpha = 0$), with primary emphasis placed on those runs wherein the flap deflection was consistent with such a zero angle of attack condition (i.e., $-\delta_F = 15°$ or $20°$). For evaluation of conical frustum data, Run 103 at Mach 4 proved to be the only case where the conical sensor array was emersed in fully turbulent flow. However, for measurements on the slice and flap, Mach 8 Runs 58 (sharp cone) and 100 (blunt nosetip with mass injection) had transitional flow sufficiently far forward that adequate turbulent data were acquired over these regions. Results from wind tunnel runs other than the above three will be introduced as necessary to evaluate effects of flap deflection and angle of attack variation, as well as transition. Cross-spectral data corresponding to additional runs are presented in Volume II.

The initial step in data evaluation consisted of compiling individual cross-power spectral densities into a set of functions corresponding to each applicable transducer array of the wind tunnel run under investigation. For longitudinal correlations, peaks of the normalized co-spectral density (C) and the quad-spectral density (Q) are expressed as functions of non-dimensionalized frequency, $\xi f/u_c(f)$, by plotting C & Q

94.

versus $\theta/2\pi$ since by definition $u_c(f) = 2\pi f\xi/\theta(f)$. It should be noted that for $\xi f/u_c(f) \to 0$ asymptotic value of normalized co-spectral density decreases for increasing values of transducer separation distance. Hence, the effect of both spatially dependent and frequency dependent cross-spectral attenuation is evident.

In the case of circumferential correlations, only the in-phase (co) cross-spectral data are relevant. These functions are expressed in terms of the quantity $\eta f/u_c(f)$, explicit values of which are generated as follows: the longitudinal convection velocity, $u_c(f)$, is defined as above by $2\pi f\xi_1/\theta_1(f)$ where ξ_1 is a specific longitudinal separation distance and $\theta_1(f)$ is the corresponding phase angle. Therefore, $\eta_1 f/u_c(f) = \eta_1 f \div 2\pi f\xi_1/\theta(f) = \eta_1/\xi_1 \times \theta_1(f)/2\pi$. As an example, consider the circumferential co-spectral density associated with transducers 5-6. For this case

$$\eta_{5-6} f/u_{c,\,Long}(f) = \frac{\eta_{5-6}}{\xi_5} \cdot \frac{\theta_{5-8}(f)}{2\pi} = \frac{.75}{.625} \frac{\theta_{5-8}(f)}{2\pi} = \frac{1.2\,\theta_{5-8}}{360^\circ}$$

In effect, then, to provide the appropriate representation as functions of $\eta f/u_c$, circumferential co-power spectral densities are plotted against scaled values of longitudinal phase angle.

The approach taken in the present investigation was to consider each of the three geometric regions of the model in turn (cone, slice, flap) and relate cross-spectral characteristics to correlation properties measured in the study of Reference 7. In that program, it was proposed that appropriate representations for the turbulent cross-spectral coefficients A_ξ and A_η over a cone are Equations (37) and (38), respectively.

2.3.1 Conical Frustum Measurements

Figures 12, 14, 15, and 88 present applicable cross-spectral data for evaluation of correlation characteristics over the cone. Measurements expressed both in terms of non-dimensional frequency and asymptotic values (as $f \to 0$) versus normalized separation distance are shown.

(a) Longitudinal Correlation

(1) Frequency Dependence

Equation (37) indicated that even if $f \to 0$, such that $f\xi/u_c \to 0$, as long as $\xi \neq 0$ (i.e., for any actual cross-power spectral density measurement), the asymptotic value for $f\xi/u_c \to 0$ will be less than 1. Therefore, measured cross-spectral data are shown

compared to an exponential envelope which has a factor in it to account for the spatial attenuation. For this reason, in Figure 88 a factor of .7 has been incorporated to account for attenuation corresponding to a separation distance of approximately 1.5". It was noted in Reference 7 that the effect of noise contribution (i.e., tunnel tare) on cross-PSD measurements is apparently to inhibit decay of the cross-spectral envelope. Hence, in this figure, the relatively constant correlation indicated for sensors A-5 and A-10 ($\xi/\delta^* = 70.2$) in the range $f\xi/u_c(f) > 1.5$ is probably an effect of tunnel tare. The comparison of available turbulent data shown in Figure 88 with the function $e^{-.1(2\pi)f\xi/u}c$) reveals that this representation does provide a reasonable envelope of measured values when factors to account for spatial attenuation are implicitly incorporated.

(2) Spatial Dependence

Figure 12 presents longitudinal data for Run 103 (Mach 4) in which asymptotic values from Figure 88 (as $f \to 0$) are plotted versus ξ/δ^*. The levels of present data are slightly higher than both the primary spread of measurements from Reference 7 and the prediction curve derived therein. Redefinition of the mathematical representation would not appear to be justified, solely on the basis of the present (limited) data. However, when the new representation shown in Figure 12 ($.58 + .42\ e^{-.0486\ \xi/\delta^*}$) is incorporated into the R/V response routine, it provides a better match to measured re-entry vibration data (Volume II). Until this ambiguity is resolved through further investigation, it is recommended that the new equation be employed in design analyses on the grounds that it constitutes a slightly more conservative representation.

(b) Circumferential Correlation

(1) Frequency Dependence

Figure 14 presents a comparison of circumferential co cross-power spectral density from Run 103 (Mach 4) with data of previous compressible measurements.[7] This figure includes from current data only the correlation data for sensors A-5 and A-6 ($\eta = .75"$), since sensor A-7 did not provide valid measurements in either Tunnel A or B. Also shown in Figure 14 is the exponential recommended in Reference 7 to represent circumferential correlation ($e^{-1.4(2\pi)f\eta/u}c$), multiplied by .85 to account

96.

for average spatial attenuation of the data. There is generally good agreement among all the measurements and the empirically developed function; hence it is recommended this exponential be maintained as an appropriate representation for decay of circumferential correlation with non-dimensional frequency.

(2) Spatial Dependence

A comparison of asymptotic measurements for circumferential cross-power spectral density is provided in Figure 15. As with the longitudinal correlation, the present data (one point) are above the previous prediction curve, and provide an exponential expression which ultimately results in better agreement with measured flight vibration data when incorporated into the R/V response routine. Therefore it is recommended that $e^{-0.0195 \ \eta/\delta^*}$ be employed in design analyses until further data are acquired.

2.3.2 Slice and Flap Measurements

From an initial evaluation of correlation characteristics of both slice and flap data, it became evident that a general similarity exists among these measurements. This is not surprising considering the planar nature of these two geometries. Therefore, data from the slice and the flap will be considered together. It should be noted that certain anomalous characteristics were evident in the output of sensor A-28 (e.g., the spectrum shown in Figure 56). Therefore, when available, the correlation relating sensors A-23 and A-25 (equivalent flap data) was substituted for cross-spectrum A-26 to A-28.

(a) Longitudinal Correlation

(1) Frequency Dependence

It is evident from an examination of Figures 89 through 93 that slice and flap cross-spectral measurements in turbulent flow exhibit a more significant loss of correlation with non-dimensional frequency than do conical frustum data discussed above. Hence, a modification to the previous prediction curve is required. One possible exponential representation which matches available data reasonably well is $e^{-.2(2\pi)f\zeta/u_c}$. It is apparent that the rate of correlation decay (i.e., the coefficient

of $f\xi/u_c$) in cross-spectral measurements for the slice and the flap is generally in-sensitive to flap deflection. Therefore the above exponential is applicable for zero angle of attack conditions and for flap deflection in the range $0 \le -\delta_F \le 20°$.

(2) Spatial Dependence

Asymptotic values (as $f \to 0$) of longitudinal cross-PSD on the slice and on the flap are presented in Figure 94. It is evident that for small values of normalized separation distance (i.e., $\xi/\delta^* \le 7$) data are generally coincident with the prediction curve which provided a good match to conical frustum data from Reference 7. How-ever, at larger values of ξ/δ^* the degree of asymptotic correlation decreases relative to this curve. This trend of both slice and flap measurements ($0 \le -\delta_F \le 20°$) mandates a revision to the conical frustum prediction curve. A possible modification which provides better agreement with present data is $0.35 + 0.65\,e^{-0.073\,\xi/\delta^*}$. This expression is applicable to the zero angle of attack situation when turbulent boundary layer flow emerses the slice and flap region. Variation with Mach number and flap deflection is automatically accounted for in the functional dependency of δ^* on these parameters.

(b) Lateral Correlation

Due to the erratic behavior of sensors A-16, 17, 18, no valid lateral cross-spectral data over the slice were acquired. From a review of lateral/circumferential measure-ments both in the present investigation (cone) and throughout the literature (cones, plates, wind tunnel walls),[61,1,78,79] it is apparent that the general level of lateral cross-correlation is much less sensitive to the geometric configuration than longitudinal correlation (see Figures 13 and 14). Therefore the functional form for lateral cross-spectral coefficient proposed in this study is identical to the expression for circum-ferential correlation discussed in Section 2.3.1 above.

In summary, the complete representations for cross-spectral coefficients de-scribing correlation in fully turbulent flow over the slice and flap ($0 \le -\delta_F \le 20°$) are as follows:

$$A_\xi(\xi, \omega) = e^{-.2\omega\,\xi/u_c(\omega)}[.35 + .65\,e^{-.073\,\xi/\delta^*}] \qquad (98)$$

$$A_\eta(\eta, \omega) = e^{-1.4\omega\,\eta/u_c(\omega)}[.3 + .7\,e^{-.055\,\eta/\delta^*}]. \qquad (99)$$

98.

2.3.3 Transition and Angle of Attack Effects

(a) Conical Frustum

Figure 95 presents Mach 4 transitional cross-spectra from the cone array compared to the frequency-dependent prediction curve proposed in Reference 7. Good agreement with the proposed exponential is evident. An examination of other conical data reveals that the location of the transition zone with respect to the sensor array can influence measured cross-correlation characteristics. However, no definitive trends in this respect were exhibited throughout the data. It is therefore recommended that the exponential developed by Howe[7] on the basis of many variations in angle of attack and freestream Reynolds number be maintained.

A comparison of asymptotic longitudinal data (as $f \rightarrow 0$) from the present program with cross-spectral measurements from Reference 7 indicates generally good agreement, as shown in Figure 96. Model angles of attack up to 14° are represented. The prediction curve apparently constitutes an upper bound to current data, particularly at larger values of normalized separation distance. The greatest discrepancy occurs for correlations between A-5 and A-10. However, an examination of OASPL distributions shown in Section IV reveals that A-10 generally registers lower values than might be expected (e.g., Figure 34). These possibly erroneous readings may be contributing to the low longitudinal correlations in Figure 96 at the largest values of ξ/δ^*.

Typical high angle of attack ($\alpha = 7°$) circumferential data measured in transitional flow over the cone are given in Figure 97. Also presented are both data and the empirically developed curve from Reference 7. Current data reveal approximately the same trend with normalized frequency as previous transitional measurements at high model angle of attack.

On the basis of the above comparisons, it is evident that conical frustum measurements from the present program exhibit the same overall characteristics as transitional cross-PSD data of Reference 7. It is therefore recommended that the empirical representations derived therein be maintained for cross-spectral coefficients in transitional flow over conical portions of a re-entry vehicle, and that the same angle of attack criterion be applied for measurements at high α.

These representations are as follows:

$$A_\xi (\xi, \omega) = e^{-.06 \omega \xi / u_c(\omega)} [.6 + .4 e^{-.024 \xi / \delta^*}] \tag{100}$$

$$A_\eta (\eta, \omega) = e^{-.68 \omega \eta / u_c(\omega)} [.6 + .4 e^{-.024 \eta / \delta^*}], \quad \alpha \le .7 \, \theta_c \tag{100}$$

$$A_\eta (\eta, \omega) = e^{-.446 \omega \eta / u_c(\omega)} [.6 + .4 e^{-.024 \eta / \delta^*}], \quad \alpha > .7 \, \theta_c \tag{102}$$

(b) Slice and Flap

Transitional flow over the control surface region of the model constitutes an extremely complex phenomenon. An example of this is exhibited in Figure 29 which presents OASPL data for two Mach 4 runs (69, 84) wherein transitional flow exists over the aft portion of the model. Although heat transfer measurements apparently indicate nominally turbulent flow on the slice and flap, acoustic data (in particular sensors A-17 and A-26) reveal much higher than anticipated fluctuating pressure environments. Measured levels on the slice and flap may be a consequence of a type of "overshoot" phenomenon for the control surface region, analogous to the characteristic of acoustic environments near the end of transition on a cone. The result of these observations is that limited cross-spectral measurements corresponding to "transitional flow" on the control surface region are inconclusive, since aerodynamic characteristics change so rapidly in that particular region of the scale model.

It was noted in Section 2.3.2 above that in fully turbulent flow, flap longitudinal cross-spectral properties tend to be independent of flap deflection. This same observation can be made with respect to model angle of attack. Therefore, Equations (98) and (99) would also be appropriate for $0° \le \alpha \le 14°$. However, since in practical applications maximum flap deflection generally occurs for minimum angle of attack, this limits the range of α, δ_F combinations for which Equations (98) and (99) are applicable (i.e., $\alpha = 14°$, $-\delta_F = 20°$ would be excluded from these equations).

100.

Figures 98 and 99 present slice cross-PSD's in turbulent flow for two angles of attack $(0°, 14°)$. The asymptotic values (as $f \to 0$) are virtually identical, and both sets of data agree reasonably well with the exponential recommended above for slice cross-spectral coefficient at $\alpha = 0$. Although the higher angle of attack measurements appear to decay slightly more rapidly with non-dimensional frequency than do the zero angle of attack cross-spectra, the trend appears too subtle to warrant re-definition of the correlation coefficient on the basis of these limited data. Hence it is similarly recommended that Equations (98) and (99) apply to slice measurements, independent of angle of attack, in the range $0° \leq \alpha \leq 14°$.

SECTION VI

REFERENCES

1. Chaump, L. E., Martellucci, A., and Monfort, A., "Aeroacoustic Loads Associated with High Beta Re-Entry Vehicles", AFFDL-TR-72-138, Vol. 1 and 2, May 1973.

2. Martellucci, A., Chaump, L., Rogers, D., and Smith, D., "Experimental Determination of the Aeroacoustic Environment about a Slender Cone", AIAA Journal, Vol. II, No. 5, May 1973.

3. "Prediction of Pressure Fluctuations Associated with Maneuvering Re-Entry Weapons", Vol I, Technical Proposal, GE Proposal No. N-73385, December 1974.

4. Donaldson, J. C. and Wallace, J. P., "Flow Fluctuations Measurements at Mach 4 in the Test Section of the 12 Inch Supersonic Tunnel (D)", AEDC-TR-71-143, August 1971.

5. Strike, W. T. and Donaldson, J. C., "Acoustical Loading and Heat Transfer Rate Distribution on a 7.2 Degree Cone at Mach Numbers 4, 8, and 10", AEDC-TR-72-129, September 1972.

6. Chaump, L. E., Lauzon, J. H., Minnich, H. R., "Vibration Response of Ballistic Re-Entry Vehicles", AFFDL-TR-72-140, Vols. 1 and 2, April 1973.

7. Howe, J. R., "Spatial and Temporal Properties of Fluctuating Pressures on Re-Entry Vehicles", AFFDL-TR-76-32, March 1976.

8. Laganelli, A. L., Martellucci, A. and Shaw, L., "Prediction of Surface Pressure Fluctuations in Hypersonic Turbulent Boundary Layers", Presented at the 9th Fluid/Plasmadynamics Conference, San Diego, California, July 1976, Paper No. 76-409.

9. Raman, K. R., "Surface Pressure Fluctuations in Hypersonic Turbulent Boundary Layers", AIAA Paper No. 73-997, October 1973. Also NASA CR2386, February 1974.

10. Heller, H. H., and Holmes, D. G., "Unsteady Aerodynamic Loads During Re-Entry of the Straight-Wing Orbiter Configuration", Bolt Beranek and Newman Inc., Final Report No. 2118, Contract No. NAS1-9559-5, March 1971.

11. Heller, H. H., and Clemente, A. R., "Fluctuating Surface Pressure Characteristics on Slender Cones in Subsonic, Supersonic, and Hypersonic Mach Number Flow", NASA CR2449, October 1974.

12. Heller, H. H., "Acoustic Technique for Determination of Flow Transition on Hypersonic Re-Entry Vehicles", AIAA Journal, No. 7, pp. 2227-2232, December 1969.

13. Heller, H. H., "Frequency Response of Acoustic Probes for Measuring Pressure Fluctuations on a Hypersonic Re-Entry Vehicle", Report No. 1498, Bolt Beranek and Newman Inc., May 1967.

14. Coe, C. F. and Chyu, W. J., and Dods, J. B., "Pressure Fluctuations Underlying Attached and Separated Supersonic Turbulent Boundary Layers and Shock Waves", Presented at Aeroacoustic Conference, Seattle, Washington, October 1973, Paper No. 73-996.

15. Dods, J. B., Jr. and Hanly, R. D., "Evaluation of Transonic and Supersonic Wind Tunnel Background Noise and Effects of Surface Pressure Fluctuation Measurements", AIAA Paper No. 72-1004, September 1972.

16. Coe, C. F. and Chyu, W. J., "Pressure Fluctuation Inputs and Response of Panels Underlying Attached and Separated Supersonic Turbulent Boundary Layers", AGARD Symposium on Acoustic Fatigue, Toulouse, France, September 1972, AGARD CP-113.

17. Coe, C. F. and Rechtien, R. D., "Scaling and Spatial Correlation of Surface Pressure Fluctuations in Separated Flow at Supersonic Mach Numbers", Presented at AIAA Str. Dyn. Aeroelasticity Specialist Conf., New Orleans, La., April 1969.

18. Chyu, W. J. and Hanly, R. D., "Power- and Cross- Spectra and Space-Time Correlations of Surface Fluctuating Pressures at Mach Numbers Between 1.6 and 2.5", TN D-5440, September 1969, NASA, also AIAA Paper No. 68-77.

19. Coe, C. F., "Surface-Pressure Fluctuations Associated with Aerodynamic Noise", SP-207, 1969, NASA, pp. 409-424.

20. Hanly, R. D., "Effects of Transducer Flushness on Fluctuating Surface Pressure Measurements", AIAA Paper No. 75-534, Presented at AIAA 2nd Aeroacoustics Conf., Hampton, Va., March 1975.

21. Panton, R. L., Lowery, R. L., and Reischman, M. M., "A Theoretical and Flight Test Study of Pressure Fluctuations under a Turbulent Boundary Layer - Part 2: Flight Test Study", NASA GRANT NGR37-002-083, also N74-33797, NASA-CR-140448, October 1974.

22. Dods, J. B., Jr. and Lewis, T. L., "Measurement of Surface Pressure Fluctuations on the XB-70 Airplane at Local Mach Numbers Up to 2.45", TN D-7226, March 1973.

23. "ACE FTV-1 Post-Flight Data Review Meeting", Aerospace Corporation DIN: AS-74-00395, January 31, 1974.

24. "FTV-2 Post-Flight Analysis Report - ACE Program", Aerospace Corporation, DIN: EX-74-06407, July 1974.

25. Final Flight Evaluation Report for RVTO Flight Test Program, Vehicle RVTO-3B-102", GE-RESD, DIN: 73SD2028A, October 5, 1973.

26. "Final Flight Evaluation Report for RVTO Flight Test Program, Phase 3B, Vehicle 103", GE-RESD, DIN: 73SD2253, March 19, 1974.

27. Pate, S. R. and Brown, M. D., "Acoustic Measurements in Supersonic Transitional Boundary Layers", AEDC TR-69-182, October 1969.

28. Robertson, J. E., "Prediction of In-Flight Fluctuating Pressure Environments Including Protuberance Induced Flow", Wyle Laboratories Research Report, WR-71-10, March 1971.

29. Robertson, J. E., "Preliminary Estimates of Space Shuttle Fluctuating Pressure Environments", Wyle Laboratory Report WR-72-10, August 1972.

30. Burton, T. E., "Wall Pressure Fluctuations at Smooth and Rough Surfaces under Turbulent Boundary Layers with Favorable and Adverse Pressure Gradient", Tech. Report 70208-9 Acoustics/Vibration Lab M.I.T., June 1973, also AD 772548.

31. DeMetz, F. C. and Casarella, M. J., "An Experimental Study of the Intermittent Properties of the Boundary Layer Pressure Field During Transition on a Flat Plate", Naval Ship Research and Development Center Report 4140, November 1973, also AD 775299.

32. Bergstrom, E. R. and Raghunathan, S., "Aerodynamic Noise and Boundary Layer Transition Measurements in Supersonic Test Facilities", AIAA Journal Vol. 10, No. 11, November 1972, p. 1531.

33a. Stainback, P. C. and Rainey, R. A., "Correlation of Freestream Pressure Disturbances in Supersonic Wind Tunnels", AIAA Journal Vol 14, No. 2, February 1976, p. 286.

33b. Stainback, P. C., Fischer, M. C., and Wagner, R. D., "Effects of Wind Tunnel Disturbances on Hypersonic Boundary Layer Transition", Presented at the 10th AIAA Aerospace Meeting, San Diego, California, January 1972, Paper No. 72-181.

34. Dougherty, N. S., "Correlation of Transition Reynolds Number with Aerodynamic Noise Levels in a Wind Tunnel at Mach Numbers 2-3", AIAA Journal Vol. 13, No. 12, December 1975, p. 1670.

35. Carlin, D., Jr., "Response of Aerospace Structures to Re-Entry Aerodynamic Excitation - Final Report", LMSC-HREC D225410, October 1971, also HREC 6338-1.

36. Revell, J. D. and Gleason, R. E., "Turbulent Wall Pressure Fluctuations Under Separated Supersonic and Hypersonic Flows", AFFDL TR-65-77, August 1965.

37. Speaker, W. V. and Ailman, C. M., "Spectra and Space Time Correlations of the Fluctuating Pressures at a Wall Beneath a Supersonic Turbulent Boundary Layer Perturbed by Steps and Shock Waves", NASA CR-486.

38. Holden, M. S., "Shock Wave - Turbulent Boundary Layer Interaction in Hypersonic Flow", AIAA Paper No. 72-74, January 1972.

39. Mabey, D. G., "Analysis and Correlation of Data on Pressure Fluctuations in Separated Flow", J. Aircraft, Vol. 9, No. 9, September 1972, pp. 642-645.

40. Owen, F. K. and Horstman, C. C., "On the Structure of Hypersonic Turbulent Boundary Layers", J. Fluid Mech. Vol. 53, Part 4, pp. 611-636.

41. Owen, F. K. and Horstman, C. C., "Hypersonic Transitional Boundary Layers", AIAA Journal Vol. 10, No. 6, June 1972, p. 769.

42. Mikulla, V. and Horstman, C. C., "Turbulence Measurements in Hypersonic Shock-Wave Boundary Layer Interaction Flows", AIAA Journal Vol. 14, No. 5, May, 1976, p. 568.

43. Demetriades, A., Laderman, A. J., "Final Progress Report - Advanced Penetration Problems Program", SAMSO TR-73-397, January 1974.

44. Laderman, A. J., and Demetriades, A., "Turbulent Fluctuations in the Hypersonic Boundary Layer Over an Adiabatic Slender Cone", The Physics of Fluids, Vol. 19, No. 3, March 1976, p. 359.

45. Demetriades, A. and Laderman, A. J., "Space-Time Correlation Structure of Hypersonic Boundary Layers", AIAA Journal, Vol. 14, No. 2, February 1976, p. 256.

46. Willmarth, W. W., "Pressure Fluctuations Beneath Turbulent Boundary Layers", Annual Review of Fluid Mechanics, Vol. 7, 1975, Annual Reviews Inc., Palo Alto, California.

47. Tam, K. W., "Intensity, Spectrum, and Directivity of Turbulent Boundary Layer Noise", J. Acoust. Soc. Am. Vol. 57, No. 1, January 1975, p. 25.

48. Siddon, T. E., "Surface Dipole Strength by Cross-Correlation Method", J. Acoust. Soc. Am. Vol. 23, No. 2, 1973, p. 619.

49. Vecchio, E. A. and Wiley, C. A., "Noise Radiated from a Turbulent Boundary Layer", J. Acoust. Soc. Am. Vol. 53, No. 2, 1973, p. 596.

50. Fricke, F. R. and Stevenson, D. C., "Estimation of Wall-Pressure Fluctuations in a Separated Flow", J. Acoust. Soc. Am., Vol. 50, No. 3, 1971, p. 985.

51. Lane, F., "Broadband Noise Generated by Turbulent Inflow to Rotor or Stator Blades in an Annular Duct", NASA CR-2503, March 1975.

52. Goldstein, M. E., Aeroacoustics, NASA SP-346, prepared by Lewis Research Center, 1974.

53. Landahl, M. T., "Wave Mechanics of Boundary Layer Turbulence and Noise", J. Acoust. Soc. Am. Vol. 57, No. 4, April 1975, p. 824.

54. Lew, H. G. and Li, H., "The Role of the Turbulent Viscous Sublayer in the Formation of Surface Patterns", GE TIS R68SD12, August 1968.

55. Lowson, M. V., "Prediction of Boundary Layer Pressure Fluctuations", AFFDL-TR-67-167, April 1968.

56. Houbolt, J. C., "On the Estimation of Pressure Fluctuations in Boundary Layers and Wakes", GE TIS 66SD296, April 1966.

57. Houbolt, J. C., "Structural Response of Re-Entry Vehicles to Boundary Layer Noise", GE TIS 65SD223A, March 1965.

58. Laufer, J., "Some Statistical Properties of the Pressure Field Radiated by a Turbulent Boundary Layer", The Physics of Fluids, Vol. 7, No. 8, August 1964.

59. Black, T. J., "An Analytical Study of the Measured Wall Pressure Field Under Supersonic Turbulent Boundary Layers", NASA Contractor Report NASA CR-888, April 1968.

60. Bradshaw, P. and Ferris, D. H., "The Response of a Retarded Equilibrium Turbulent Boundary Layer to the Sudden Removal of Pressure Gradient", National Physical Lab., Aero. Report 1145, March 1965.

61. Bull, M. K., "Wall-Pressure Fluctuations Associated with Subsonic Turbulent Boundary Layer Flow", J. Fld. Mech. Vol. 28, Part 4, 1967.

62. Bull, M. K. and Thomas, A. S. W., "High Frequency Wall Pressure Fluctuations in Turbulent Boundary Layers", The Physics of Fluids, Vol. 19, No. 4, April 1976, p. 597.

63. Bies, D. A., "A Review of Flight and Wind Tunnel Measurements of Boundary Layer Pressure Fluctuations and Induced Structural Response", NASA CR-626, 1966.

64. Blake, W. K., "Turbulent Boundary Layer Wall Pressure Fluctuations on Smooth and Rough Walls", J. Fld. Mech. Vol. 44, Part 4, December 1970.

65. White, F. M., "A Theory of Boundary Layer Flow Noise, with Application to Pressure Gradients and Polymer Solutions", J. Hydronautics, Vol. 3, No. 2, April 1969, p. 95.

66. Cliff, W. C. and Sandborn, V. A., "Measurements and a Model for Convective Velocities in the Turbulent Boundary Layer", NASA TN D-7416, October 1973.

67. Murphy, D. A., Bies, D. A., Speaker, W. W., and Franken, P. A., "Wind Tunnel Investigation of Turbulent Boundary Layer Noise as Related to Design Criteria for High Performance Vehicles", NASA TN D-2247, April 1964.

68. Kistler, A. L. and Chen, W. S., "The Fluctuating Pressure Field in a Supersonic Turbulent Boundary Layer", J. Fluid. Mech., Vol. 16, Part 1, 1963, pp. 41-64.

69. Roberts, D. R., "Boundary Layer Pressure Fluctuations at High Reynolds Numbers on a Free Flight Test Vehicle", London Aeron. Res. Council, February 1974.

70. Lilley, G. M., "A Review of Pressure Fluctuations in Turbulent Boundary Layers at Subsonic and Supersonic Speeds", Arch. Mech. Stosow. No. 16, 1964, p. 301.

71. Lilley, G. M., "Wall Pressure Fluctuations Under a Turbulent Boundary Layer at Subsonic and Supersonic Speeds", AGARD Report 454, 1963.

72. Bendat, J. S. and Piersol, A. G., Measurement and Analysis of Random Data, John Wiley Inc., New York, 1966.

73. vanDriest, E. R., "Turbulent Boundary in Compressible Fluids", J. of Aero. Sci., Vol. 1, No. 3, March 1951.

74. Cebeci, T., "Calculation of Compressible Turbulent Boundary Layers with Heat and Mass Transfer", AIAA Journal, Vol. 9, No. 6, June 1971.

75. Laganelli, A. L., "An Examination of Coupling Between Mass Transfer and Roughness in a Compressible, Pressure Gradient Region using an Eddy Viscosity Concept", GE TIS SDR004, January 1975.

76. Emmerling, R., Meier, G. E. A., and Dinkelacker, A., "Investigation of the Instantaneous Structure of the Wall Pressure under a Turbulent Boundary Layer Flow", AGARD Report CP-131, 1974.

77. Bradshaw, P., "Inactive Motion and Pressure Fluctuations in Turbulent Boundary Layers", J. of Fluid Mech., No. 30, pp. 241, 1967.

78. Willmarth, W. W. and Woolridge, C. E., "Measurements of the Fluctuating Pressure at the Wall Beneath a Thick Boundary Layer", J. Fluid Mech., Vol. 14, p. 187, 1962.

79. Mastrello, L., "Radiation from and Panel Response to a Supersonic Turbulent Boundary Layer", Boeing Scientific Research Laboratories, D1-82-0719, September 1968.

80. Bull, M. K., "Properties of the Fluctuating Wall Pressure Field of a Turbulent Boundary Layer", AGARD Report 455, April 1963.

81. Willmarth, W. W., "Wall Pressure Fluctuations in a Turbulent Boundary Layer", J. Acoustical Soc. of America, Vol. 27, No. 6, p. 1048, 1956.

82. Corcos, G. M., "The Structure of the Turbulent Pressure Field in Boundary Layer Flows", J. Fluid Mech. Vol. 18, p. 353, 1964.

83. Laganelli, A. L., Fogaroli, R. P., and Martellucci, A., "The Effects of Mass Transfer and Angle of Attack on Hypersonic Turbulent Boundary Layer Characteristics", AFFDL TR-75-35, Wright Patterson Air Force Base, April 1975.

84. Rie, H., "The GE-RESD Equilibrium Non-Similar Boundary Layer Program", GE
    TIS 71SD212, February 1971.

85. Laganelli, A. L., "Evaluation of Turbulent Heating Predictions", GE TIS 72SD229,
    June 1972; also NASA CR130251, November 1972.

86. Martellucci, A., Hahn, J., and Laganelli, A. L., "Effect of Mass Addition and Angle
    of Attack on the Turbulent Boundary Layer Characteristics of a Slender Cone", GE
    Doc. No. 73SD210, SAMSO TR-73-147, April 1973.

87. Donaldson, J. C. - Arnold Engineering Development Center - Unpublished Results
    from Tunnel B (Mach 8) - Private Communication, April 1976.

88. Schlichting, H., Boundary Layer Theory, McGraw Hill Co., New York, 6th Edition,
    1968.

89. Schloemer, H. H., "Effects of Pressure Gradients on Turbulent Boundary Layer Wall
    Pressure Fluctuations", J. Acoustical Society of Amer. Vol. 42, 1967, pp. 93-113.

90. Kistler, A. L., "Fluctuating Wall Pressure Under a Separated Supersonic Flow",
    J. ASA 36, No. 3, March 1964.

91. Belcher, P. M., "Prediction of Boundary Layer Turbulence Spectra and Correlations
    for Supersonic Flight", Presented at 5th Intern. Acoustical Congress, Belgium,
    September 1965.

92. Williams, D. J. M., "Measurements of the Surface Pressure Fluctuations in a Tur-
    bulent Boundary Layer in Air at Supersonic Speeds", A ASU Report 162, December 1965.

93. Kyriss, C. L., "A Three-Dimensional Flow Field Computer Program for Maneuvering
    and Ballistic Re-Entry Vehicles", GE-RESD TIS75SDR013, July 1975.

94. Hecht, A. M., "3-D Viscous Code Development", GE-RESD Tech. Memo. 9154-75-03,
    December 1975.

95. Laderman, A. J., "Review of Wind Tunnel Freestream Pressure Fluctuations", AIAA
    Jour. Vol. 15, No. 4, April 1977, p. 605.

96. Wallace, J. E., "Hypersonic Turbulent Boundary Layer Measurements Using an Electron
    Beam", Cornell Aero. Lab. Rpt. No. AN-2112-Y-1, August 1968.

97. Harvey, W. D., Bushnell, D. M., and Beckwith, I. E., "Fluctuating Properties of
    Turbulent Boundary Layers for Mach Numbers up to 9", NASA TN D-5496, October 1969.

98. Beckwith, I. E., "Development of a High Reynolds Number Quiet Tunnel for Transition
    Research", AIAA Jour. Vol. 13, March 1975, pp. 300-306.

99. Chaump, L. E., Lauzon, J. H., and Minnich, H. R., "Vibration Response of Ballistic Re-Entry Vehicles", AFFDL-TR-72-140, November 1972.

TABLE I - TEST SUMMARY

$$M_\infty = 4$$

$Re_\infty/ft.$ $\times 10^{-6}$	α Deg.	R_N/R_B	φ	λ_∞	FLAP ANGLE $(-\delta_F)$ Deg.
3.6	0, -3 1/2, 0.2, 0.5 3 1/2, 7, 14	0, 0.1	0	0, 0.021 0.03	0, 3 1/2, 7, 15, 20, 40
2.5	0, -3 1/2, 0.2, 0.5 3 1/2, 7, 14	0	0	0	0, 7, 15, 20

$$M_\infty = 8$$

$Re_\infty/ft.$ $\times 10^{-6}$	α Deg.	R_N/R_B	φ	λ_∞	FLAP ANGLE $(-\delta_F)$ Deg.
3.6	0, -1 1/2, -3 1/2, -7 -14, 1 1/2, 3 1/2, 7, 14	0, 0.1	0, 90°	0, 0.011, 0.013 0.015 0.018 0.028 0.06	0, 7, 15, 20, 40
2.5	0, -3 1/2, -7 3 1/2, 7, 14	0	0, 90°	0	0, 7, 15, 20, 40

*Details concerning exact test combinations are contained in Volume II - Tables III and IV

TABLE II. DATA ANALYSIS SUBSET

FACILITY	α Deg.	λ_∞	$\dot{m}$ lbm/sec.	R_N/R_B	$-\Lambda_F$ Deg.	$Re_\alpha/ft.$ x 10^{-6}	X_{TR_0} (in.)	X_{TR_E} (in.)
TUNNEL A (M_∞ = 4)	0	0	0	0	0	3.6	15.6	24.5
	7				0		13.7	18
	14				0		10.8	14.5
	0				7		15.6	24.5
	7				7		15.6	18.5
	0				15		15.6	24.5
	7				15		15.6	18.5
	0				20		15.6	24.5
					15	2.5	20	30
					20	2.5	20	30
				.1	0	3.6	20	30
		.021	.005	.1	0		NOSETIP	
		0	0	.1	20		20	30
		.021	.005	.1	20		NOSETIP	
		0	0	0	0		13.7	20
TUNNEL B (M_∞ = 8)	7	0	0	0	0	3.6	10.8	20.4
	0		0	0	0		10.8	19
	14		0	0	0		10.8	18.5
	7		0	0	7		10.8	20.5
	0		0	0	15		10.8	19
	0		0	0	20		10.8	19
	0		0	0	15	2.5	12.6	27
	0		0	0	20	2.5	12.6	27
	0		0	0.1	0	3.6	LAMINAR	
	0	.018	.0025	0.1	0	3.6	8.2	22.5
	0	.018	.0025	0.1	15	3.6	8.2	22.5
	0	0	0	0.1	20	3.6	LAMINAR	
	0	.018	.0025	0.1	20	3.6	8.2	22.5
	0	.015	.002	0.1	20	3.6	11.2	23.5
	3 1/2	.018	.0025	0.1	0	3.6	LAMINAR	

TABLE III. NOMINAL LOCAL FLOW PROPERTIES* TUNNEL A (M_∞ = 4) SUBSET

GEOMETRY	Re_∞/ft / Re_s x 10^{-6}	α Deg.	R_N/R_B	$-\delta_F$ Deg.	P_e lbf/ft²	h_w/h_{aw}	u_e ft/sec	M_e	q_e lbf/ft²	$\dot{b}_w$ x 10^3 ft²/sec	τ_w lbf/ft²	$u_{\tau w}$ ft/sec
CONE	3.6/6.5	0	0	-	93	0.78	2558	3.72	890	3.86	1.2	112
SLICE	3.6/7.5			-	47	0.78	2642	4.27	600	7.7	.94	130
FLAP	3.6/8.7			0	48	0.78	2637	4.22	600	7.4	.83	126
FLAP	3.6/11.0			7	94.5	0.82	2554	3.7	900	4.14	1.46	123
FLAP	3.6/14.4			15	175	0.84	2476	3.33	1350	2.34	2.4	118
FLAP	3.6/17.1			20	245	0.84	2432	3.15	1680	1.74	3.2	115
CONE[1]	3.6/6.2			-	62.2	1.0	2265	3.7	595	5.85	.95	122
SLICE[1]	3.6/8.2			-	31.5	1.0	2357	4.4	420	11.6	.53	126
FLAP[1]	3.6/9.4			0	32.5	1.0	2351	4.3	427	10.5	.53	122
CONE	2.5/4.5			-	61.2	0.8	2558	3.73	595	5.8	.31	68
SLICE	2.5/5.0			-	31.2	0.6	2643	4.26	395	11.2	.6	132
FLAP	2.5/9.8			15	117	0.84	2478	3.33	900	3.5	1.8	125
FLAP	2.5/11.6			20	163	0.84	2433	3.15	1130	2.5	2.3	122
CONE	3.6/1.9		0.1	-	90	0.78	2175	2.4	355	3.9	.3	54
SLICE	3.6/2.5			-	43	0.78	2400	3.0	290	7.8	.65	117
FLAP	3.6/4.0			0	50	0.78	2460	3.3	375	7.1	.83	124
FLAP	3.6/12.0			20	225	0.83	2330	2.8	1250	1.8	3.0	115
CONE[2]	3.6/2.8			-	90	0.78	2330	2.8	500	4.2	1.3	116
SLICE[2]	3.6/4.0			-	43	0.78	2537	3.61	400	8.3	.75	125
FLAP[2]	3.6/5.7			0	50	0.78	2540	3.64	465	7.3	.8	122
FLAP[2]	3.6/13.0			20	225	0.84	2365	2.9	1330	1.8	2.9	113
CONE	3.6/8.2	7	0	-	165	0.84	2470	3.3	1260	2.5	2.3	120
SLICE	3.6/8.7			-	87	0.84	2550	3.7	830	4.6	1.25	118
FLAP	3.6/10.0			0	88	0.84	2550	3.7	840	4.4	1.22	115
FLAP	3.6/13.2			7	161	0.85	2471	3.3	1235	2.6	2.03	113
FLAP	3.6/18.0			15	290	0.88	2392	3.0	1830	1.53	3.31	109
CONE	3.6/11.5	14		-	408	0.86	2290	2.68	2050	1.06	4.0	102
SLICE	3.6/8.9			-	146	0.84	2431	3.14	1010	2.85	1.55	103
FLAP	3.6/10.5			0	150	0.84	2428	3.14	1030	2.72	1.55	101

NOTES:

(1) GROUP 36 (GE TEST 113) - P_∞ = 43.3 psia, T_∞ = 582°R - ADIABATIC

(2) NOSETIP BLOWING @ $\dot{m}$ = 0.005 lbm/sec

*VALUES GENERATED USING GE-RESD 3DFF[93] AND 3DV[94]

TABLE IV. NOMINAL LOCAL FLOW PROPERTIES ** TUNNEL B (M_∞ = 8) SUBSET

GEOMETRY	Re_∞/ft / Re_2 x 10^{-6}	σ Deg.	R_N/R_B	$-\delta_F$ Deg.	P_e lbf/ft	h_w/h_{aw}	u_e ft/sec	M_e	q_e lbf/ft²	ν_w x 10^3 ft²/sec	τ_w lbf/ft²	u_{-w} ft/sec
CONE	3.6/7.6	0	c	-	34.5	0.5	3826	6.76	1120	12.5	1.15	188
SLICE	3.6/15.9			-	8.8	0.46	3935	10.12	631	44	.34	195
FLAP	3.6/17.5			0	9.5	0.33	3930	9.85	645	39.3	.36	188
FLAP	3.6/17.5			15	94	0.53	3740	5.6	2060	5.6	2.65	182
FLAP	3.6/22			20	150	0.59	3700	5.2	2850	4.0	4.12	184
CONE	2.5/5.5			-	24	0.47	3827	6.76	780	17.4	.7	175
SLICE	2.5/11.2			-	6.0	0.47	3938	10.23	444	68.0	.25	204
FLAP	2.5/11.8			15	65	0.54	3740	5.6	1430	8.5	1.95	192
FLAP	2.5/14.5			20	108	0.56	3700	5.2	1950	5.6	3.12	188
CONE*	3.6/.77		0.1	-	30.5	0.45	3380	3.45	255	12.2	.33	109
SLICE*	3.6/.7			-	13.0	0.47	3500	4.0	143	29.5	.14	103
FLAP*	3.6/.74			0	11.2	0.47	3530	4.0	128	36.0	.12	101
FLAP*	3.6/3.5			20	75/150	0.5	3270	3.12	600/100	4.1	.65	85
CONE[1]	3.6/1.21			-	32	0.46	3525	4.0	370	13.0	.97	175
SLICE[1]	3.6/1.8			-	13.3	0.45	3710	5.3	258	28.9	.47	184
FLAP[1]	3.6/2.16			0	11.3	0.44	3740	5.6	248	34.0	.40	182
FLAP[1]	3.6/6.21			15	50/75	0.54	3640	4.7	750/1160	8.0	2.0	186
FLAP[1],[2]	3.6/9.3			20	75/150	0.57	3600	4.5	1000/2130	5.2	2.9	185
CONE[1]	3.6/1.3	3 1/2		-	55	0.46	3380	3.45	460	7.0	0.5	94
SLICE[1]	3.6/1.2			-	18.5	0.45	3560	4.2	230	21.0	.16	88
FLAP[1]*	3.6/1.4		0	0	18.0	0.46	3570	4.3	232	22.0	.14	87
CONE	3.6/9.0	7	0	-	88.5	0.52	3724	5.4	1810	5.6	2.4	177
SLICE	3.6/9.1			-	31.7	0.48	3811	6.5	940	13.2	.9	172
FLAP	3.6/10.5			0	35.4	0.47	3811	6.5	1025	13.0	.88	170
FLAP	3.6/14.4			7	86	0.53	3728	5.45	1860	6.0	2.1	165
CONE	3.6/	14	0	-	173	0.51	3562	4.23	2170	2.8	3.8	158
SLICE	3.6/			-	79.4	0.50	3634	4.67	1212	5.9	1.7	153
FLAP	3.6/			0	84	0.50	3634	4.67	1250	5.7	1.64	150

NOTES:
(1) NOSETIP BLOWING @ $\dot{m}$ = 0.0025 lbm/sec
(2) NOSETIP BLOWING @ $\dot{m}$ = 0.002 lbm/sec
* BASED ON LAMINAR BOUNDARY LAYER
** IBID - TUNNEL A CONDITIONS

113

TABLE V. DISPLACEMENT THICKNESS $M_\infty = 4$ SUBSET $\delta^* \times 10^3$ FT.

SENSOR GROUP NO. Inches	2(6)	2(9)	2(10)	5(23)	5(25)	6(27)	6(30)	9(42)	14(69)	17(94)	18(99)	20(91)	31(102)	32(103)	36(113)
A-1 7.64	1.15	.9	.6	1.16	.91	1.16	.91	1.16	1.41	1.4	1.42	2.44	1.43	2.44	1.39
A-3 10.15	1.34	1.06	.7	1.36	1.0C	1.33	1.06	1.36	1.64	1.63	1.55	2.96	1.57	2.96	1.62
A-5 13.3	1.5	1.15	1.48	1.52	1.18	1.52	1.19	1.52	1.83	1.82	1.66	3.48	1.68	3.5	1.82
A-7 17.06	1.77	2.13	2.45	1.8	1.45	1.8	1.46	1.8	2.08	2.07	1.83	3.68	1.85	3.87	2.73
A-8 17.72	1.98	2.46	2.6	2.01	1.89	2.0	1.69	2.01	2.13	2.12	1.86	3.94	1.88	3.93	3.1
A-9 18.60	2.45	2.88	2.8	2.48	2.17	2.47	2.17	2.48	2.19	2.18	1.9	4.02	1.92	4.02	3.63
A-10 20.51	3.54	3.53	3.2	3.57	3.07	3.56	3.07	3.57	2.3	2.3	1.99	4.2	2.0	4.2	4.47
A-13 25.27	9.92	8.6	10.4	10.0	8.14	10.1	8.02	3.94	7.4	7.4	5.96	10.63	5.07	9.1	11.1
A-14 25.9	10.2	8.82	10.6	10.1	8.27	10.2	8.3	10.2	7.9	7.3	5.9	10.55	5.2	9.26	11.4
A-15 26.56	10.4	9.06	10.7	10.3	8.51	10.4	8.53	10.4	8.4	8.3	5.9	10.31	5.4	9.4	11.7
A-16 28.94	11.0	9.61	11.1	10.9	9.12	11.0	9.15	11.0	9.43	9.4	5.9	10.0	5.9	9.86	12.3
A-26 29.65	11.7	10.22	11.5	6.15	5.56	3.47	3.28	2.59	3.19	2.4	6.27	10.2	1.54	2.33	12.9
A-27 30.38	11.9	10.5	11.7	6.35	5.74	3.7	3.41	2.8	3.46	2.65	6.59	10.5	1.88	2.56	13.1
A-28 31.87	12.4	11.0	12.1	6.71	5.98	3.96	3.57	3.03	3.79	2.95	7.04	10.9	2.08	2.66	13.6

*Measured from sharp cone apex

114

TABLE VI. DISPLACEMENT THICKNESS M_∞ = 8 SUBSET δ^* x 10^3 FT.

SERIES / GROUP		42	44	46	50	52	58	74	77	87°	87°°	90	94	98°	99°°	100	102	106°	106°°
A-1	7.64	1.05	1.80	.82	1.23	1.01	1.9	2.3	2.3	2.5		2.4	2.5	2.5		2.5	2.4	1.8	
A-2	10.16	2.33	2.22	1.06	1.40	2.3	2.3	2.7	2.7	2.7		2.7	2.7	2.6		2.8	2.6	1.8	
A-3	13.3	4.33	2.86	1.53	2.1	2.9	2.9	3	3	2.9		3.8	3.8	2.8		3.8	2.9	1.9	
A-5	17.60	10.17	5.4	3.63	4.47	5.4	5.4	4.5	4.5	3.1		5	5	3		5	4	2.05	
A-6	17.71	10.94	5.9	2.98	4.8	5.88	5.9	5	4.9	3.2		5.2	5.2	3.1		5.2	4.3	2.09	
A-9	16.60	11.92	6.5	4.23	5.25	6.53	6.5	5.7	5.7	3.2		5.5	5.5	3.2		5.5	4.6	2.14	
A-10	20.51	12.6	7.6	4.67	6.02	7.6	7.5	7.2	7.2	3.4		6.2	6.2	3.3		6.2	5.5	2.3	
A-13	25.27	40.24	34.2	12.7	19.9	34.6	34.5	36.3	36.1	7.9		16	17.3	8.4		17.2	16.3	7.2	
A-14	25.9	40.76	34.8	13.08	20.2	35.0	35	37	36.8	8.2		16.5	17.6	8.6		17.6	16.7	7.2	
A-15	26.16	41.3	34.3	13.3	20.4	35.4	35.4	37.5	37.3	8.5	17.8	17.1	17.9	8.8	18.6	17.9	17.1	7.3	20
A-16	26.64	43.1	34.6	14.0	21.2	35.9	36.1	38.3	38.2	9.2		18.8	19.4	9.3		19.4	18.6	7.6	
A-20	29.65	44.3	34.6	14.3	8.4	3.94	2.64	4.2	2.97	10	21.1	20	4.6	1.5	3.22	3.2	3.1	7.8	22
A-27	30.26	46.0	35	15.2	9.0	4.52	3.27	4.9	3.45	10.5	22.2	21.2	4.5	1.3	2.82	2.9	2.8	8.2	22.9
A-28	31.67	46.3	35.8	16.3	9.67	4.94	3.17	5.3	3.37	11.1	23.3	22.4	4	1.13	2.6	2.5	2.5	8.5	23.6

*Based on laminar boundary layer flow
**Based on turbulent boundary layer flow
+ Measured from sharp cone apex

TABLE VII. ANALOG REPRESENTATION OF STATISTICAL PARAMETERS

STATISTICAL PARAMETERS	SYMBOLS	UNITS	MATHEMATICAL REPRESENTATION	REMARKS
ROOT MEAN-SQUARE PRESSURE	$\bar{p}(t)$	PSF		$p(t)$ denotes time history of pressure
OVERALL SOUND PRESSURE LEVEL	OASPL	dB	$20 \log_{10} \dfrac{p(t)}{p_o(t)}$	$p_o(t)$ is reference pressure θ, 0002 dynes/cm^2
POWER-SPECTRAL DENSITY (PSD)	$\theta_{(f)}$	(PSF)^2	$\lim_{\substack{f \to \infty \\ T \to \infty}} \dfrac{1}{\Delta f T} \int_0^T p_x^2(f, t, \Delta f, \eta) dt$	$p(f, t, \Delta f)$ is filtered portion of $p(t)$ in frequency range $(f - \Delta f/2)$ to $(f + \Delta f/2)$
CROSS-SPECTRAL DENSITY	$\theta_{12}(f)$	(PSF)^2/Hz	$q(f, \eta) = \eta_x, f, \eta$	
CO-SPECTRUM (CSD)	$c(f, \eta)$	(PSF)^2/Hz	$\lim_{\substack{\Delta f \to 0 \\ T \to \infty}} \dfrac{1}{\Delta f T} \int_0^T p_x(f, t, \Delta f) p_{x+r}(f, t, \Delta f, \eta) dt$	$p_x(f, t, \Delta f)$ and $p_{x+r}(f, t, \Delta f)$ are pressure time histories taken at points separated by ζ
QUADRATURE SPECTRUM (QSD)	$q(f, \eta)$	(PSF)^2/Hz	$\lim_{\substack{\Delta f \to 0 \\ T \to \infty}} \dfrac{1}{\Delta f T} \int_0^T p_x(f, t, \Delta f) p_{x+r}(f, t, \Delta f, \eta) dt$	$p_x + \hat{p}(\zeta)$ denotes 90° phase shift from $p_x + \zeta(\cdot)$
NORMALIZED CO-SPECTRUM	$\gamma(f, \eta)_{NORM}$	NON DIM.	$c(f, \eta) / \left[\zeta(f, \eta) \theta_x, \zeta(f) \right]^{1/2}$	$\theta_x, r(f)$ is PSD of sensor at x, ζ
NORMALIZED QUAD-SPECTRUM	$q(f, \eta)_{NORM}$	NON DIM.	$q(f, \eta) / \left[\theta_x(f) \theta_{x+r}(f, \eta) \right]^{1/2}$	
PHASE ANGLE	$\theta(\zeta, \eta)$	RADIANS	$\tan^{-1} \left[\dfrac{q(f, \zeta, \eta)}{c(f, \zeta, \eta)} \right]$	phase angle between signals measured ζ apart at frequency f
NARROW-BAND CONVECTION VELOCITY	$U_c(r)$	FPS	$\dfrac{2 \pi f \zeta}{\theta(\zeta, \eta)}$	
AUTO-CORRELATION	$R_x(r)$	NON DIM.	$\lim_{T \to \infty} \dfrac{1}{T} \int_0^T p_x(t) p_x(t - r) dt$	Fourier transform of θ_x
CROSS-CORRELATION	$R(\zeta, r)$	NON DIM.	$\lim_{T \to \infty} \dfrac{1}{T} \int_0^T p_x(t) p_{x+r}(t + r) dt$	Fourier transform of $\theta(\zeta, \eta)$
NORMALIZED AUTO-CORRELATION	$R_x(r)_{NORM}$	NON DIM.	$\dfrac{R_x(r)}{R_x(0)}$	
NORMALIZED CROSS-CORRELATION	$R(\zeta, r)_{NORM}$	NON DIM.	$\dfrac{R(\zeta, r)}{\bar{p}_1 \bar{p}_2}$	
BROAD-BAND CONVECTION VEL.	U_{CB}	FPS	$\sum_{n=1}^{k} U_c(f_n) \Delta f_n / \sum_{n=1}^{k} \Delta f_n$	
REDUCED FREQUENCY PARAMETER	$\dfrac{f \zeta}{U_c}$	NON DIM.	$\dfrac{f \zeta}{U_c}$	Required in spectral plots

*Basis for representing fluctuating pressure properties.

116

TABLE VII. ANALOG REPRESENTATION OF STATISTICAL PARAMETERS (Continued)

STATISTICAL PARAMETER	SYMBOL	UNITS	MATHEMATICAL REPRESENTATION	REMARKS
NARROW-BAND AUTO-CORRELATION	$R_X(\tau; f, \Delta f)$	NON DIM.	$\lim_{T \to \infty} \frac{1}{T} \int_0^T P_X(t; f, \Delta f) P_X(t+\tau; f, \Delta f) dt$	Fourier Transform of $\Phi_X(f, \Delta f)$
NARROW-BAND CROSS-CORRELATION	$R(\xi, \tau; f, \Delta f)$	NON DIM.	$\lim_{T \to \infty} \frac{1}{T} \int_0^T P_X(t; f, \Delta f) P_{X+\xi}(t+\tau; f, \Delta f) dt$	Fourier Transform of $\Phi(\xi, f, \Delta f)$
NORMALIZED NARROW-BAND AUTO-CORRELATION	$R_X(\tau; f, \Delta f)_{NORM}$	NON DIM.	$R_X(\tau; f, \Delta f)/R_X(0, f, \Delta f)$	
NORMALIZED NARROW-BAND CROSS-CORRELATION	$R(f, \tau; f, \Delta f)_{NORM}$	NON DIM.	$\dfrac{R(\xi, \tau; f, \Delta t)}{P_1(f, \Delta f) P_2(f, \Delta f)}$	
COHERENCE FUNCTION	$\gamma(f, f)$	NON DIM.	$|\phi_{12}(f)|^2 / |\phi_1(f)| \, |\phi_2(f)|$	$\phi_1(f), \phi_2(f)$ are PSD's at locations 1 and 2 separated by distance ξ

$^*P_X(t; f, \Delta f)$ is that portion of pressure time history at location X in a frequency range $\left(f - \frac{\Delta f}{2}\right)$ to $\left(f + \frac{\Delta f}{2}\right)$
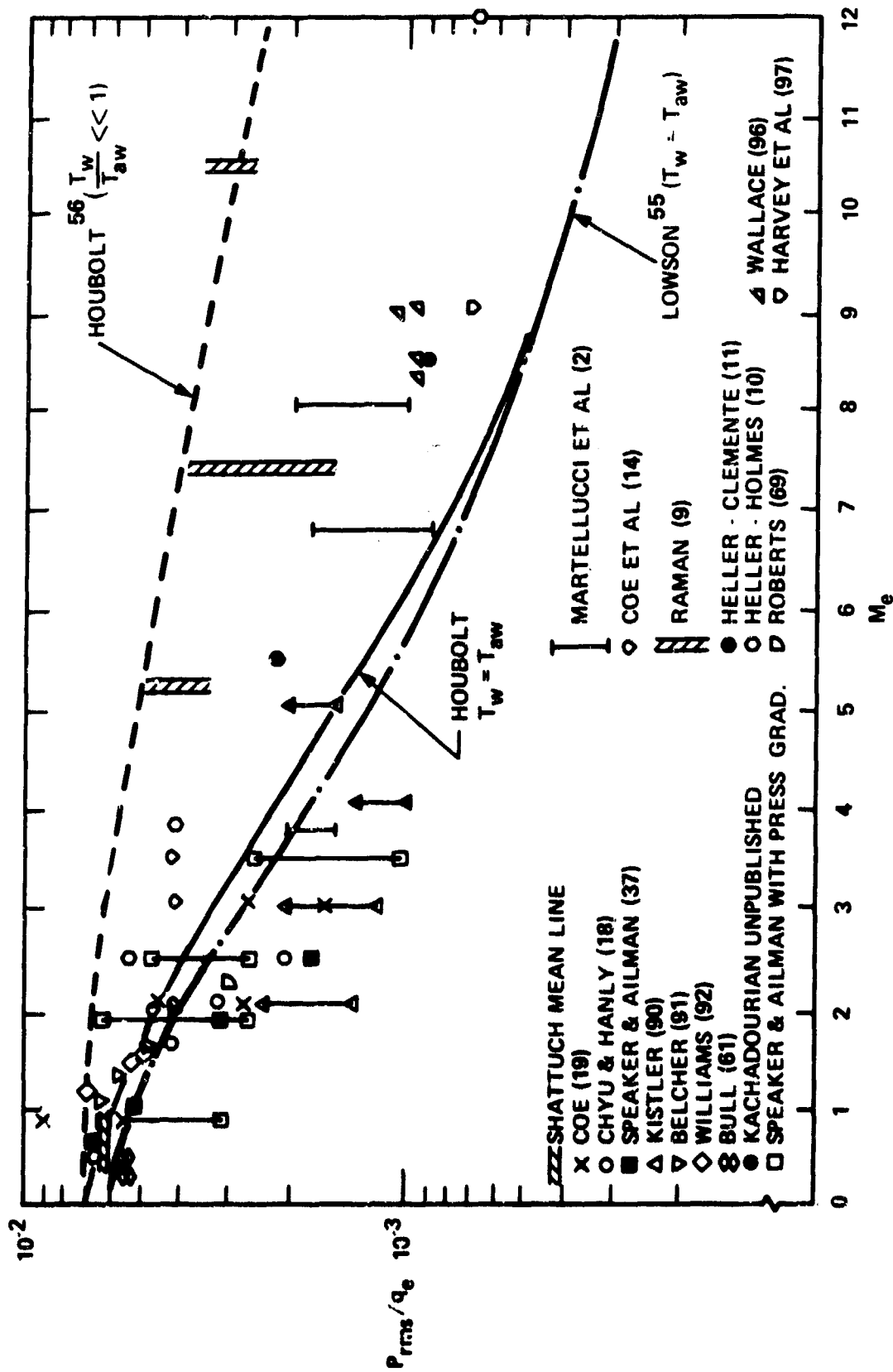
Figure 1. RMS Pressure Variation with Mach Number – Attached Turbulent Boundary Layer Flow
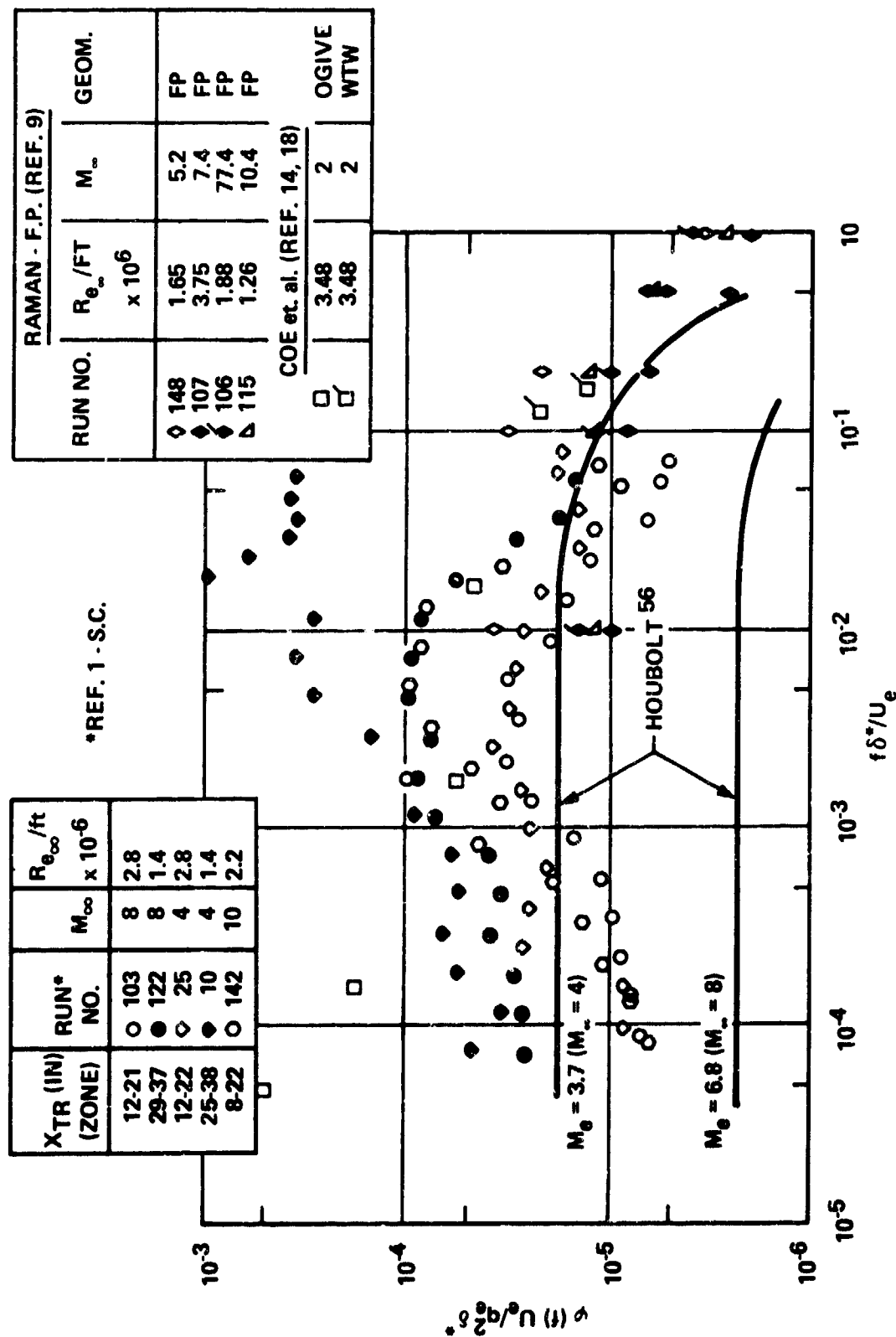
Figure 2. Normalized Power Spectral Density with Far Field ($y > \hat{q}$) Strouhal Number ($\alpha = 0^0$)

119
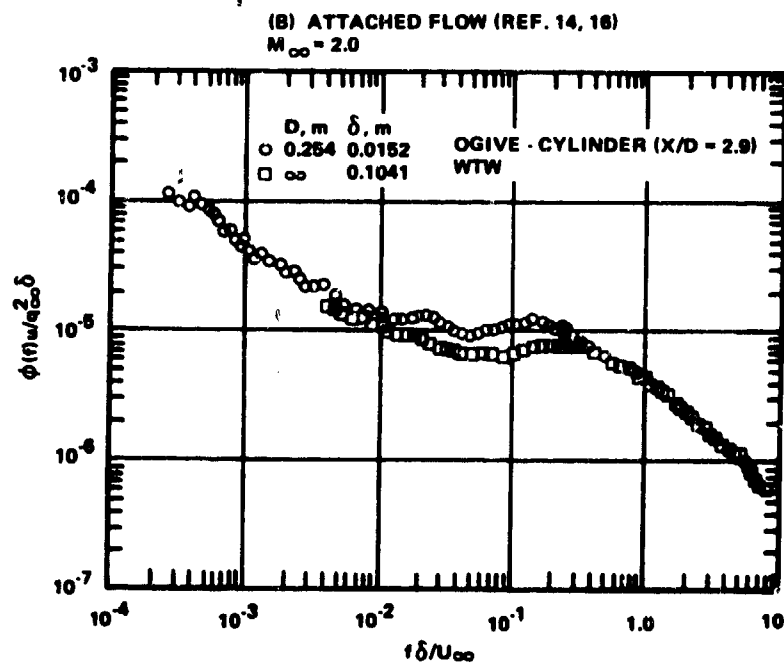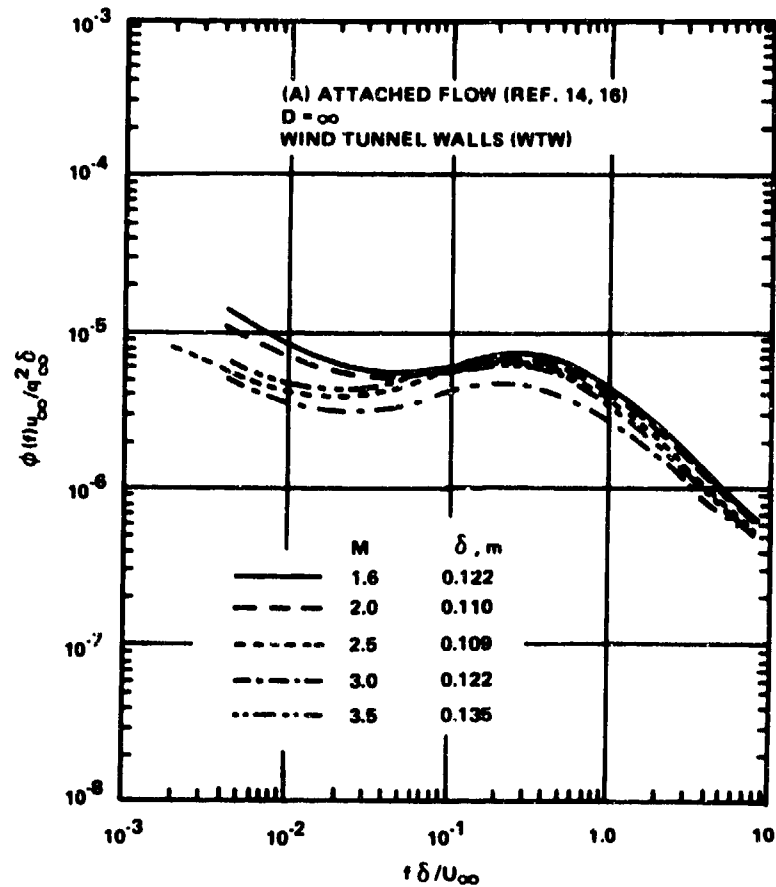
Figure 3. Power Spectral Density Variation with Strouhal Number

120
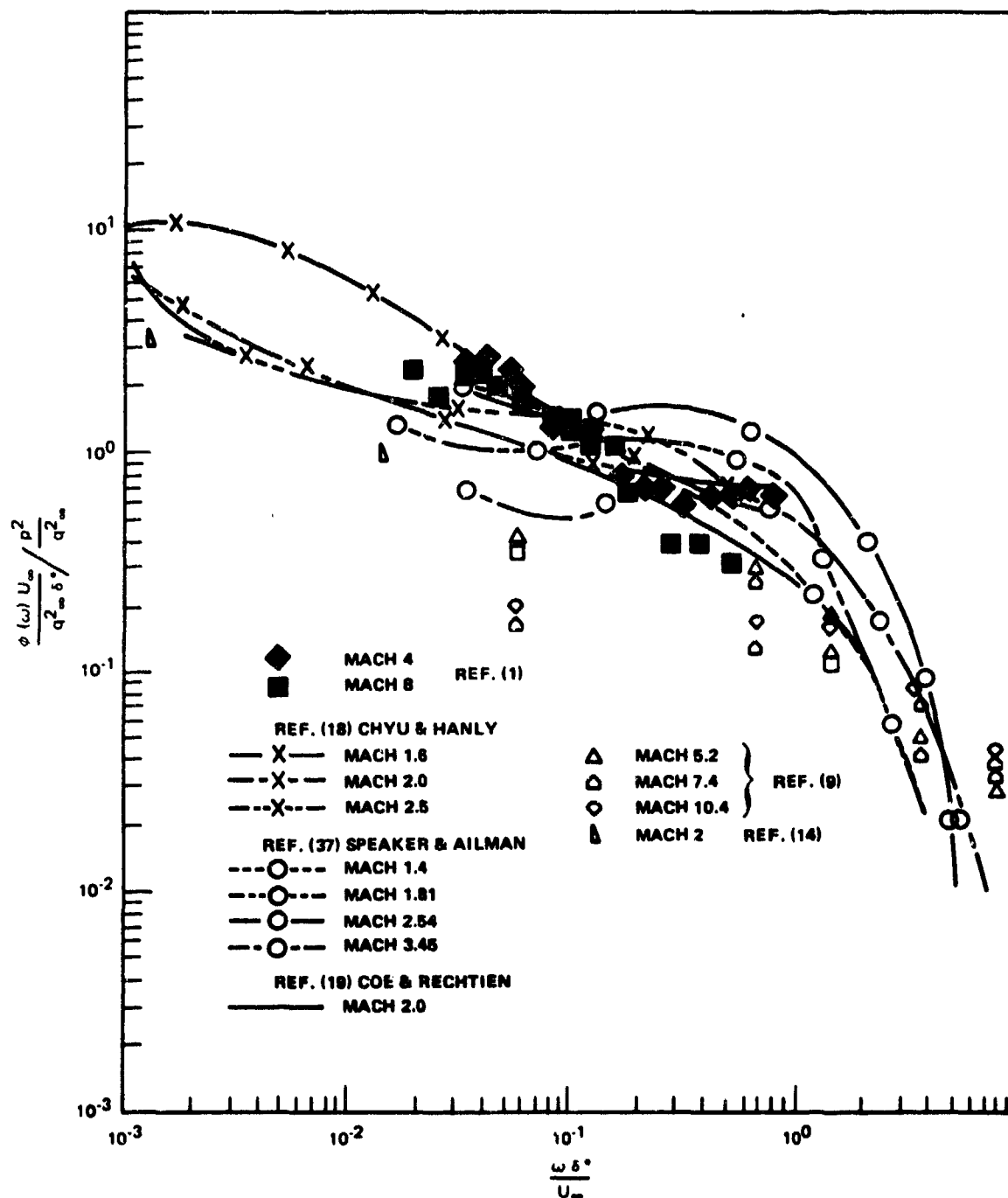
Figure 4. Comparison of Normalized Power Spectral Density Data
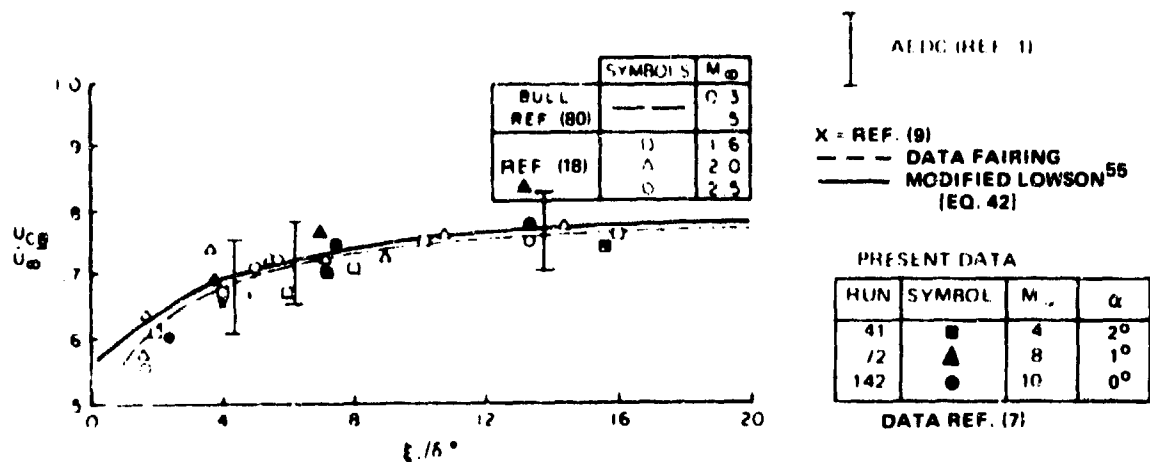
5A. Broad Band Convection Velocity
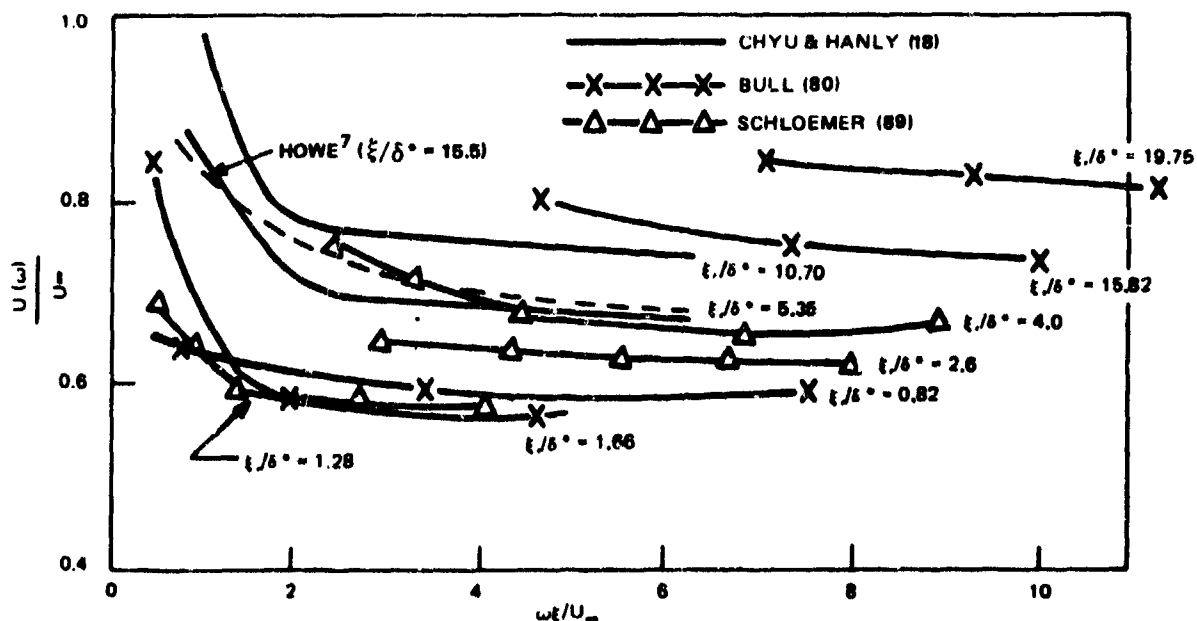
5B. Variation of Narrow-Band Convection Velocity with Frequency for
Various Separation Distances

Figure 5. Comparison of Convection Velocities
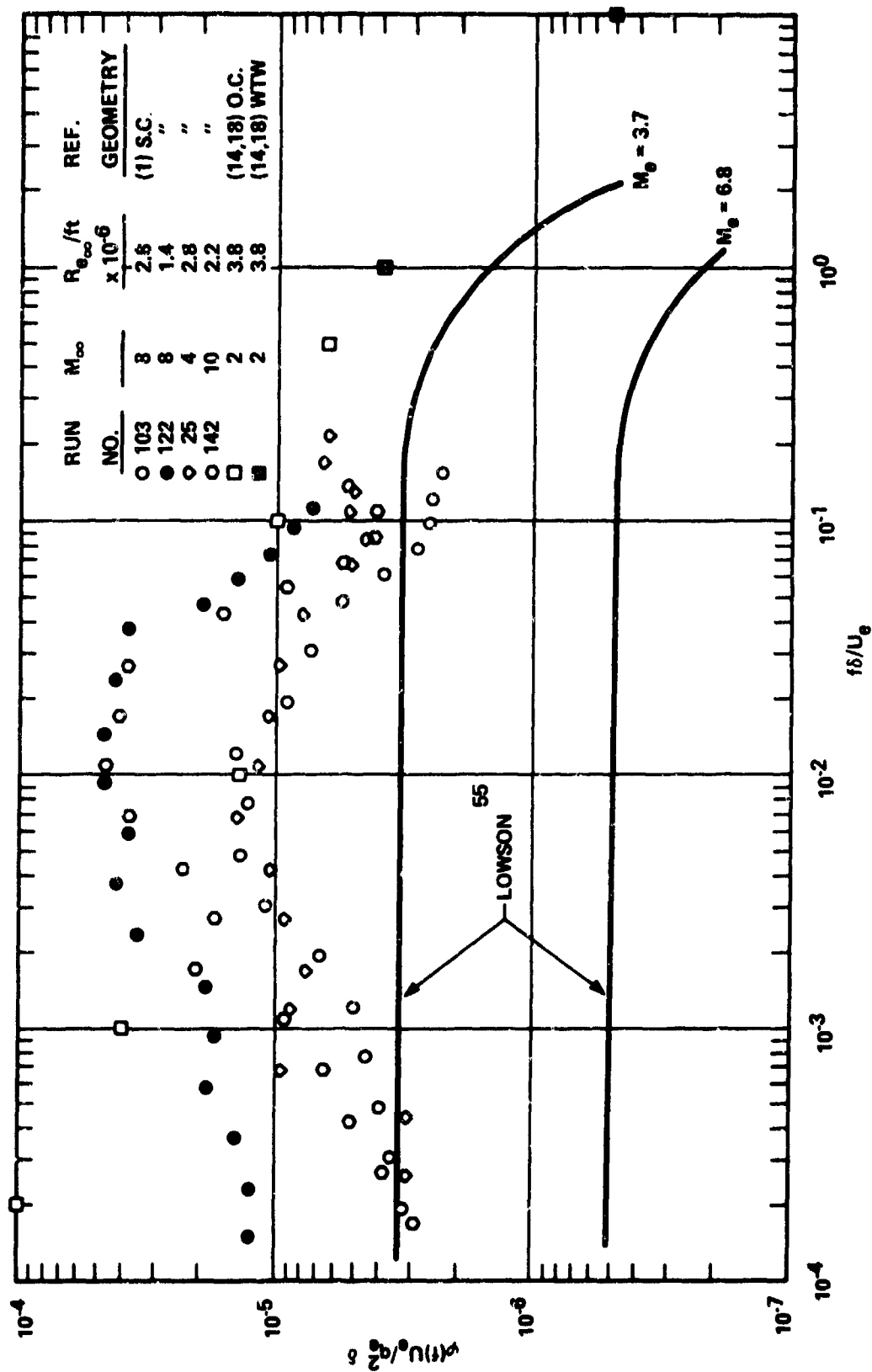
Figure 6. Comparison of Data and Theory for Power Spectral Density ($\alpha = 0^\circ$)

123
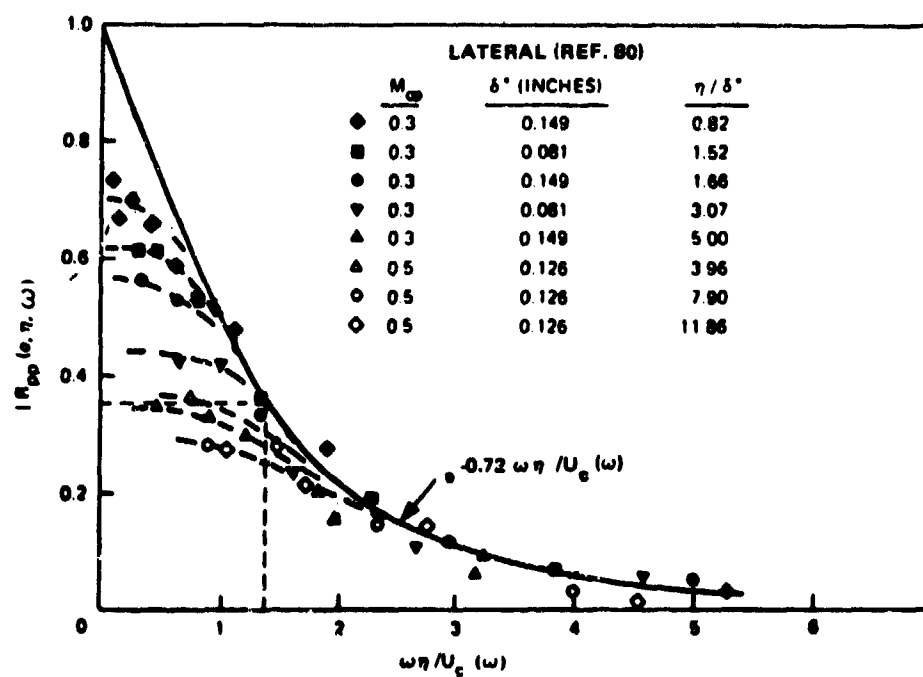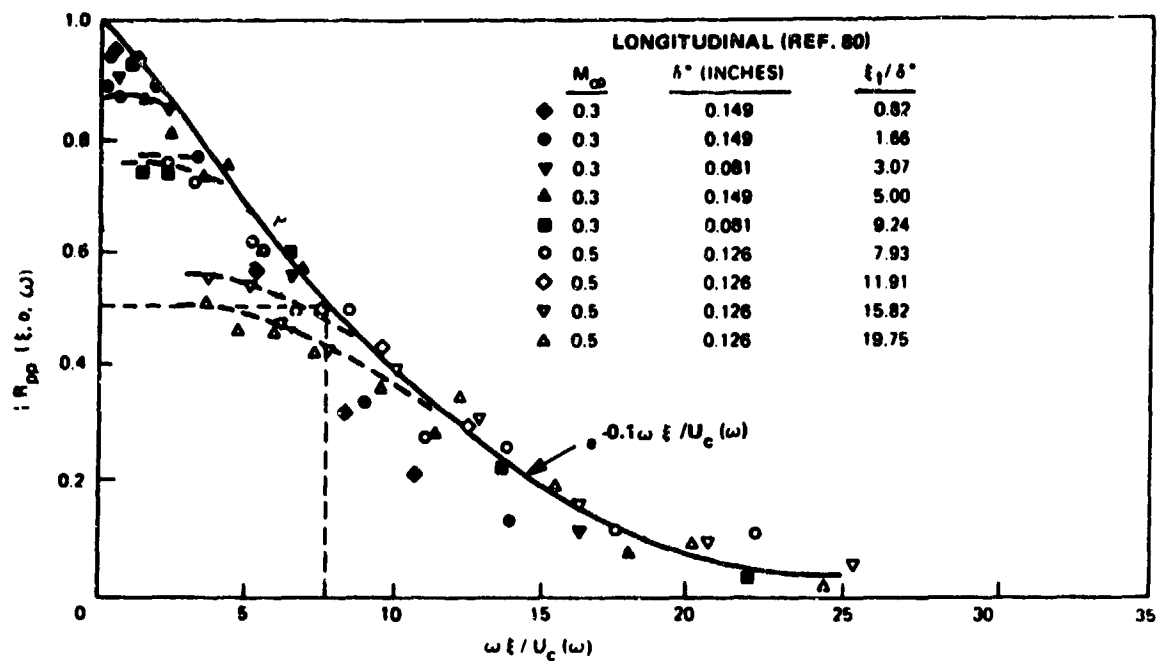
Figure 7. Narrow Band Space - Time Correlation Coefficients for Attached Turbulent Flow

124
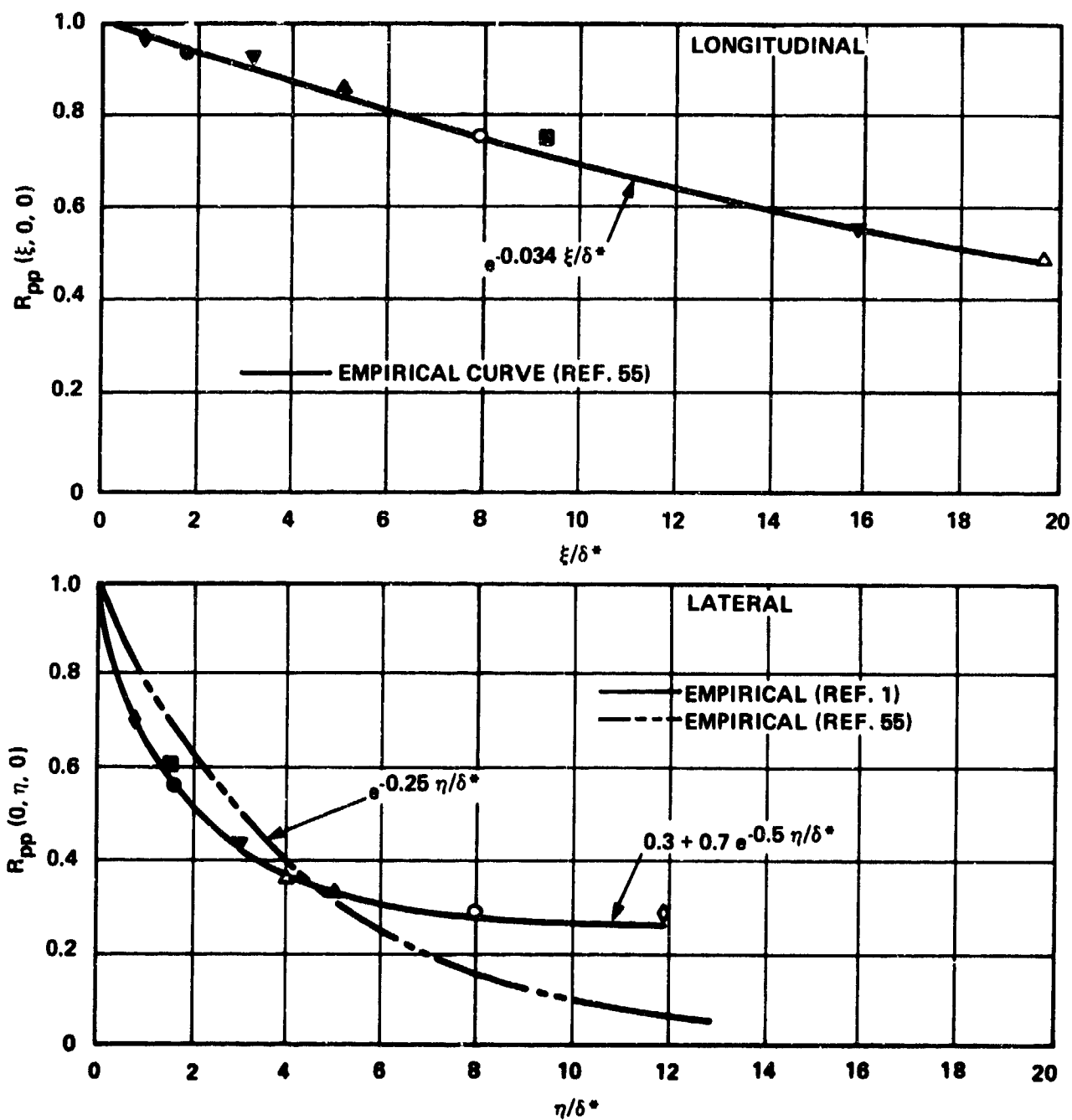
Figure 8.   Asymptotic Values of Narrow Band Pressure Coefficients for Attached
Turbulent Flow

125
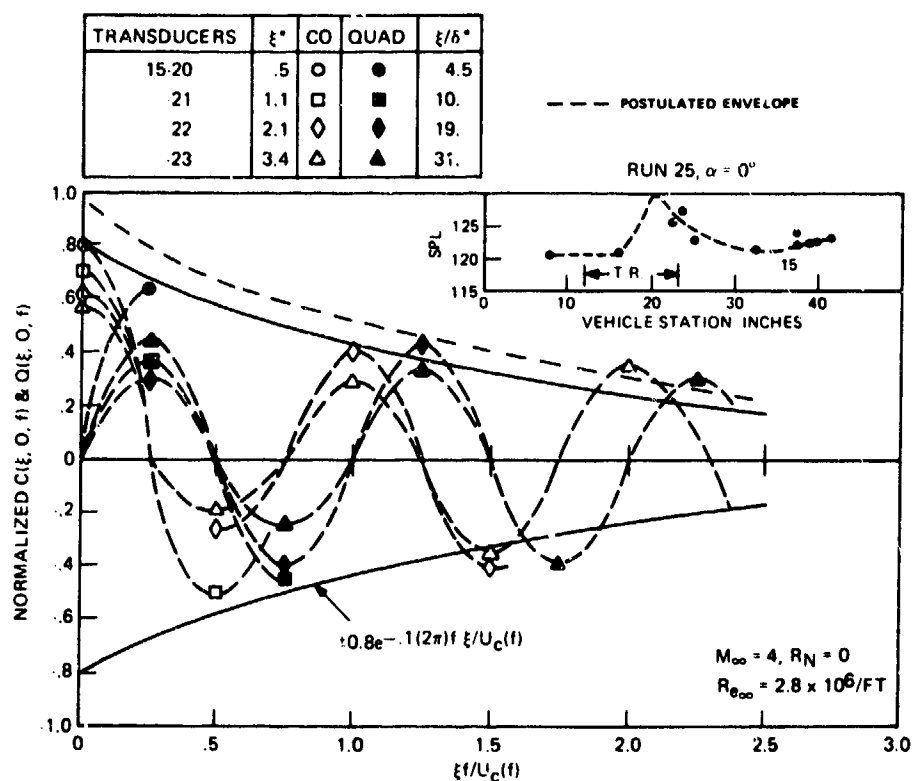
Figure 9. Longitudinal Cross-Power Spectral Density - Mach 4
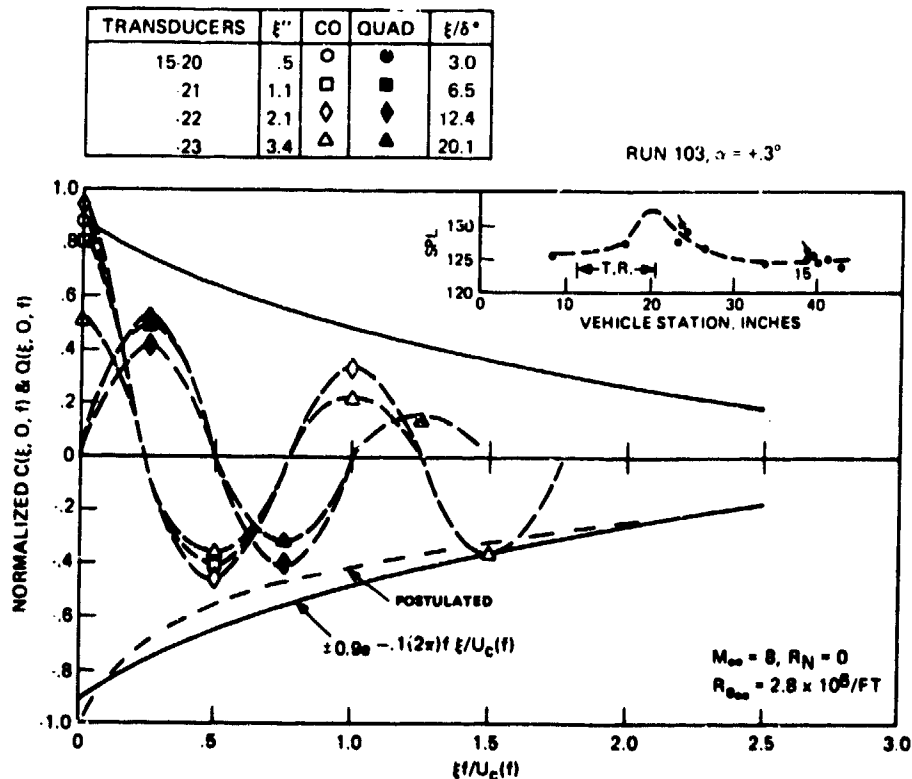
Figure 10. Longitudinal Cross-Power Spectral Density - Mach 8

126

TRANSDUCERS	ξ''	CO	QUAD	$\xi/\delta°$
20-21	.6	O	●	2.8
-22	1.6	□	■	7.5
-23	2.9	◊	◆	13.6

RUN 142, $\alpha = 0°$

NORMALIZED $C(\xi, O, f)$ & $Q(\xi, O, f)$

SPL

VEHICLE STATION, INCHES

T.R.

POSTULATED

$\pm 0.9 e^{-.1(2\pi)f \, \xi/U_c(f)}$

$M_\infty = 10, R_N = 0$
$R_{e_\infty} = 2.2 \times 10^6/FT$

$\xi f/U_c(f)$

TRANSDUCERS	ξ''	CO	QUAD	$\xi/\delta°$
20-21	.6	O	●	3.1
-22	1.6	□	■	8.2
-23	2.9	◊	◆	14.9

RUN 149, $\alpha = +.9°$

NORMALIZED $C(\xi, O, f)$ & $Q(\xi, O, f)$

SPL

VEHICLE STATION, INCHES

T.R.

$M_\infty = 10, R_N = .066$
$R_{e_\infty} = 2.2 \times 10^6/FT$

$\xi f/U_c(f)$
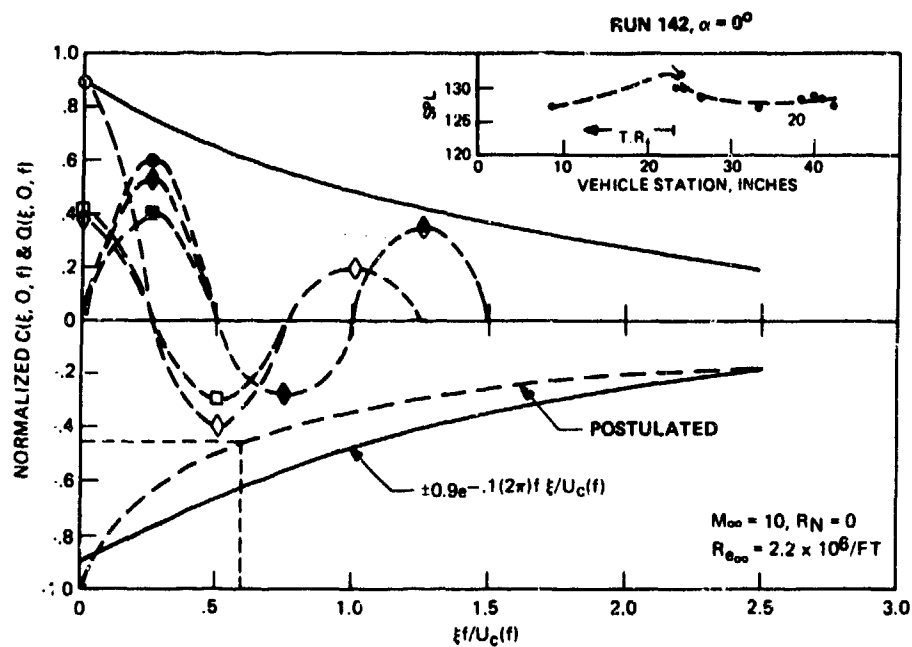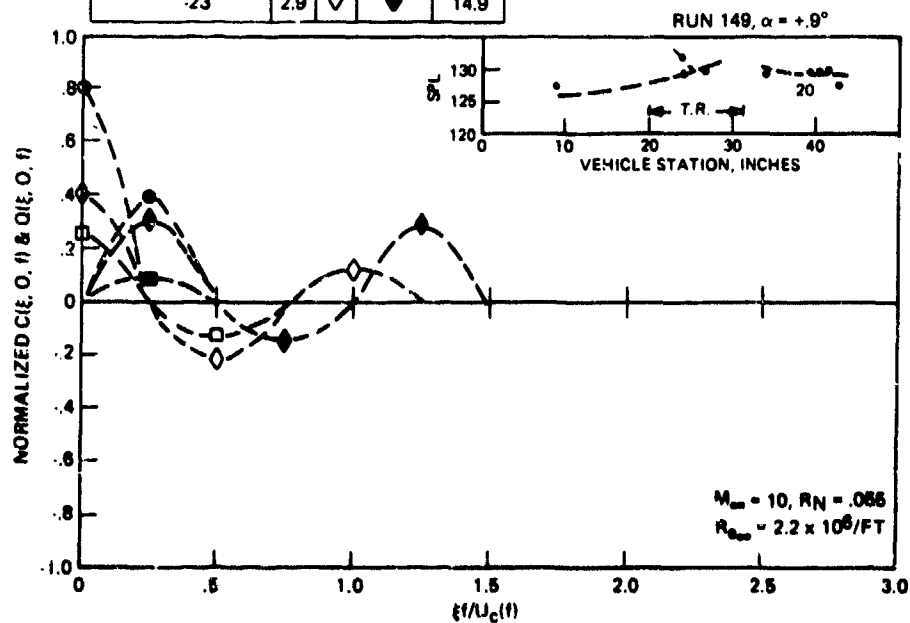
Figure 11. Longitudinal Cross-Power Spectral Density - Fully Turbulent Flow

127
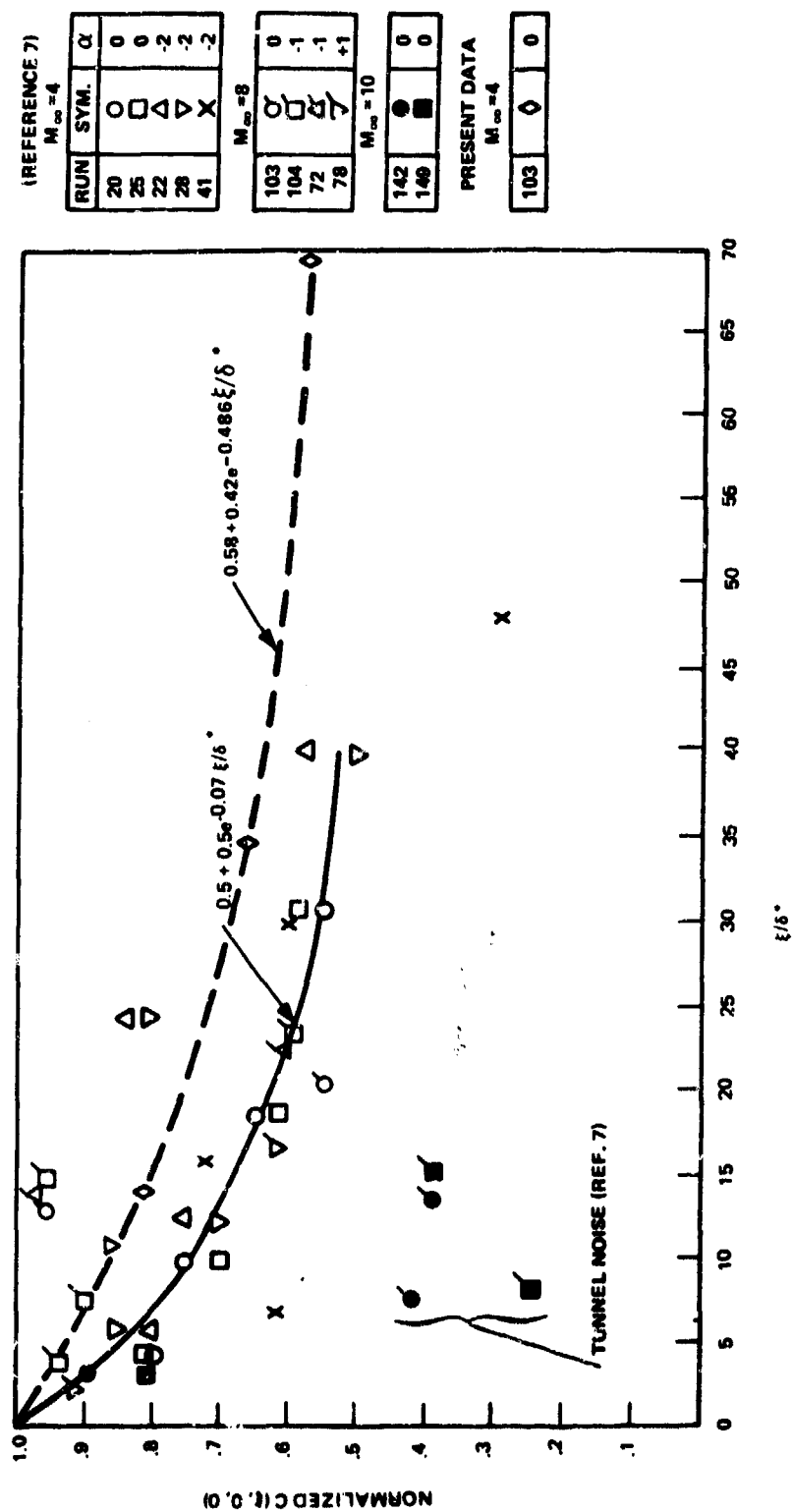
Figure 12. Asymptotic Values of Longitudinal Cross-Power Spectral Density at $f \xi/U_c$ $(f) = 0$ – Fully Turbulent Flow.

128

CORRELATION COEFFICIENT, Rpp(η; ω)

1.0

0.8

0.6

$e^{-0.72\eta\omega/U_c}$

0.4

$e^{-2.0\eta\omega/U_c}$

0.2

0

2   4   6   8   10

$\eta\omega/U_c$

○ MAESTRELLO CENTER FREQ 1200 Hz (REF. 79)

△ MAESTRELLO CENTER FREQ 2400 Hz

□ MAESTRELLO CENTER FREQ 3600 Hz

● WILLMARTH&WOOLDRIDGE CENTER FREQ 500 Hz (REF. 78)

✛ BULL CENTER FREQ 1200,2000,3200&5000 Hz (REF. 80)

● HOWE RUN 20 (α = 0°) (REF. 7)

Figure 13. Comparison of Narrow Band Lateral Space Correlation
Coefficients from the Literature

129
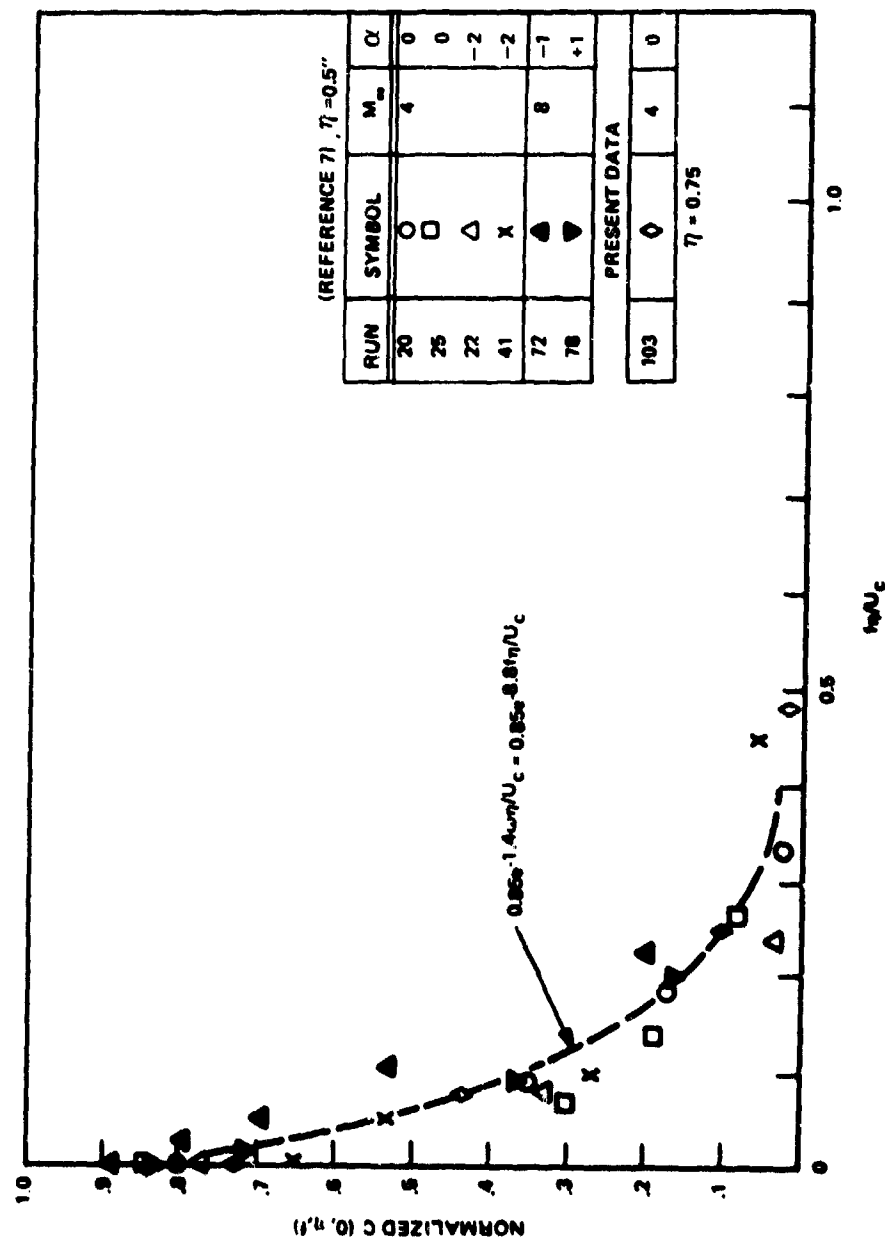
Figure 14. Circumferential Cross–Power Spectral Density Fully Turbulent Flow (M_∞ = 4, 8)
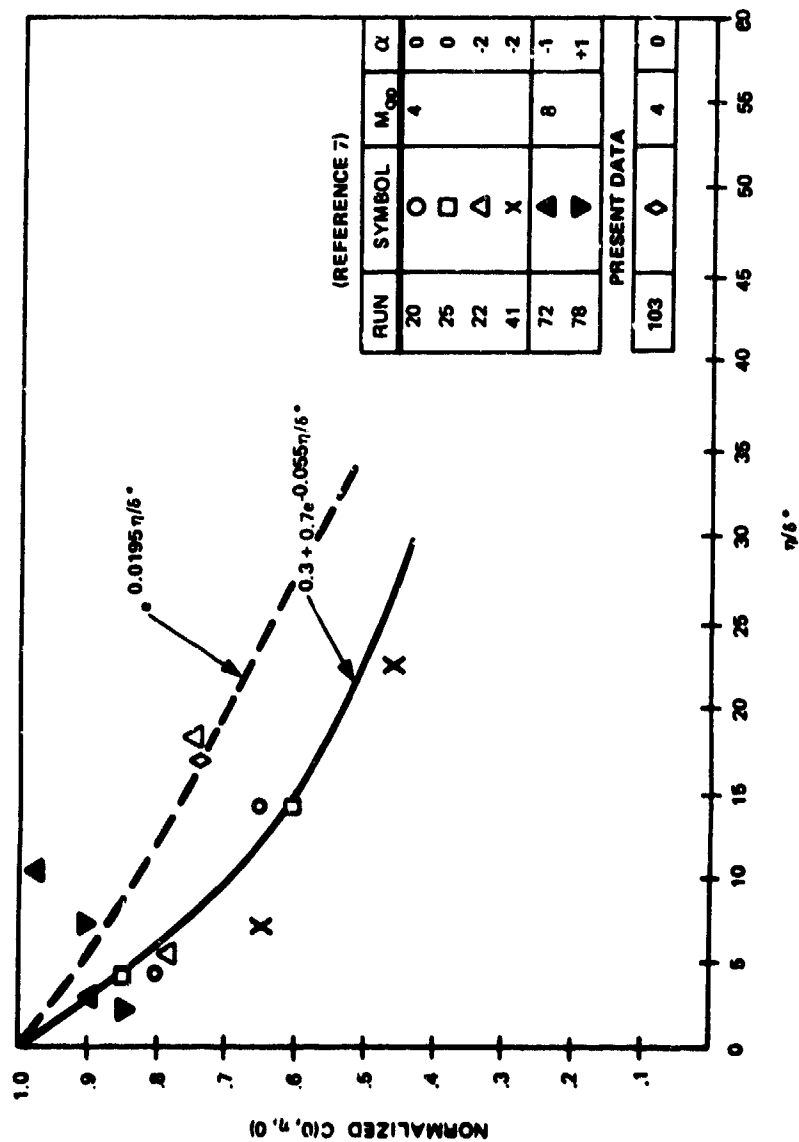
Figure 15. Asymptotic Values of Circumferential Cross-Power Spectral Density at $f\eta/U_c = 0$ – Fully Turbulent Flow ($M_\infty = 4, 8$)

131
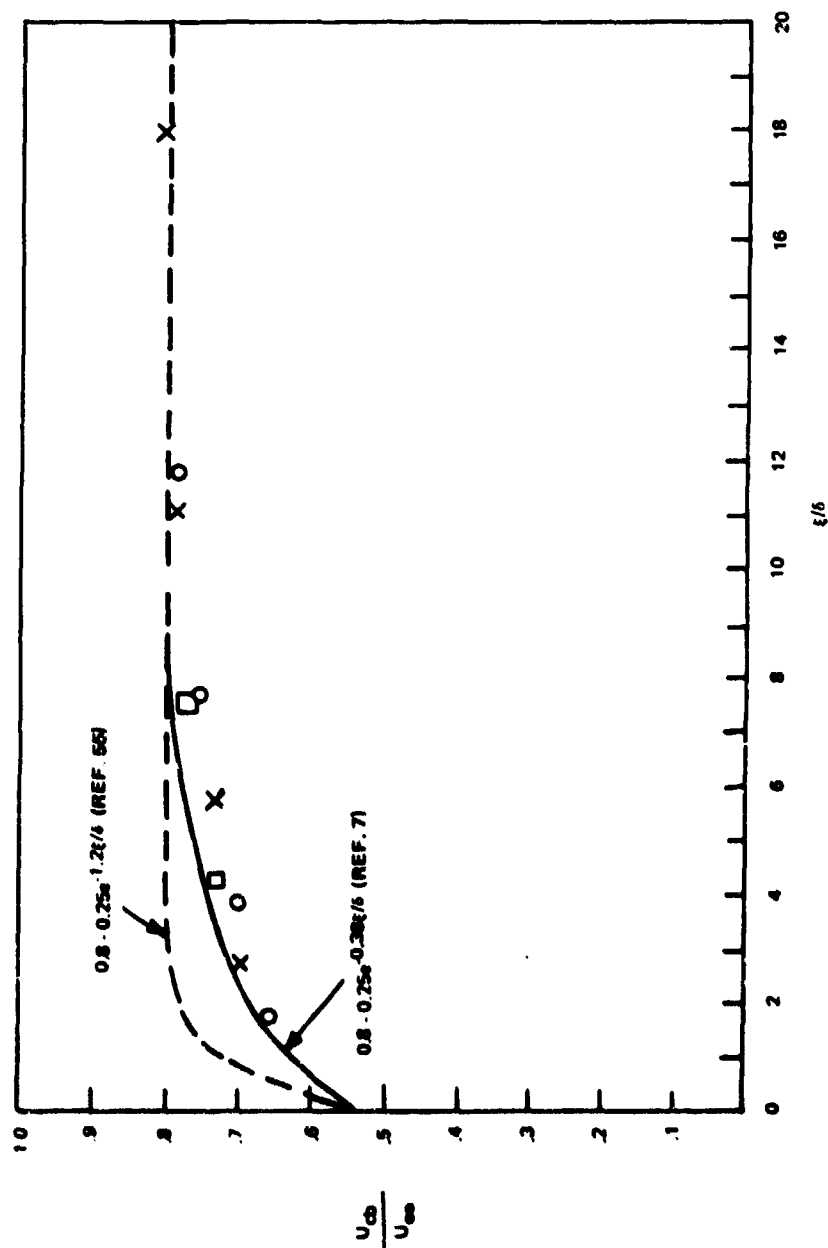
Figure 16. Comparison of Broad-Band Convection Velocity with Prediction Equations – Fully Turbulent Flow

132
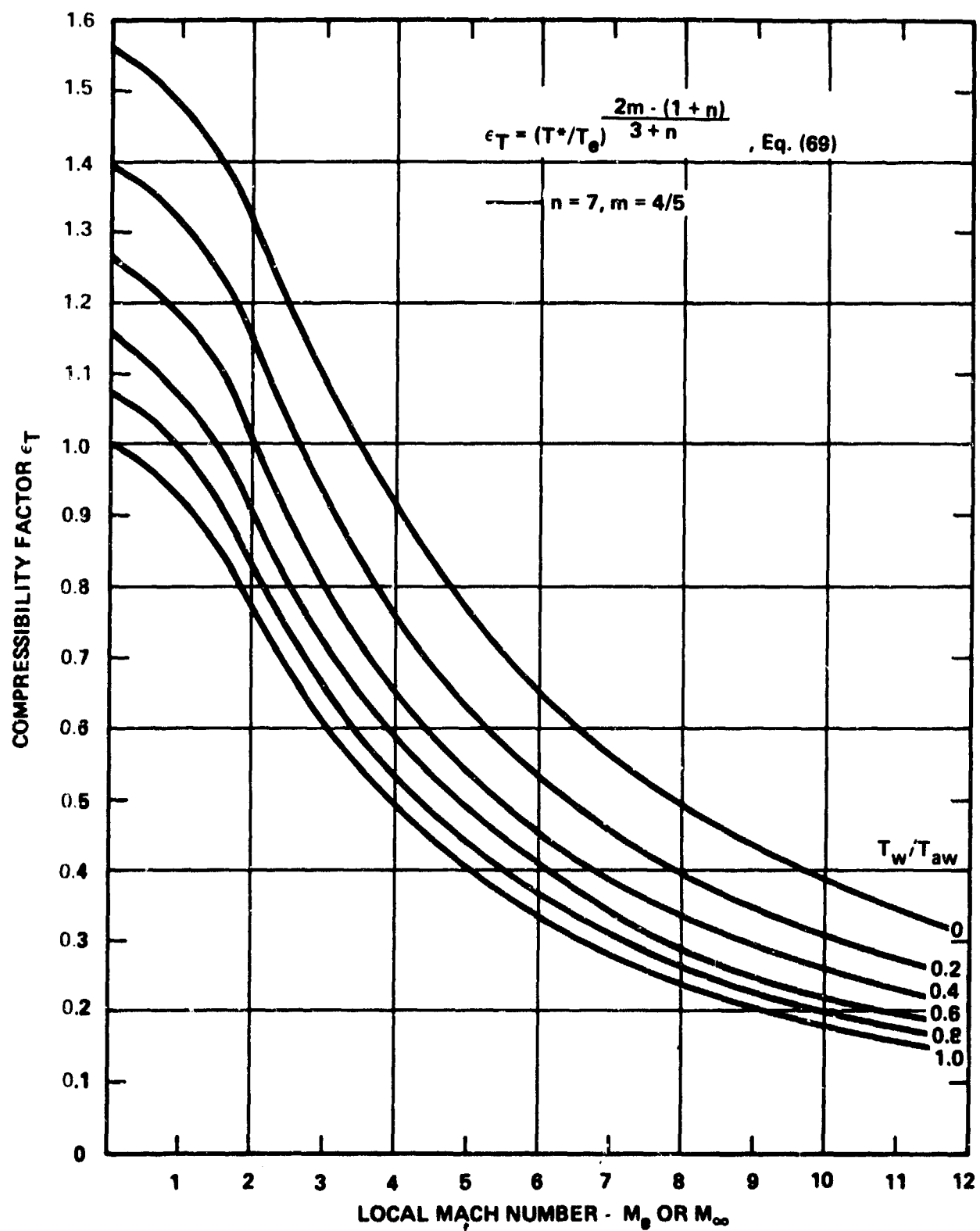
Figure 17. Variation of Compressibility Factor with Mach Number and Wall Temperature
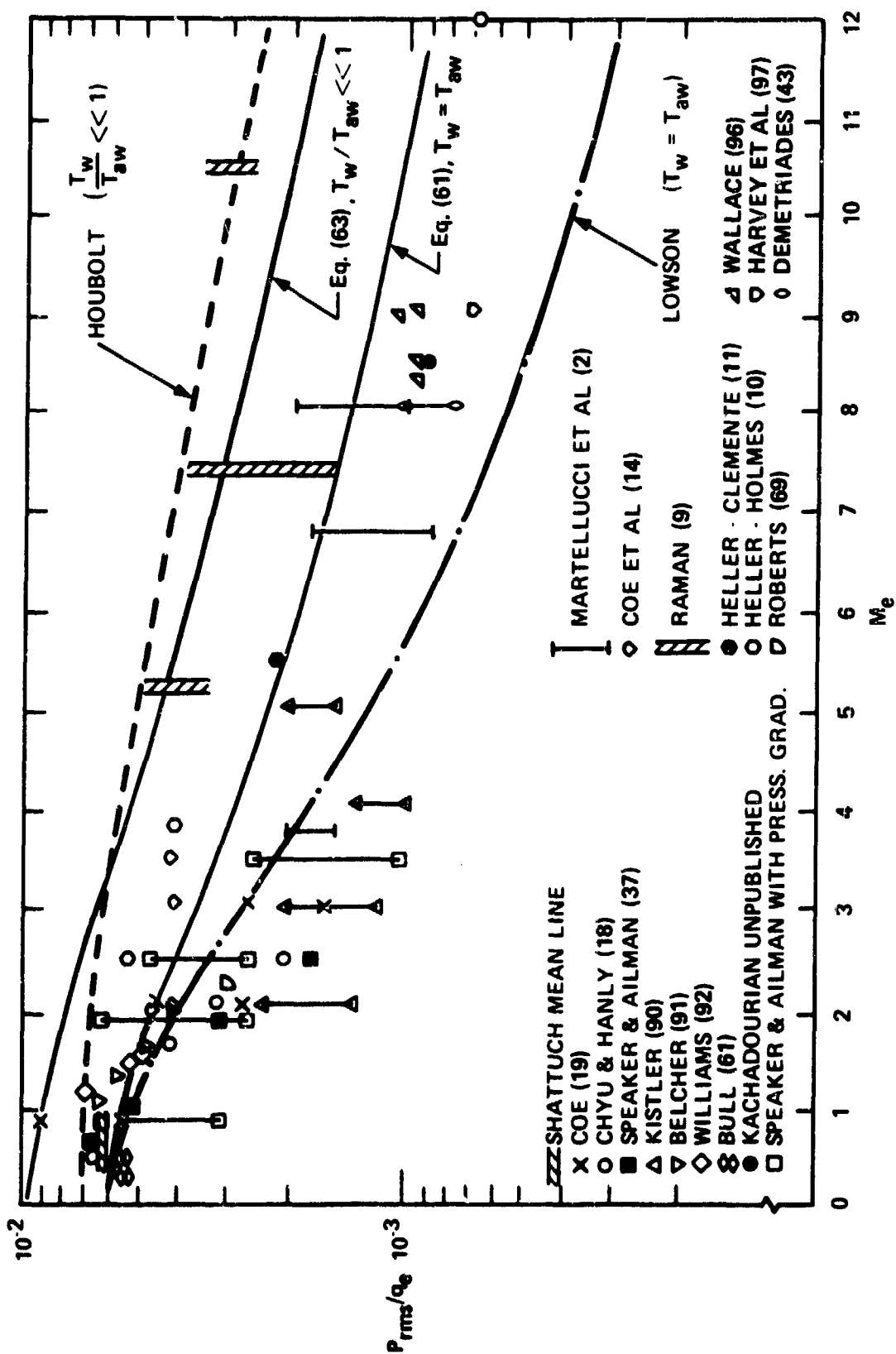
Figure 18. Comparison of Theory with Data for RMS Pressure-Attached Turbulent Boundary Layer Flow

134
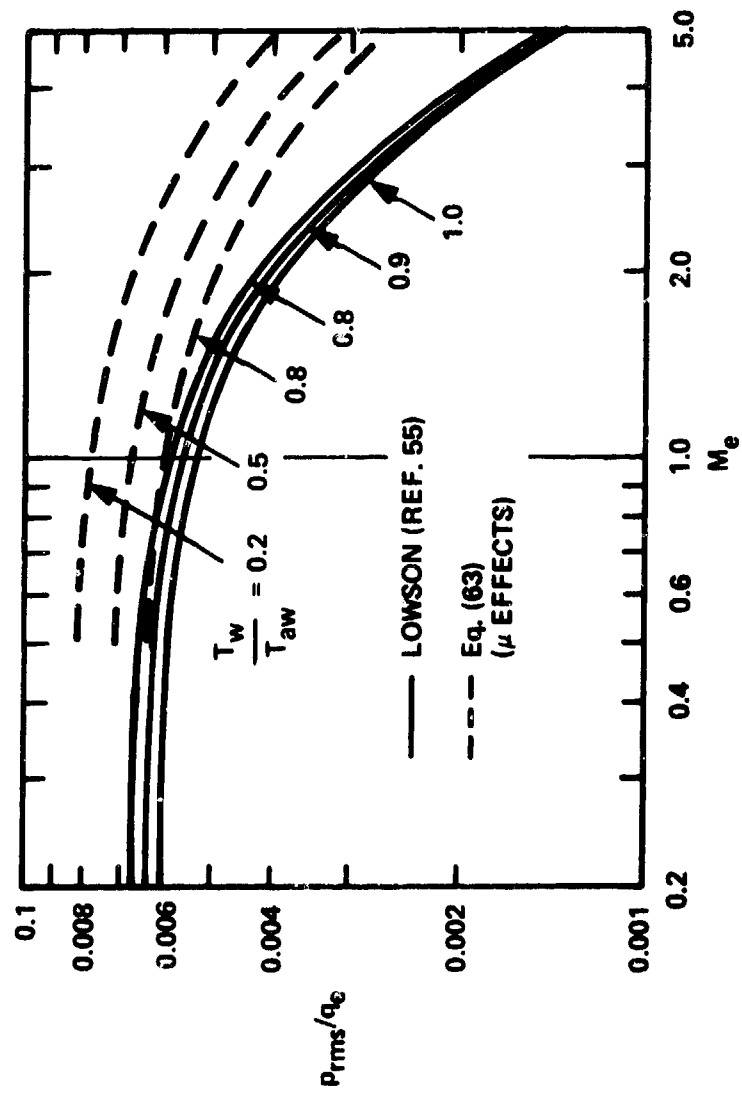
Figure 19. Wall Temperature Effects on RMS Pressure-Attached Turbulent Boundary Layer Flow

PRESSURE MAGNITUDE NORMALIZED WITH STATIC VALUE

5×10^{-1}

RMS PRESSURE VARIATION WITH MACH NO.

COLD WALL – Eq. (66a)
$(T_w/T_{aw} \ll 1)$

10^{-1}

HOT WALL – Eq. (65a)
$(T_w \approx T_{aw})$

LOWSON [55]
$T_w = T_{aw}$

$\tilde{p}/p$ local, static

HW = HOT WIRE

◇ LADERMAN - HW (95)
✕ DEMETRIADES - HW (43)
◁ STAINBACK LBL - CONE (33)
○ MARTELLUCCI et al (2)
△ RAMAN (9)
▽ KISTLER-CHEN (68)
○ COE et al (14)
◇ CHYU-HANLY (18)
□ HELLER-CLEMENTE (11)
◭ DONALDSON - HW (87)
▽ STAINBACK - HW (33)
○ LAUFER - HW (58)

10^{-2}

2×10^{-3}

0   4   8   12   16   20   24

LOCAL MACH NO. (M_e)

Figure 20. Normalized RMS Pressure Variation with Mach Number

136

NORMALIZED FIRST MOMENT
(Re$_\infty$/FT EFFECT)

$\alpha = 0^\circ$

RUN NO.	M$_\infty$	Re$_{e\infty}$/ft x 10^{-6}	REF.
○ 142	10	2.2	S.C. GE'72 (REF. 1)
○ 103	8	2.8	
● 122	8	1.4	
◇ 25	4	2.8	
◆ 10	4	1.4	
◇ 106	7.4	1.88	9
◁ 148	5.2	1.65	9
△ 107	7.4	3.75	9
▽ 115	10.4	1.26	9
□	2	3.48	14,18
◁	2	3.48	14,18

fδ*/U$_e$

f$_\psi$(f)/($\bar{p}$)^2
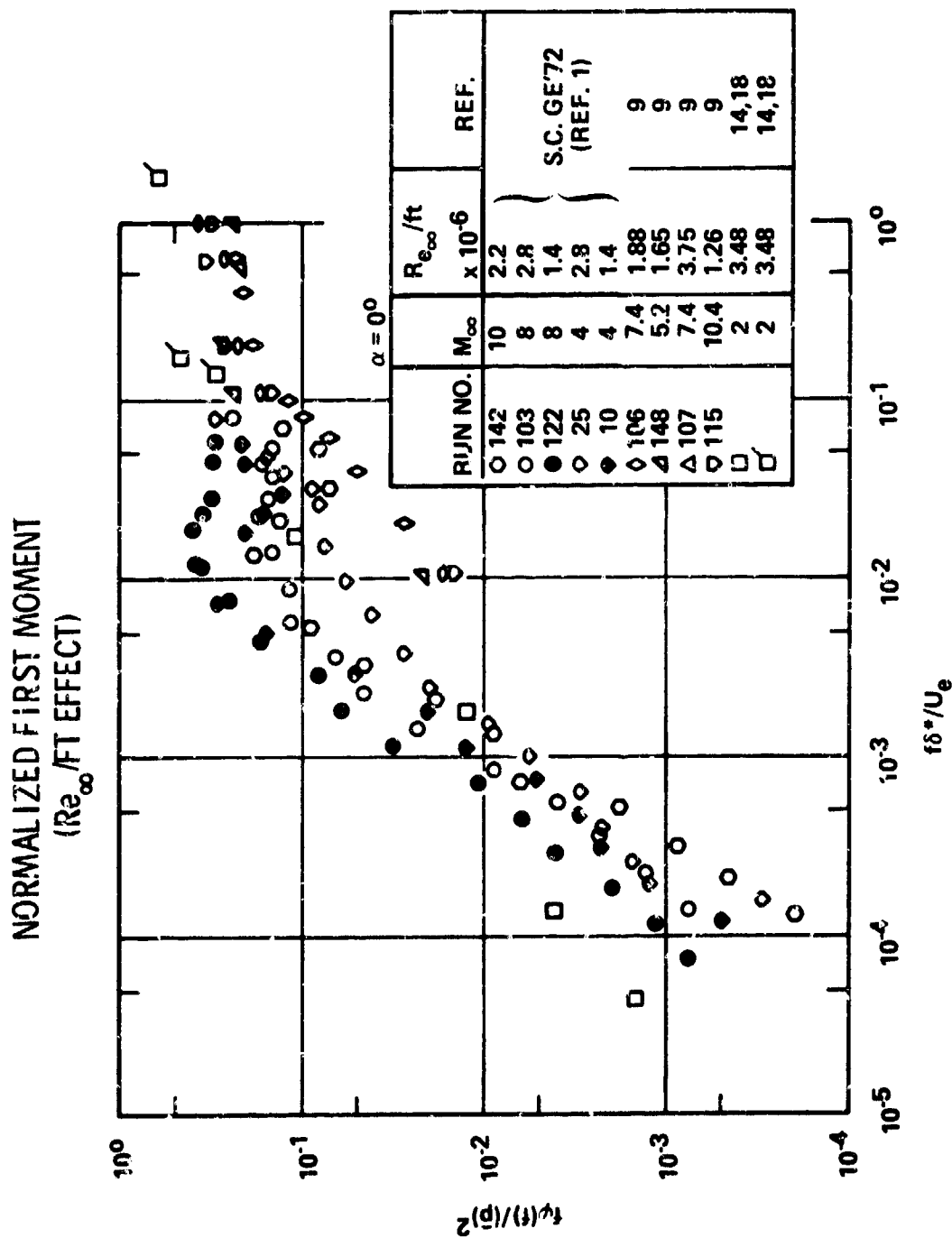
Figure 21.   First Moment of Power Spectral Density with Far Field ($y > \delta_1$) Strouhal Number ($\alpha = 0^\circ$)
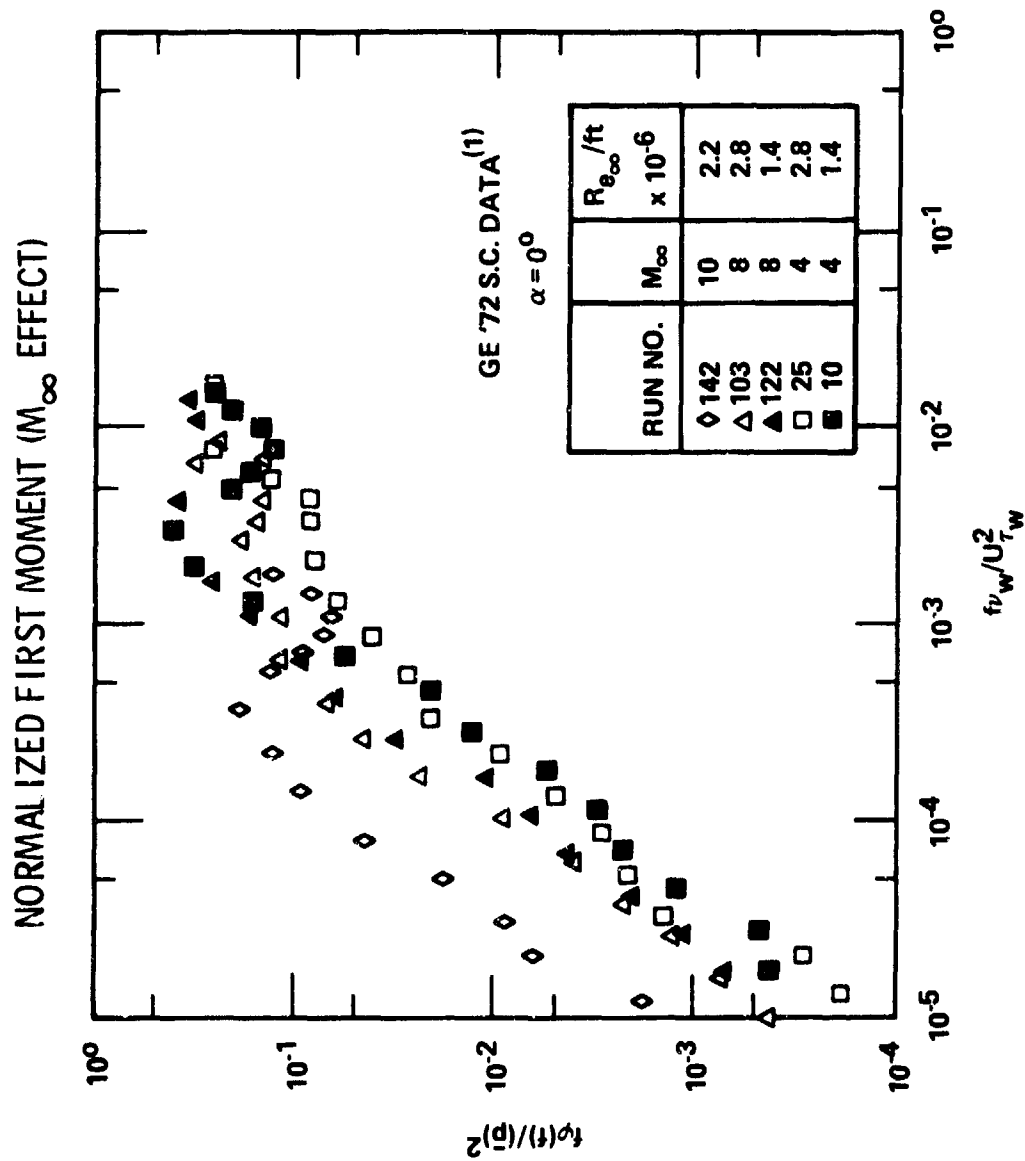
Figure 22. First Moment of Power Spectral Density with Near Field ($y < \delta_1$) Strouhal Number
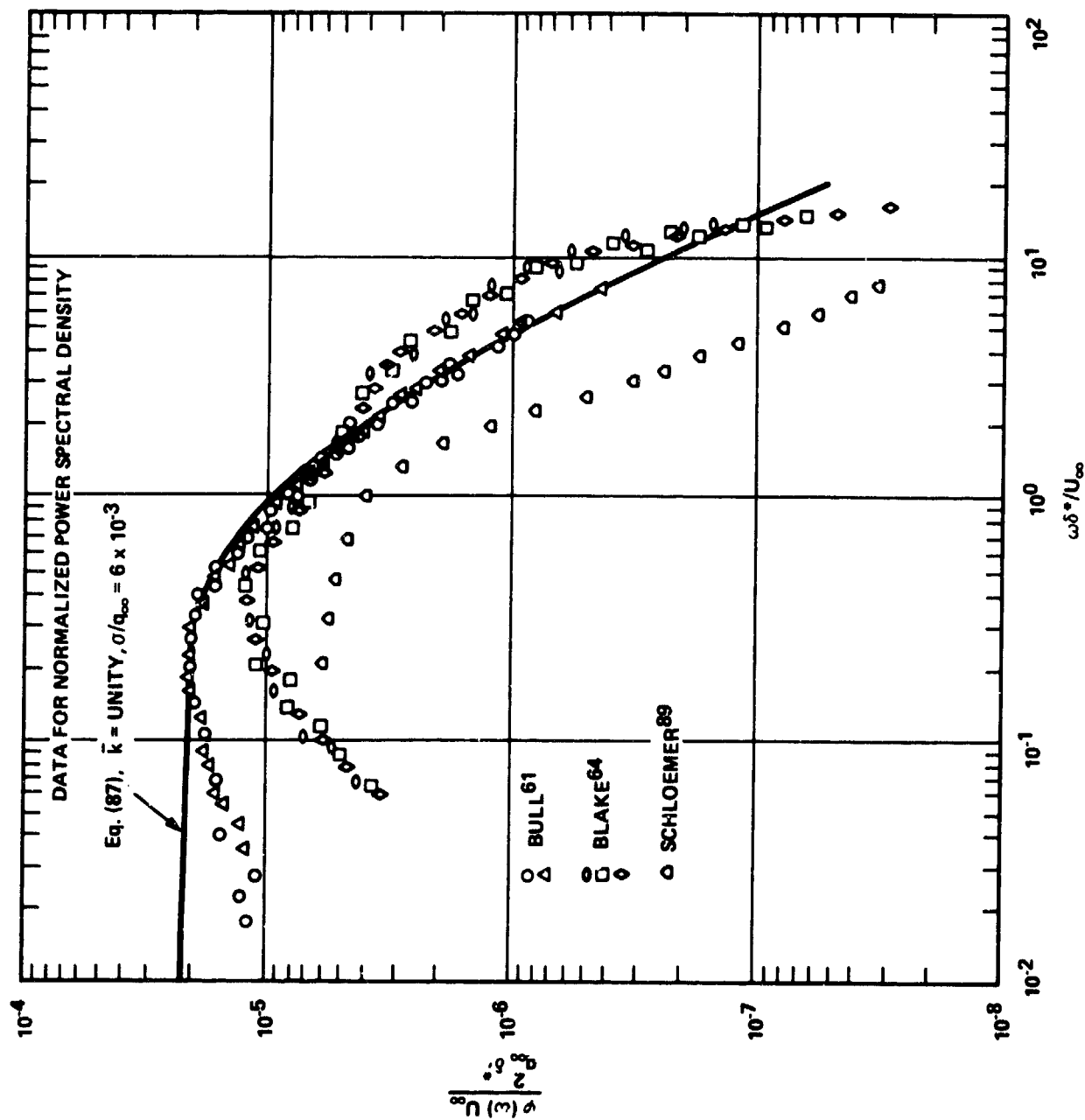
Figure 23. Comparison of Empirical Correlation with Incompressible Data for Normalized Power Spectral Density

139
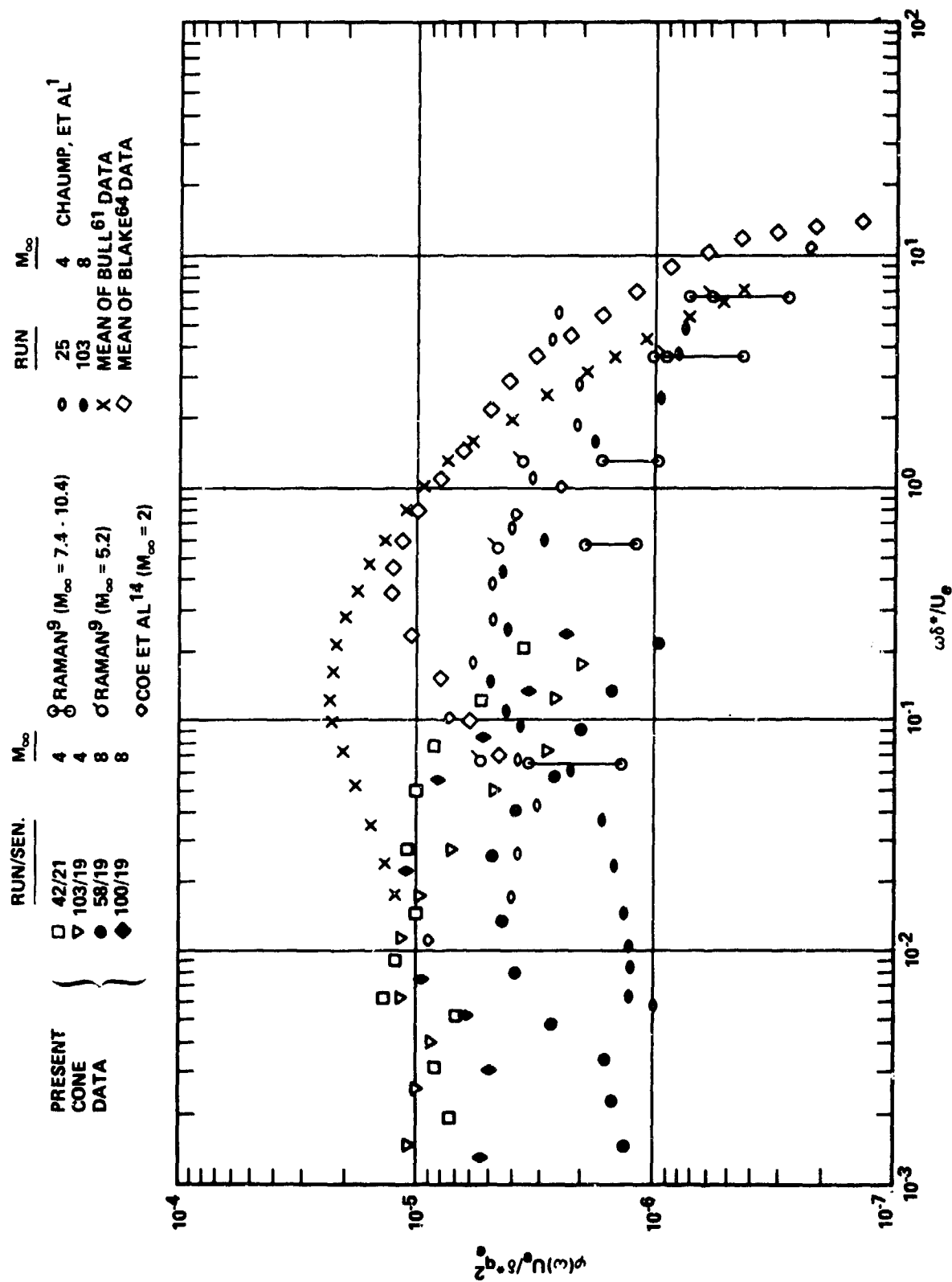
Figure 24. Comparison of Incompressible/Compressible Normalized Power Spectral Density Data

140

Figure 25. Surface Sensor Location – Identification
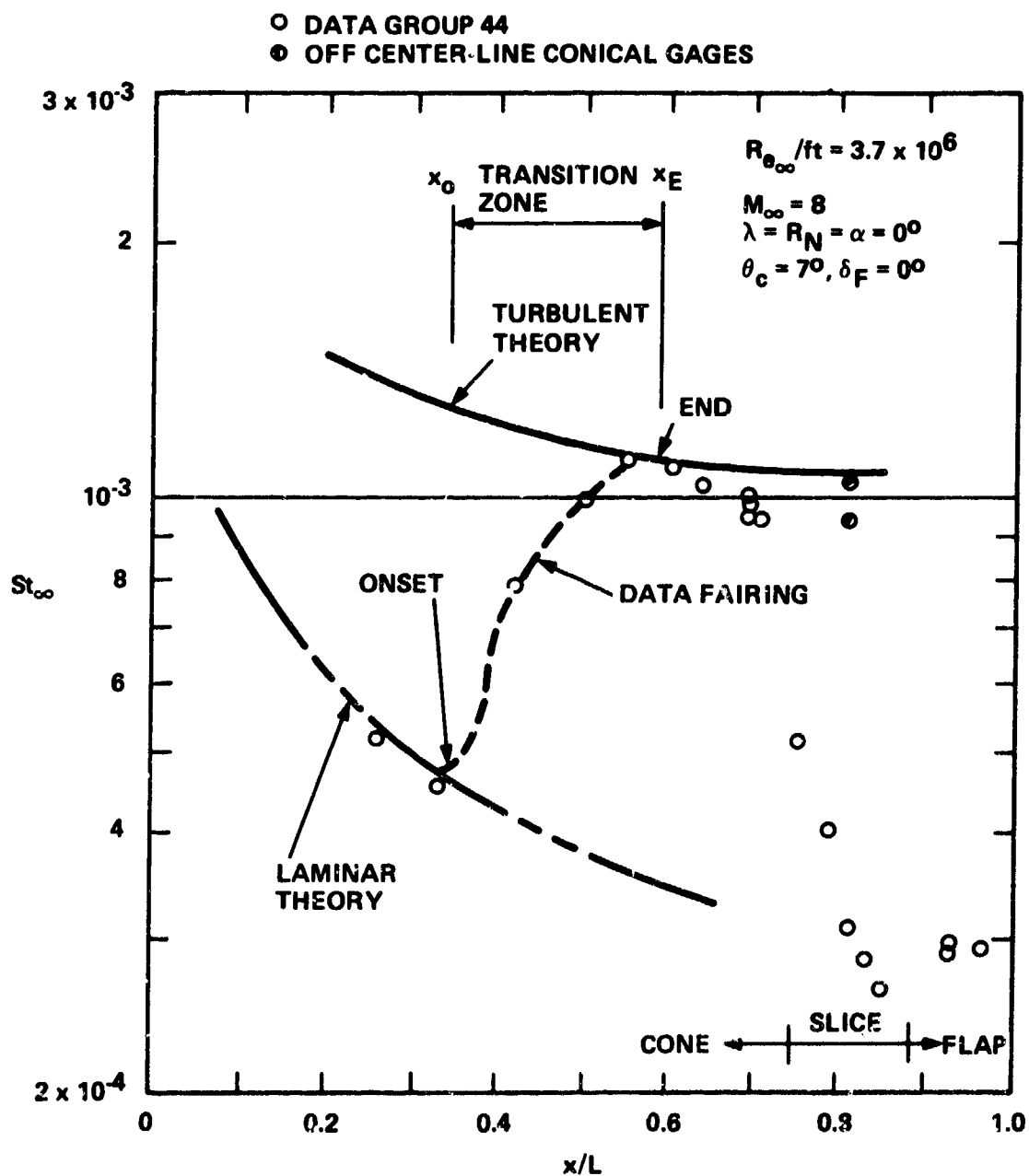
Figure 26. Typical Heat Transfer Distribution Defining Transition Zone

142
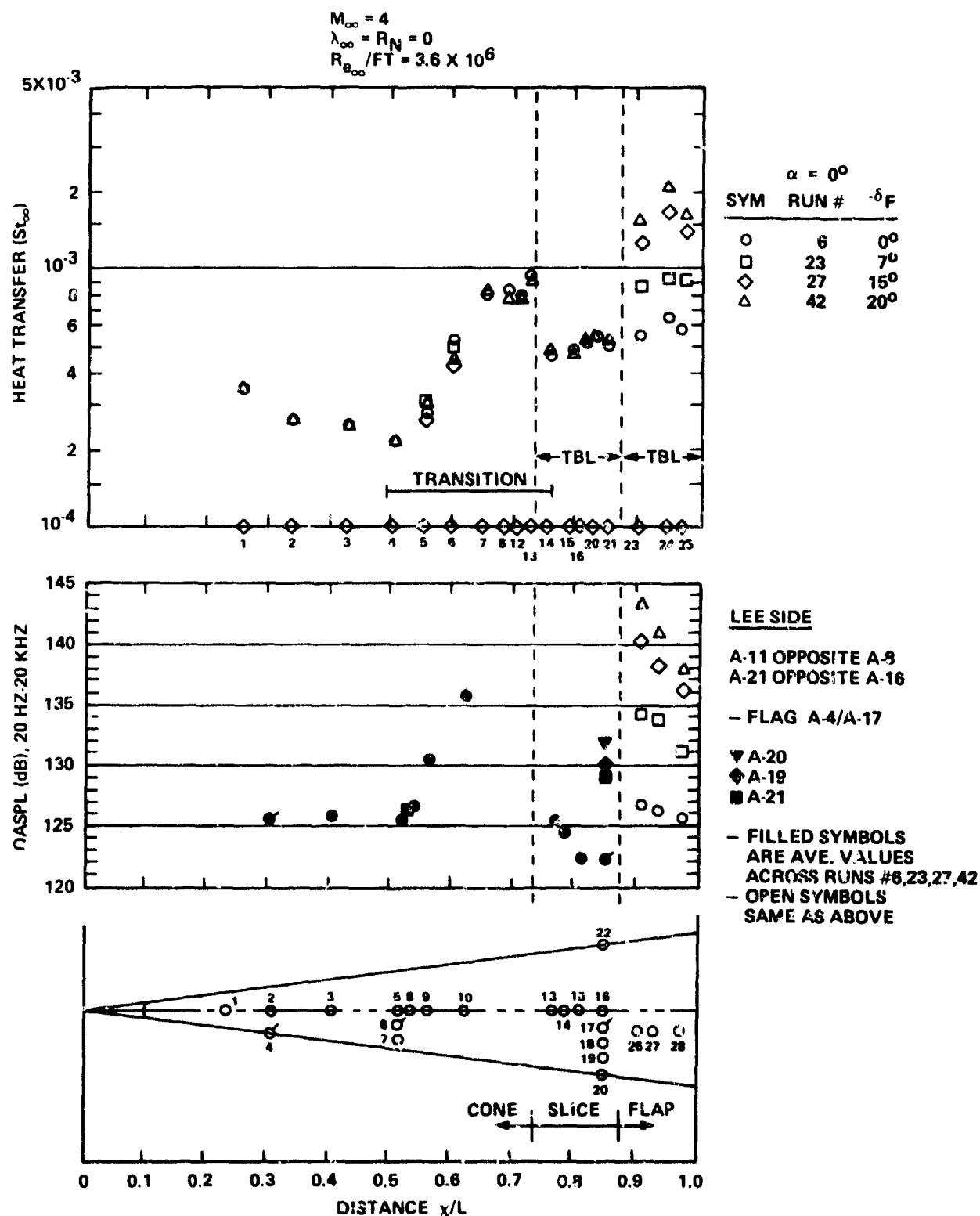
Figure 27. Acoustic and Thermal Distribution (Mach 4) – δ_F Effect at $\alpha = 0^\circ$
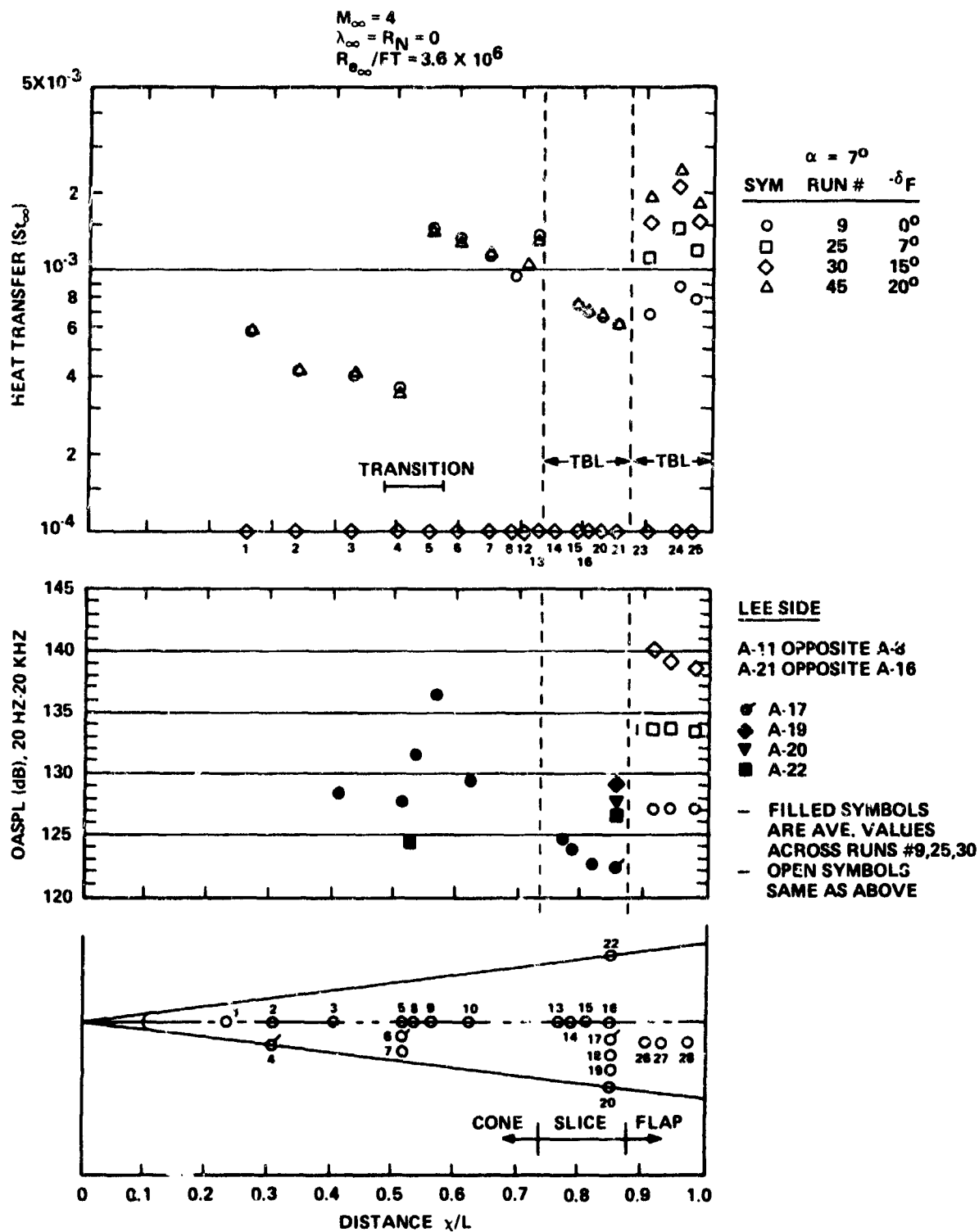
Figure 28. Acoustic and Thermal Distribution (Mach 4) - δ_F Effect at $\alpha = 7^O$

144
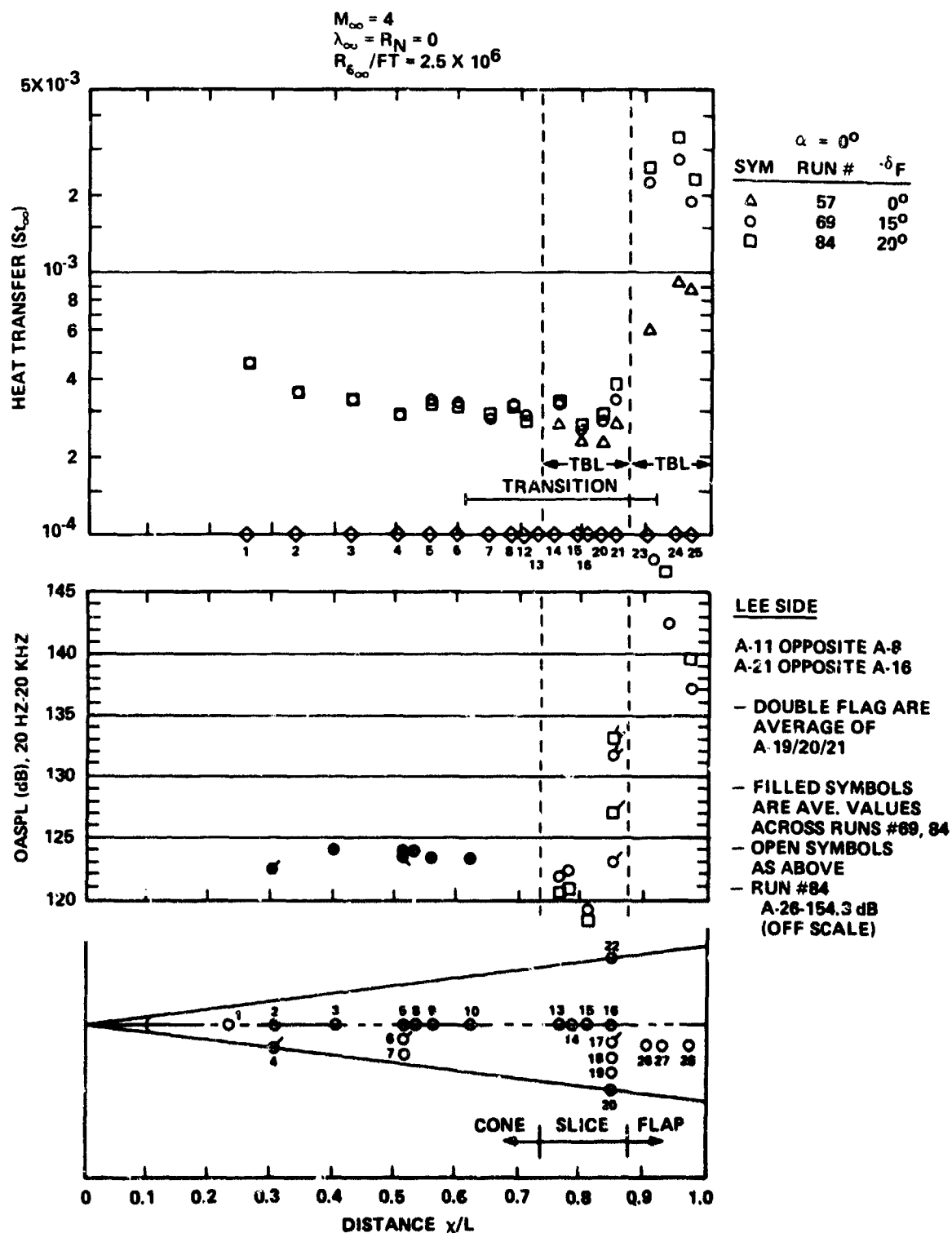
Figure 29. Acoustic and Thermal Distribution (Mach 4) – δ_F Effect at $R_{e_\infty}/ft = 2.5 \times 10^6$
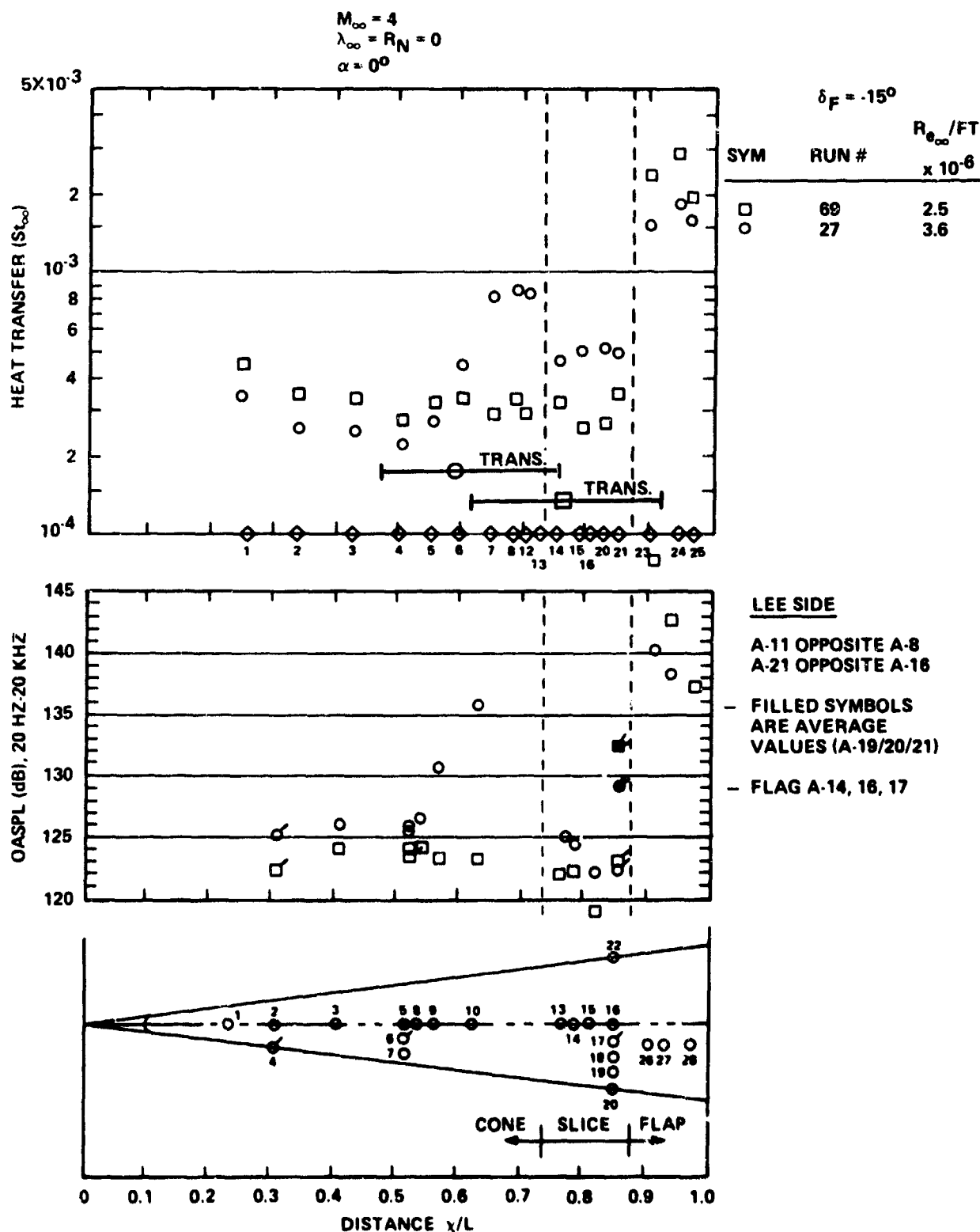
Figure 30. Acoustic and Thermal Distribution (Mach 4) – R_{θ_∞} Effect at $\gamma = 0^\circ$
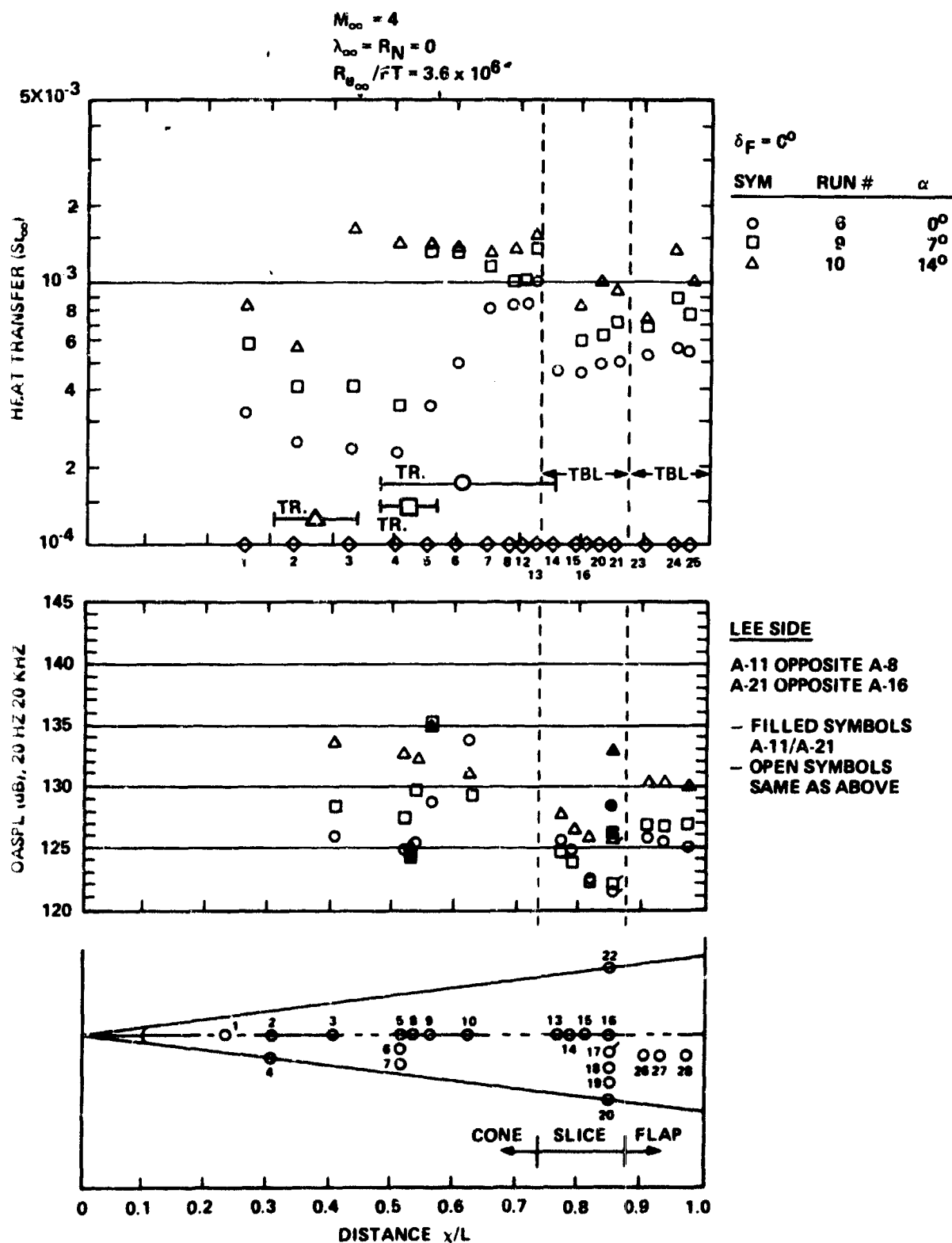
Figure 31. Acoustic and Thermal Distribution (Mach 4) – γ Effect at $\delta_F = 0$

147
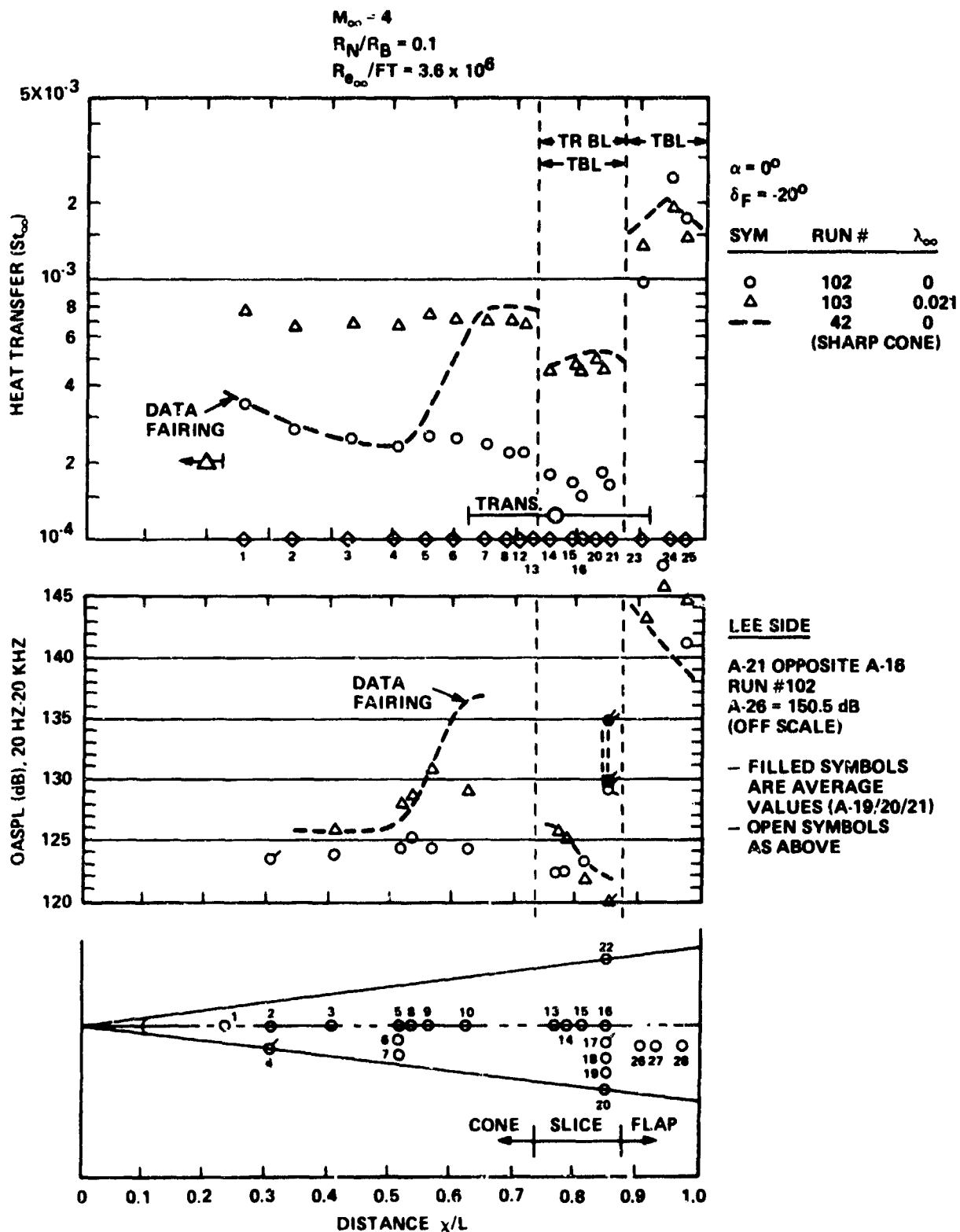
Figure 32. Acoustic and Thermal Distribution (Mach 4) – λ_∞ Effect at $\alpha = 0^O$

148
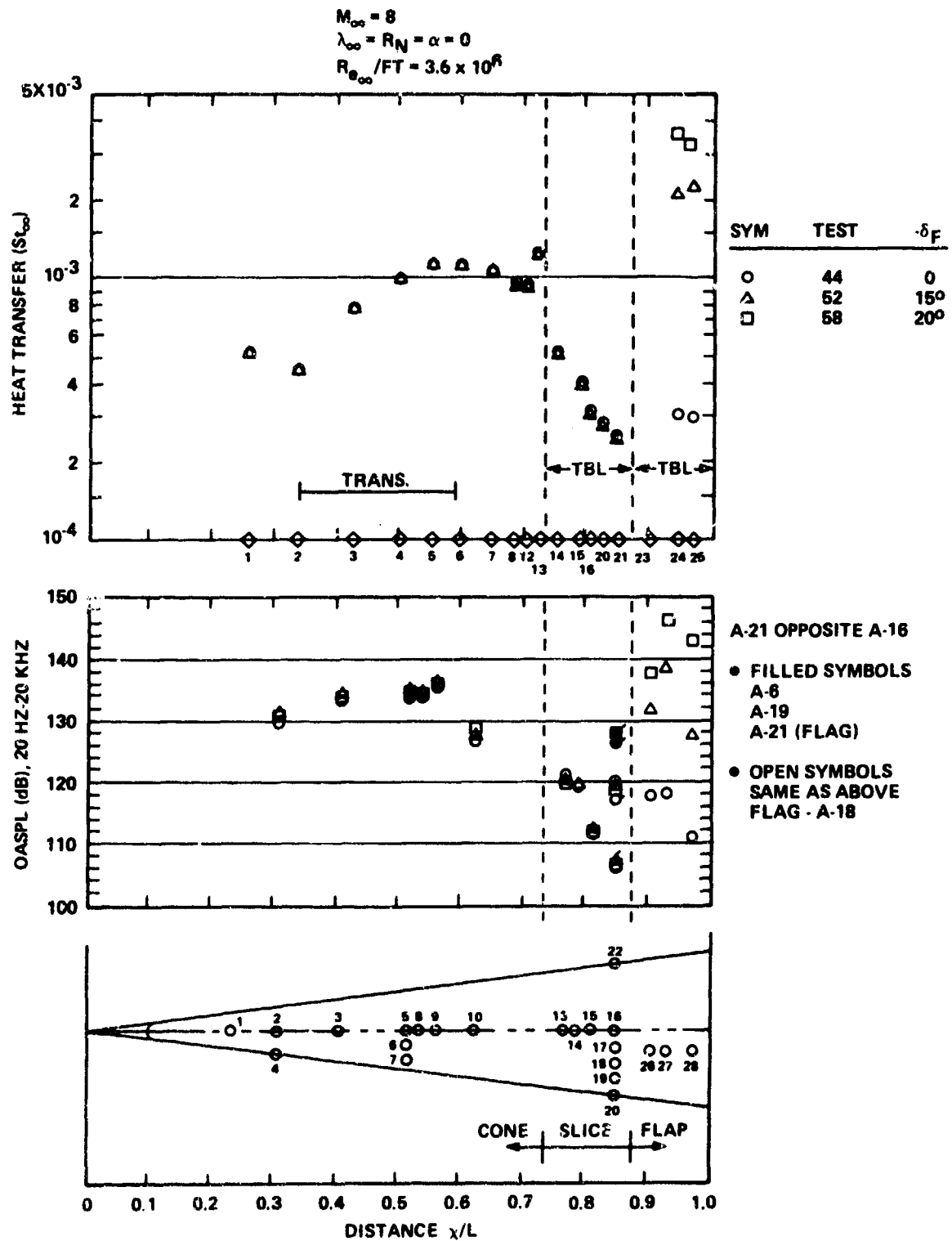
Figure 33. Acoustic and Thermal Distribution (Mach 8) – δ_F Effect at $\gamma = 0^\circ$

149
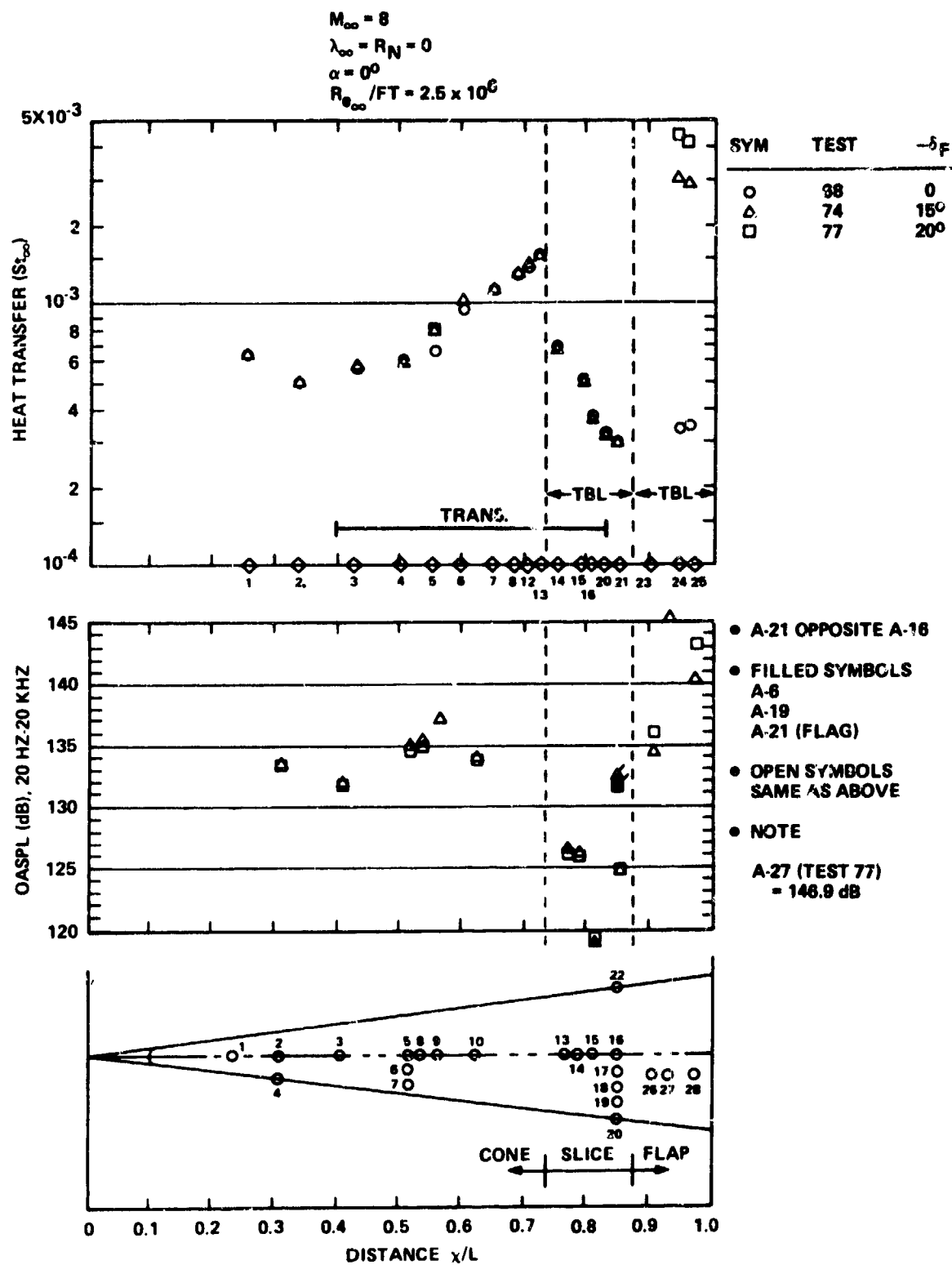
Figure 34. Acoustic and Thermal Distribution (Mach 8) – δ_F Effect at $R_{e_\infty}/ft = 2.5 \times 10^6$
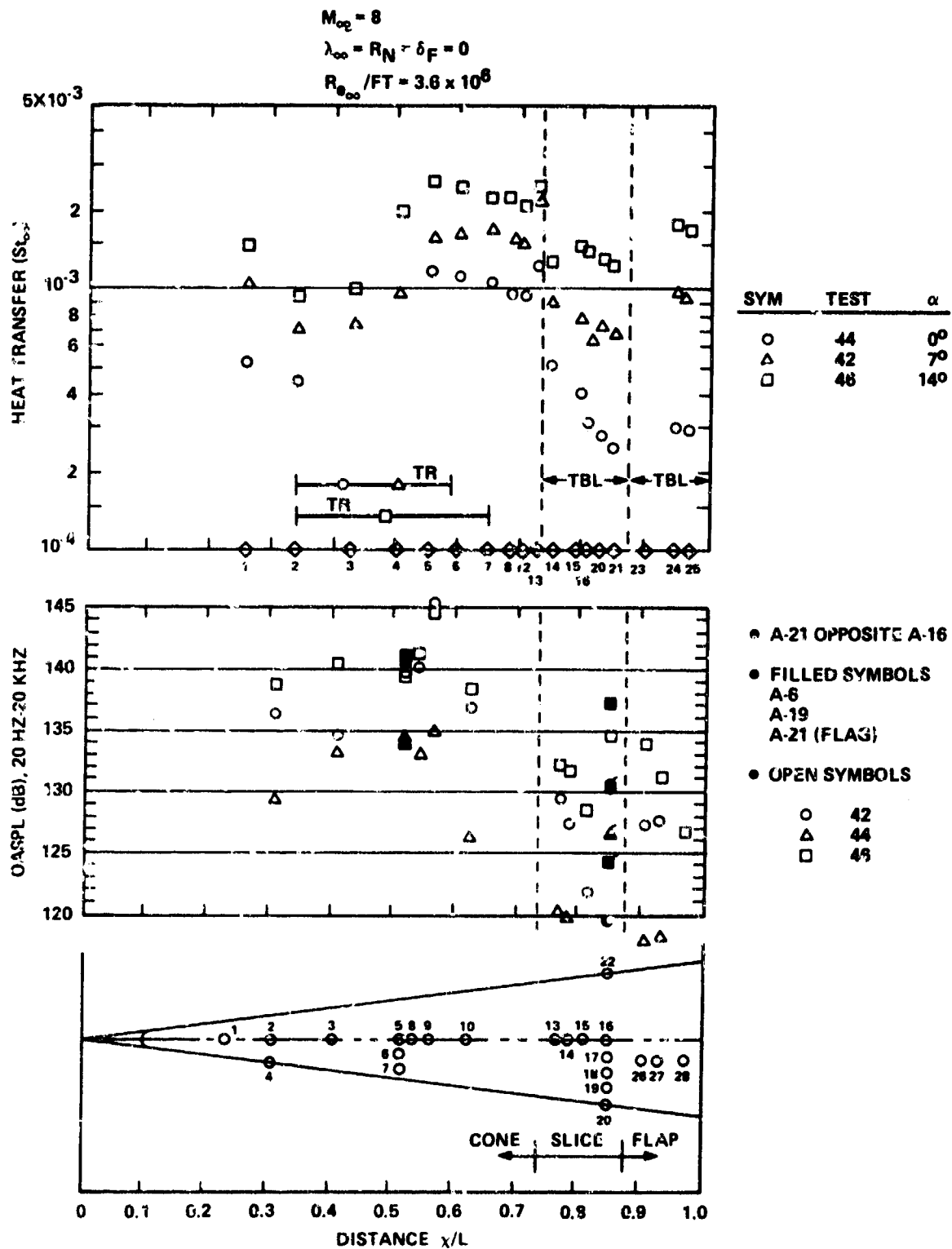
Figure 35. Acoustic and Thermal Distribution (Mach 8) - α Effect at $\delta_F = 0$

151

$M_\infty = 8$

$\alpha = 0^0$, $R_N/R_B = 0.1$

$R_{e_\infty}/FT = 3.6 \times 10^6$

HEAT TRANSFER (St_∞)

5×10^{-3}

10^{-3}

10^{-4}

← O → LAMINAR

TRANS.

SYM	TEST	$-\delta_F$	λ_∞
O	87	0^0	0
□	100	20^0	0.018
△	102	20^0	0.015

OASPL (dB), 20 HZ-20 KHZ

A-21 OPPOSITE A-16

● FILLED SYMBOLS
A-6
A-19
A-21 (FLAG)

● OPEN SYMBOLS
SAME AS ABOVE

NOTE
A-28 (TEST 87)
= 110.1 dB
A-15 (TEST 100)
= 111.6 dB
A-27 (TEST 102)
= 147.6 dB
A-28 (TEST 102)
= 144.8 dB

CONE | SLICE | FLAP

DISTANCE x/L
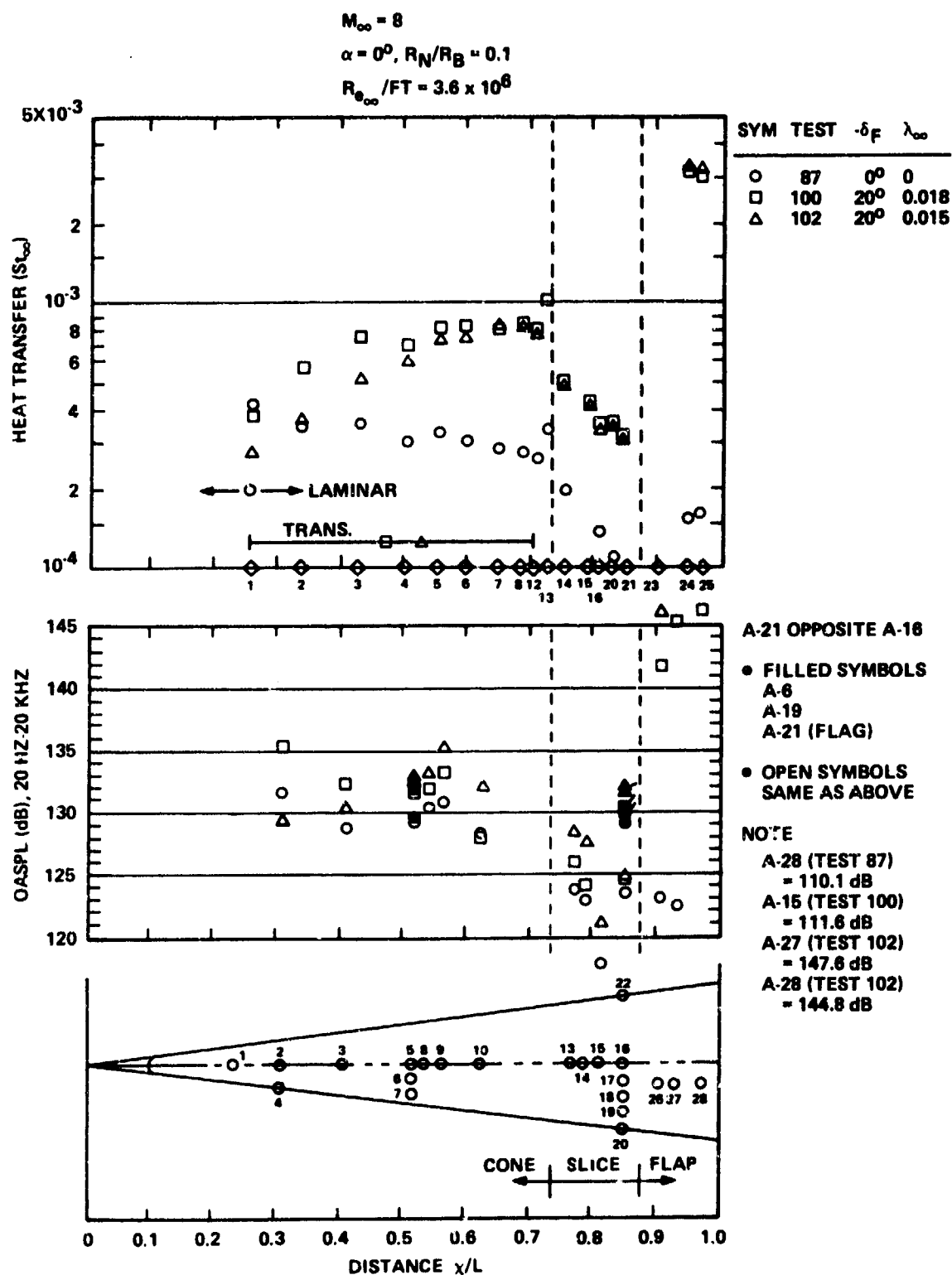
Figure 36. Acoustic and Thermal Distribution (Mach 8) – λ_∞ Effect at $\alpha = 0^0$
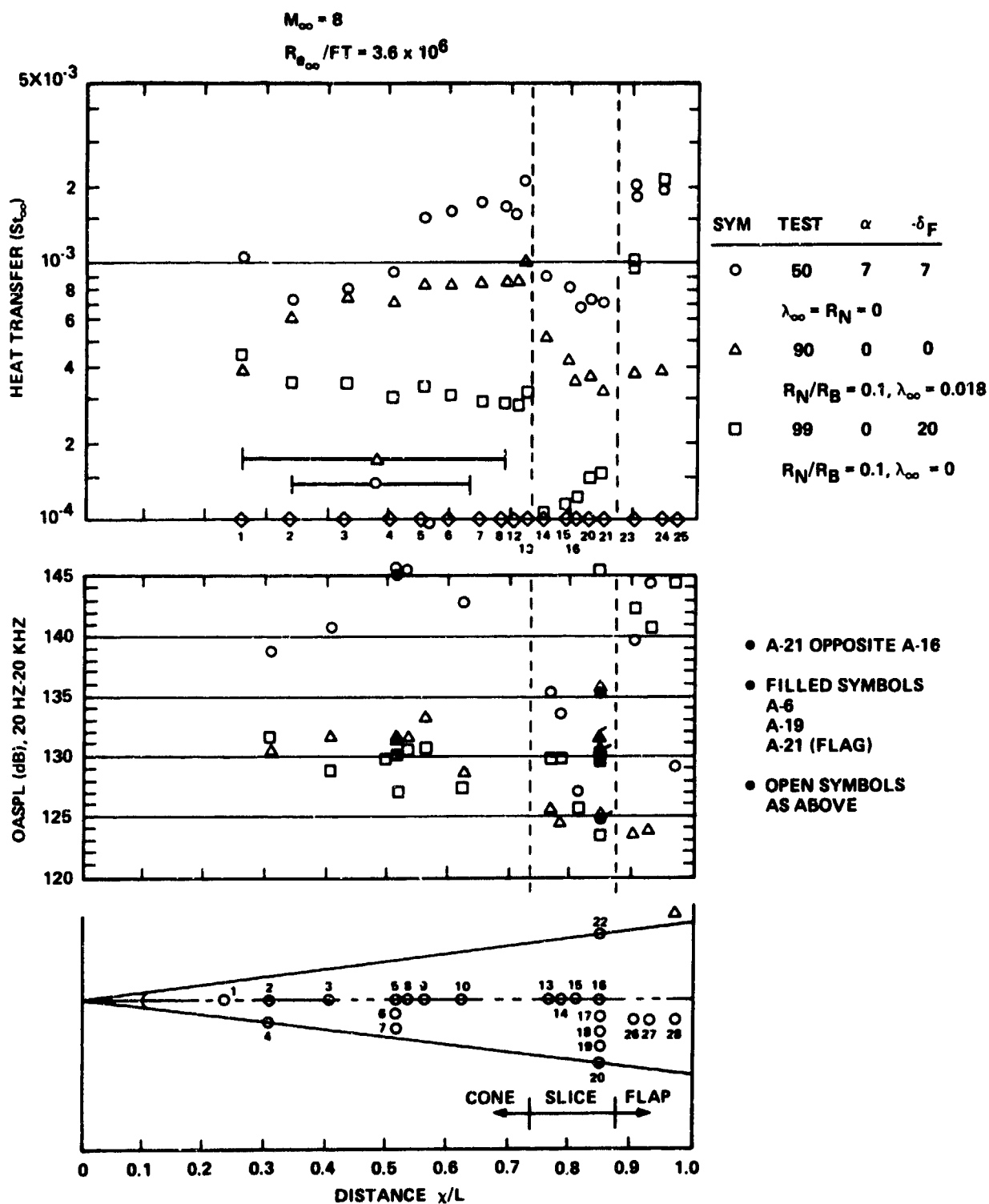
Figure 37. Acoustic and Thermal Distribution (Mach 8) for Sharp and Blunt Nosetips

153

REENTRY DATA MACH 4

Sensor	Symbol	OASPL
A-5	△	128.3
A-10*	--○--	130.2
A-19	□	128.7

*Add 1 dB to A-10

dB

Spatial Dist. (cone)

SOUND PRESSURE LEVEL - DB (RE 0.00002 PASCAL)

ONE-THIRD OCTAVE BAND CENTER FREQUENCY - HZ
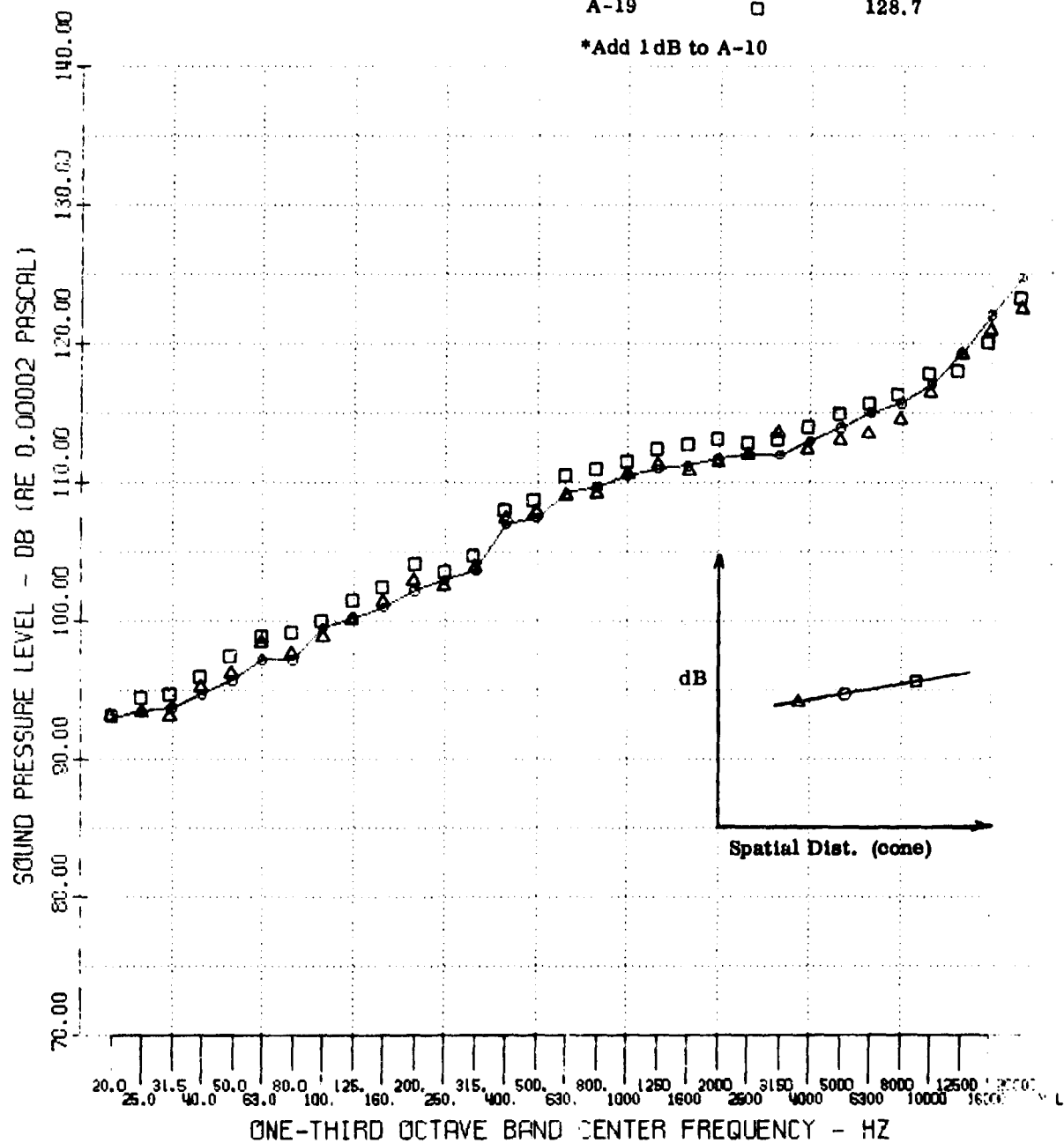
Figure 38.   Comparison of Conical Frustum Spectra in Turbulent Flow
(Blunt Nosetip with Mass Injection) - Mach 4

154
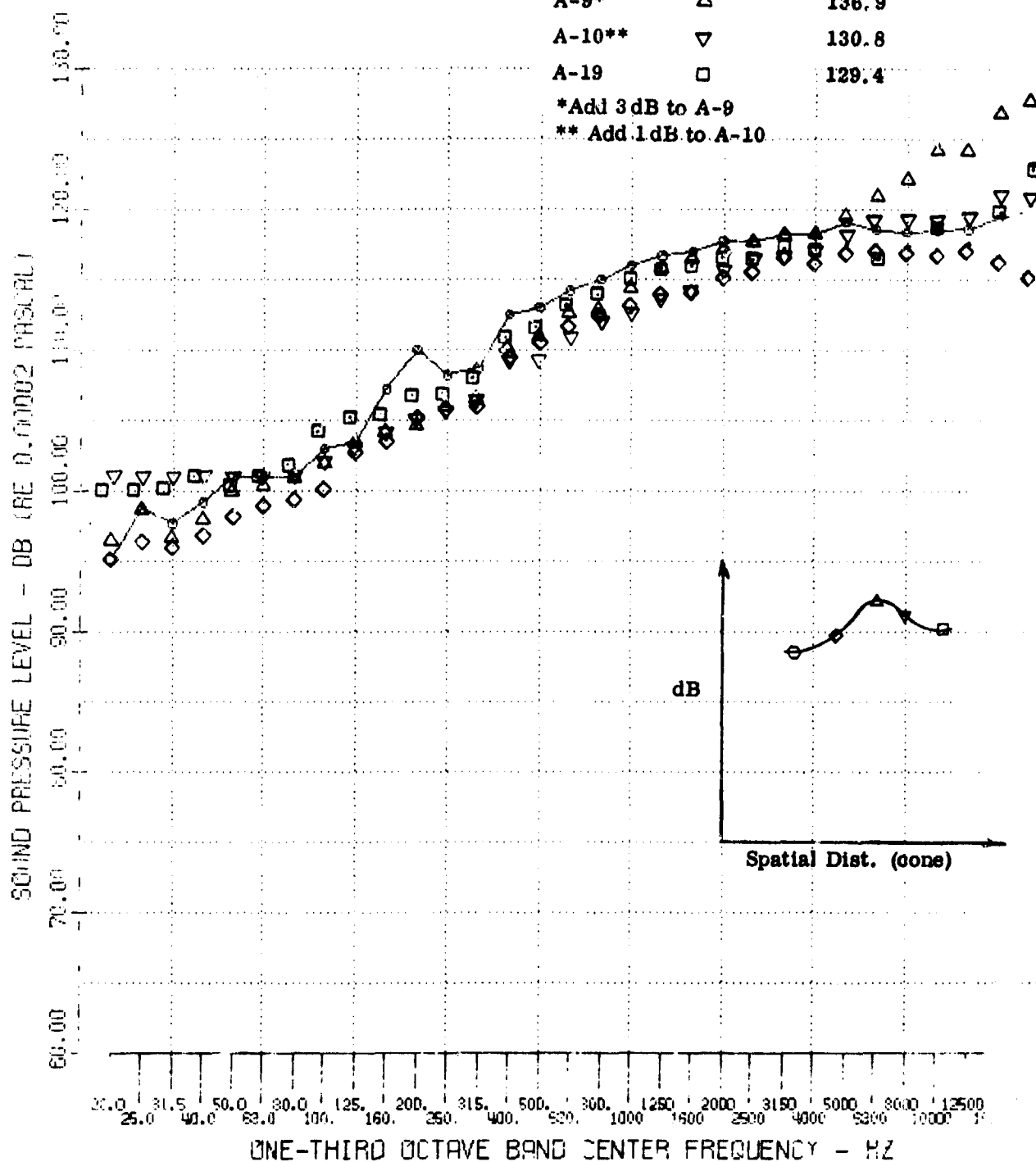
Figure 39   Development of Transitional Spectra Over the Sharp Cone Model – Mach 4
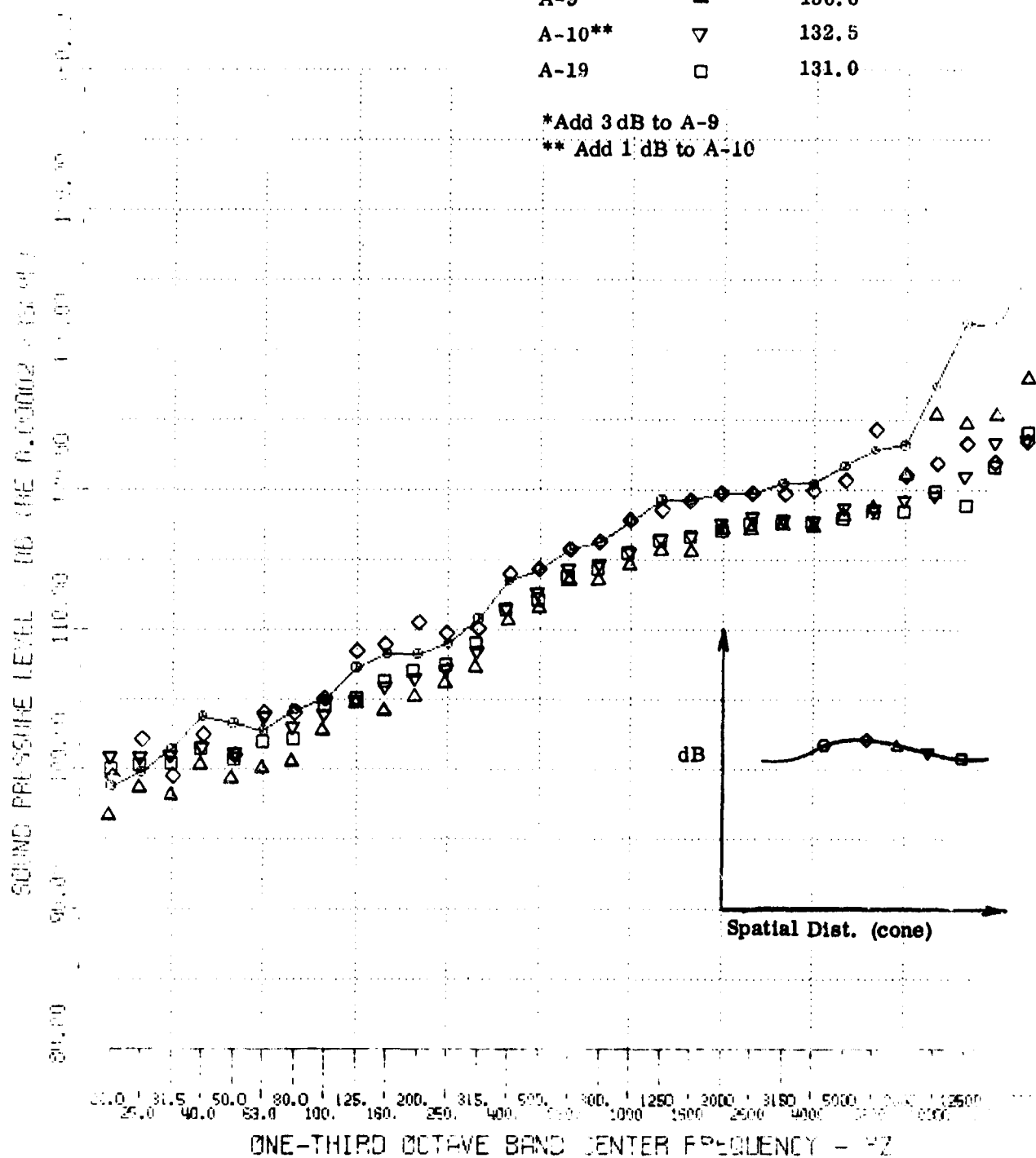
Figure 40   Decay of Transitional Spectra at 14° Angle of Attack - Mach 4

156

Figure 41   Comparison of Conical Frustum Spectra in Laminar Flow for Various
            Conditions – Mach 4

157

Figure 42   Comparison of Slice Spectra in Turbulent Flow for Various Values
of Flap Deflection - Mach 4

158

ENTRY DATA MACH 4

Sensor	Symbol	OASPL
A-13	--o--	125.5
A-14	◇	124.5
A-15	△	122.9
A-17	▽	122.3
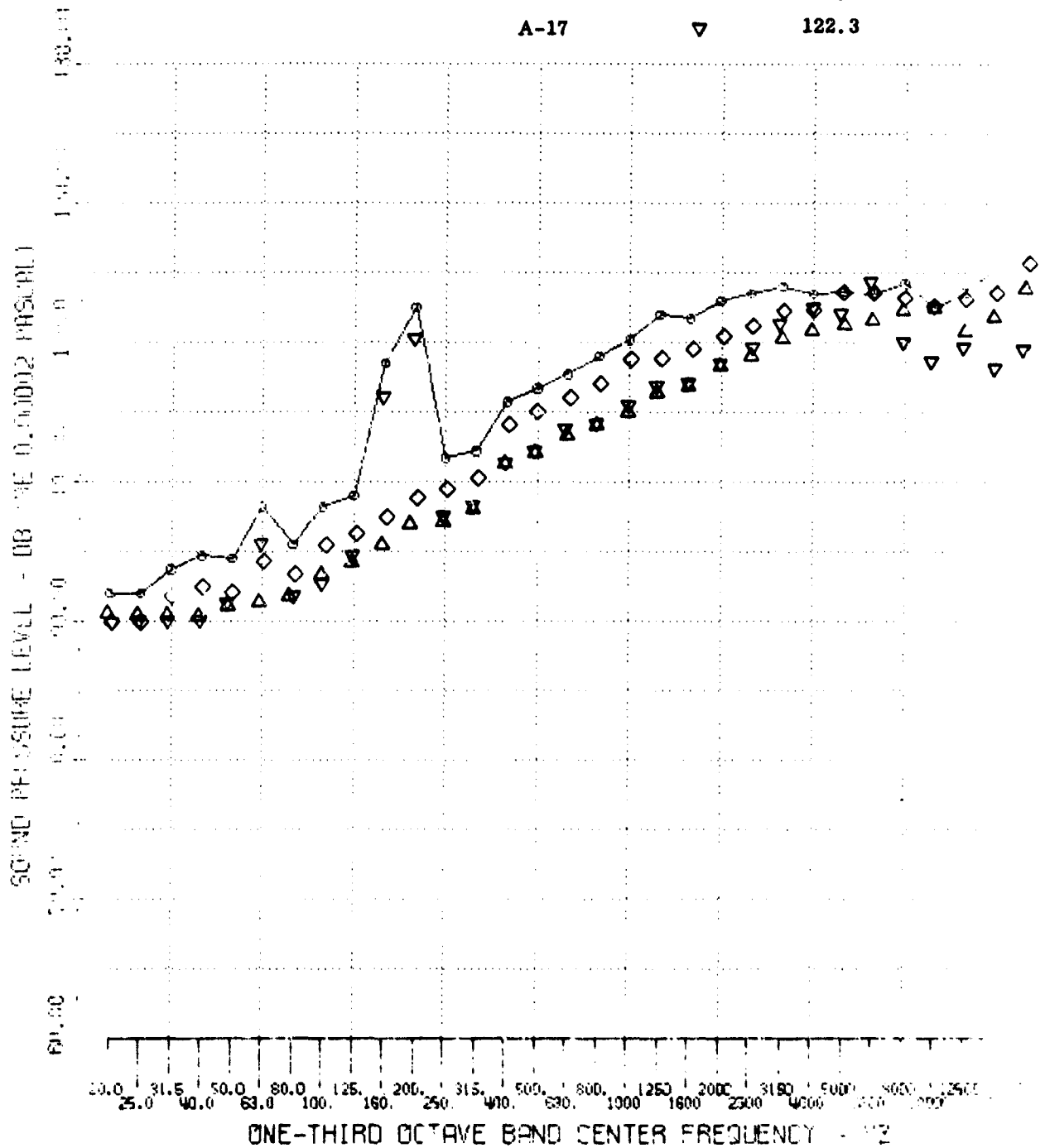
Figure 43   Comparison of Turbulent Spectra at Different Slice Locations (Sharp Cone) - Mach 4
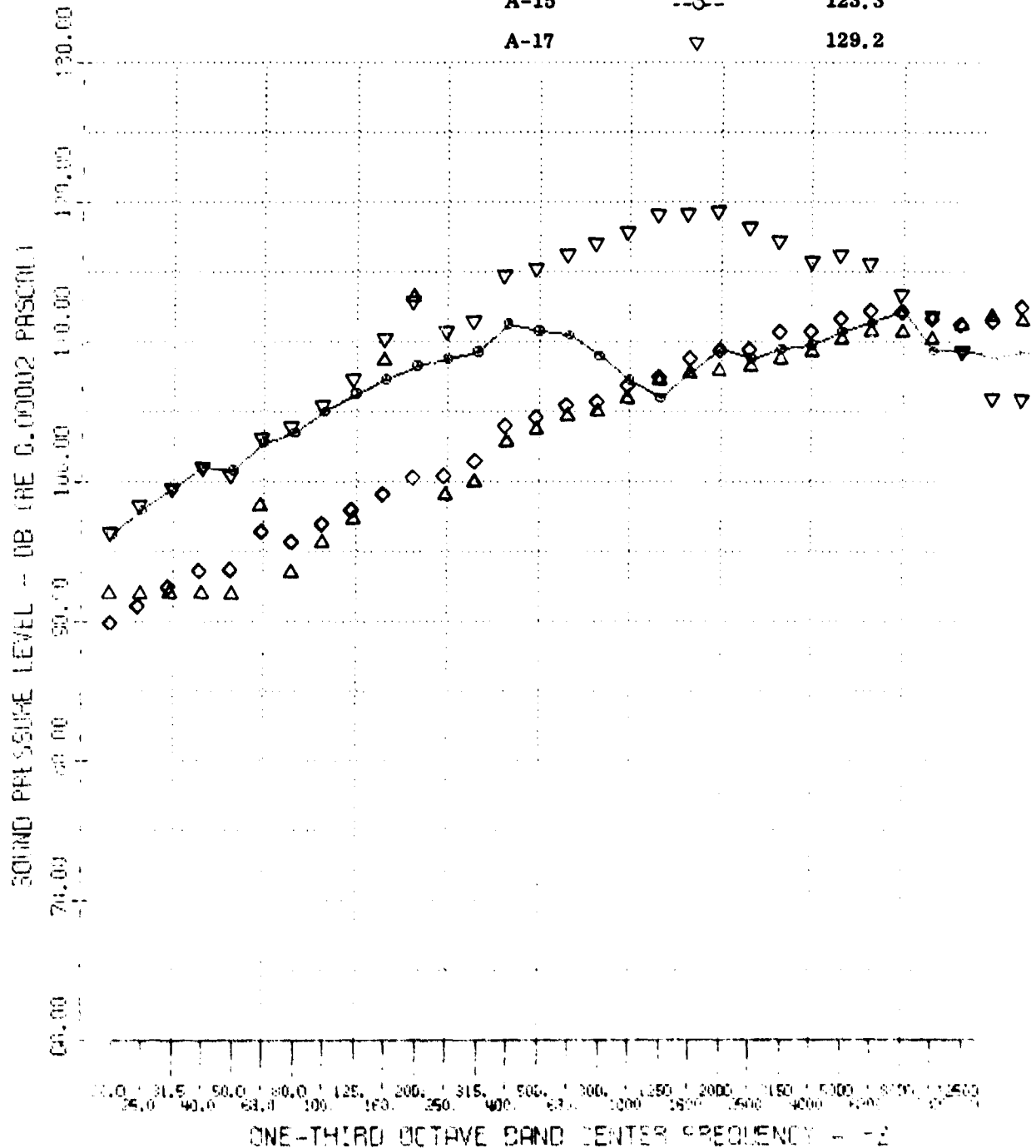
Figure 44   Comparison of Slice Spectra Measured in Transitional Flow (Blunt Nosetip) - Mach 4

160

ANGLE 00   RE∞ 3.6*10**6

Sensor A-27
REENTRY DATA MACH 4
$R_N/R_B = 0$

Test No.	Sym.	$-\delta_F$ (Deg.)	OASPL
6	▽	0	126.2
23	△	7	133.7
27	◇	15	138.1
42	--O--	20	140.5

ONE-THIRD OCTAVE BAND CENTER FREQUENCY – HZ
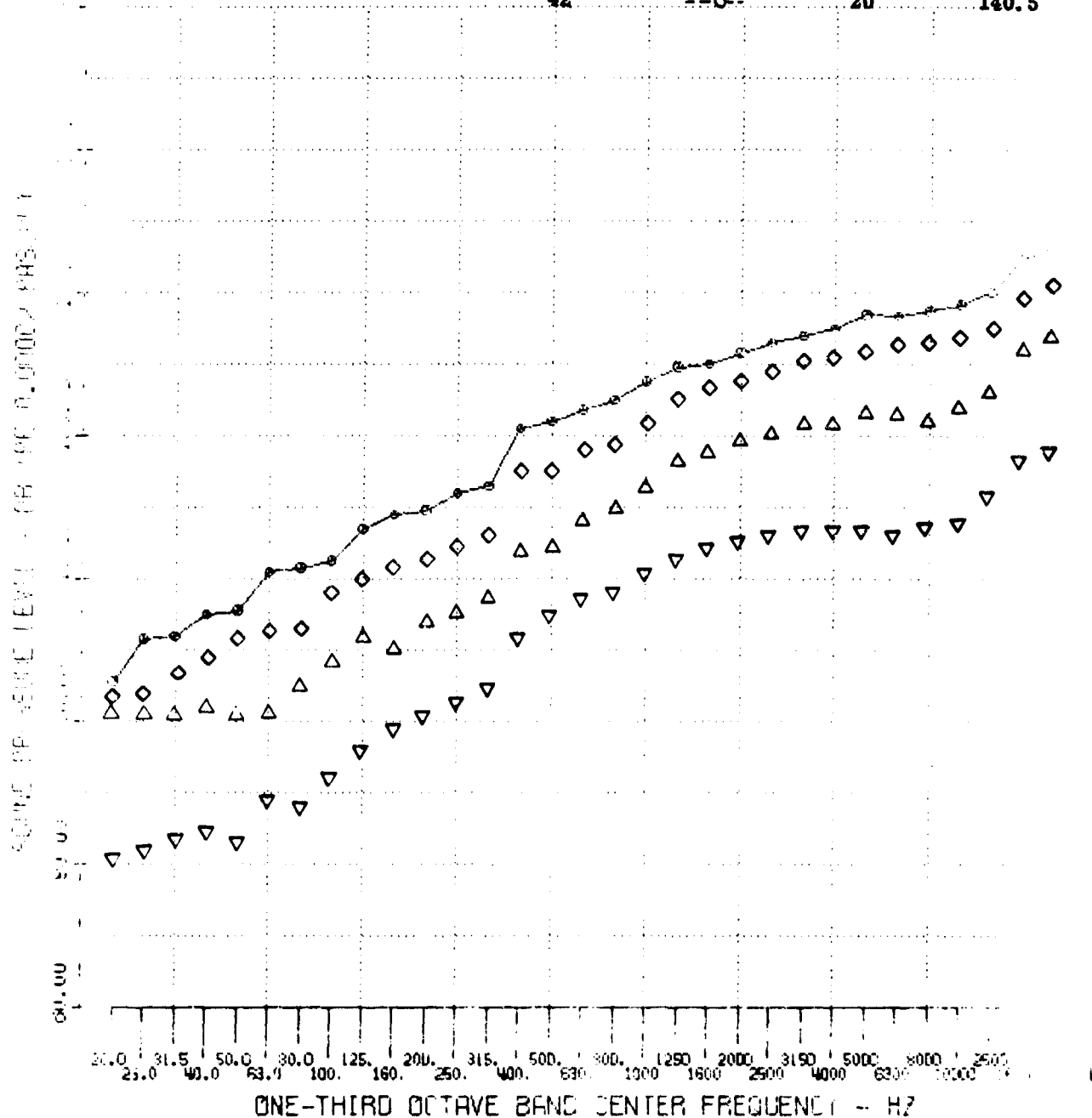
Figure 45   Comparison of Flap Spectra in Turbulent Flow at Various Values of
Flap Deflection - Mach 4

161

RE ENTRY DATA MACH 4

Sensor	Symbol	OASPL
A-26	--o--	143.2
A-27	o	140.5
A-28	△	137.6

ONE-THIRD OCTAVE BAND CENTER FREQUENCY - HZ
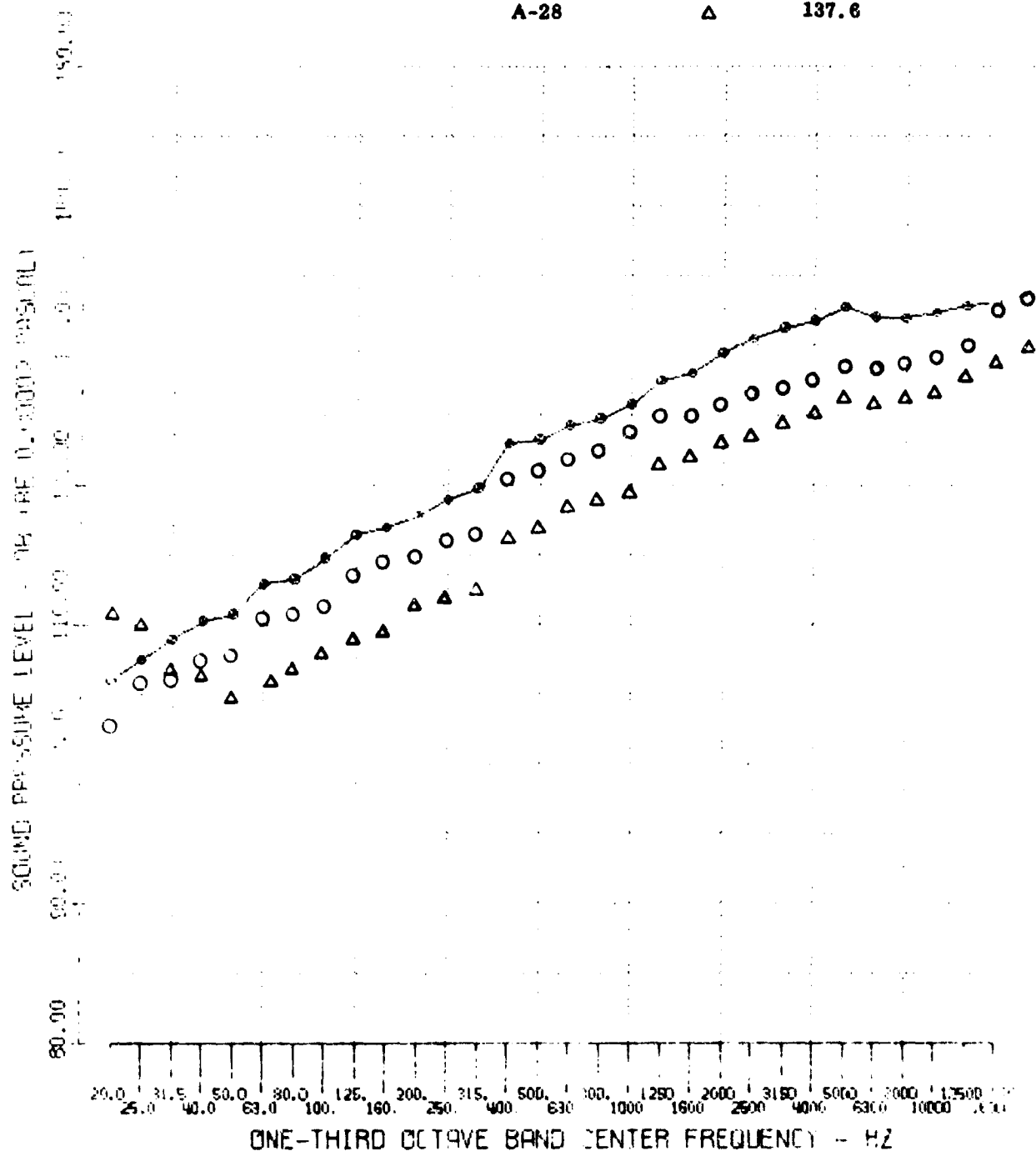
Figure 46   Comparison of Flap Spectra in Fully Turbulent Flow For Sensors
A-26, -27, and -28 - Mach 4

Figure 47   Comparison of Conical Frustum Spectra in Laminar Flow for Various Conditions - Mach 8
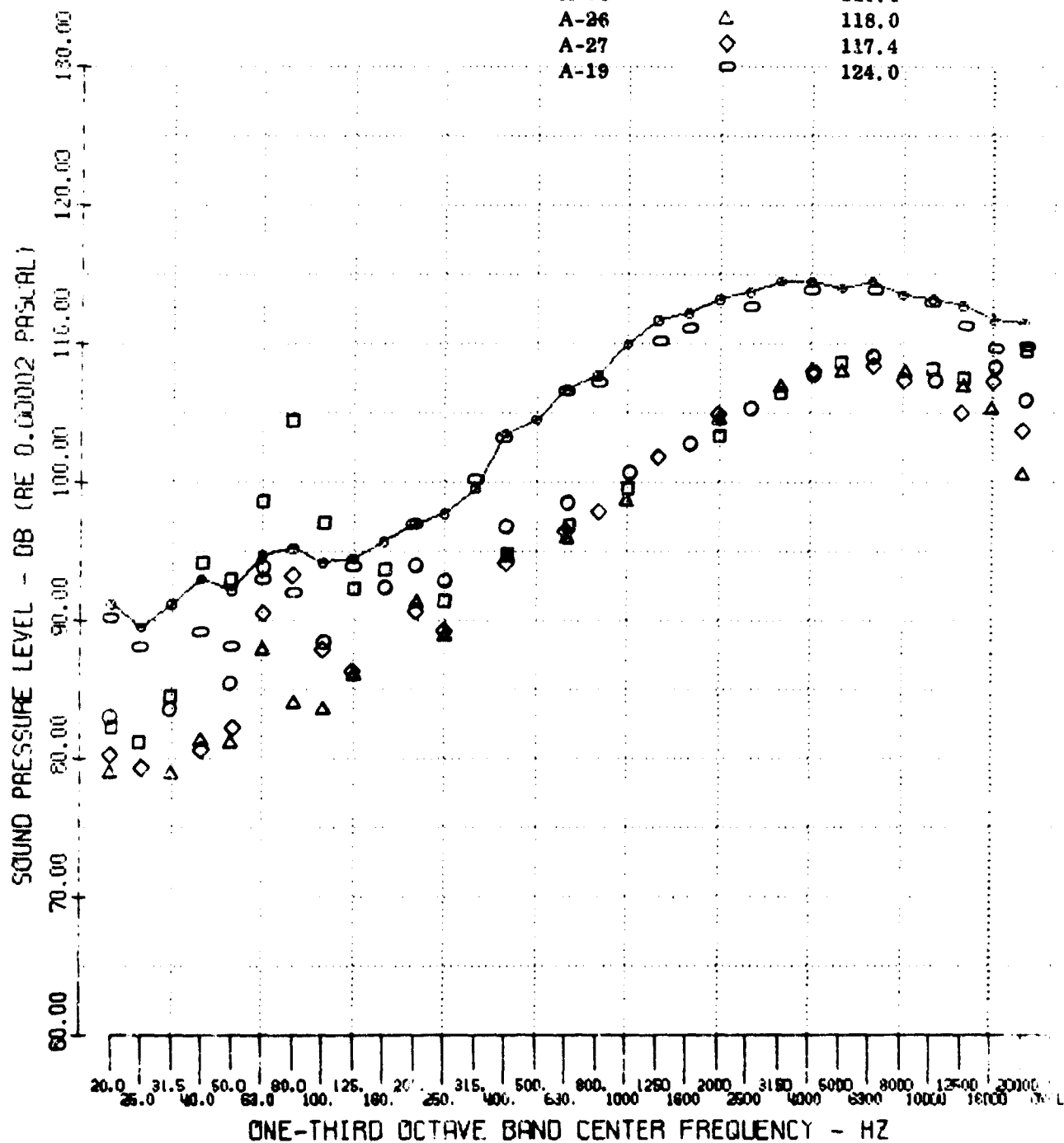
Figure 48   Comparison of Laminar Boundary Layer Spectra Along
Model Surface - Blunt Body - Mach 8

164
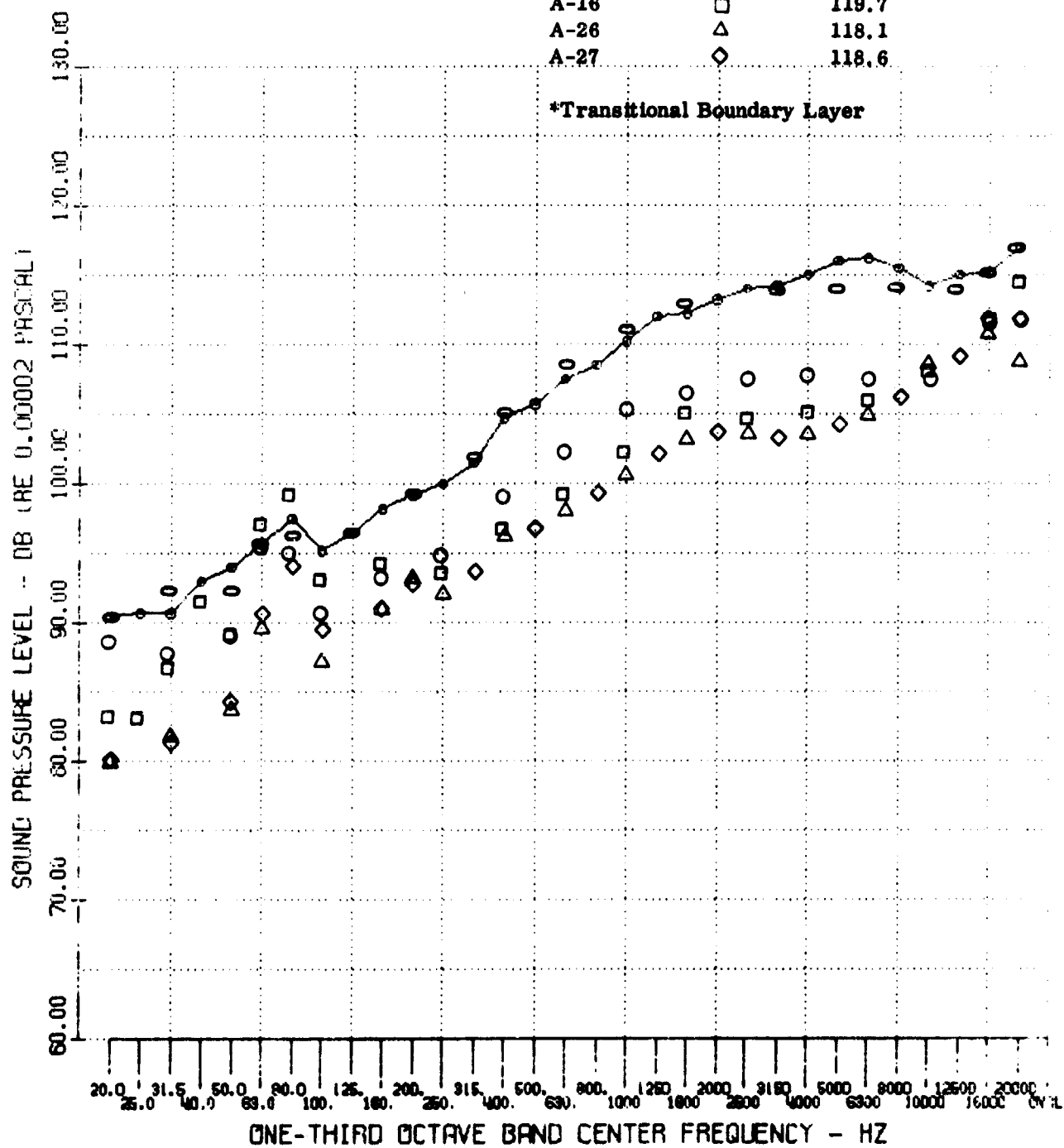
Figure 49   Comparison of Turbulent Boundary Layer Spectra Along
Model Surface - Blunt Body - Mach 8

REENTRY DATA MACH 8

Sensor	Symbol	OASPL
A-6*	- - o - -	134.0
A-19	⊘	126.6
A-13	○	120.3
A-16	□	119.9
A-26	△	117.5
A-27	◇	118

*Transitional Boundary Layer
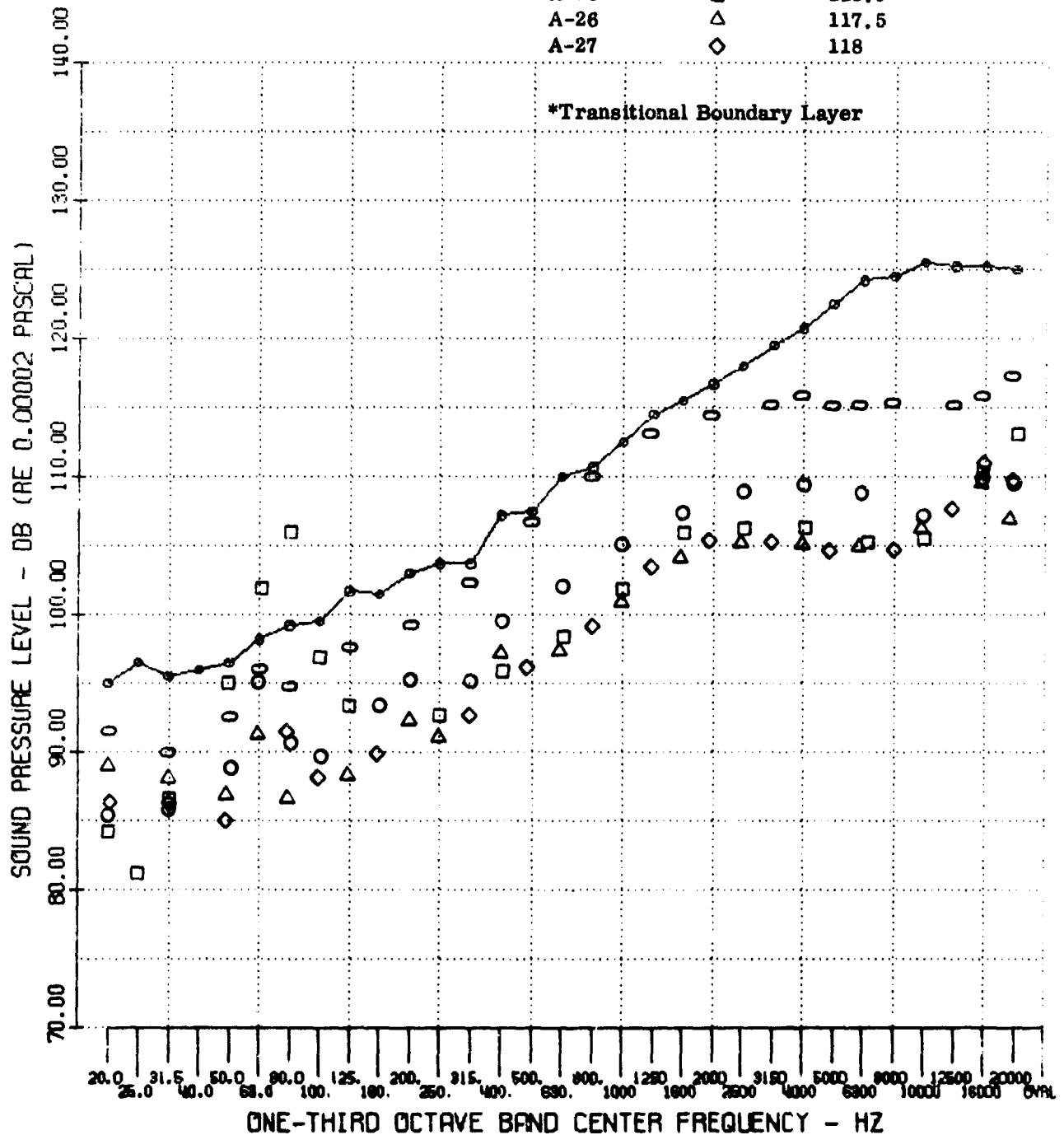
Figure 50   Comparison of Turbulent Boundary Layer Spectra Along Model
Surface - Sharp Body - Mach 8

186

Figure 51   Development of Transitional Spectra Over the Sharp Cone Model – Mach 8

167

REENTRY DATA MACH 8

Sensor	Symbol	OASPL
A-19	△	130.2
A-21	--o--	120.5
A-22	□	126.6

α = 7°

SOUND PRESSURE LEVEL - DB (RE 0.00002 PASCAL)

ONE-THIRD OCTAVE BAND CENTER FREQUENCY - HZ
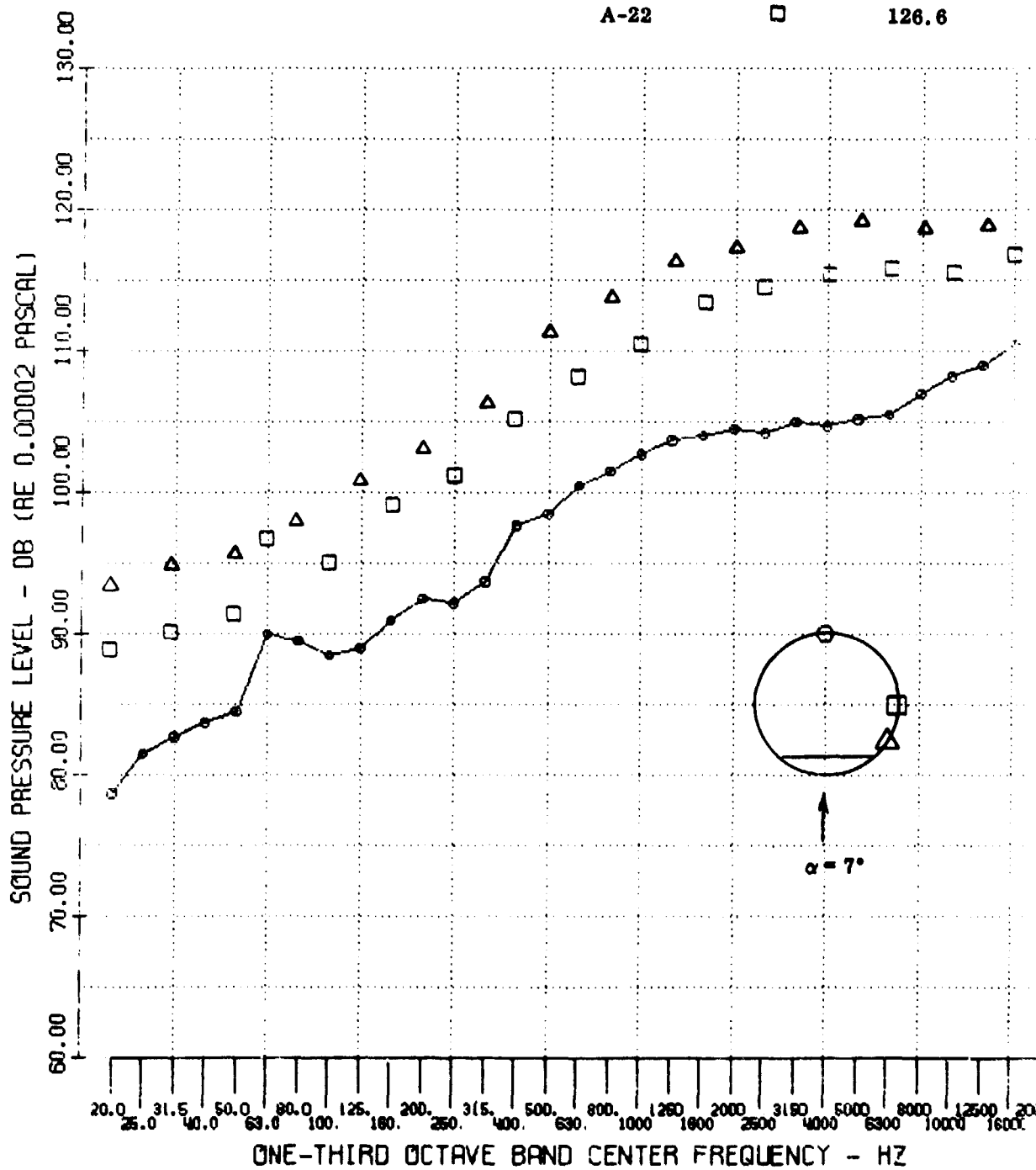
Figure 52   Comparison of Turbulent Circumferential Spectra at Angle of Attack - Mach 8

TEST 058   MDGT 00000   ALPHA 000   RE∞3.7*10**G   DELF -20   RN/RB 000

REENTRY DATA MACH 8

Sensor	Symbol	OASPL
A-13	--o--	120.5
A-14	◇	119.2
A-15	◆	111.7
A-16	□	118.9
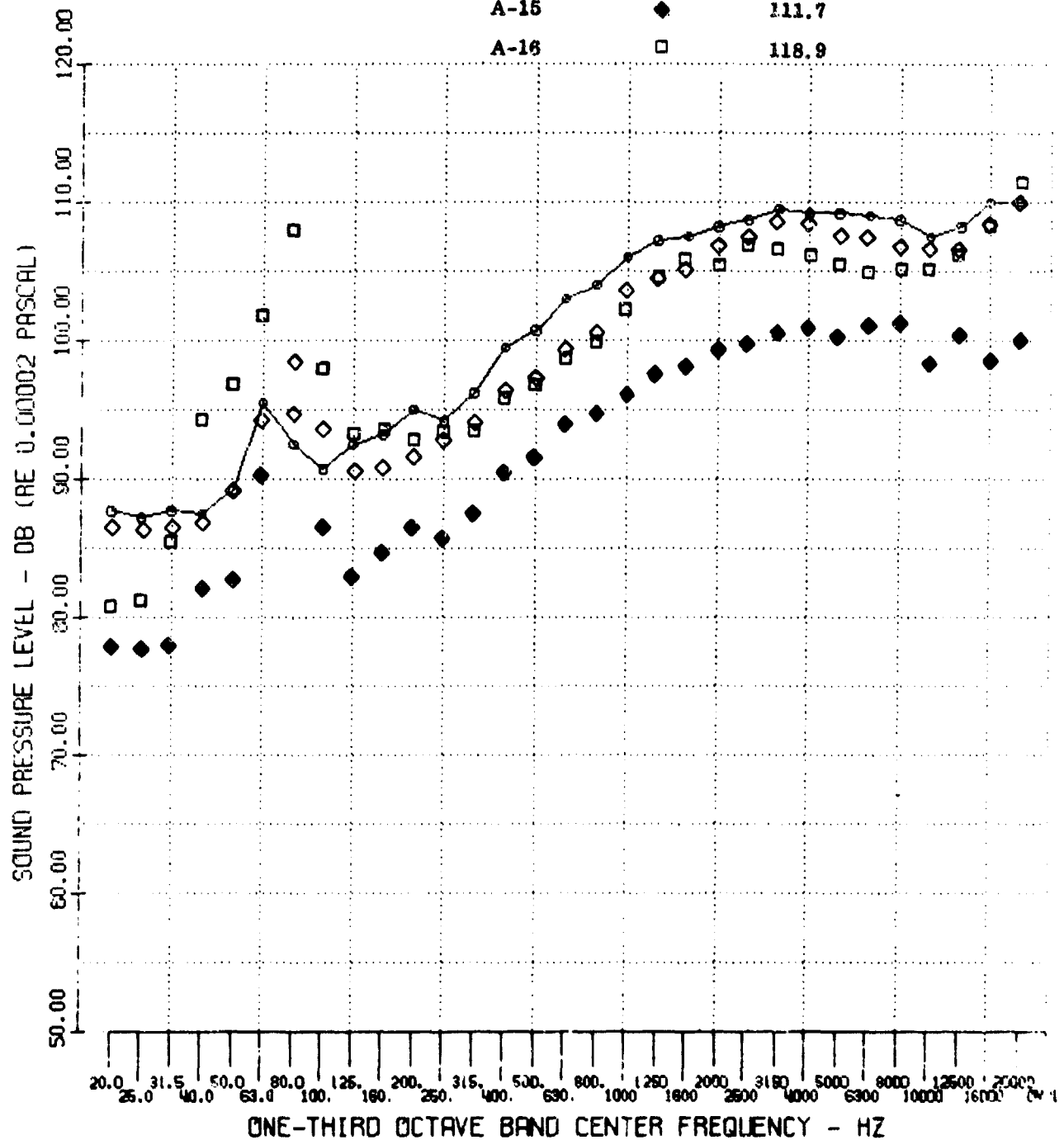
Figure 53   Comparison of Turbulent Spectra at Different Slice Locations (Sharp Cone) -
Mach 8

189

ALPHA 000 RE∞3.7*10**6

Sensors A-15 and A-16
REENTRY DATA MACH 8
Flag - A-15
$R_N/R_B = 0$

Test No.	Sym.	$-\delta_F$(Deg.)	OASPL A-15	A-16
44	--O--	0	111.2	119.9
52	△	15	111.8	118.9
58	□	20	111.7	118.9
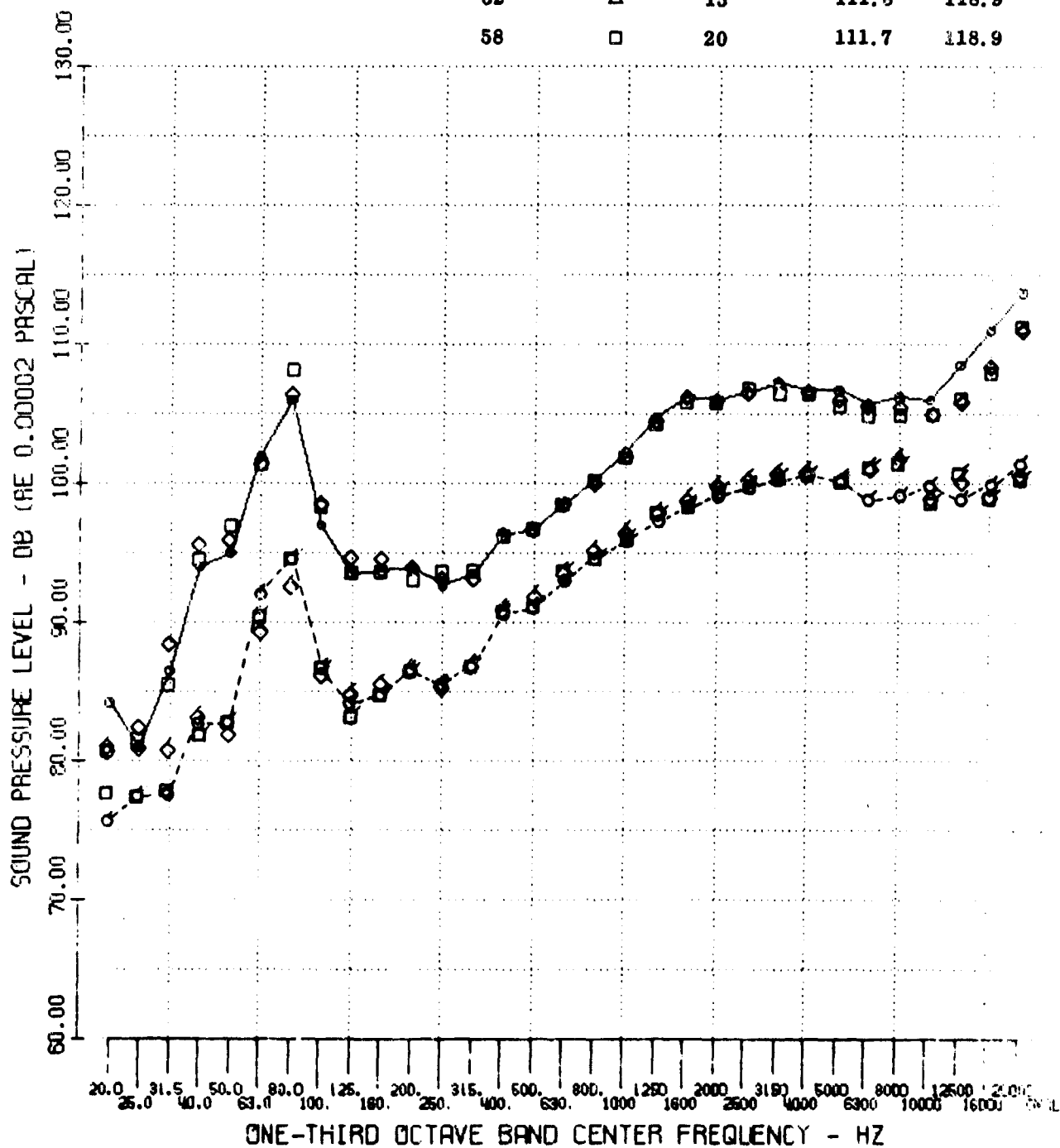
Figure 54 Comparison of Slice Spectra in Turbulent Flow for Various Values of Flap Deflection - Mach 8

170
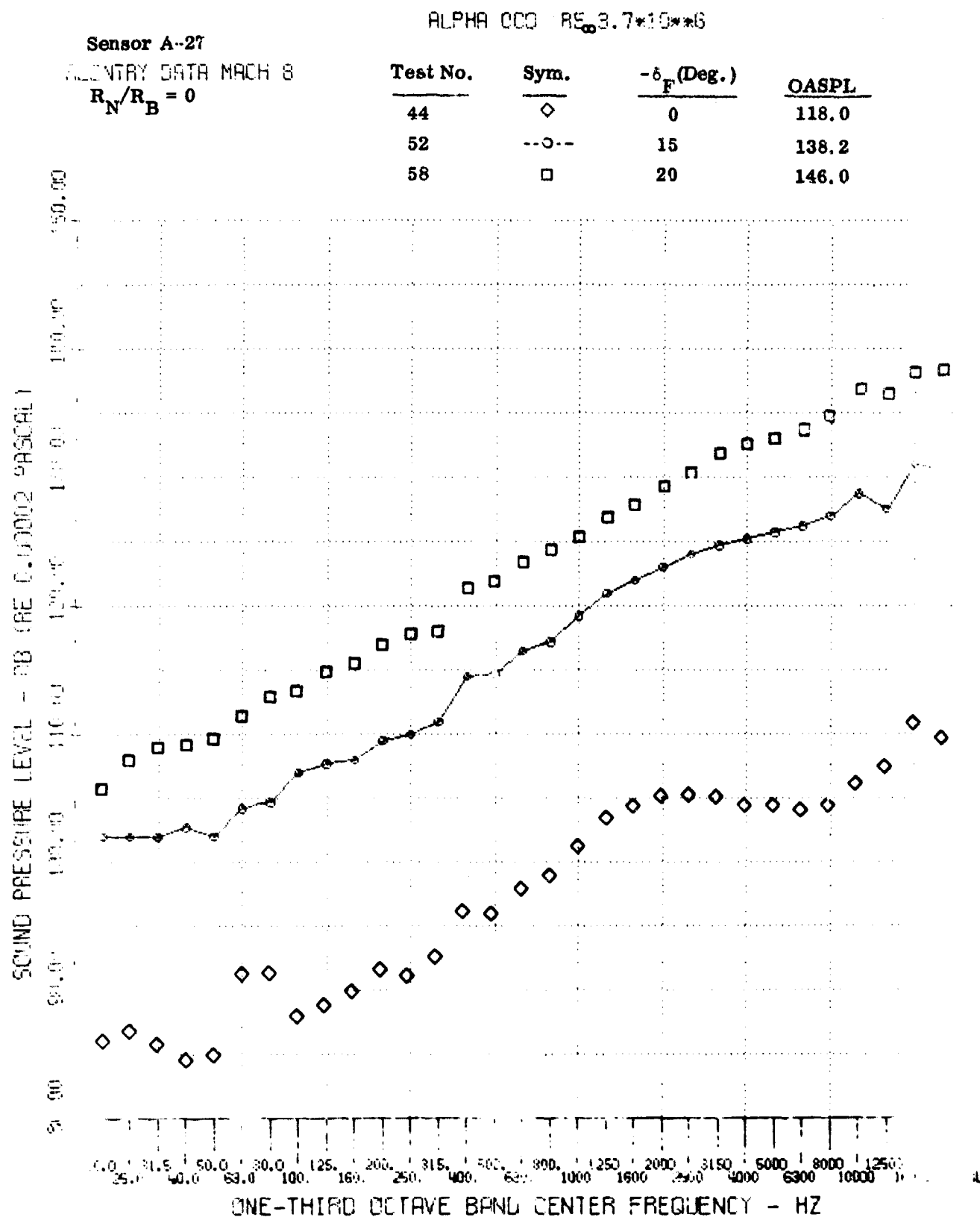
Figure 55 Comparison of Flap Spectra in Turbulent Flow at Various Values of
Flap Deflection – Mach 8

MOLTRY DATA MACH 8

Sensor	Symbol	OASPL
A-26	□	137.5
A-27	--o--	146.0
A-28	◇	142.2
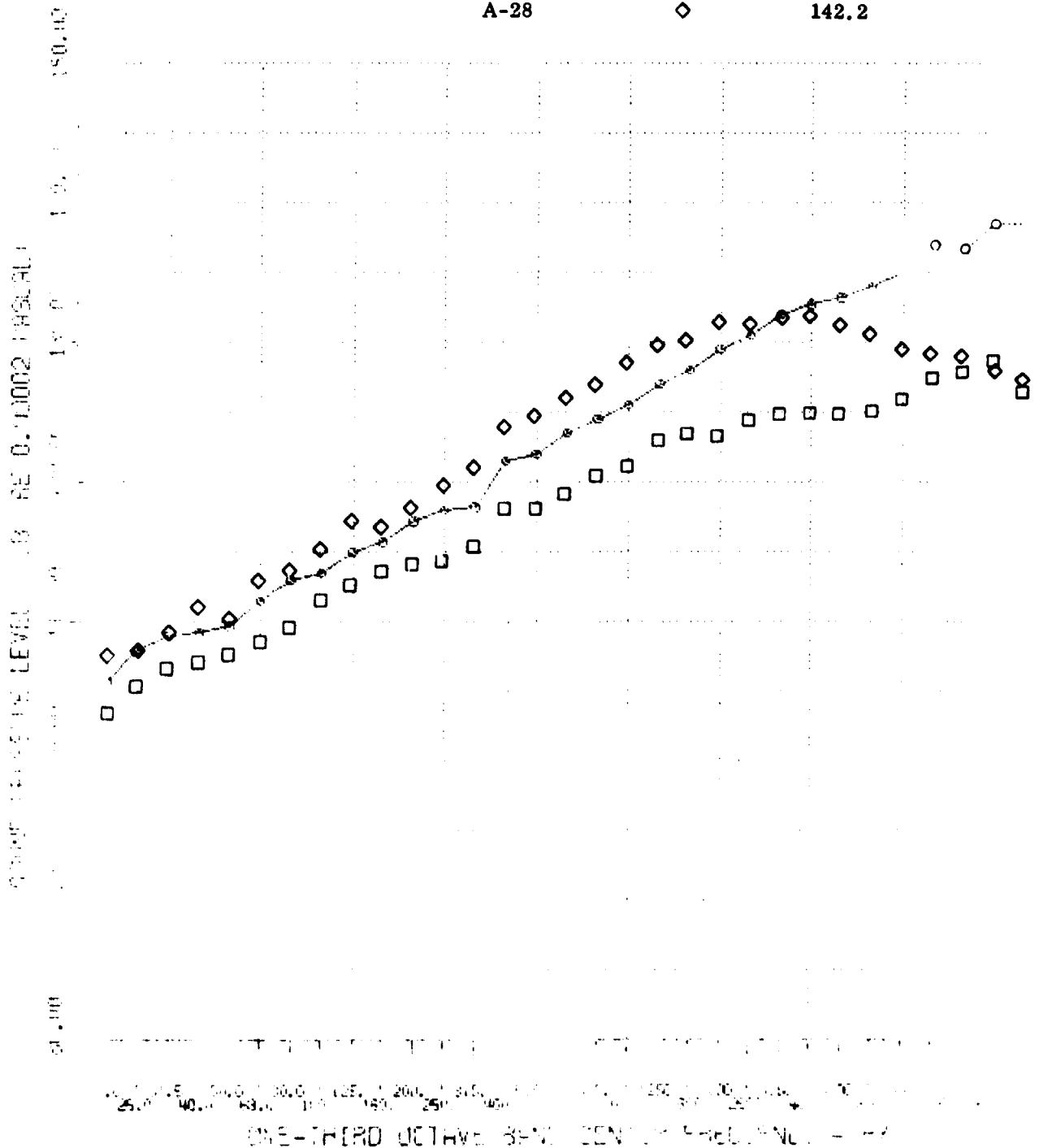
Figure 56   Comparison of Flap Spectra in Fully Turbulent Flow for Sensors A-26, -27, and -28 - Mach 8
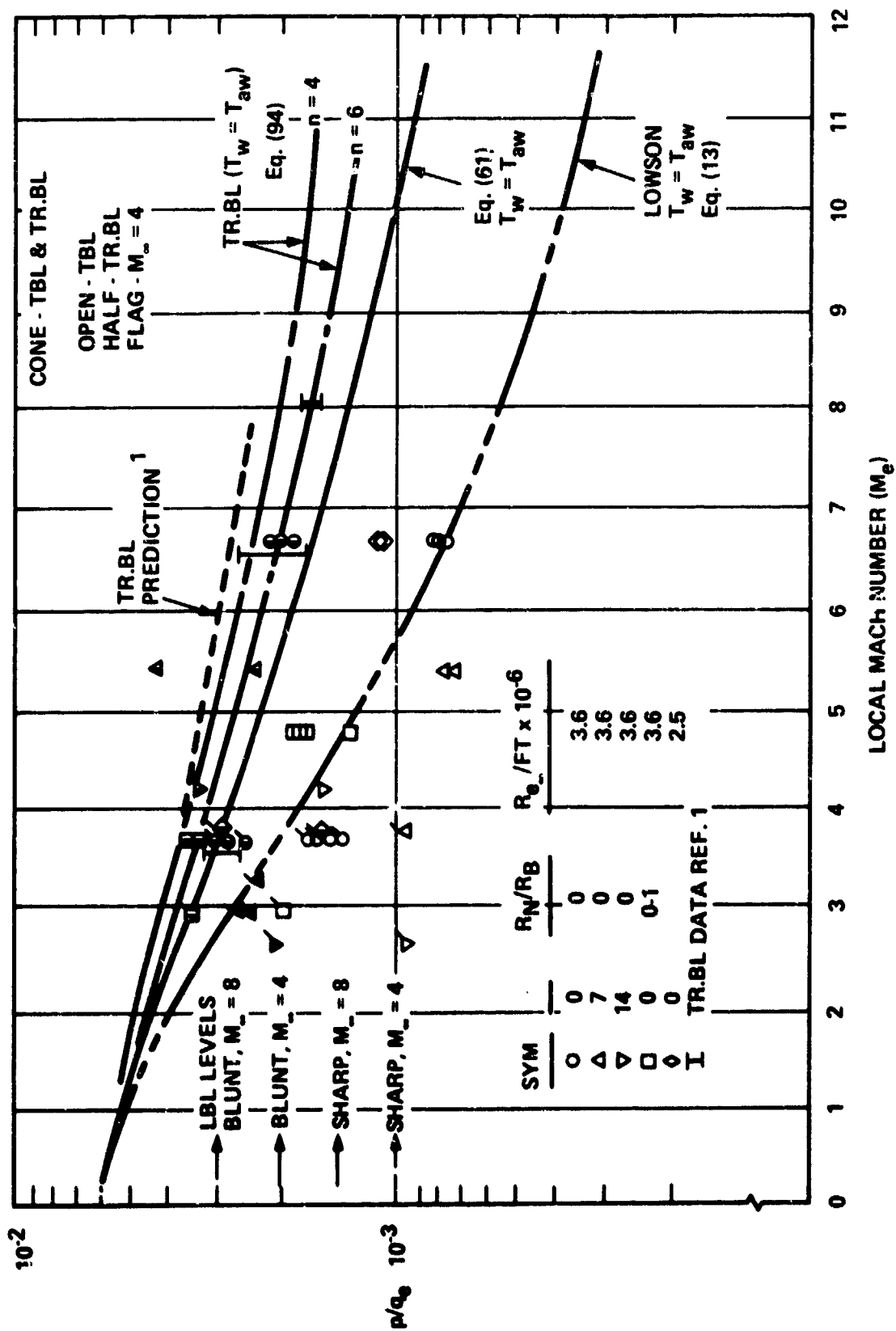
Figure 57. Normalized RMS Pressure Measurements Compared to Prediction - Conical Frustum
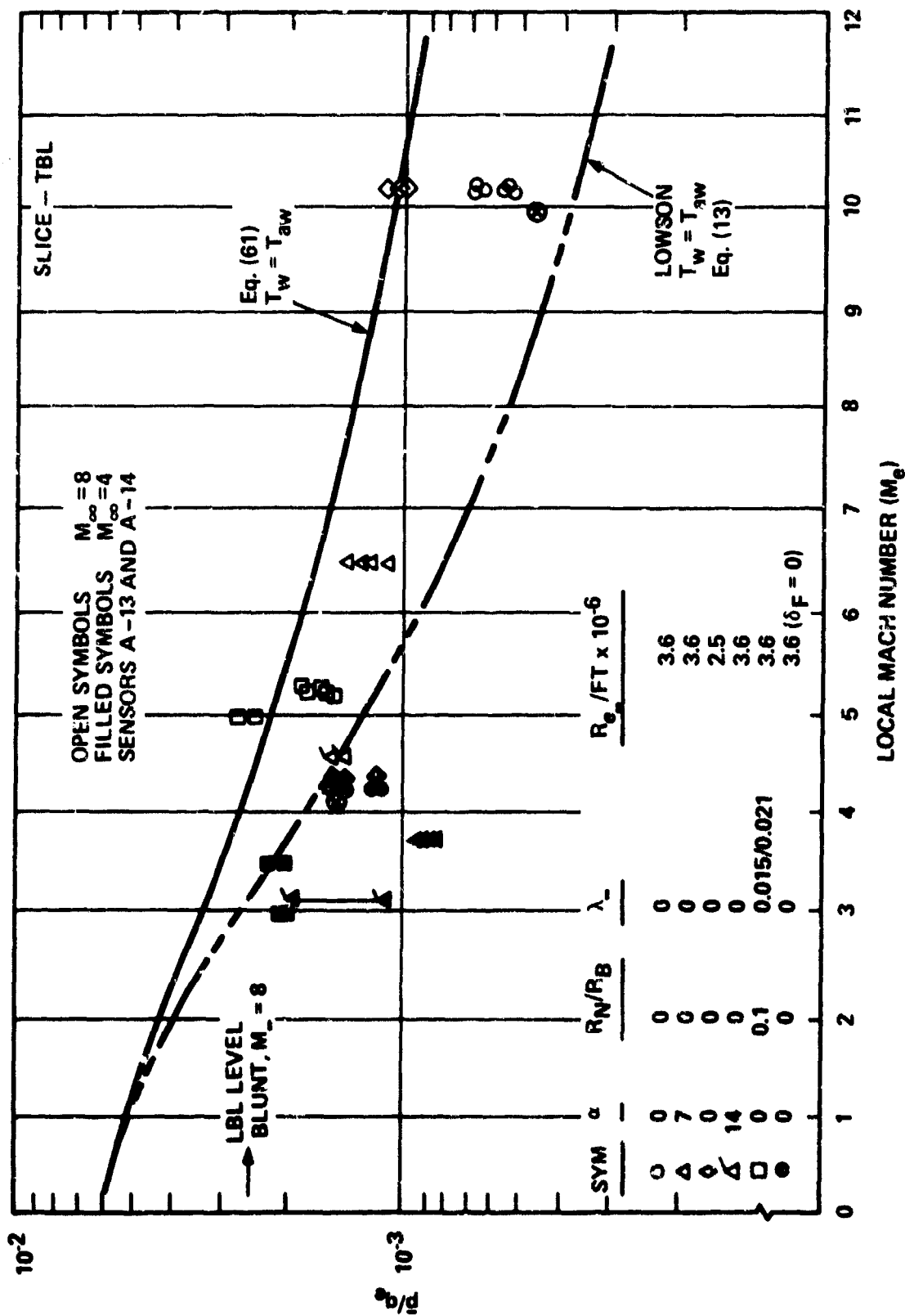
Figure 58. Normalized RMS Pressure Measurements Compared to Prediction - Slice Region

174
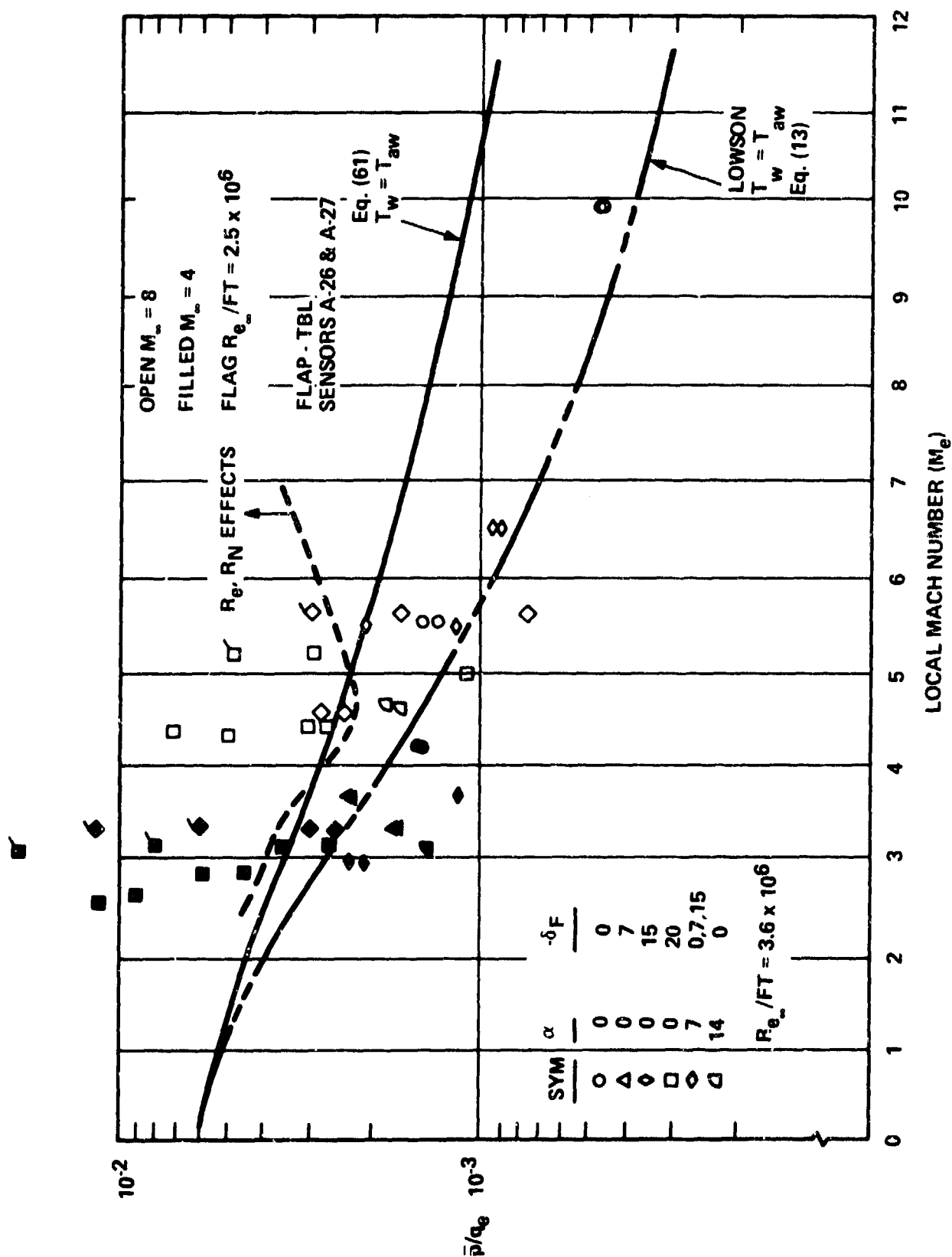
Figure 59. Normalized RMS Pressure Measurements Compared to Prediction - Flap Region
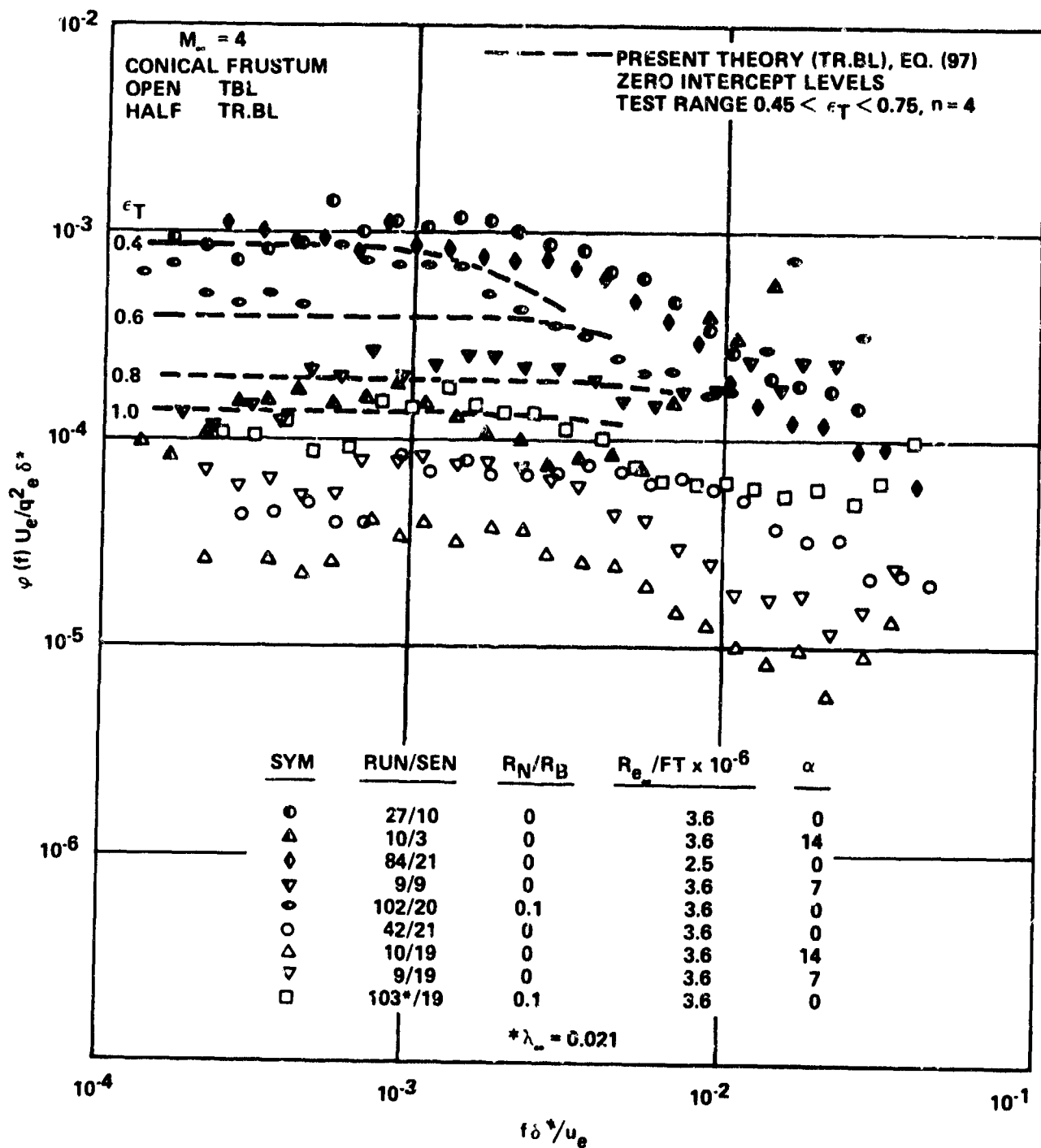
Figure 60. Normalized Power Spectral Density for Turbulent/Transition Flow
on Conical Frustum - Mach 4

176
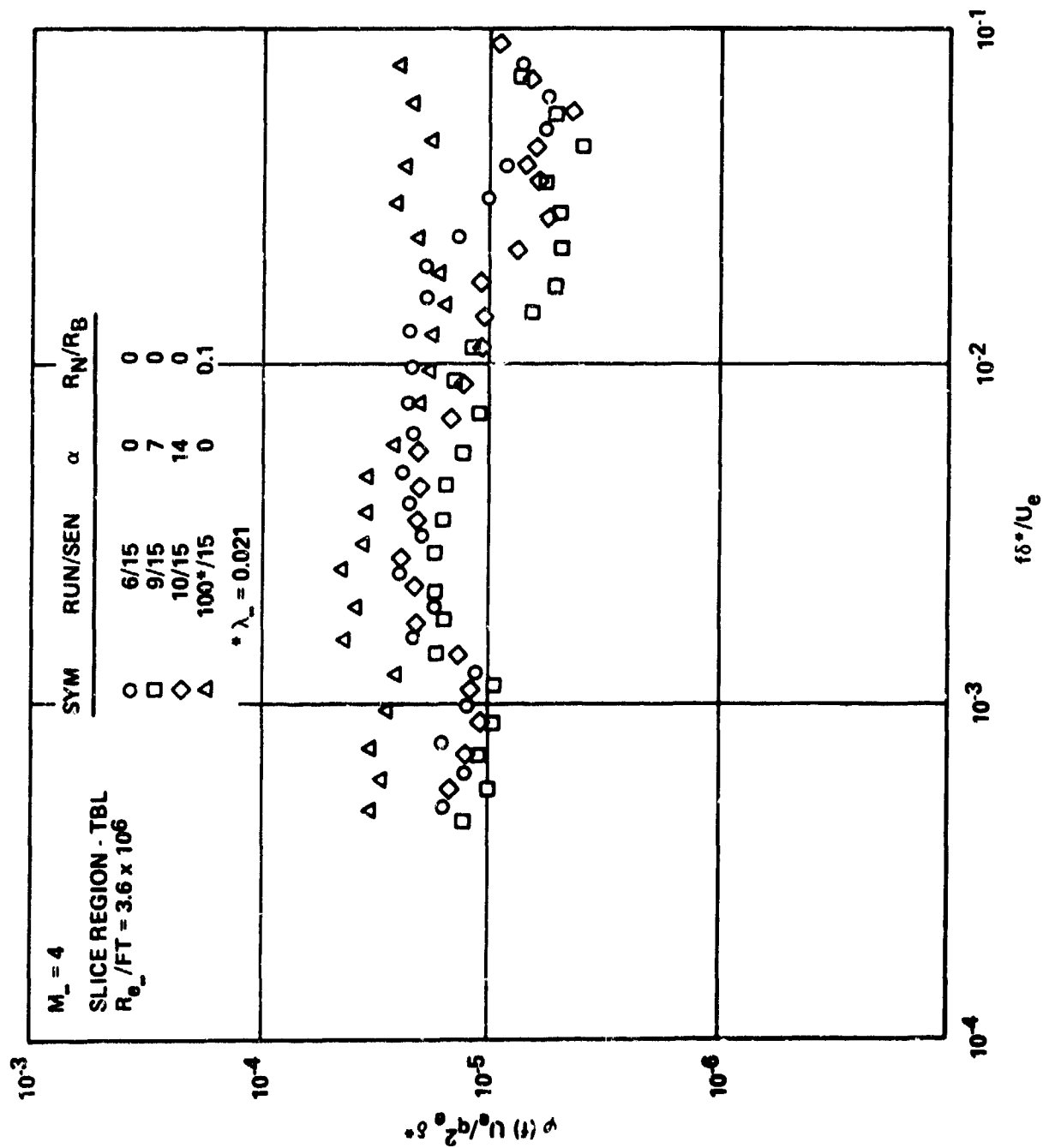
Figure 61. Normalized Power Spectral Density for Turbulent Flow on Slice Region – Mach 4

177

$M_\infty = 4$

FLAP REGION - TBL SENSOR A-27

SYM	RUN	α	$\cdot\delta_F$	R_θ/FT x 10^{-6}
◆	69	0	15	2.5
▲	84	0	20	2.5
○	6	0	0	3.6
□	23	0	7	
◇	27	0	15	
△	42	0	20	
◉	9	7	0	
◼	25	7	7	
◆	30	7	15	
○	10	14	0	
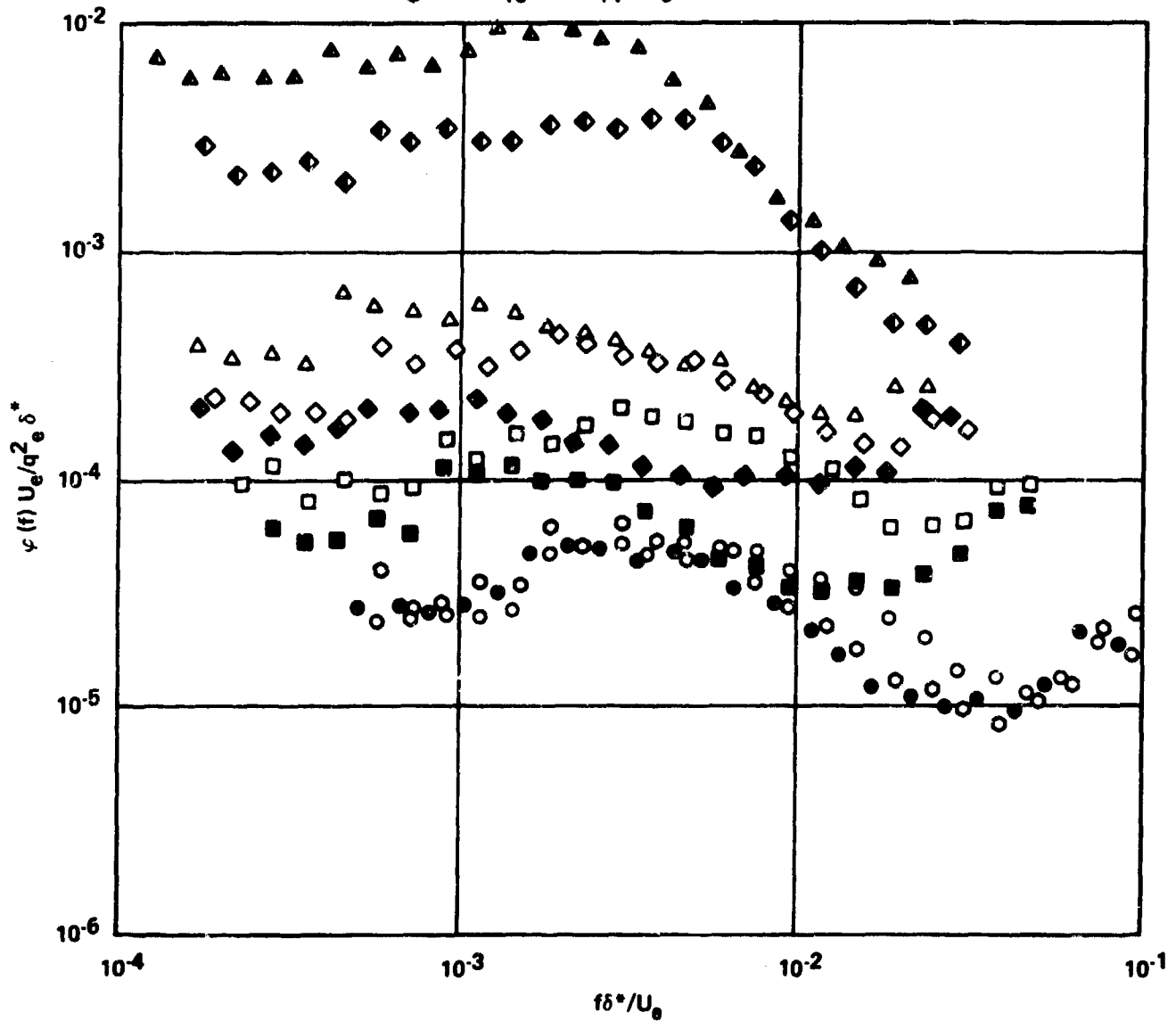
Figure 62. Normalized Power Spectral Density for Turbulent Flow
on Flap Region (Mach 4) - α and δ_F Effects

178

$M_\infty = 4$
FLAP REGION - TBL

10^{-1}
10^{-2}
10^{-3}
10^{-4}
10^{-5}

$\varphi\,(f)\,U_e/q^2_e\,\delta^*$

SYM	RUN/SEN	R_N/R_B	λ_∞
O	102/27	0.1	0
●	42/26	0	0
▲	42/27	0	0
⬤	42/28	0	0
□	103/27	0.1	0.021

$\alpha = 0,\ \delta_F = -20^0$

$R_{\theta_\infty}/FT = 3.6 \times 10^6$

10^{-4} 10^{-3} 10^{-2} 10^{-1}

$f\delta^*/U_e$
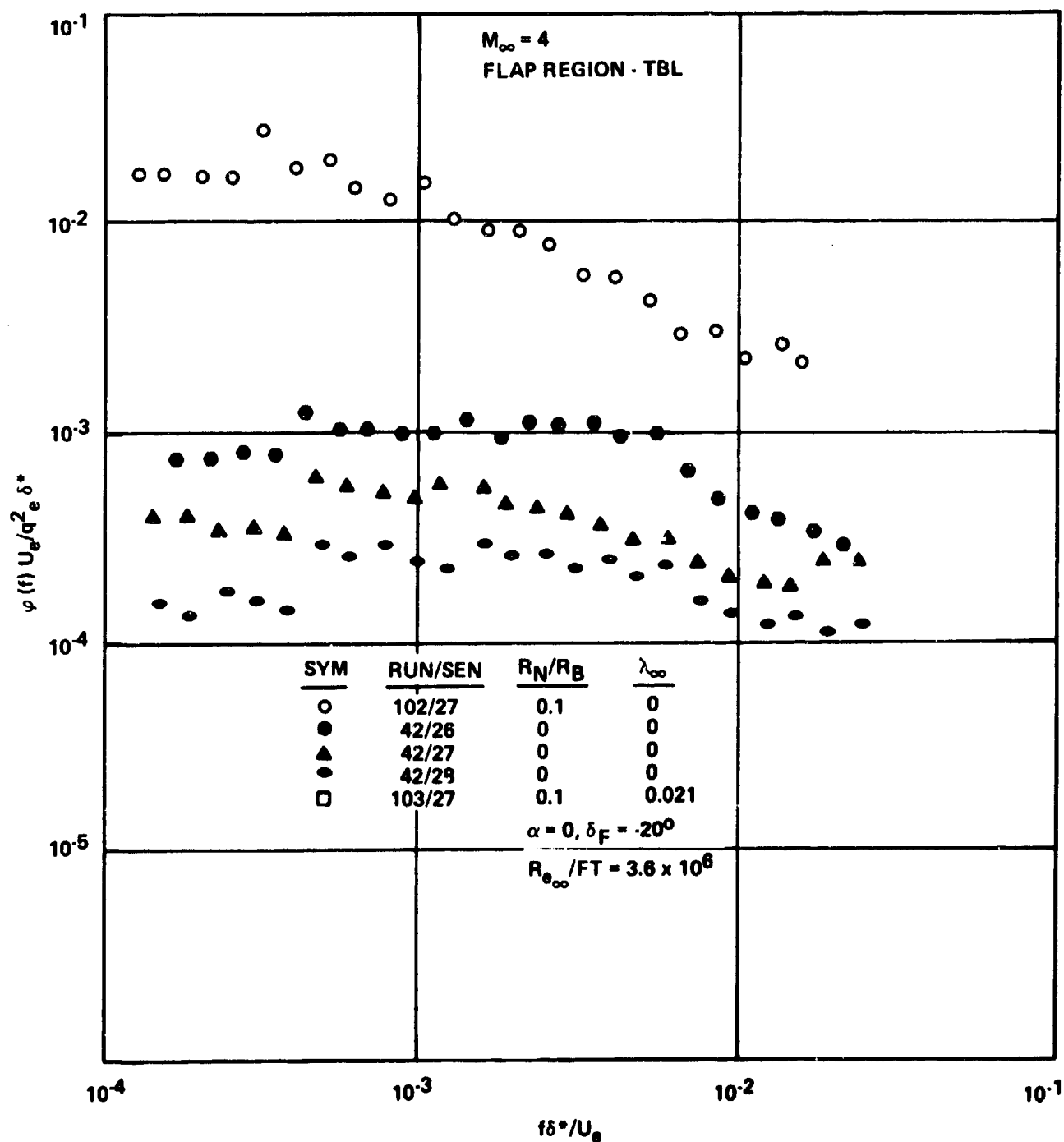
Figure 63. Normalized Power Spectral Density for Turbulent Flow
on Flap Region (Mach 4) - R_N Effects

179
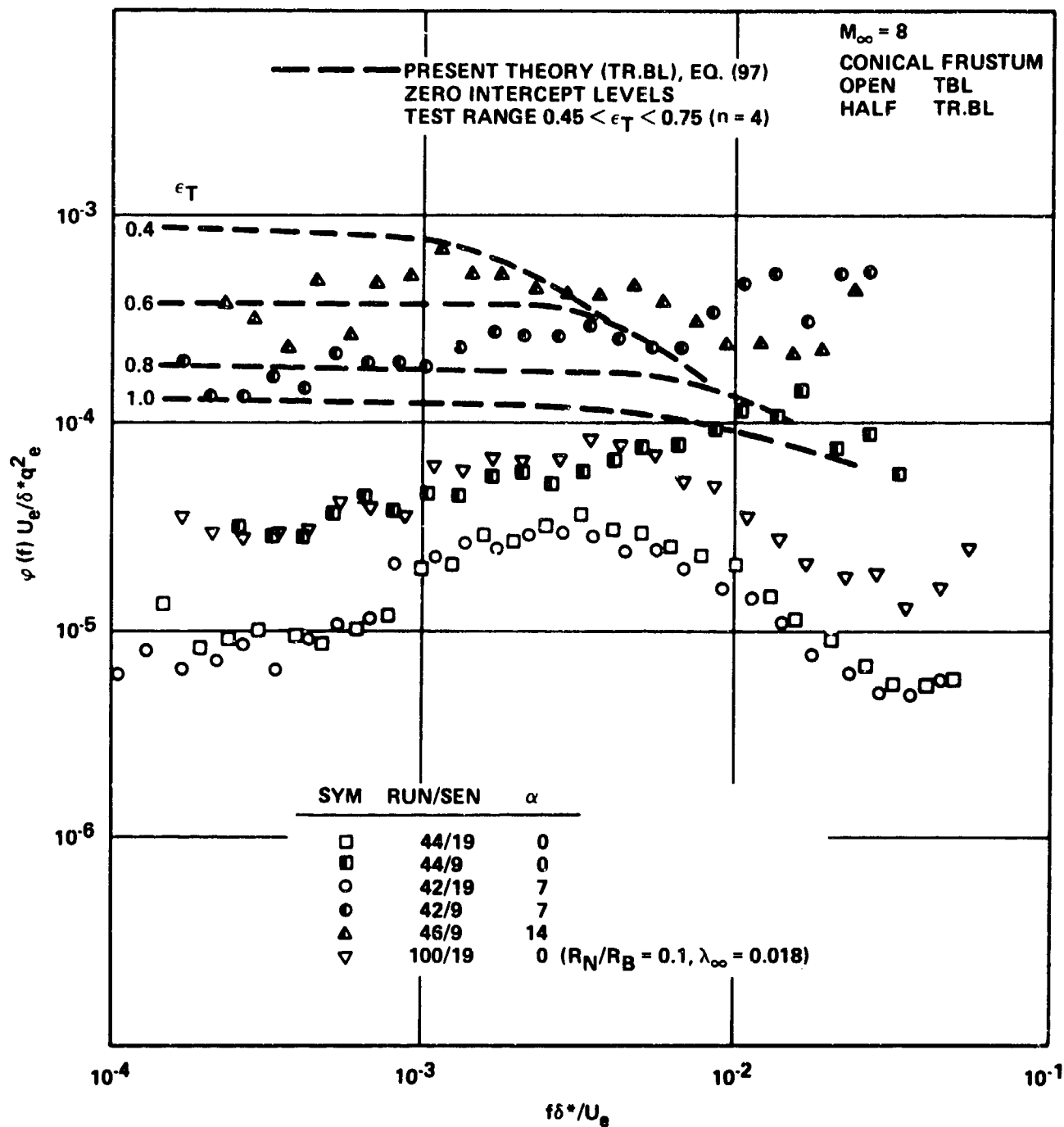
Figure 64. Normalized Power Spectral Density for Turbulent/
Transitional Flow on Concial Frustum – Mach 8

180
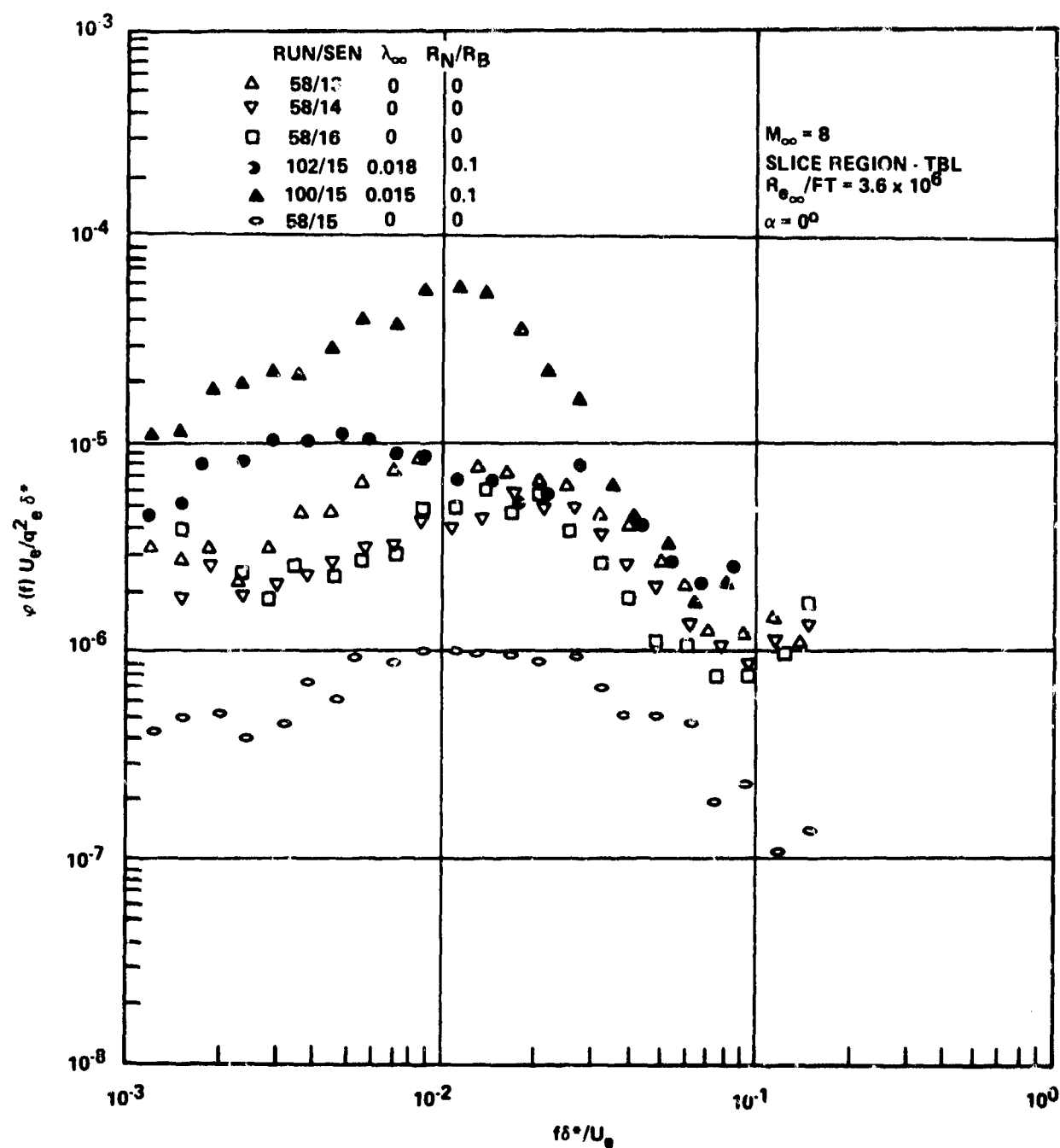
Figure 65. Normalized Power Spectral Density for Turbulent Flow
on Slice Region (Mach 8) - R_N and Spatial Effects

181
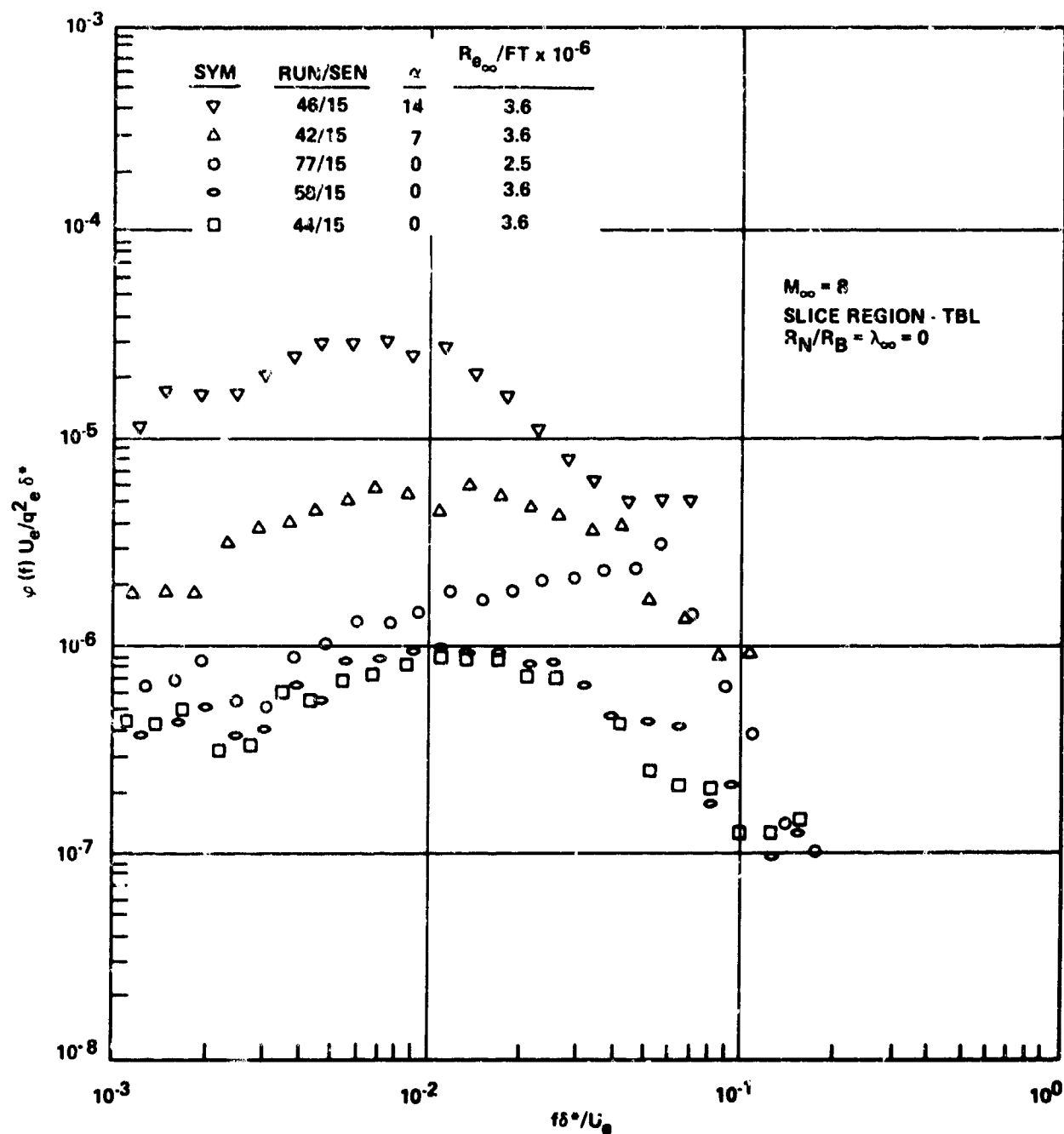
Figure 66. Normalized Power Spectral Density for Turbulent Flow
on Slice Region (Mach 8) - α and Re_∞ Effects

182
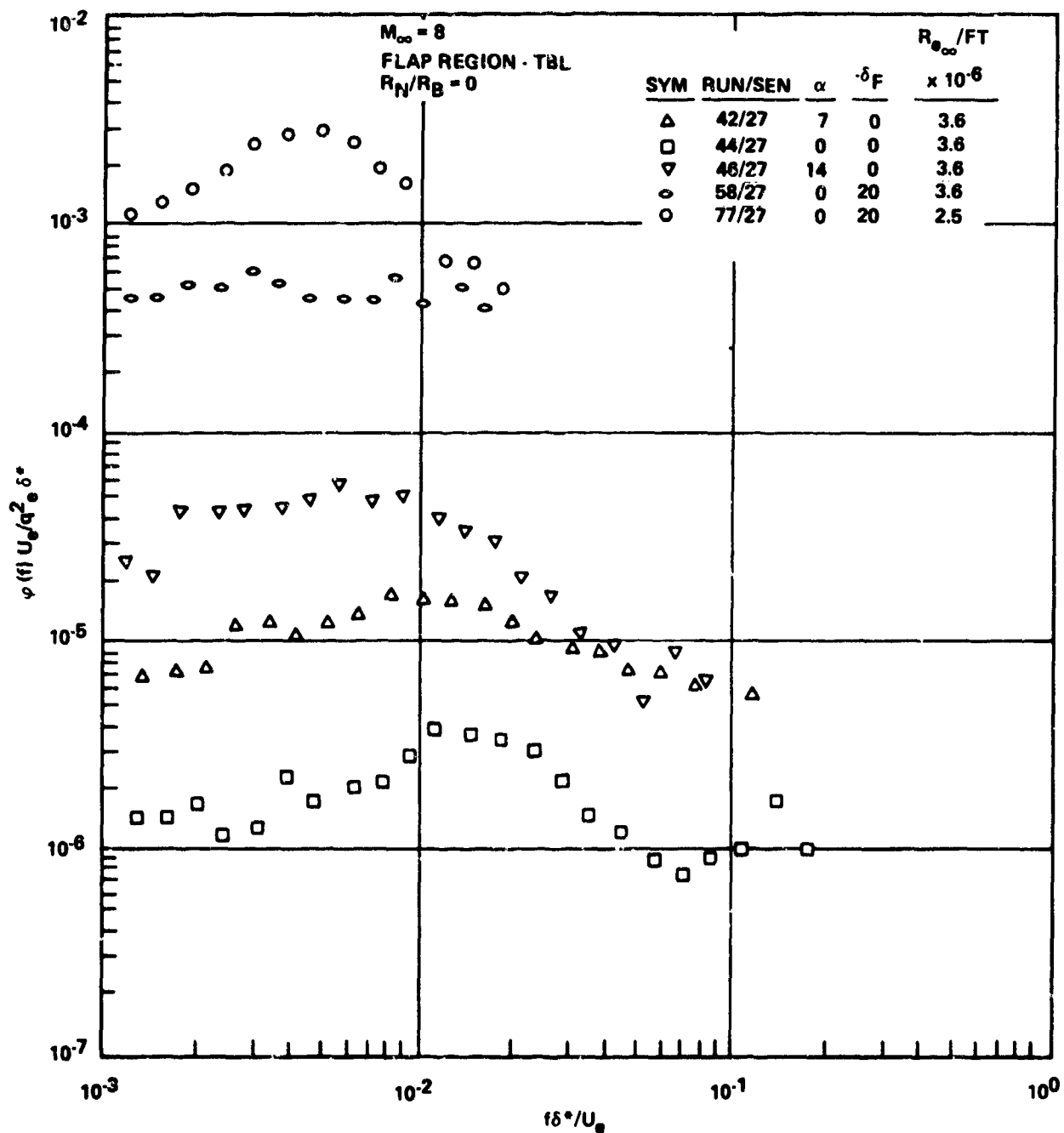
Figure 67. Normalized Power Spectral Density for Turbulent Flow
on Flap Region (Mach 8) - α and δ_F Effects

183
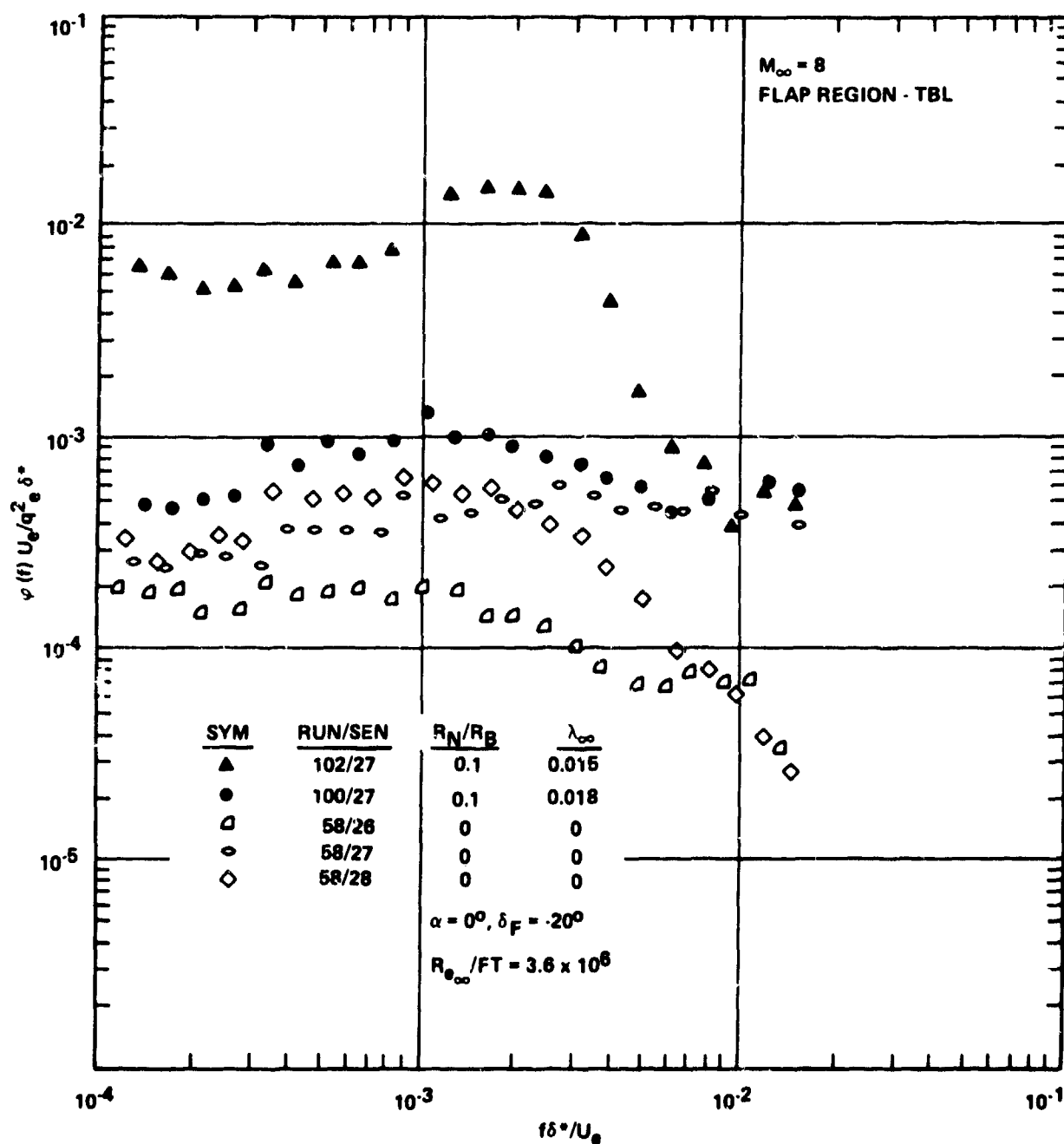
Figure 68. Normalized Power Spectral Density for Turbulent Flow
on Flap Region (Mach 8) - R_N Effects

184
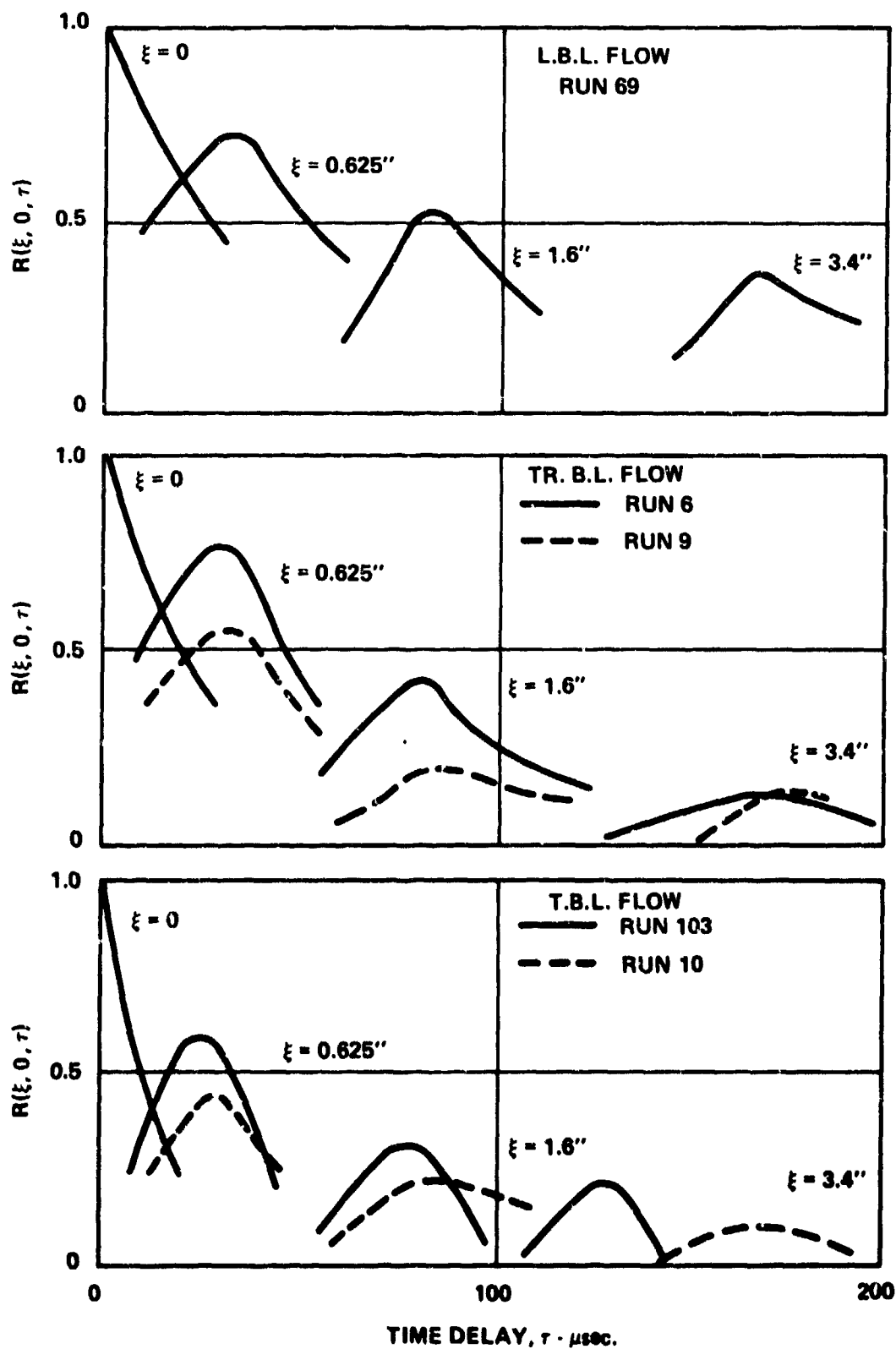
Figure 69. Broad-Band Space - Time Correlation Functions (Longitudinal) Measured on the Conical Frustum - Mach 4

185
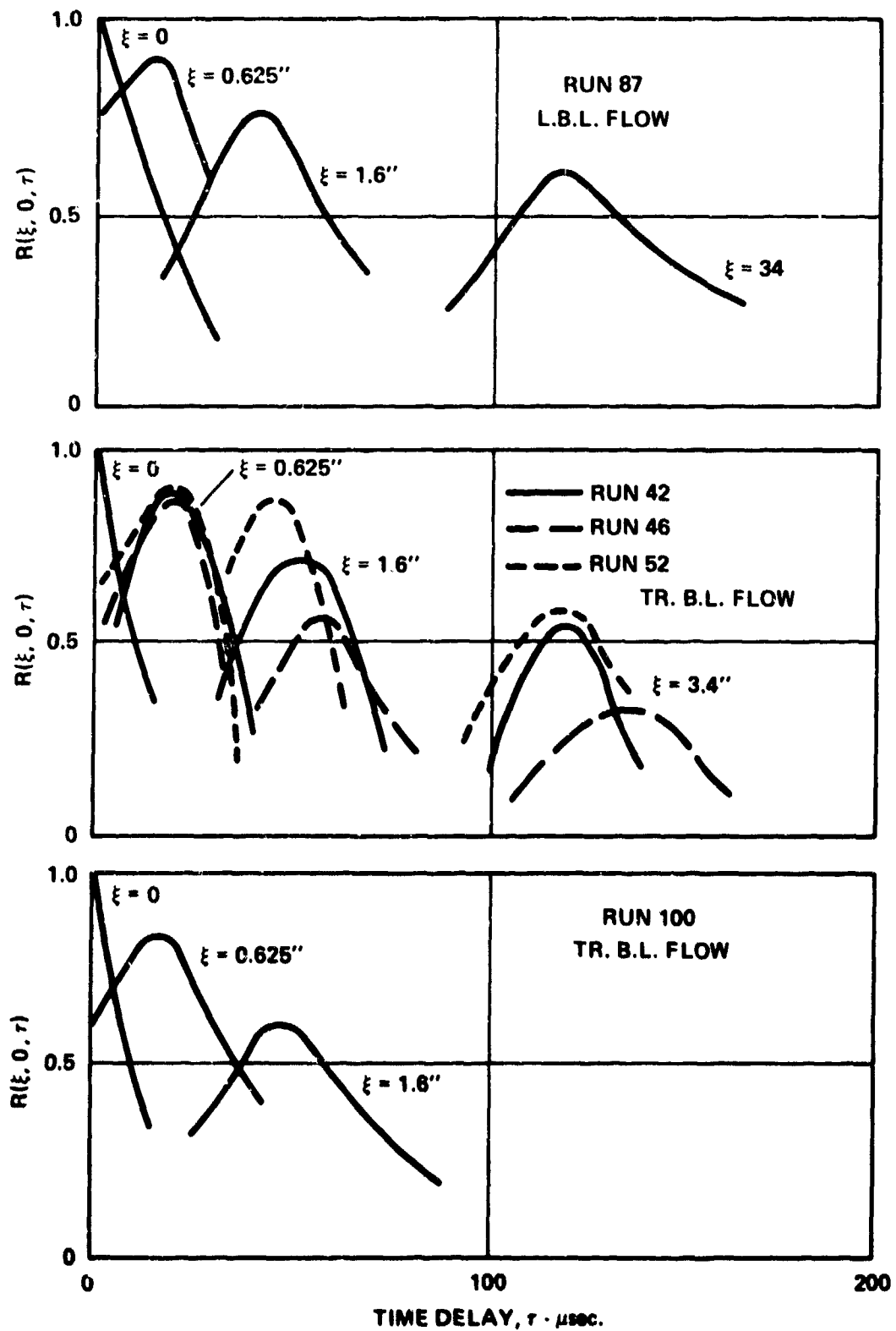
Figure 70. Broad-Band Space-Time Correlation Functions (Longitudinal) Measured on
the Conical Frustum – Mach 8

186
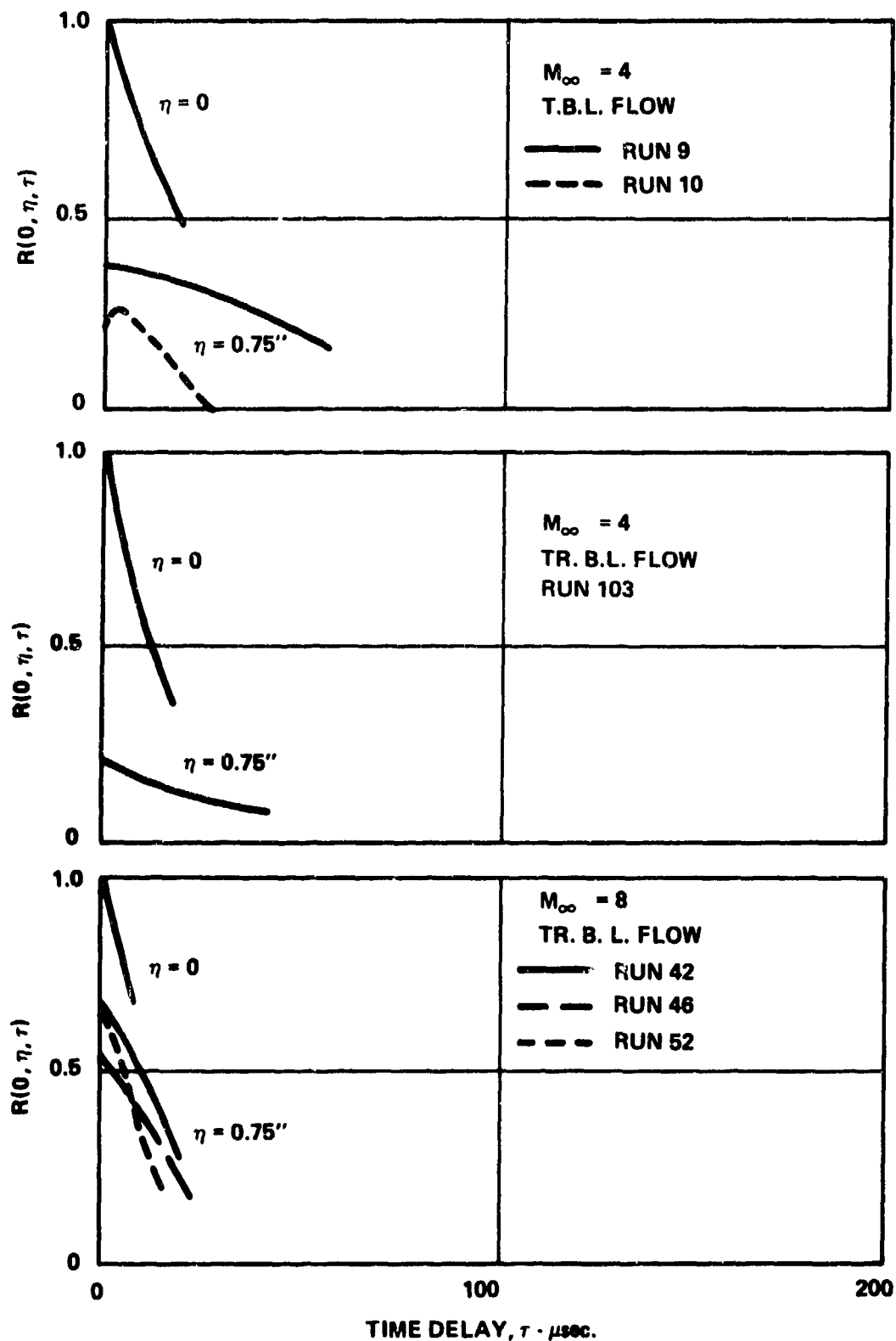
Figure 71. Broad-Band Space-Time Correlation Functions (Circumferential) Measured on Conical Frustum - Mach 4, 8

187
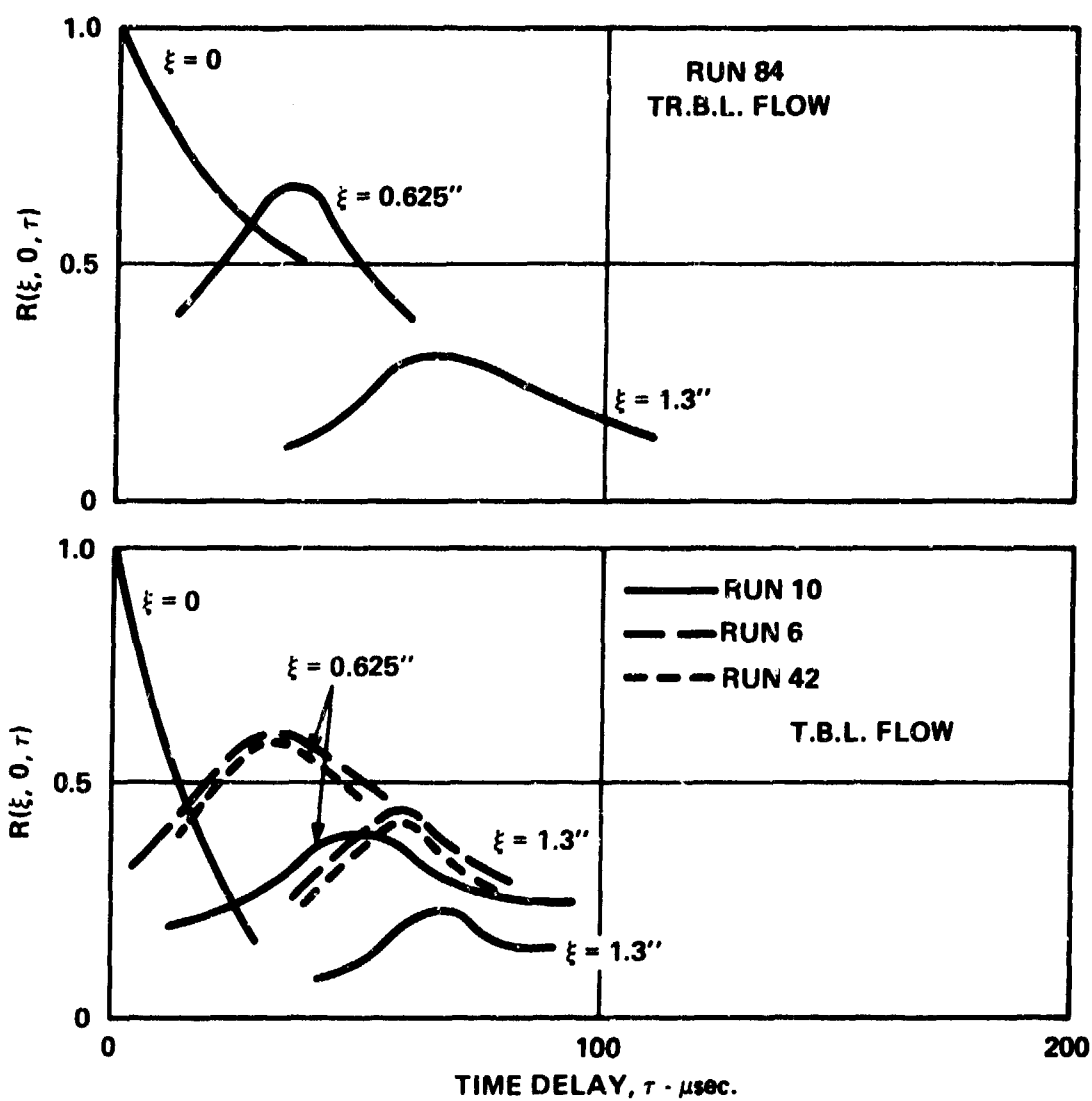
Figure 72. Broad-Band Space-Time Cross-Correlation Functions (Longitudinal) Measured on Slice - Mach 4

188
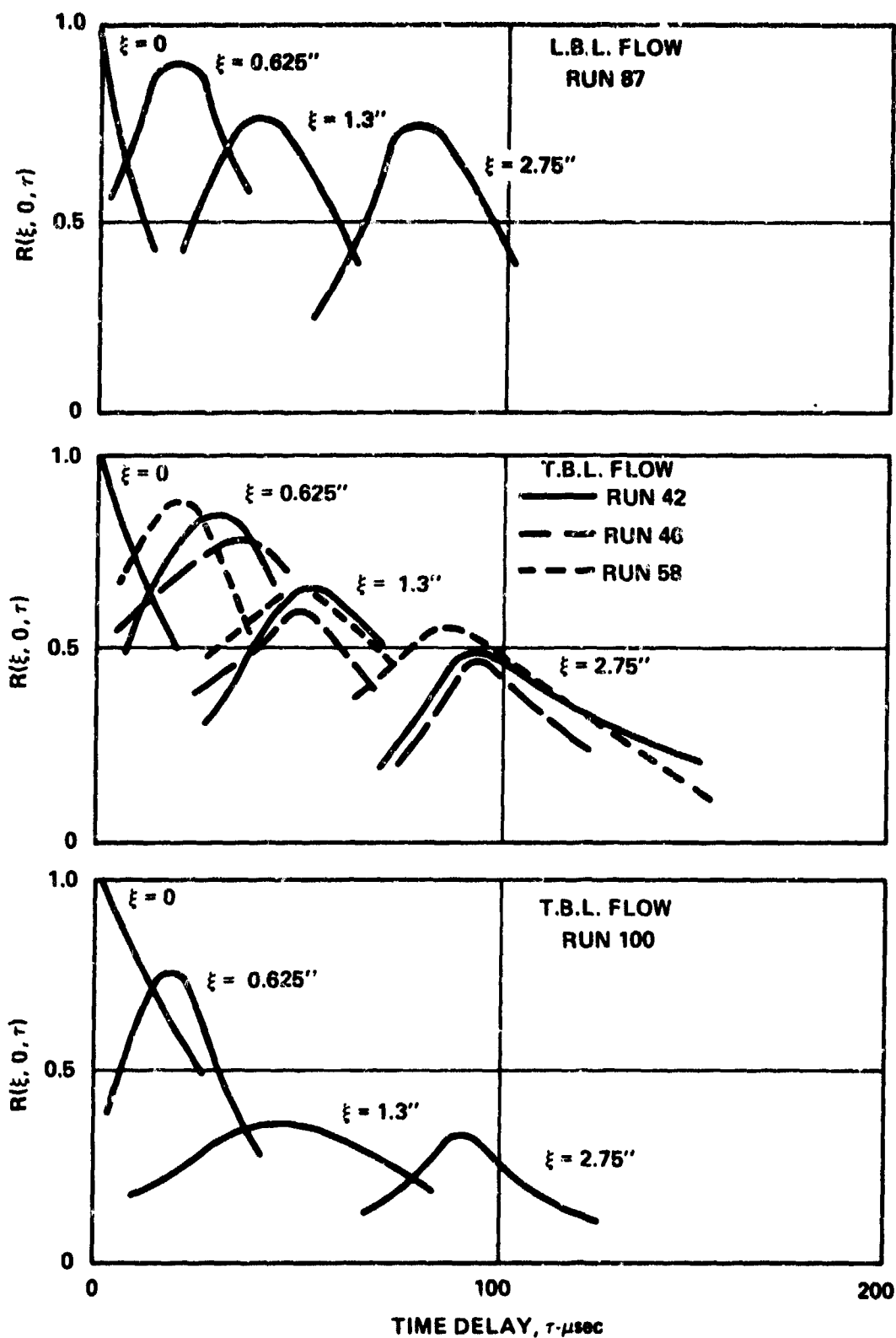
Figure 73. Broad-Band Space-Time Cross-Correlation Functions (Longitudinal) Measured on Slice - Mach 8

189
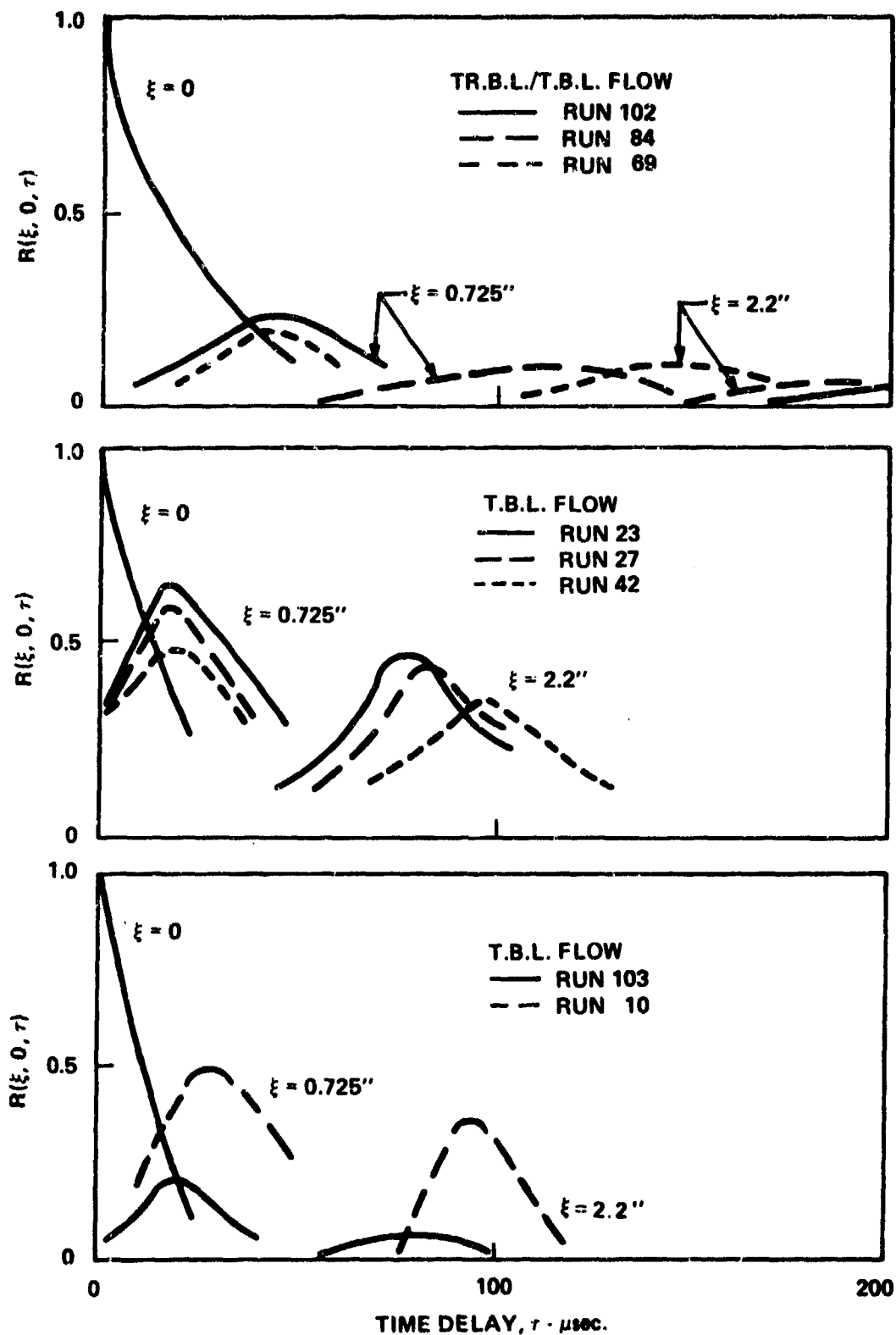
Figure 74. Broad-Band Space-Time Correlation Functions (Longitudinal) Measured on the Flap - Mach 4

190
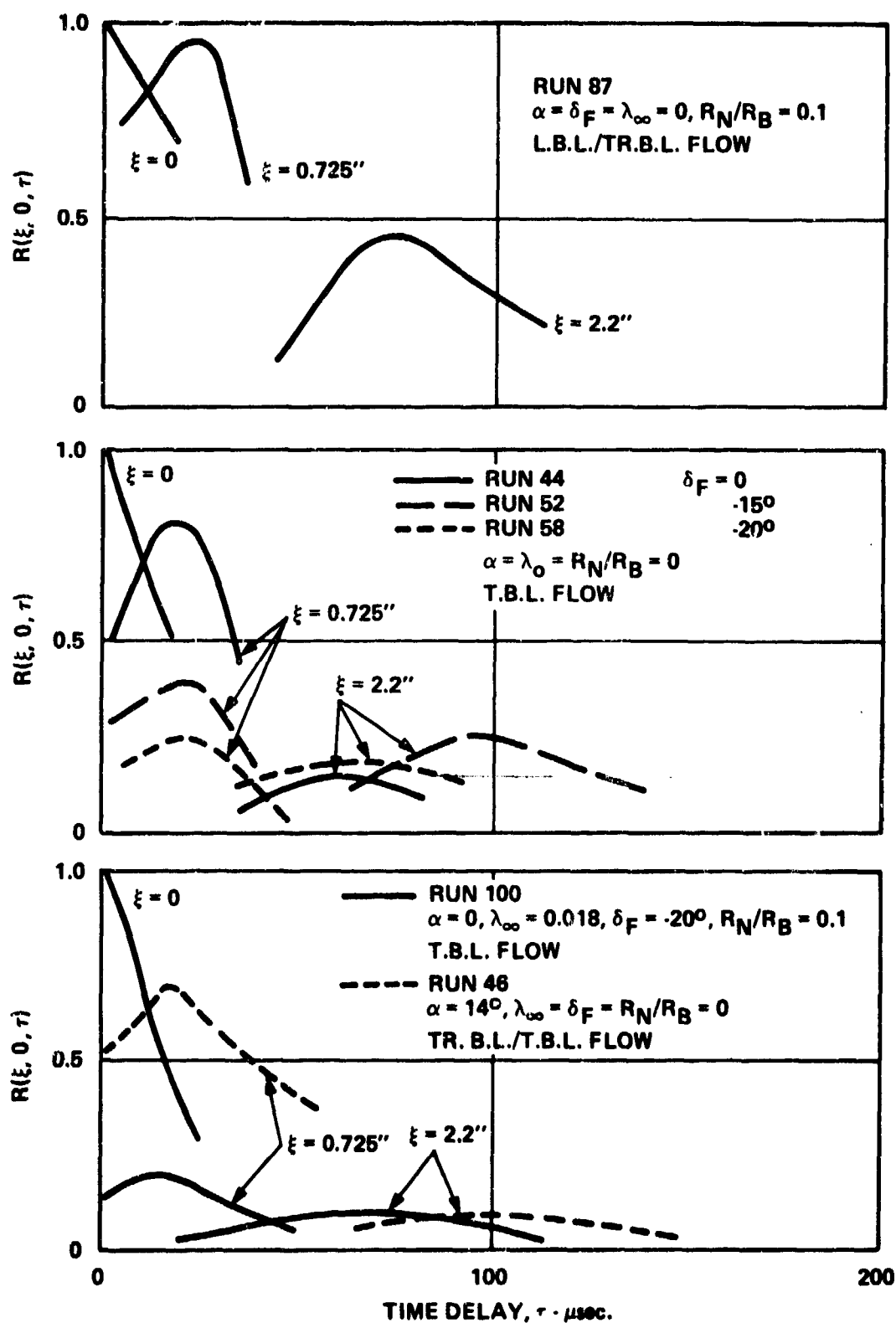
Figure 75. Broad-Band Space-Time Correlation Functions (Longitudinal) Measured on the Flap - Mach 8, $Re_\infty/ft. \doteq 3.6 \times 10^6$

191

q ~ **Heat-Transfer Output**
p̃ ~ **Pressure Fluctuating Signal**
p ~ **dc Pressure Signal**
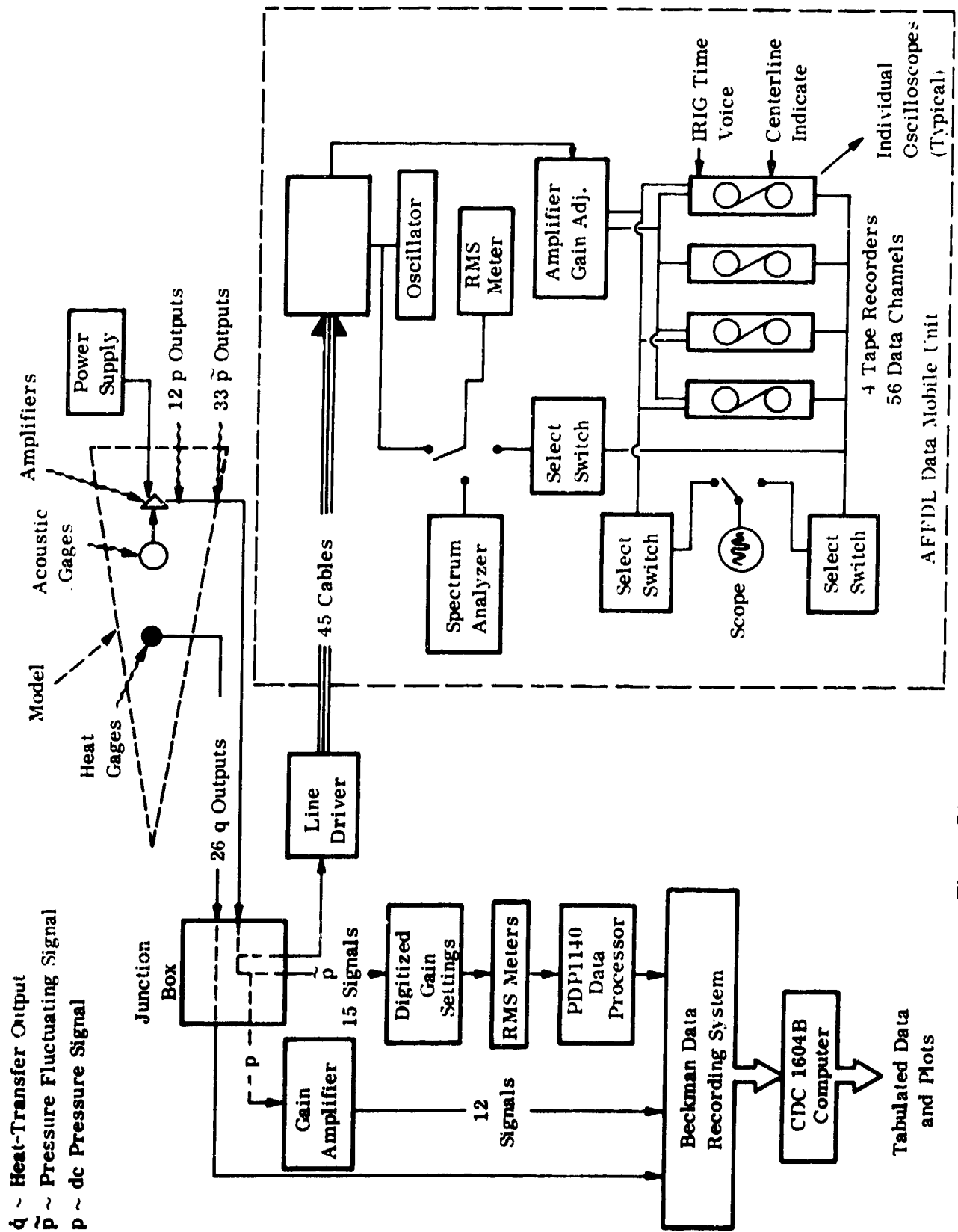
Figure 76. Transducer Channel Recording Network

(ANALYSES TO BE PERFORMED ON SELECTED SENSORS & TESTS)

DIGITIZED ACOUSTIC DATA

TUNNEL CONDITIONS

*POWER SPECTRA

*CROSS-SPECTRA

CROSS-CORRELATION
(BROAD & NARROW)

AUTO-CORRELATION

NORMALIZED
QUAD-SPECTRUM

*NORMALIZED
SPACE–CORRELATION
(LONG.)

NORMALIZED
SPACE–CORRELATION
(LONG.)

NORMALIZED
CO-SPECTRUM

*NORMALIZED
SPACE-CORRELATION
(LAT.)

NORMALIZED
AUTO–CORRELATION
(LAT.)

NARROW-BAND
CONVECTION
VELOCITY

*REQUIRED FOR VIBRATION RESPONSE PREDICTIONS

BROAD-BAND
CONVECTION
VELOCITY

Figure 77. Data Processing Analysis Diagram

193
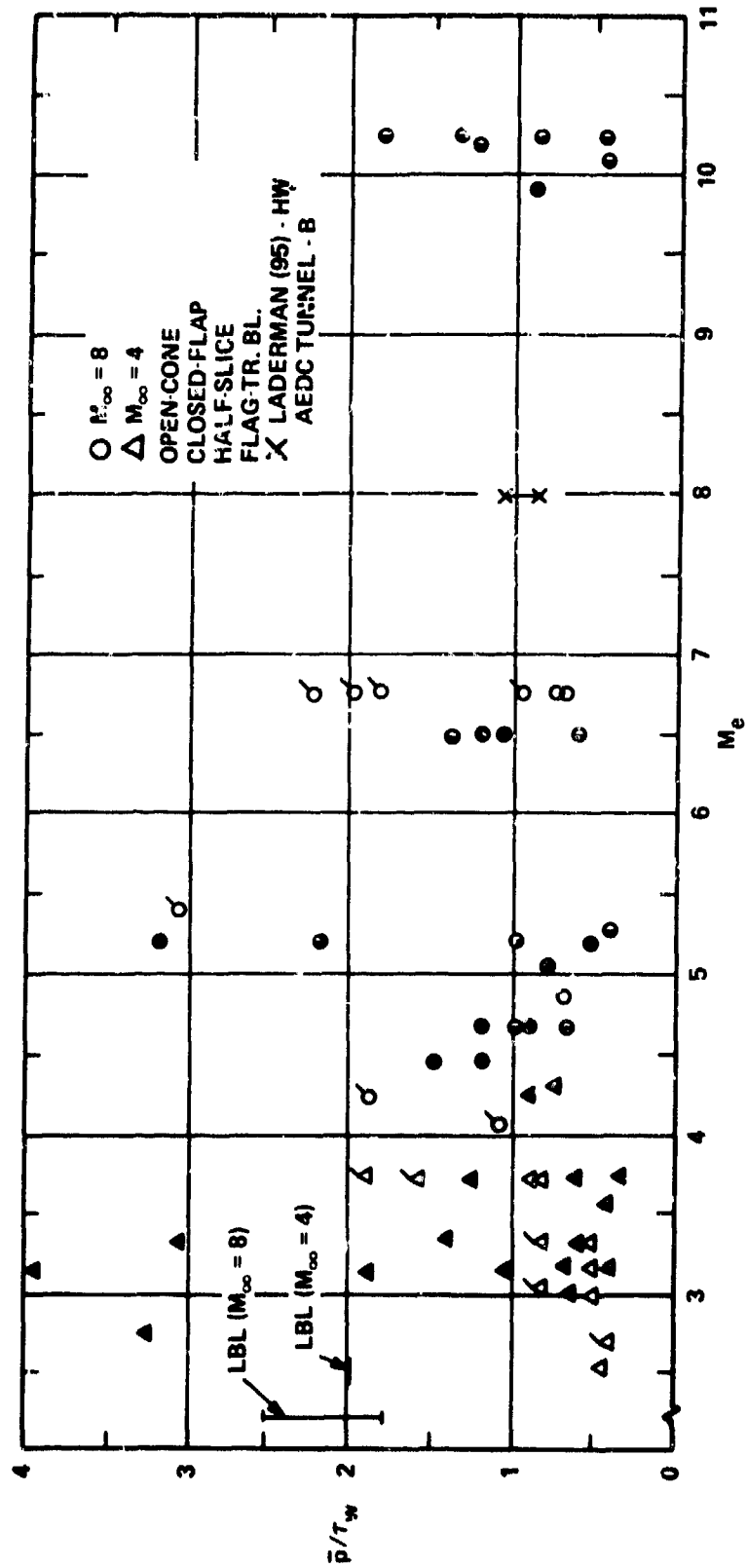
Figure 78. Normalized RMS Pressure (with wall shear) Distribution with Mach Number for Mach 4 and 8 Test Measurements

CONICAL FRUSTUM
OPEN-TBL
HALF-TR. BL
FLAG-$M_\infty = 4$
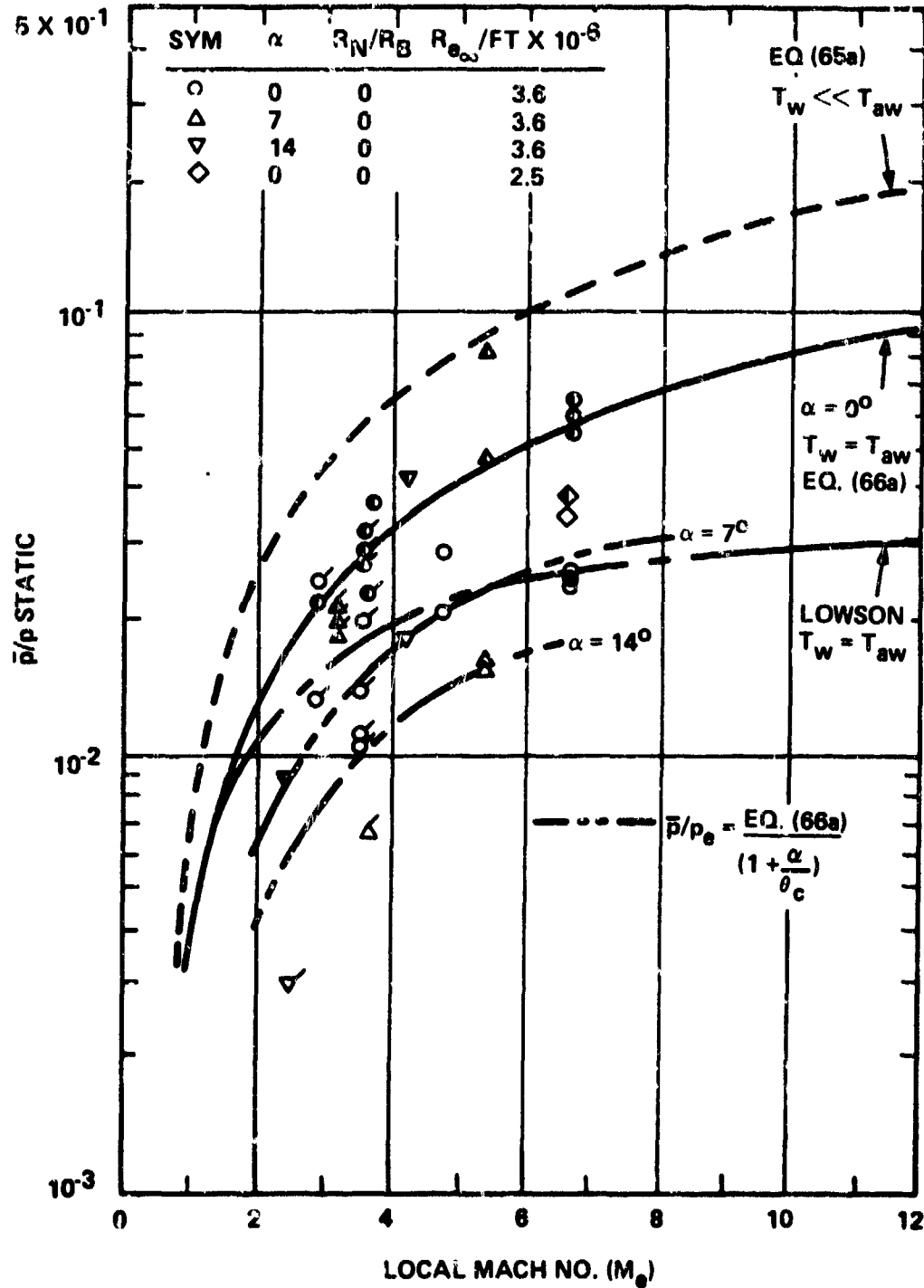
Figure 79. Normalied RMS Pressure (with Static Pressure) Variation with Mach Number – Conical Frustum Measurements

195

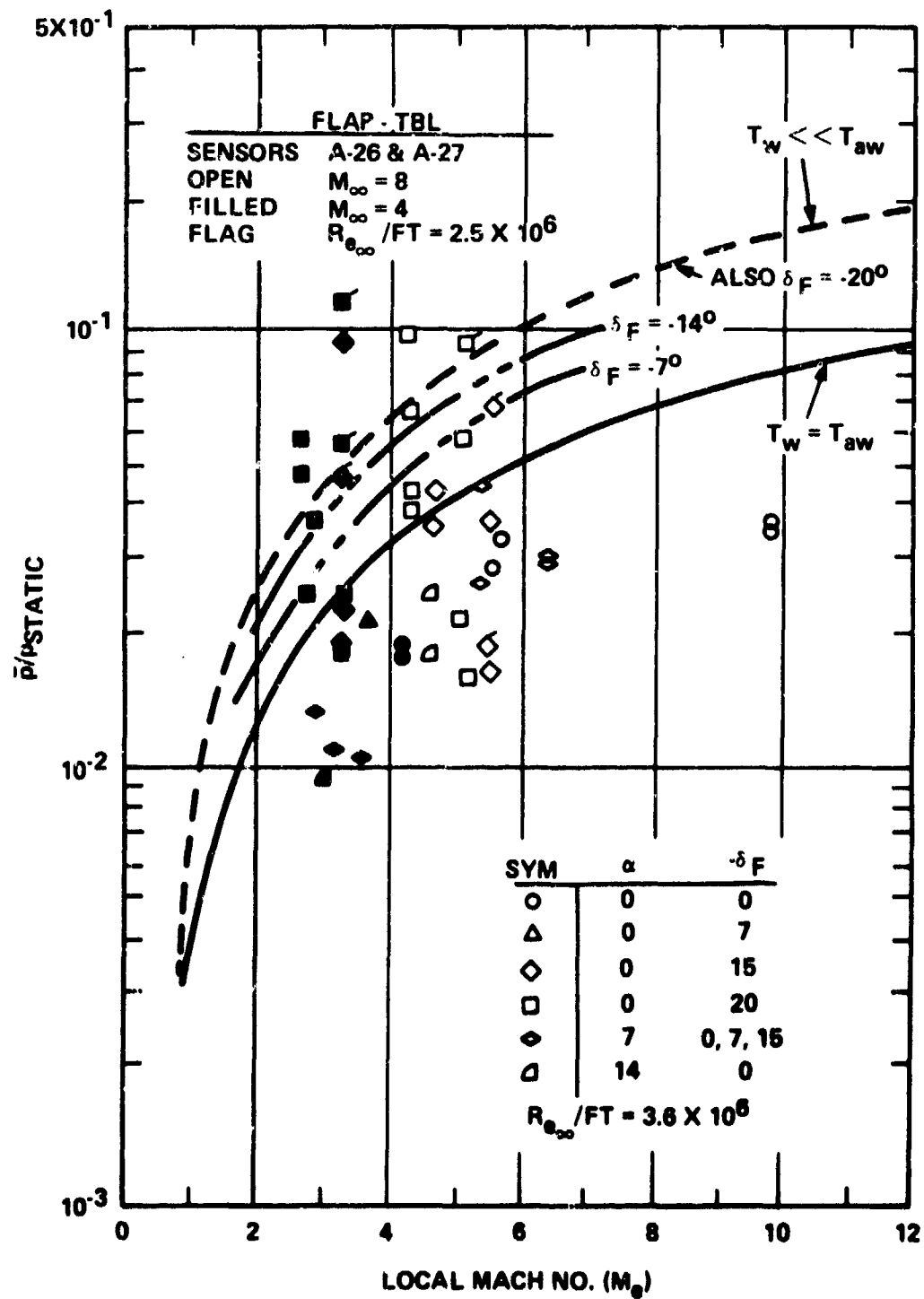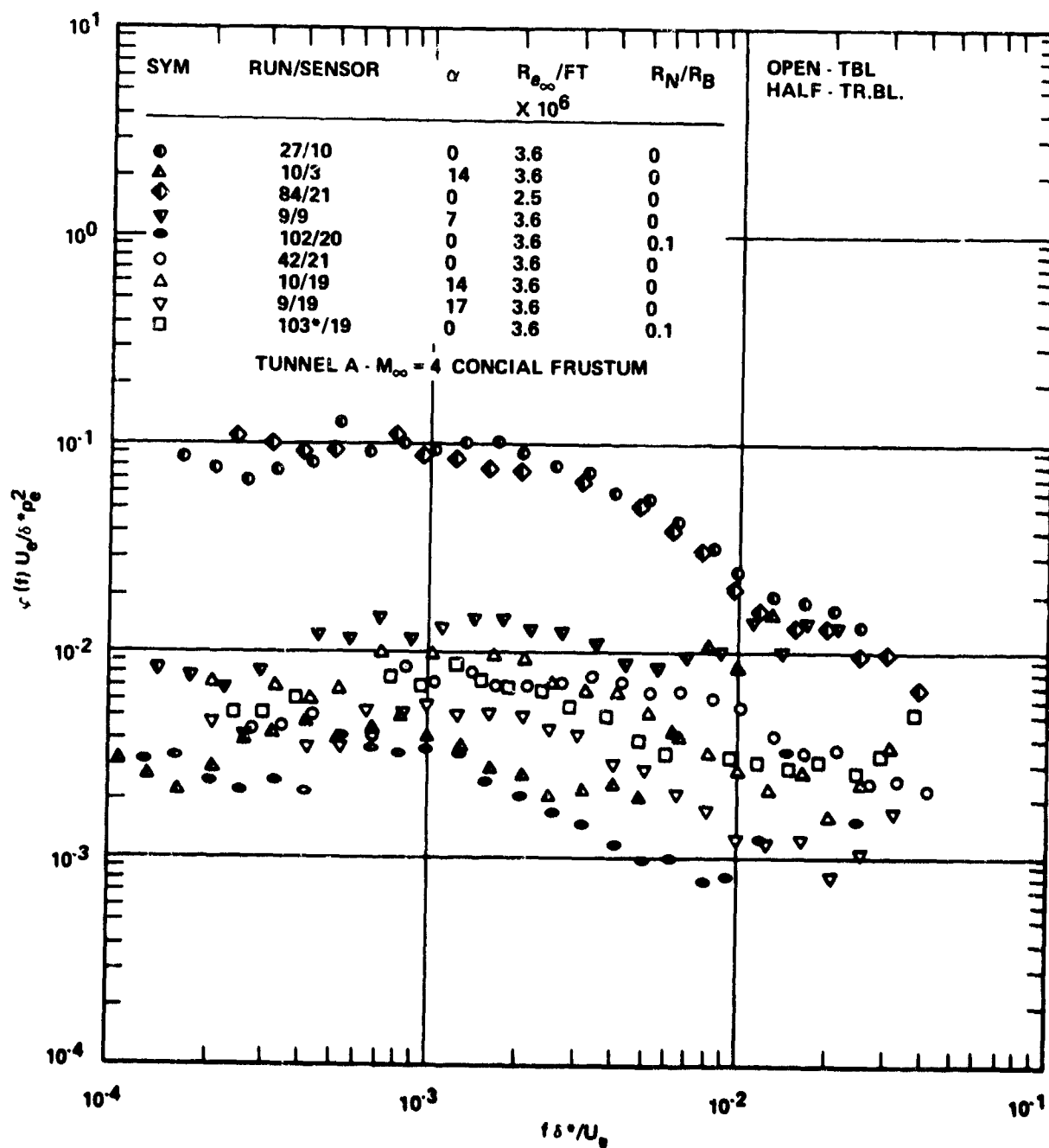Figure 80. Normalized RMS Pressure (with Static Pressure) Variation with Mach Number - Slice Region Measurements

196

Figure 81. Normalized RMS Pressure (with Static Pressure) Variation with
Mach Number - Flap Region Measurements

197

Figure 82. Normalized Power Spectral Density (with Static Pressure) – Mach 4 Conical Frustum Measurements

198
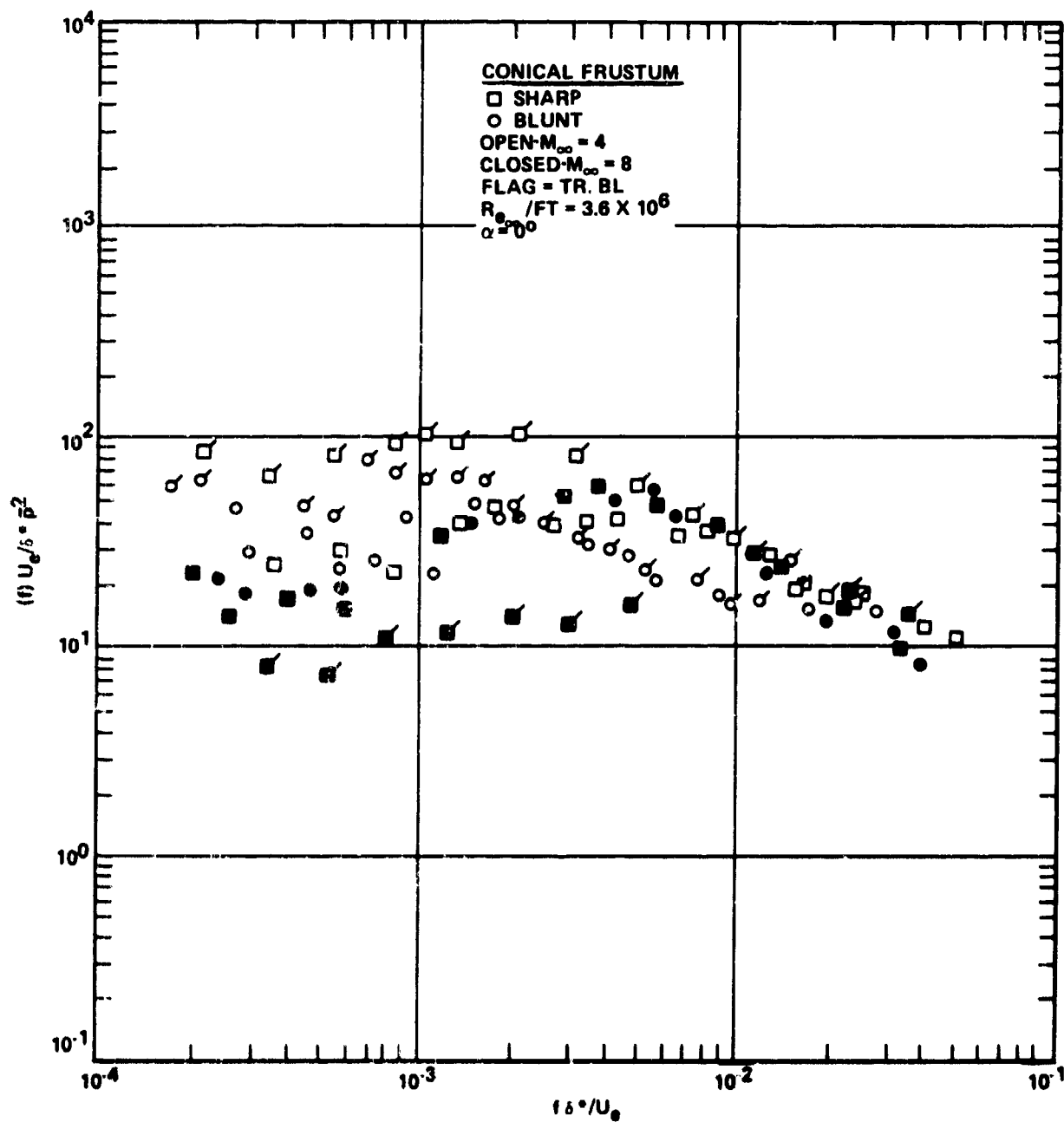
Figure 83. Normalized Power Spectral Density (with RMS Pressure) Variation with High Scale Strouhal Number - Conical Frustum Measurements
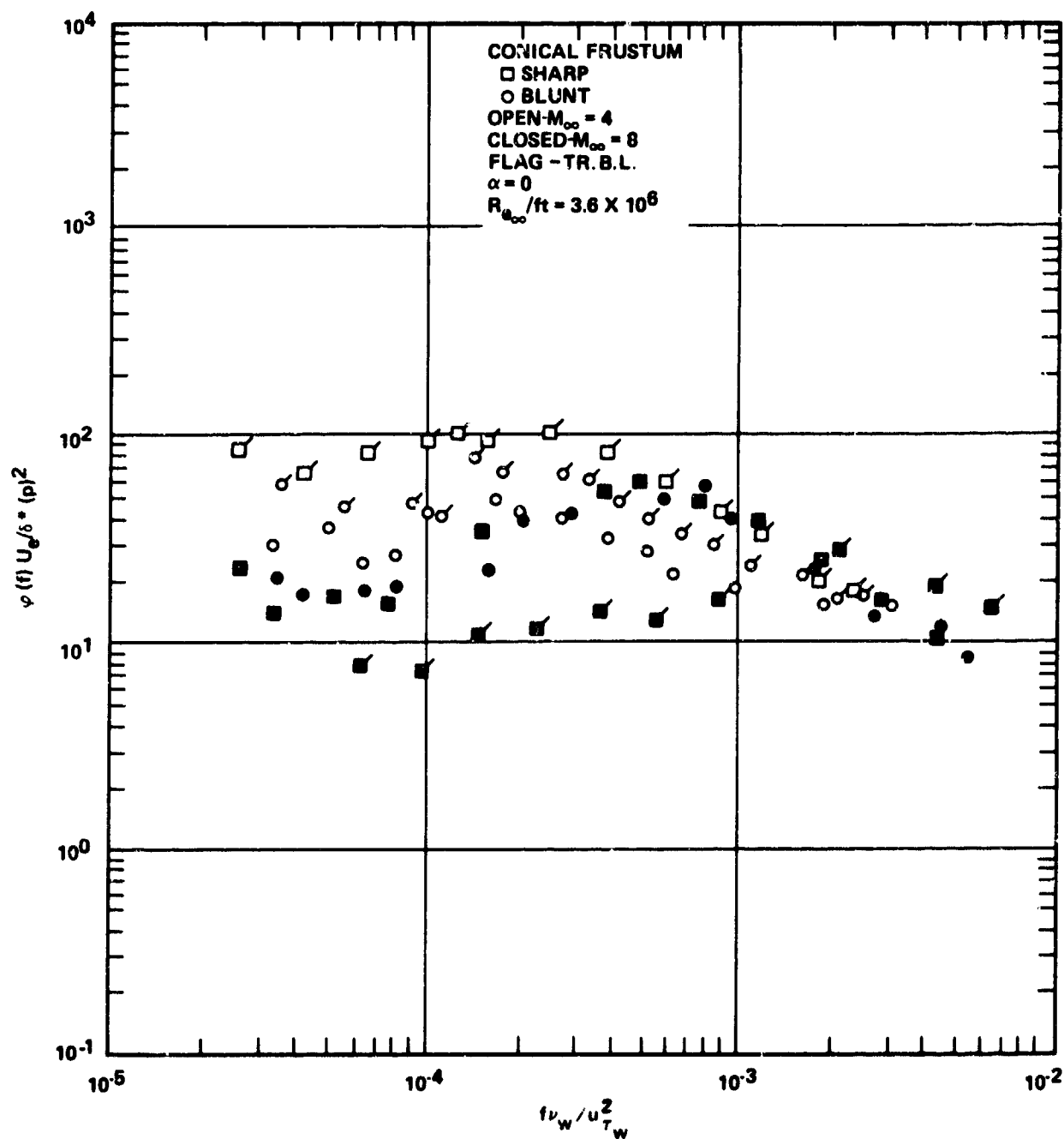
199

Figure 84. Normalized Power Spectral Density (with RMS Pressure) Variation with Low Scale Strouhal Number - Conical Frustum Measurements
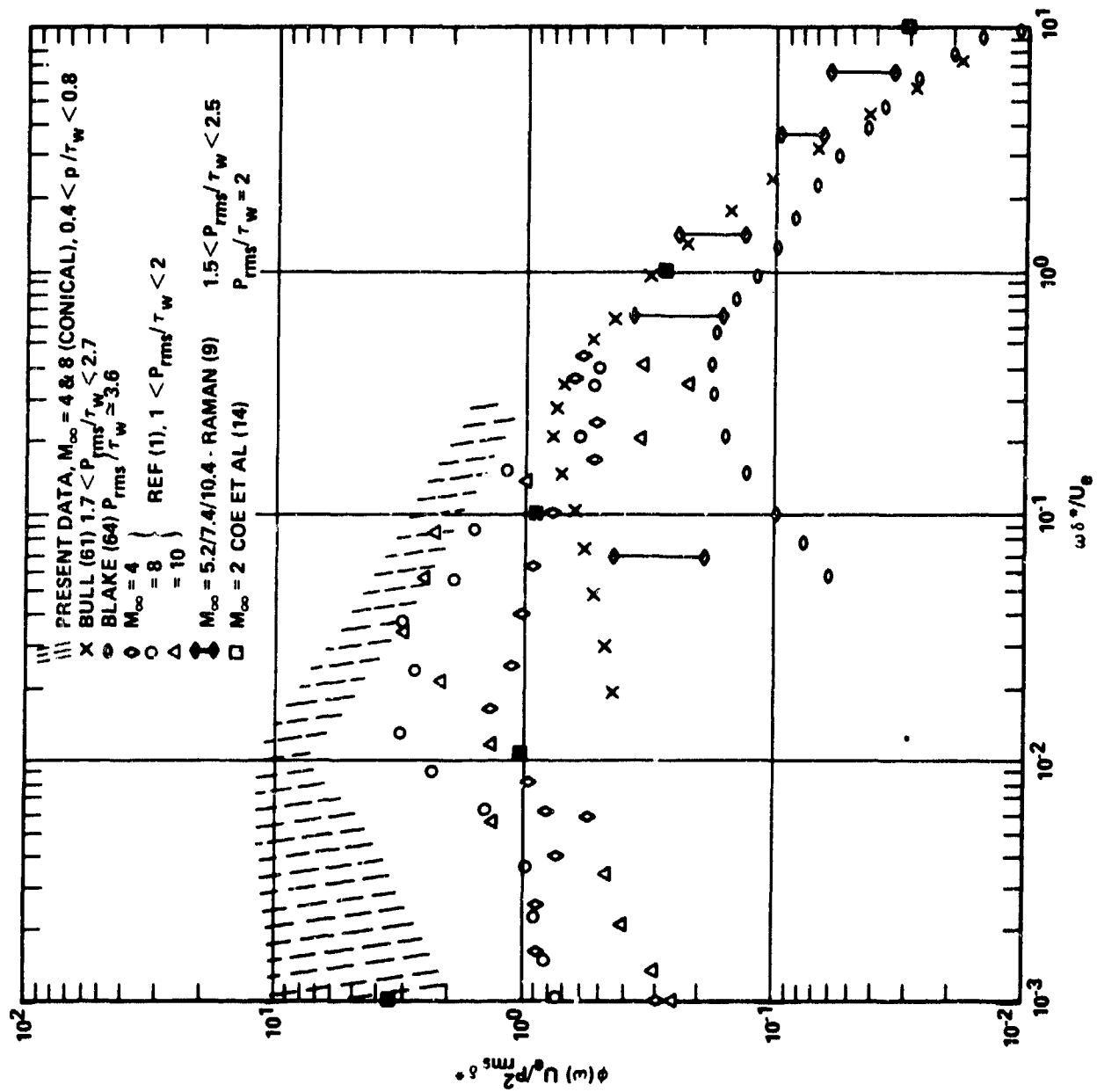
200

Figure 85. Comparison of Normalized Power Spectral Density for Incompressible and Compressible Conditions
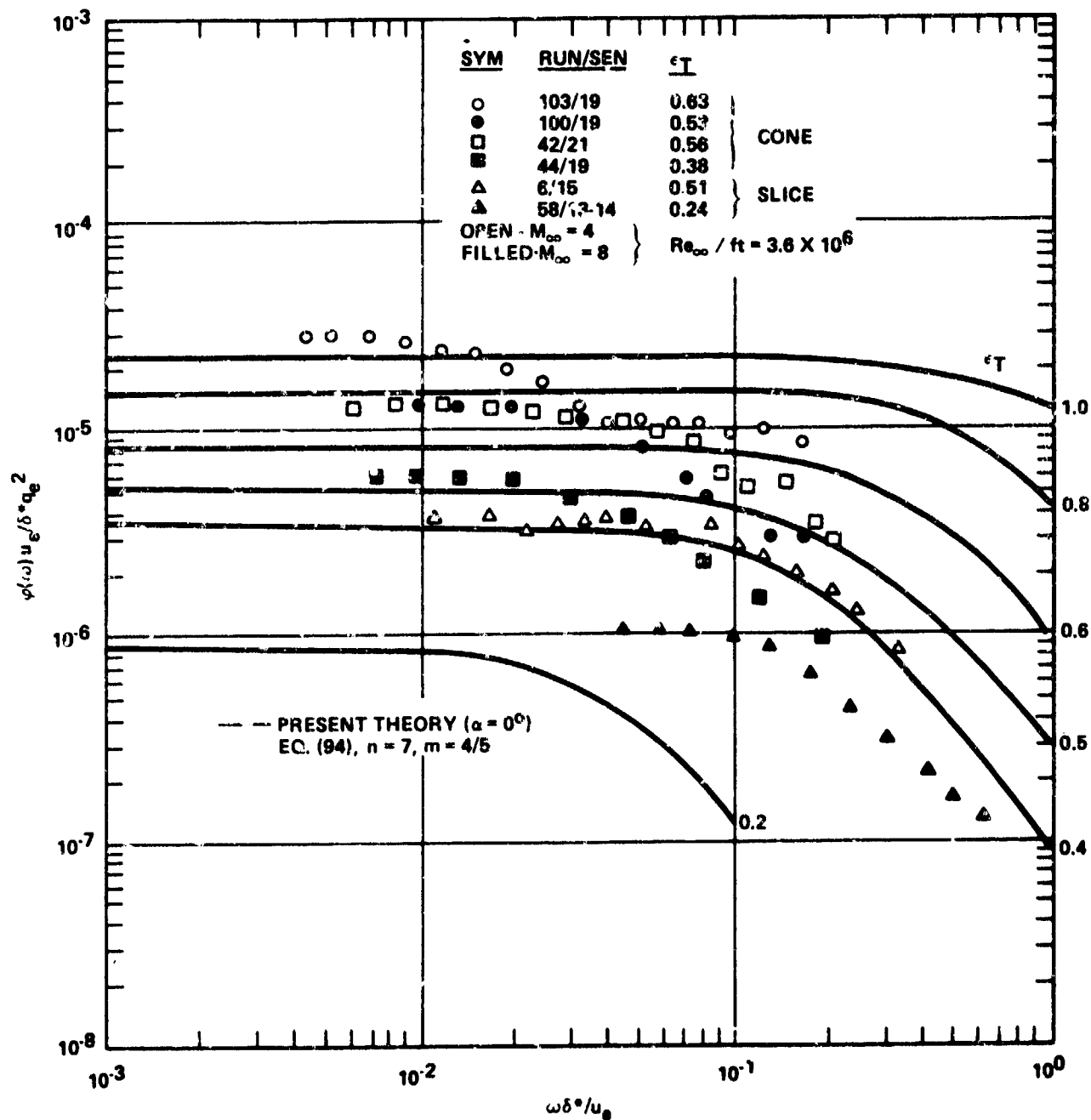
Figure 86. Comparison of Experimental Normalized Power Spectral Density with Theory
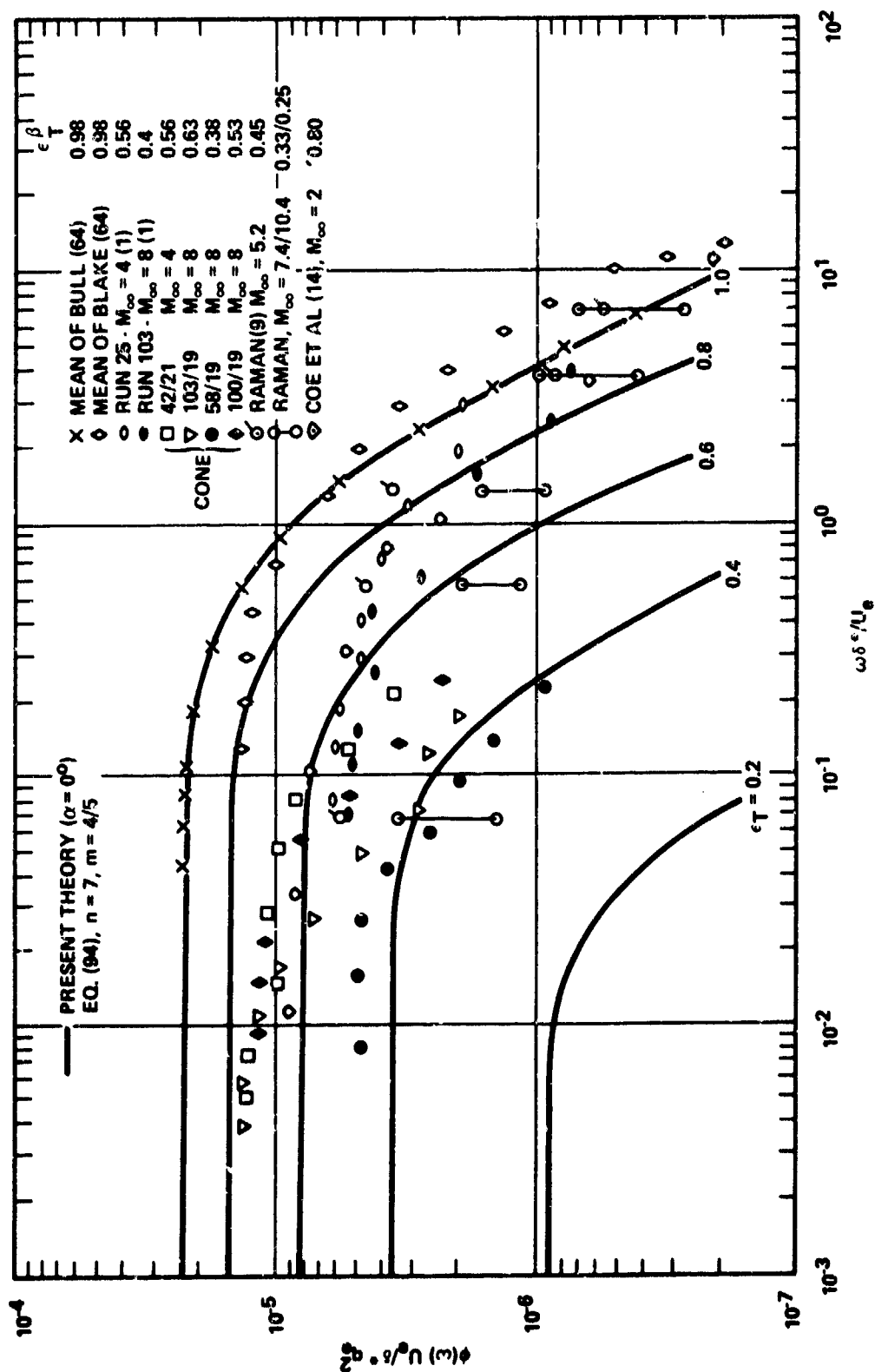
202

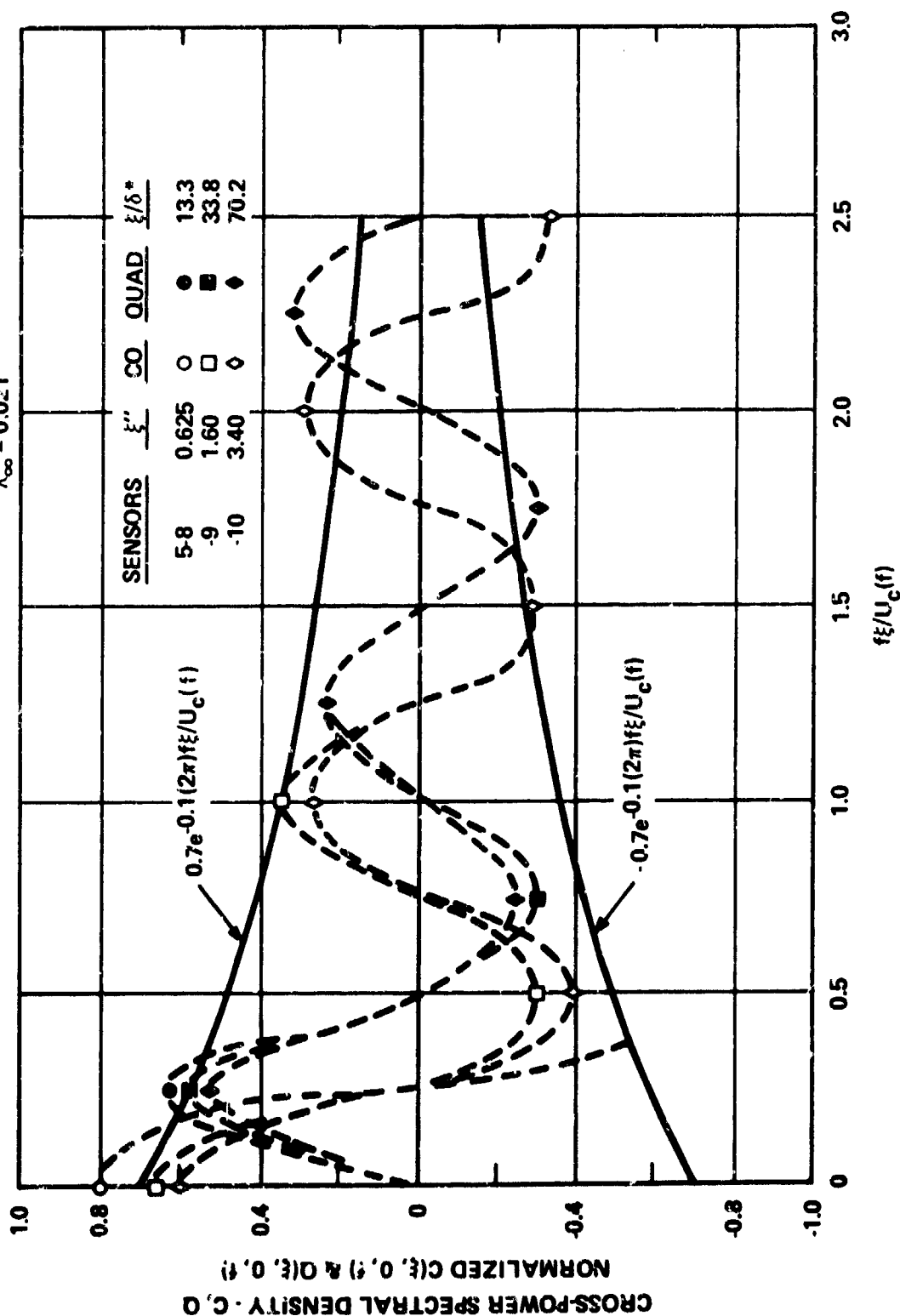Figure 87. Comparison of Present Normalized Spectral Measurements with Other Spectral Data and Theory

Figure 88. Longitudinal Cross-Power Spectral Density Measured in Fully Developed Turbulent Flow - Conical Frustum ($M_\tau = 4$)
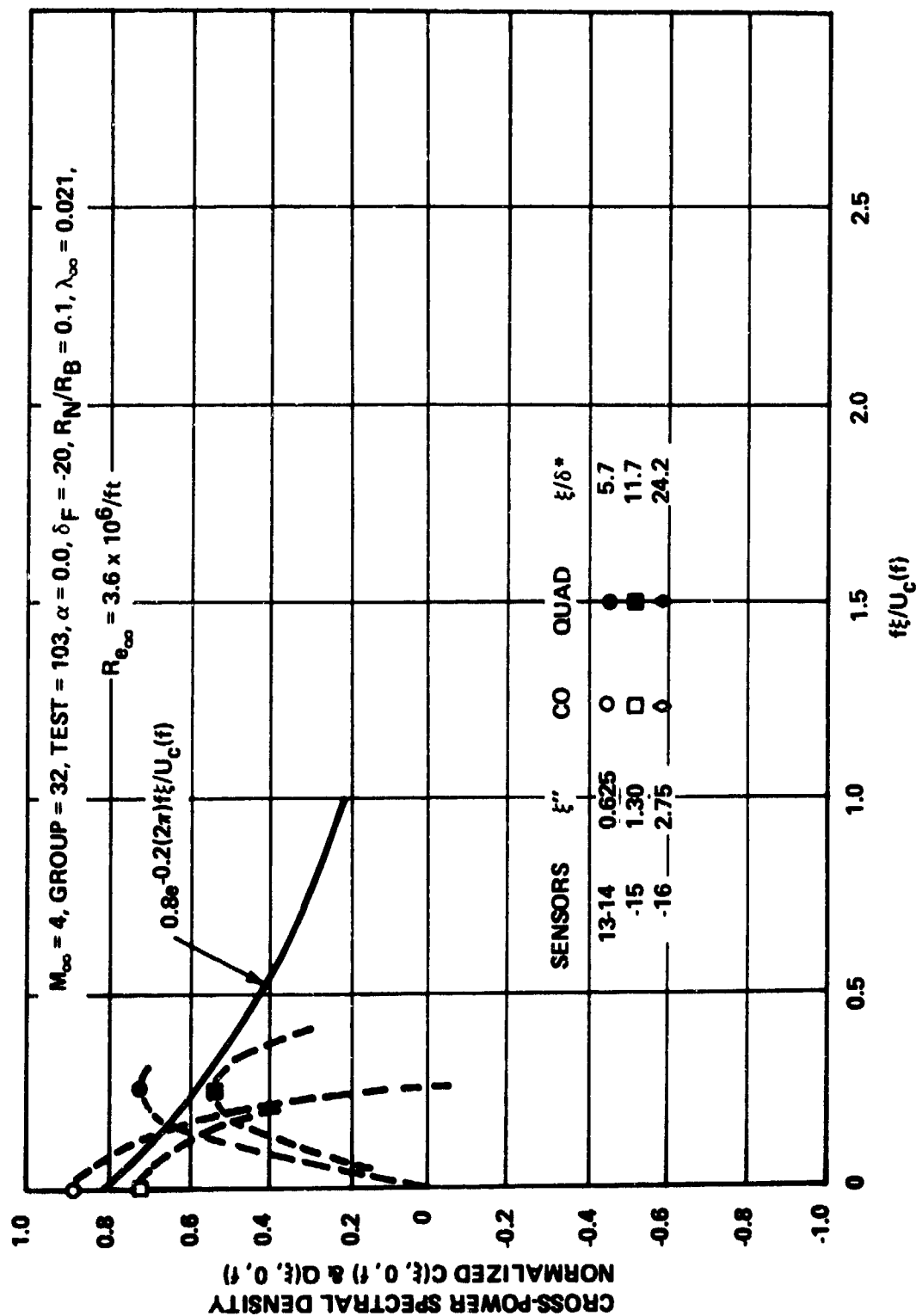
204

Figure 89. Longitudinal Cross-Power Spectral Density Measured in Fully Turbulent Flow - Slice ($M_\infty = 4$)

Figure 90. Longitudinal Cross-Power Spectral Density Measured in Fully Turbulent Flow - Slice ($M_\infty = 8$)

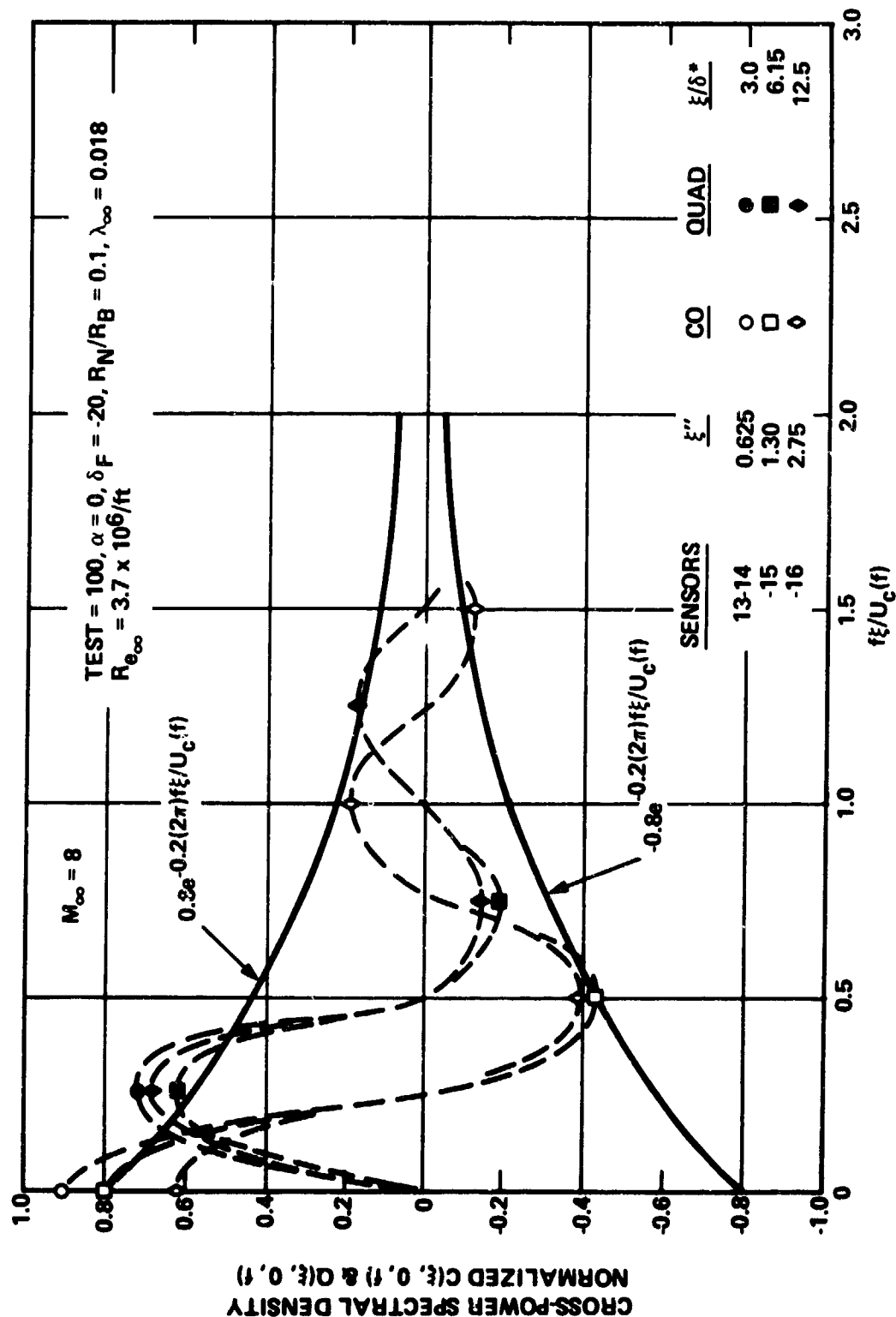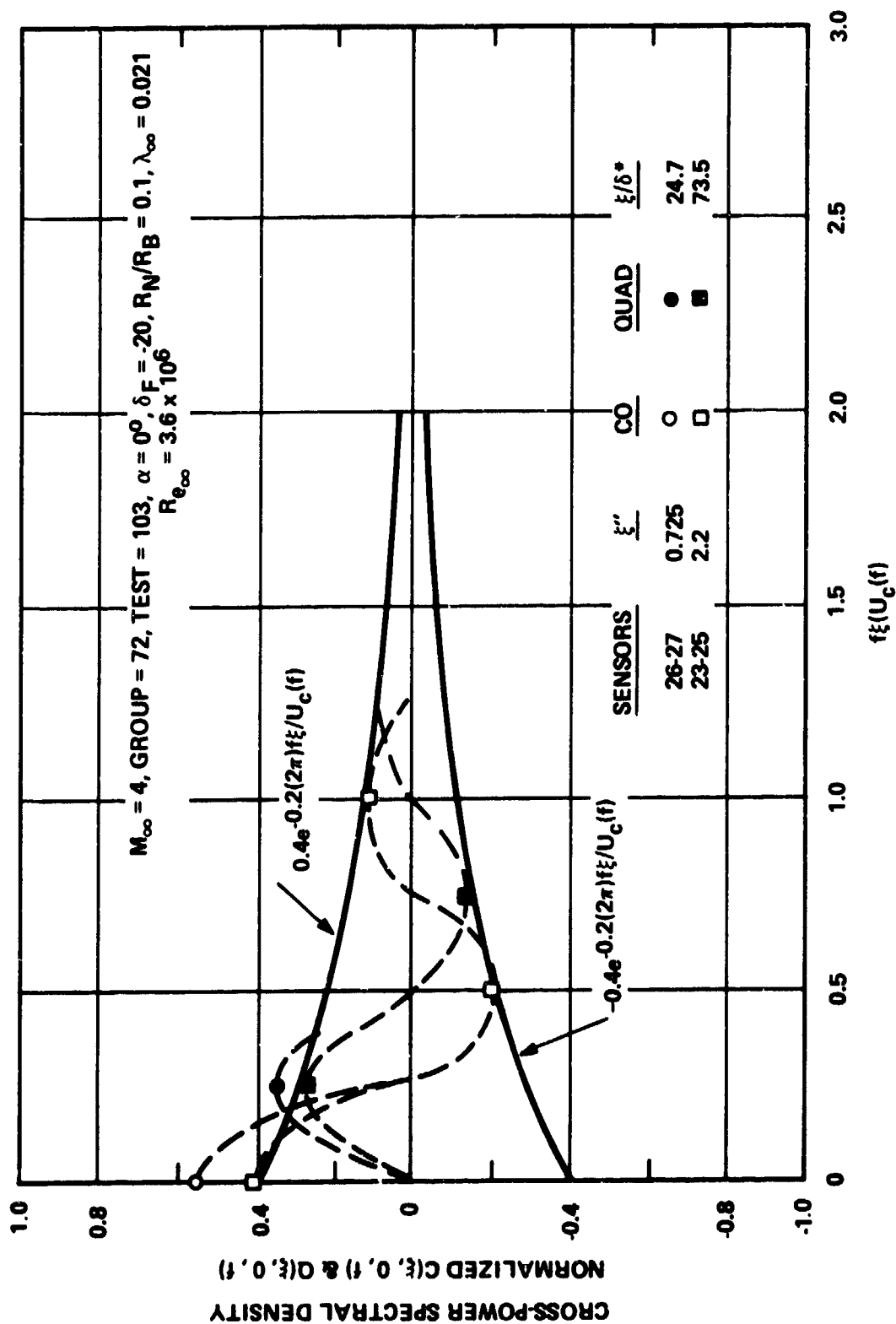Figure 91. Longitudinal Cross-Power Spectral Density Measured in Fully Turbulent Flow - Flap (M_∞ = 4)
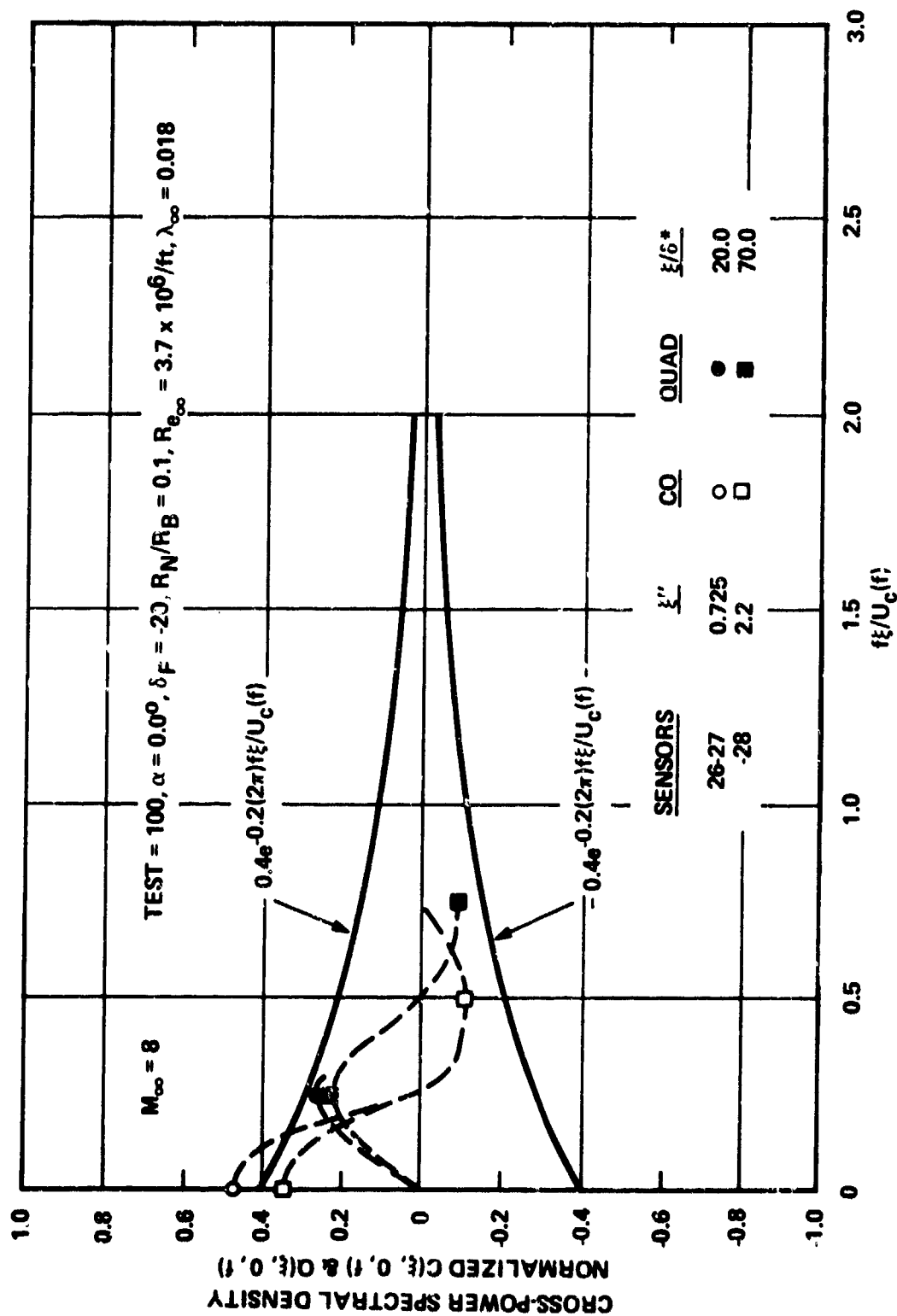
Figure 92. Longitudinal Cross-Power Spectral Density Measured in Fully Turbulent Flow - Flap ($M_\infty = 8$)
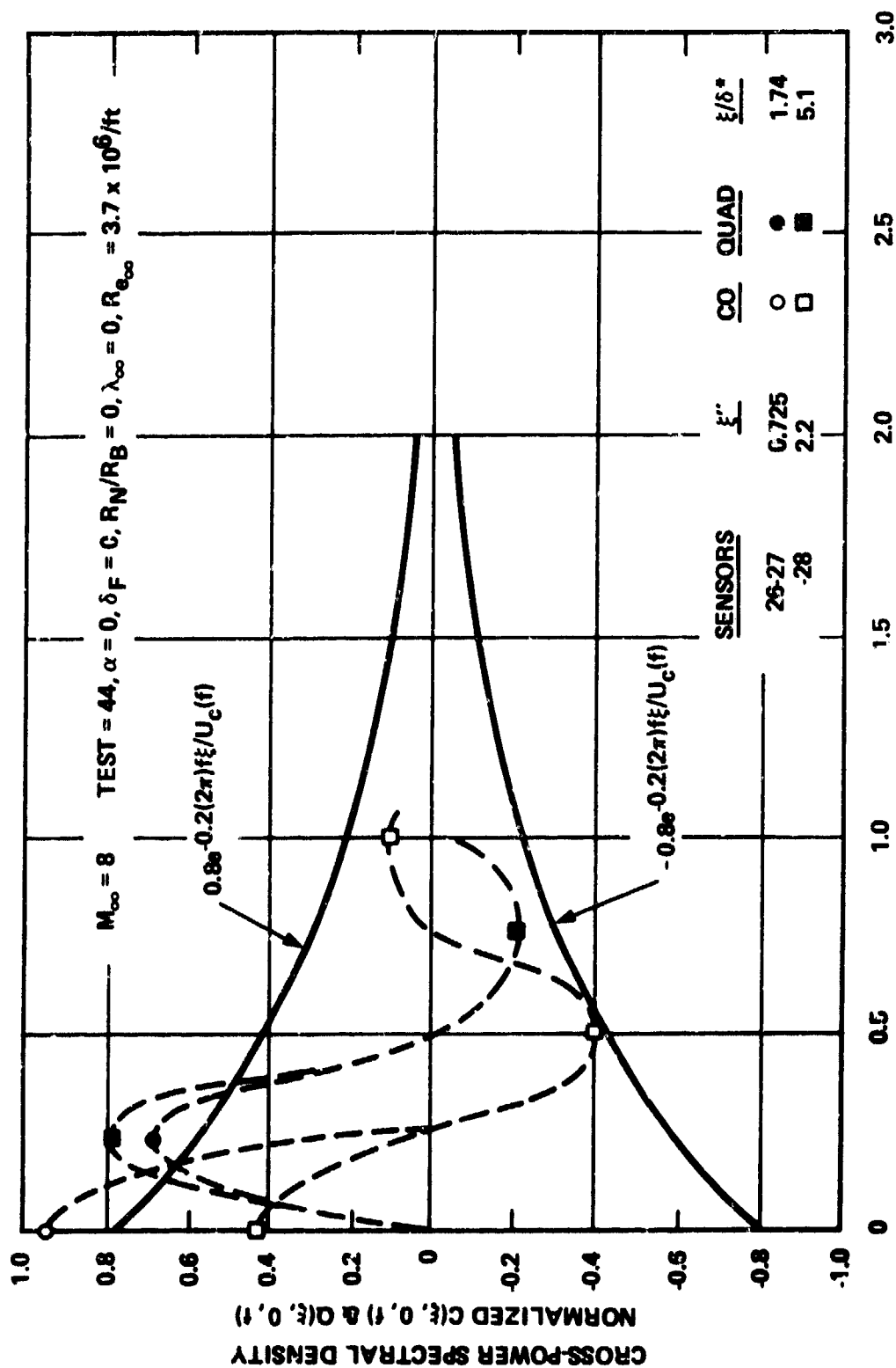
Figure 93. Longitudinal Cross-Power Spectral Density Measured in Fully Turbulent Flow - Flap, Sharp Cone Model (M_∞ = 8)
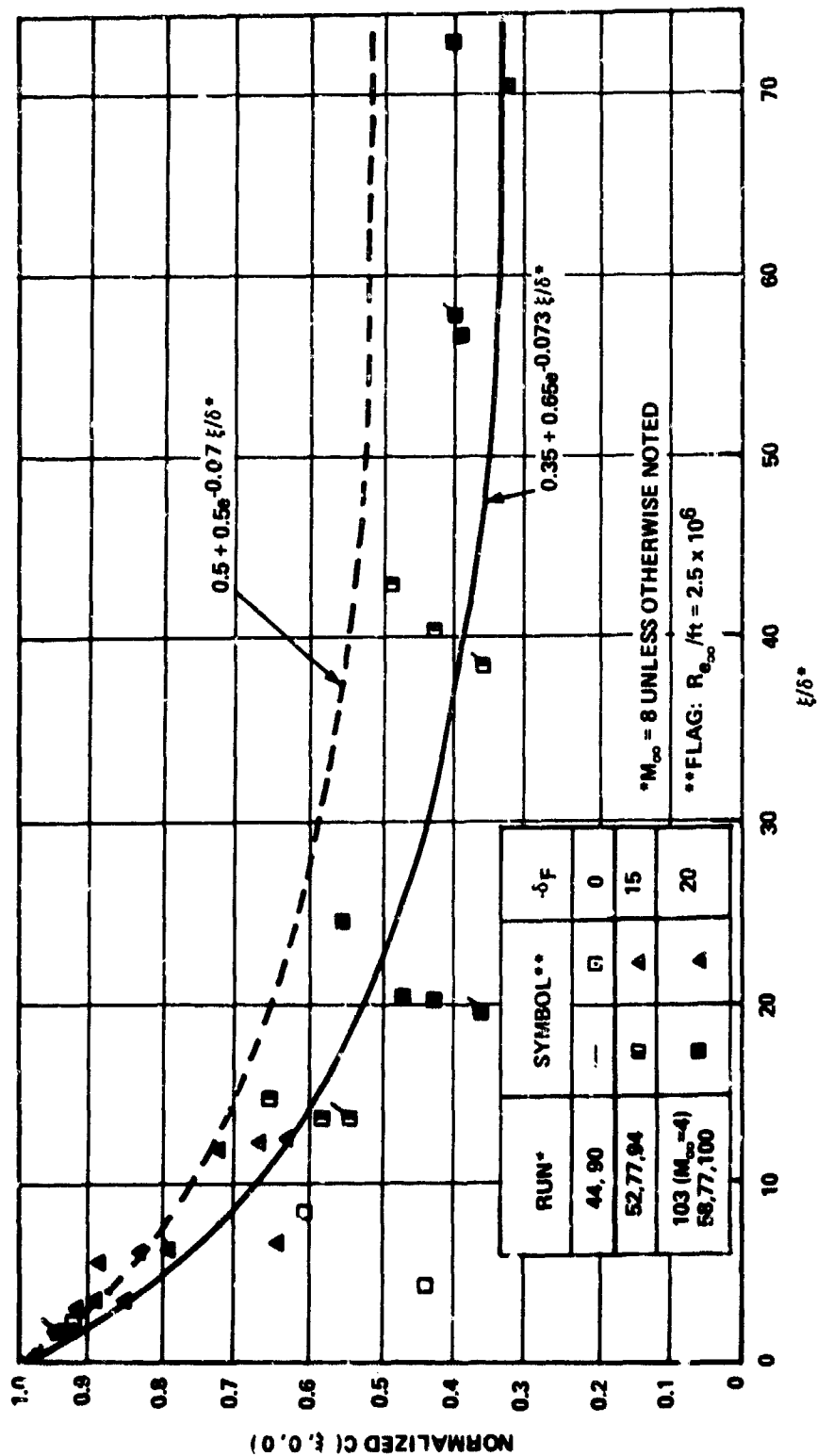
Figure 94. Asymptotic Values of Longitudinal Cross-PSD at $f\xi/u_c(\Omega) = 0$ Measured on the Slice and Flap ($M_\infty = 4, 8$)

Figure 95. Longitudinal Cross–Power Spectral Density Measured in Transitional Flow - Conical Frustum (M = 4)
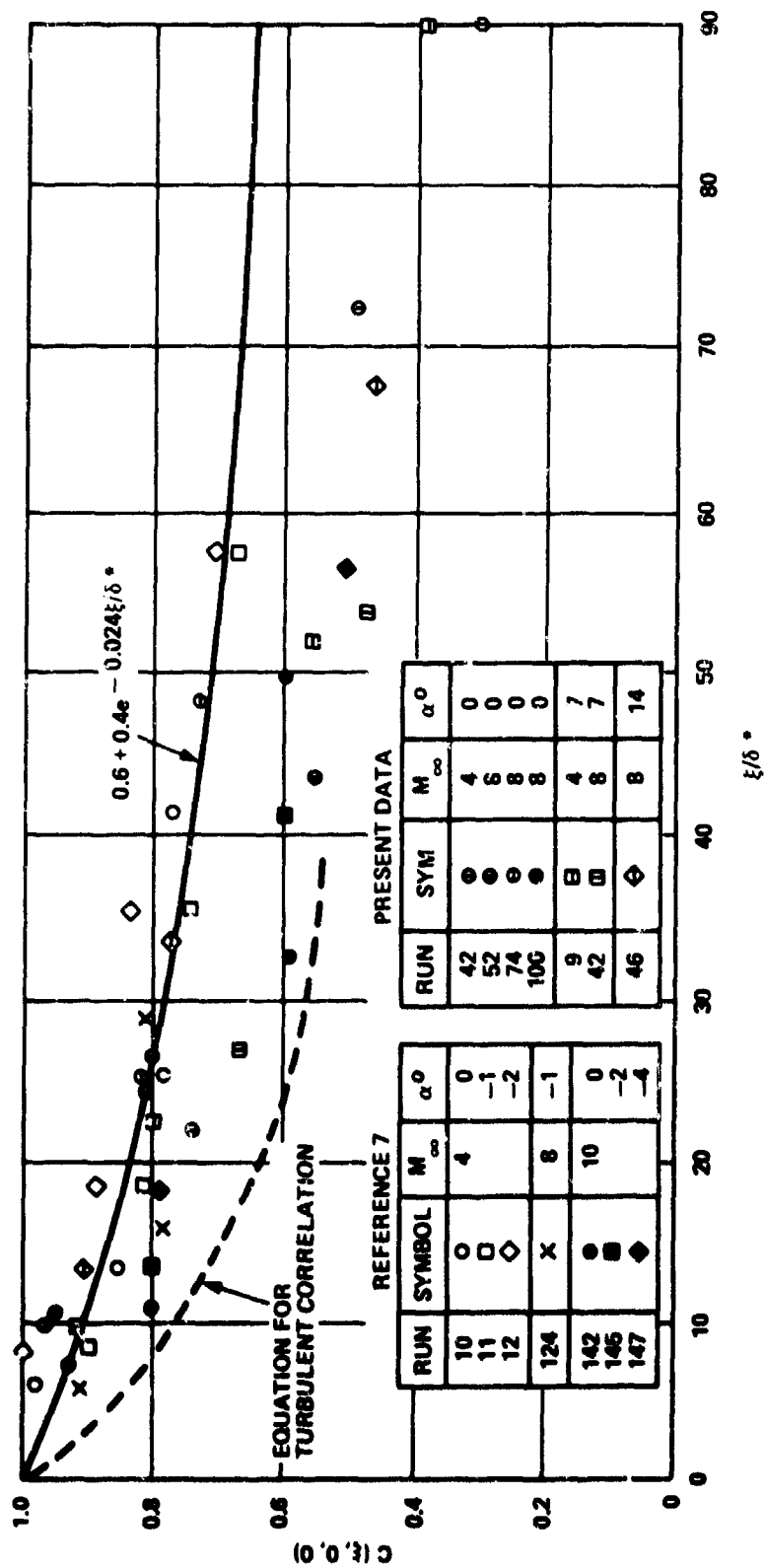
Figure 96. Asymptotic Values of Longitudinal Cross-Power Spectral Density at $f\xi / u_c$ (f) = 0 - Transitional Flow (M_∞ = 4, 8, 10)

212
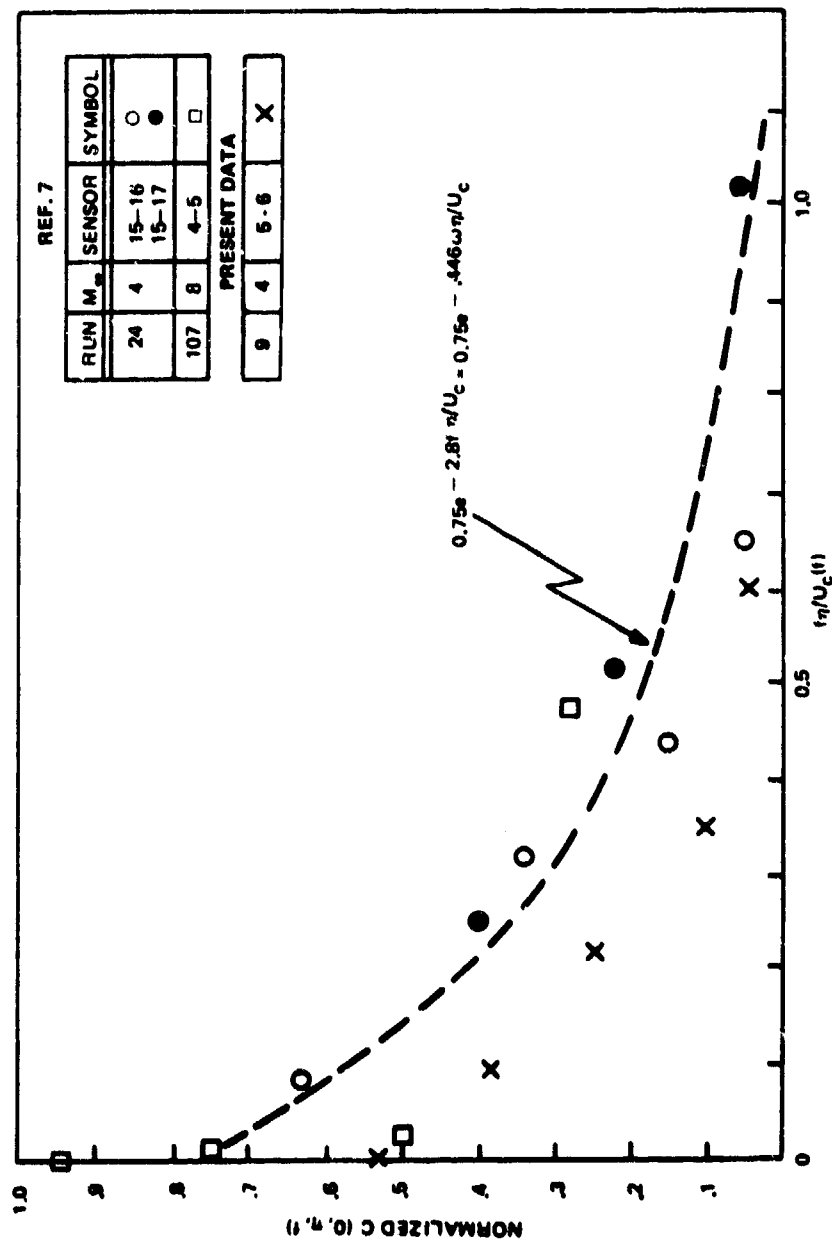
Figure 97. Circumferential Cross-Power Spectral Density - Transitional Flow at High Angle of Attack ($M_\infty = 4, 8$)

$M_\infty = 4$, GROUP 9, TEST = 42, $\alpha = 0.0$, $\delta_F = -20$, $R_N/R_B = 0$, $\lambda_\sigma = 0$,

$R_{e_\infty} = 3.6 \times 10^6/FT$

*NOTE: A-16 DISPLAYED ERRATIC BEHAVIOR AT MACH 4

$-0.2 (2\pi) f\xi/U_c (f)$

$0.6e$

$-0.2 (2\pi) f\xi/U_c (f)$

$-0.6e$

SENSORS	$\frac{\xi''}{L}$	CO	QUAD	$\xi/\delta*$
13-14	0.625	○	●	5.17
-15	1.30	□	■	10.7
-16*	2.75	◇	◆	21.9

$f\xi/U_c (f)$

CROSS-POWER SPECTRAL DENSITY
NORMALIZED C (ξ, 0, f) & Q (ξ, 0, f)

Figure 98. Longitudinal Cross-Power Spectral Density Measured in Fully Turbulent Flow - Slice, Sharp Cone Model ($M_\infty = 4$)

214

Figure 99. Longitudinal Cross-Power Spectral Density Measured in Fully Turbulent Flow - Slice, High α ($M_\infty = 4$)

APPENDIX: APPLICATION OF VIBRATION PREDICTION METHODS TO A BALLISTIC RE-ENTRY VEHICLE

1.0 INTRODUCTION

Computation of R/V response to boundary layer fluctuating pressures is performed by extending the principles developed in a previous GE/AFFDL contract (Reference 99). Response of both a ballistic and a maneuvering design are investigated in Volume II, utilizing the overall approach indicated in Figure A-1. This appendix summarizes the unclassified techniques/results of the ballistic R/V analysis which incorporates key parameters of the fluctuating pressure environment derived in Volume I for the conical portion of the model. These parameters are the overall rms pressure, power spectral 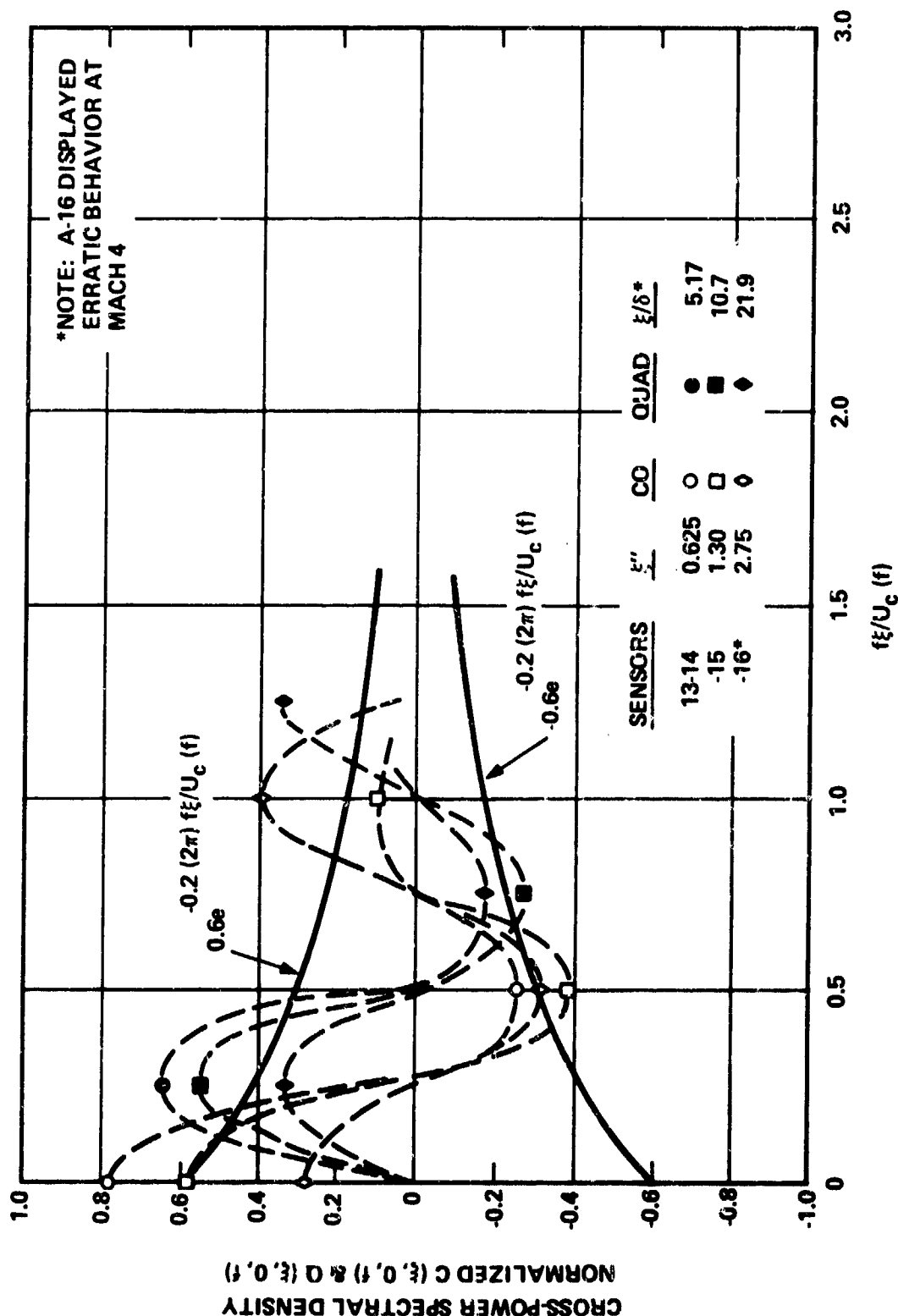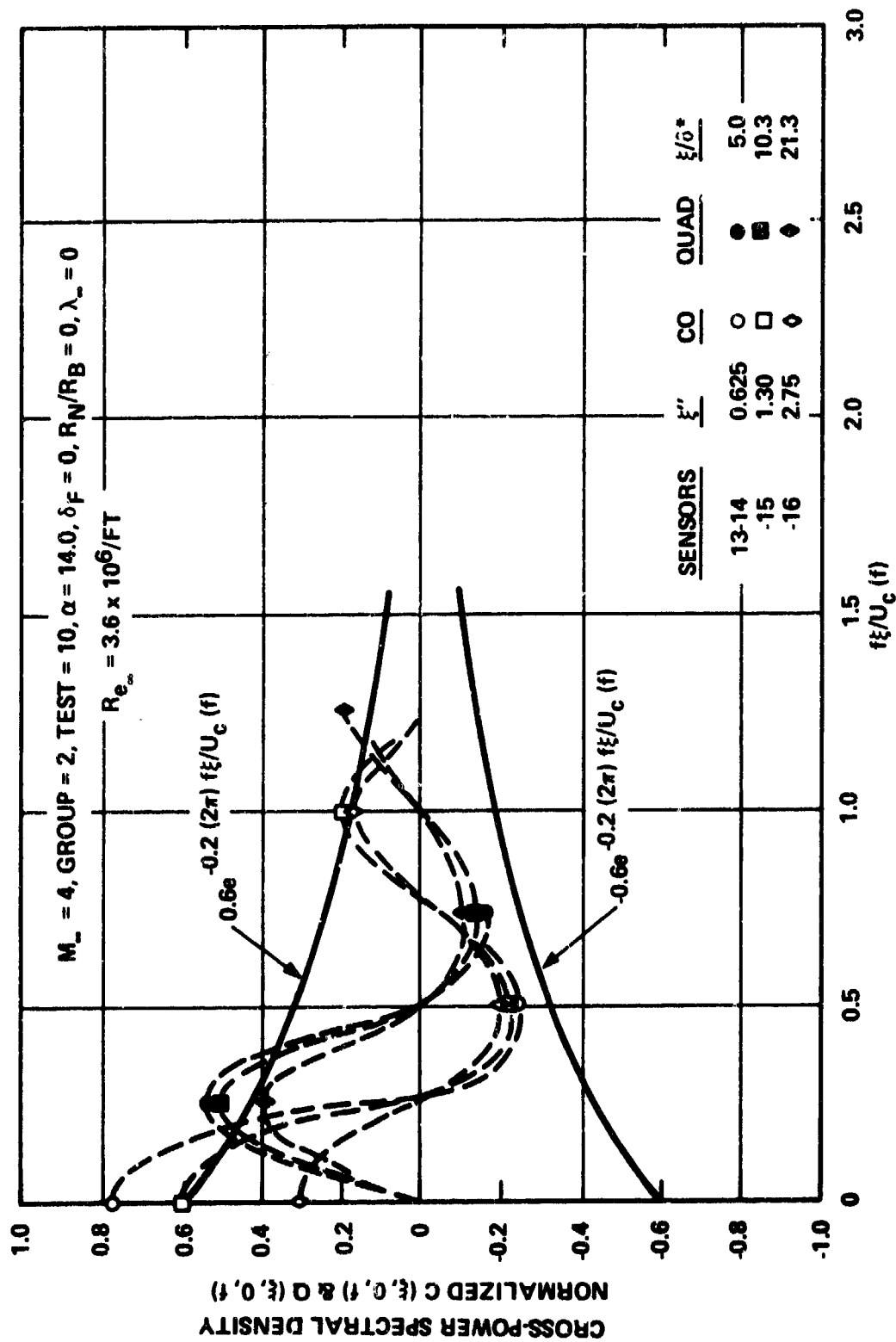density, and cross-power spectral density (narrow-band spatial correlation function). Ballistic re-entry flight data and corresponding vibration predictions at one altitude are compared as a baseline which establishes overall validity of the upgraded computational technique.

The particular ballistic configuration investigated consists of a prototype operational design. Responses at various internal locations (see Figure A-2) were monitored for several flights having approximately the same trajectory and freestream aerodynamic characteristics. A typical vibration response power spectral density compilation for the axial direction is presented in Figure A-3. For the ESD, lateral flight data are generally higher than those vibration levels which would be applicable in component ground testing, due to the fact that the component extremity, rather than the CG or the individual mounting location, was instrumented. Maximum vibration levels corresponding to fully developed turbulent boundary layer flow were measured to be approximately the following: $.007 \text{ g}^2/\text{Hz}$ axially on the payload, $.02 \text{ g}^2/\text{Hz}$ laterally on the aft bulkhead, and $.3 \text{ g}^2/\text{Hz}$ laterally at the tip of the ESD.

2.0 ANALYSIS

In the ballistic vehicle dynamic model, the R/V structure is idealized as an axisymmetric lumped-parameter (spring-mass) system. As a consequence of basic vehicle symmetry, axial motions and bending motions (lateral, rotational) are mutually uncoupled and are therefore treated separately; further, bending motions are simplified by considering planar motion only. Dynamic motions are described by totals of 46 axial and 80 lateral-rotation degrees-of-freedom at vehicle mass points (model nodes).

The structural dynamic model is comprised of the following subsystems: the nosetip-forward frustum, mid frustum, aft frustum, aft cover, payload, bulkhead with components, and the forward component. A beam finite-element formulation is the basis for the frustum subsystems, which together contain a total of 27 nodes (26 elements) representing the vehicle external structure (shell) and include the effects of the two field joints. The remaining subsystems are basically semi-empirical in that they were originally defined by analysis and subsequently updated on the basis of correlations with ground test results. The aft cover subsystem comprises seven model nodes, and couples to the aftmost vehicle shell node; in the bending model, this subsystem is simplified to a mass effect only at this shell location because of the high frequency nature of the aft cover lateral characteristics. Ten model nodes describe the motions of the payload and its support structure, and this subsystem, defined by the payload contractor, is supported at three points on the vehicle shell. The component bulkhead model subsystem consists of seven nodes, representing the shell support point, bulkhead center and five principal components individually. Finally, the forward component subsystem contains five nodes, four representing vehicle shell support locations and one the motion at the assembly center.

Total model stiffness and mass matrices were developed by assembling the parameters of the model subsystems. Then the eigenvalue problem posed by these matrices in the equations of motion was solved by computer to give the R/V natural resonant frequencies and mode shapes. These dynamic characteristics, summarized in Table A-I, were then recorded on computer tape for subsequent use in response analyses.

Analysis of ballistic vehicle response concentrated on the point in the trajectory where dynamic pressure is a maximum. Boundary layer characteristic parameters corresponding to this particular attitude were calculated along the vehicle surface using GE-RESD computer program 3DFF.[93] Applicable boundary layer properties so computed are summarized for R/V aft cone locations in Table A-II.

Equations utilized to convert aerodynamic characteristics to the form required for computation of R/V structural response using the approach of Figure A-1 are described below.

2.1 PSD

Equation (94) of Volume I yields the following expression for power spectral density:

$$\varphi(f) = 2\pi\varphi(\omega) = \frac{4\delta^* q_e^2 \, (\sigma/q_e)_i^2 \, \epsilon_T^2 / u_e}{1 + \epsilon_T^{-4} \, (2\pi f \delta^*/u_e)^2} \tag{A1}$$

where

$$(\sigma/q_e)_i = .006$$

and

$$\epsilon_T = (T^*/T_e)^{[2m - (1+n)]/[3+n]} \tag{A2}$$

with

$$T^*/T_e = [1/2 \, (1 + T_w/T_e) + .22 \, r \, (\tfrac{\gamma-1}{2}) \, M_e^2 \,] \tag{A3}$$

For fully turbulent conditions during re-entry, in which the R/V wall temperature is very much less than the adiabatic wall temperature, (A2) reduces to

$$\epsilon_T = [0.5 + 0.02 \, M_e^2 \,]^{-.68} \tag{A4}$$

with r = turbulent recovery factor = .896,

γ = 1.2 for re-entry,

n = 7,

and m = .6 (from Reference 85).

Therefore Equations (A1) and (A4) define the PSD over a ballistic re-entry vehicle subjected to fully turbulent flow.

2.2 Cross-PSD

It was discovered that the longitudinal cross-spectral coefficient representation which was generated on the basis of extremely limited TBL data over the cone (Run 103, Tunnel A) provided a better match with ballistic flight data. Therefore this cross-PSD representation is presented here. Equations utilized in the computation of ballistic re-entry vibration response are:

218

$$A_\xi(\xi,\omega) = e^{-0.1\omega\xi/u_c}[0.58 + 0.42\, e^{-0.0486\,\xi/\delta*}] \tag{A5}$$

$$A_\eta(\eta,\omega) = e^{-1.4\omega\eta/u_c}\, e^{-0.0195\,\eta/\delta*} \tag{A6}$$

3.0 RE-ENTRY VIBRATION PREDICTIONS

Table A-III summarizes computations for the ballistic vehicle and presents maximum response levels for various internal and external (nose, shell) locations. It is evident that there is quite good correlation with flight measurements derived from envelopes of response spectra in fully turbulent flow, except for bulkhead axial responses. Here, one notes an order of magnitude discrepancy between maximum flight data and the predictions (Figure A-3). However, it should be pointed out that the particular response PSD which contributes the .022 g^2/Hz peak is approximately one decade higher than the majority of power spectra obtained in other similar flights for the same instrumented location. Therefore this bulkhead axial measurement represents a 3σ or higher response, while predictions based on nominal conditions provide generally good agreement with other data shown.

For bulkhead lateral responses, flight data are respectively slightly less than or greater than predicted levels, depending on location. That is, for locations designated NG and FS, flight measurement stations are closer to the aft bulkhead than the model node points, such that the moment arms which affect lateral response are shorter. This situation is reversed for the ESD where measurements were acquired on the tip of the component; hence at lateral rocking frequencies, flight responses are magnified over levels predicted at the ESD center of gravity.

Maximum vibration levels computed for the R/V nose and for the shell are also presented in Table A-III. Axial and lateral responses correspond respectively to the 0th and 1st harmonics of the vehicle structural dynamic model. If effects of higher harmonics were accounted for, significantly higher shell responses would result, but component levels would be virtually unchanged. This is due to the fact that component packages are generally mounted on support structure such that their primary behavior is simple beam-column motion. The support structure does not transmit vibration levels associated with high harmonic shell response.

TABLE A-I
BALLISTIC R/V DYNAMIC MODEL:
SUMMARY OF DYNAMIC CHARACTERISTICS
TO ≈ 2000 HZ

ORDER	AXIAL		LATERAL	
	NAT. FREQ. (HZ)	MODE SHAPE DESC.	NAT. FREQ. (HZ)	MODE SHAPE DESC.*
1	0	RIGID BODY	0	RIGID BODY
2	110.4	AFT COVER	0	RIGID BODY
3	159.8	AFT BULKHEAD	184.6	SHELL
4	216.2	FORWARD COMP	213.5	SHELL-P/L-AFT B/H
5	334.9	AFT BULKHEAD	236.4	AFT BULKHEAD
6	459.7	SHELL-PAYLOAD	272.2	PAYLOAD
7	531.8	AFT BULKHEAD	378.1	SHELL-P/L
8	568.9	AFT COVER	410.7	AFT BULKHEAD
9	841.2	AFT COVER	423.0	AFT BULKHEAD
10	875.7	AFT BULKHEAD	459.9	AFT B/H-SHELL
11	921.0	R/V AXIAL	494.7	SHELL-P/L
12	966.8	AFT BULKHEAD	564.7	SHELL-F/C-AFT B/H
13	1089.2	SHELL-PAYLOAD	596.4	AFT B/H-P/L
14	1102.1	AFT COVER	634.2	AFT B/H-P/L
15	1206.5	AFT COVER	692.9	AFT B/H-P/L
16	1638.4	SHELL	738.4	P/L-AFT B/H-SHELL
17	1755.1	AFT BULKHEAD	772.1	PAYLOAD
18	1815.6	PAYLOAD	900.3	SHELL-F/C-P/L
19	2107.1	AFT COVER	1059.8	P/L-SHELL
20	—		1324.3	SHELL
21	—		1363.0	SHELL-F/C
22	—		1626.0	SHELL-AFT B/H
23	—		1746.1	AFT BULKHEAD
24	—		2065.3	AFT BULKHEAD

*P/L = PAYLOAD

A/C = AFT COVER

B/H = BULKHEAD

F/C = FORWARD COMP.

TABLE A-II. SUMMARY OF TRAJECTORY AND MAXIMUM AERO-ACOUSTIC CONDITIONS FOR BALLISTIC VEHICLE

		VALUES AT R/V AFT CONE
AERODYNAMIC	δ^* (IN)	.112
PARAMETERS	U_e (IN/SEC)	1.7×10^5
(q_∞ = MAX)	M_e	9.23
	q_e (PSI)	2130
AEROACOUSTIC	$\varphi(0)$ (PSI^2/HZ)	1.4×10^{-4}
ENVIRONMENTS	OASPL (dB)	188

TABLE A-III. BALLISTIC VEHICLE RE-ENTRY RANDOM VIBRATION DATA

(MAXIMUM LEVELS IN TURBULENT BOUNDARY LAYER FLOW)*

ITEM (Location**)	FLIGHT MEASUREMENTS (Peak Spectral Levels From 7 Flights)				RESPONSE PREDICTIONS			
	Axial		Lateral		Axial		Lateral	
	Level (g^2/Hz)	Freq. (Hz)	Level (g^2/Hz)	Freq. (Hz)	Level (g^2/Hz)	Freq. (Hz)	Level (g^2/Hz)	Freq. (Hz)
Payload (Aft Station)	.007	600	.005	180	.0047	460	.0046	495
	.006	500	.004	320	.00024	532	.0030	738
Aft Bulkhead (NG,FS)	.02	500	.022	450	.0035	160	.059	1746
	.013	550	.022	800	.0032	460	.044	1626
							.038	236
							.018	460
(ESD)	--	--	.3	450	--	--	.11	634
			.2	300			.049	596
Nose	--	--	--	--	.02	921	.45	495
Shell	--	--	--	--	.033	1638	.038	495
					.022	460	.027	1626

* Responses listed in descending order by magnitude.
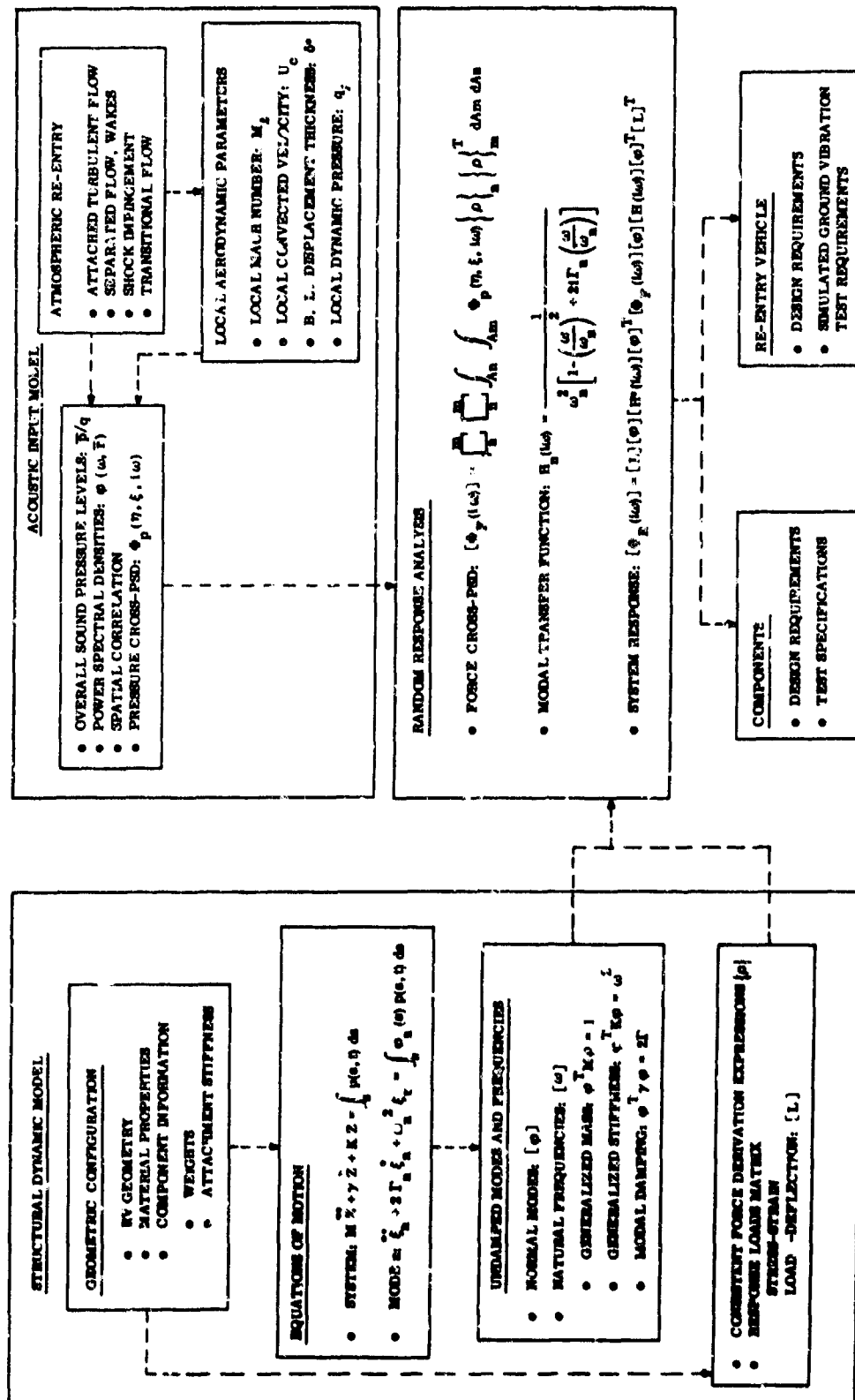
** Flight location as identified in sketch

FIGURE A-1. SUMMARY OF VIBRATION RESPONSE PREDICTION TECHNIQUE

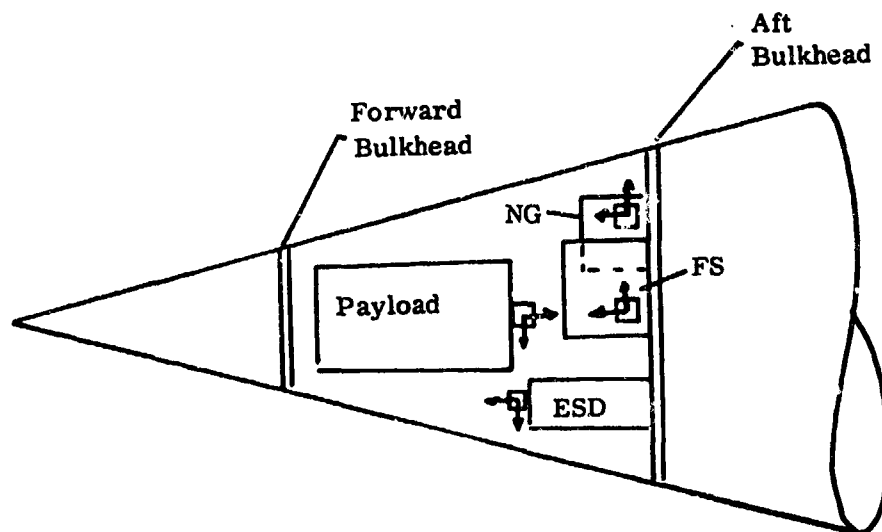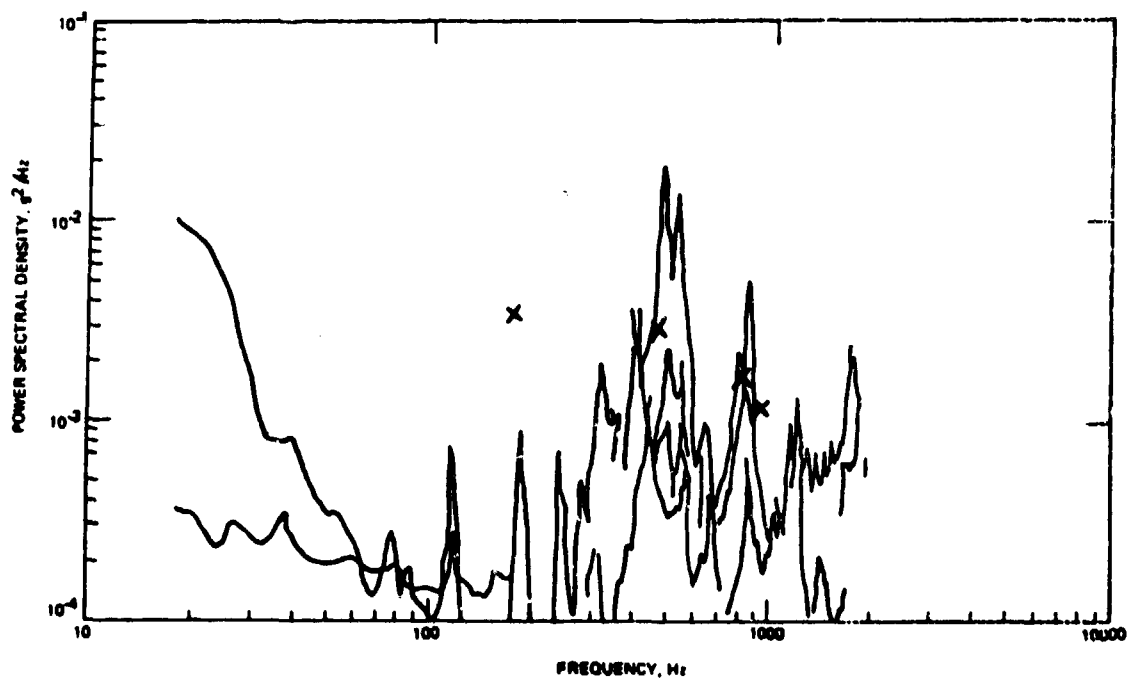## FIGURE A-2. R/V FLIGHT ACCELEROMETER LOCATIONS

FIGURE A-3. COMPARISON OF ANALYSIS WITH BALLISTIC RE-ENTRY FLIGHT DATA (TBL)

AFT BULKHEAD AXIAL RESPONSE

——————— FLIGHT DATA

X   ANALYSIS PEAKS